



Structural and Corrosion Properties of Hydrogenated Amorphous Carbon Films with
Silicon-Based Interlayer

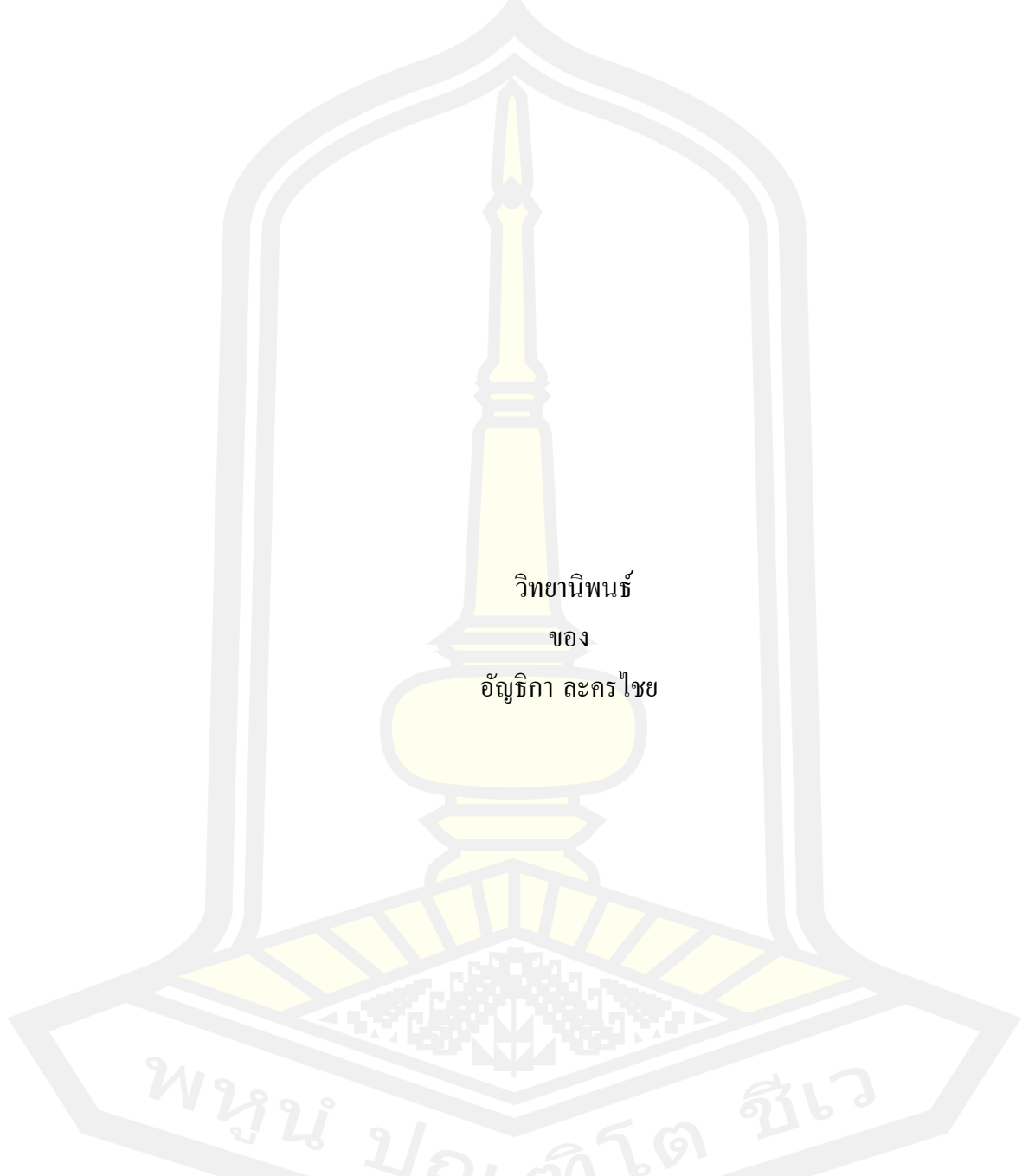
Anthika Lakhonchai

A Thesis Submitted in Partial Fulfillment of Requirements for
degree of Doctor of Philosophy in Physics

May 2022

Copyright of Mahasarakham University

สมบัติเชิงโครงสร้างและการกักกรองของฟิล์มไฮโดรเจนเทตอะเมอร์ฟัสคาร์บอนที่มีซิลิกอนเป็น
ชั้นรองพื้น



เสนอต่อมหาวิทยาลัยมหาสารคาม เพื่อเป็นส่วนหนึ่งของการศึกษาตามหลักสูตร
ปริญญาปรัชญาดุษฎีบัณฑิต สาขาวิชาฟิสิกส์

พฤษภาคม 2565

ลิขสิทธิ์เป็นของมหาวิทยาลัยมหาสารคาม

Structural and Corrosion Properties of Hydrogenated Amorphous Carbon Films with
Silicon-Based Interlayer



Anthika Lakhonchai

A Thesis Submitted in Partial Fulfillment of Requirements
for Doctor of Philosophy (Physics)

May 2022

Copyright of Mahasarakham University



The examining committee has unanimously approved this Thesis, submitted by Miss Anthika Lakhonchai , as a partial fulfillment of the requirements for the Doctor of Philosophy Physics at Maharakham University

Examining Committee

.....	Chairman
(Prof. Vittaya Amornkitbamrung , Ph.D.)	
.....	Advisor
(Asst. Prof. Artit Chingsungnoen , Ph.D.)	
.....	Co-advisor
(Asst. Prof. Phitsanu Poolcharuansin , Ph.D.)	
.....	Committee
(Nitisak Pasaja , Ph.D.)	
.....	Committee
(Asst. Prof. Kwanruthai wongsaprom , Ph.D.)	
.....	Committee
(Assoc. Prof. Paveena Laokul , Ph.D.)	

Maharakham University has granted approval to accept this Thesis as a partial fulfillment of the requirements for the Doctor of Philosophy Physics

.....
(Prof. Pairoit Pramual , Ph.D.)
Dean of The Faculty of Science

.....
(Assoc. Prof. Krit Chaimoon , Ph.D.)
Dean of Graduate School

TITLE	Structural and Corrosion Properties of Hydrogenated Amorphous Carbon Films with Silicon-Based Interlayer		
AUTHOR	Anthika Lakhonchai		
ADVISORS	Assistant Professor Artit Chingsungnoen , Ph.D. Assistant Professor Phitsanu Poolcharuansin , Ph.D.		
DEGREE	Doctor of Philosophy	MAJOR	Physics
UNIVERSITY	Maharakham University	YEAR	2022

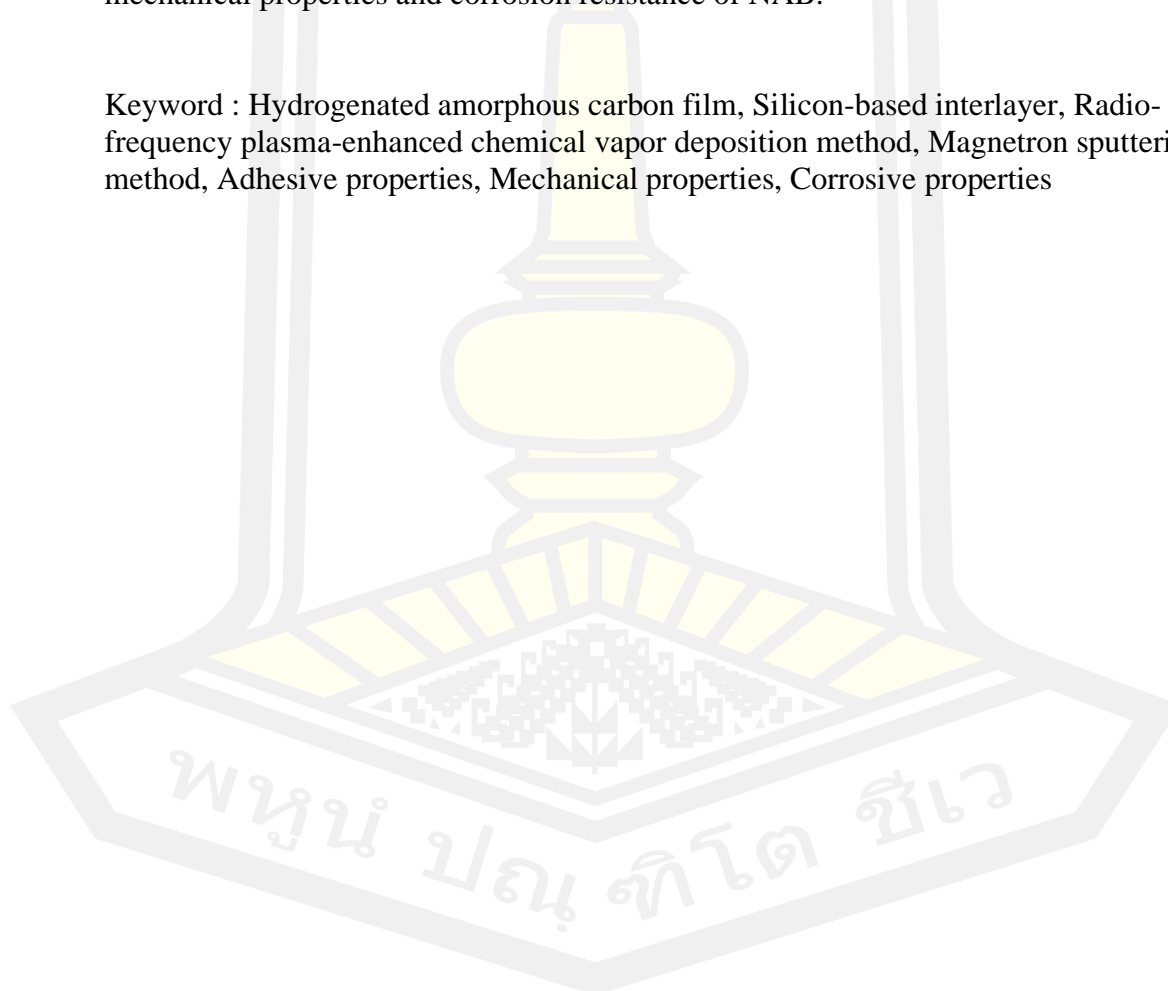
ABSTRACT

The main objective of this work is to improve the mechanical properties and corrosion resistance of chromium-plated and NAB substrates by a-C:H coating using the RF-PECVD method. For the chromium-plated substrate, the silicon-based interlayers were prepared using the DCMS method. The a-C:H films with silicon-based interlayers were characterized by X-ray photoelectron spectroscopy (XPS), Raman spectroscopy, field emission-secondary electron microscopy, nanoindentation, micro-scratching, and electrochemical corrosion measurements in terms of structure, morphology, mechanical and adhesive properties, and corrosion resistance. The surface morphology shows very homogeneous, smooth and dense microstructures without microparticle defects. The cross-sectional morphology between the a-C:H films and the interlayers shows a clear boundary at the interface without delamination and cracking, indicating good adhesive properties. The average thickness of the a-C:H films and the silicon-based interlayers was determined to be 317 ± 12.99 and 306 ± 14.23 nm, respectively. The Raman spectra of the a-C:H films clearly show the presence of D and G peaks at $1,413\text{--}1,417\text{ cm}^{-1}$ and $1,562\text{--}1,569\text{ cm}^{-1}$ with the I_D/I_G of about 1.26, indicating the typical structure of the amorphous carbon films. The XPS results show that the bonding of C=C sp^2 and C-C sp^3 hybridizations with the carbon content of all samples is about 51.26 ± 0.22 and $30.11 \pm 2.52\%$, respectively. The a-C:H films with a-Si:H interlayer exhibit the lowest corrosion current density, which is about 36 times lower than that of the uncoated chromium-plated substrate. Moreover, the hardness increases from 8.48 GPa for the uncoated substrate to 20.98 GPa for the a-C:H/a-Si:H sample. The mixing with hydrogen gas could reduce the residual oxygen during the deposition process, which could reduce the Si-O and Cr-O bonding and improve the adhesion between the a-Si:H interlayer and the a-C:H film and between the chromium-plated substrate and the a-Si:H interlayer. Therefore, based on the adhesive, hardness and corrosive properties, the a-C:H film with the a-Si:H interlayer can be very useful to meet the multifunctional applications of the chromium plated products.

For the NAB substrate, the multilayer DLC films were fabricated with the a-Si film as the adhesive layer. The a-Si interlayer was prepared by the DCMS method. A combination of DCMS and RF-PECVD was used to deposit the Si-doped DLC film. The a-Si interlayer has a high density of up to 93%, which is a good

quality for the adhesive layer. The DLC and Si-doped DLC films with density of 1.98 and 1.86 g/cm³ were used as hard and soft layers, respectively. The multilayer design was investigated in terms of deposition period or stack (1, 3, and 5 stacks) with the same thickness. The surface morphology of the multilayer DLC exhibits a dense and smooth surface with an average total thickness of $\sim 1,373 \pm 6.15$ nm. The XPS and Raman spectroscopy results indicate that the silicon atoms are not bonded to the carbon atoms to form a Si–C bond, leading to an increase in graphite disorder in a Si-doped DLC structure. The a-Si interlayer (5.43 ± 0.35 GPa) has a higher hardness than the NAB substrate (3.71 ± 0.34 GPa). All multilayer coatings have favorable adhesion strength on NAB with Lc_3 value higher than 12 N. The multilayer DLC film with 5 stacks (15.57 ± 0.51 GPa) has about 4.2 times higher hardness and about 70 times lower corrosion current density ($0.02 \mu\text{A}/\text{cm}^2$) compared to the uncoated NAB substrate. These good mechanical and corrosive properties can be explained by the thickness term of the top DLC layer and the number of interfaces of the coating. The protective coating with multiple DLC layers can positively influence the excellent mechanical properties and corrosion resistance of NAB.

Keyword : Hydrogenated amorphous carbon film, Silicon-based interlayer, Radio-frequency plasma-enhanced chemical vapor deposition method, Magnetron sputtering method, Adhesive properties, Mechanical properties, Corrosive properties



ACKNOWLEDGEMENTS

This work has been supported and guided by many others. First and foremost, I would like to thank my sincere appreciation to my thesis advisor, Asst. Prof. Artit Chingsungnoen, and my co-advisor, Asst. Prof. Phitsanu Poolcharuansin, my sincere appreciation for their guidance, encouragement, meticulous, time and support in all problems throughout my PhD programme. Their recommendations and experiences were always useful and helped me to find a concept to find a way out of a problem. It is very fortunate that I had the best advisor during my PhD studies at Mahasarakham University in Thailand. I do not want to believe that this work would have been possible without their valuable support.

In addition, I am grateful to my committee members Prof. Vittaya Amornkitbamrung (chair), Dr. Nitisak Pasaja, Asst. Prof. Kwanruthai Wongsaprom and Asst. Prof. Paveena Laokul for their helpful discussions and valuable suggestions on my thesis. Moreover, their doubts and challenging questions give me the incentive to move forward with my research.

I am deeply indebted to the Department of Physics, Faculty of Science, Khon Khan University, and the Synchrotron Light Research Institute (SLRI), Public Organization, Thailand, for providing facilities and characterization support. I would like to acknowledge researcher Dr.Narong Chanlek for his insightful comments and discussions on XPS analysis, Dr. Sarayut Tunmee for valuable suggestions on corrosion resistance analysis and other related topics, and research assistant Ukit Rittihong for his assistance with Raman spectroscopy and XPS measurements. Their service, kindness and comments are very helpful to my research.

The author would like to thank the Science Achievement Scholarship of Thailand (SAST) for scholarships with financial support during the years of my doctoral studies, covering tuition and living expenses. I am also profoundly grateful for the promotion of educational opportunities in my life.

The author is deeply grateful to the National Council of Thailand (NRCT) and the Faculty of Science, Mahasarakham University (Grant Year 2021) for the financial support of my research. Through this financial support, the research can be continued smoothly.

Last but not least, I would like to heartfelt thank my lovely family from the bottom of my heart, Mr.Surasak Lakhonchai and Mrs.Yupin Lakhonchai, who have prayed for my success and whose motivation, encouragement and support have been a constant source of inspiration. I would like to honestly thank all the members of the Technological Plasma Research Unit (TPRU) for their friendly assistance and all support throughout the research and writing of this thesis and in my life. Finally, I would like to thank special grateful to my dual friend, Mr.Nopphon Saowing for the best friendship and our long journey from undergraduate and graduate studies until now. We have learned together to overcome various obstacles in our studies, have always been together, and have always encouraged and supported each other. My doctorate would not have been possible and would not have happened without the support of those who have stood by me. With that in mind, I would like to give myself a hug and thank myself for being able to fight my way through all the problems to success.

Anthika Lakhonchai

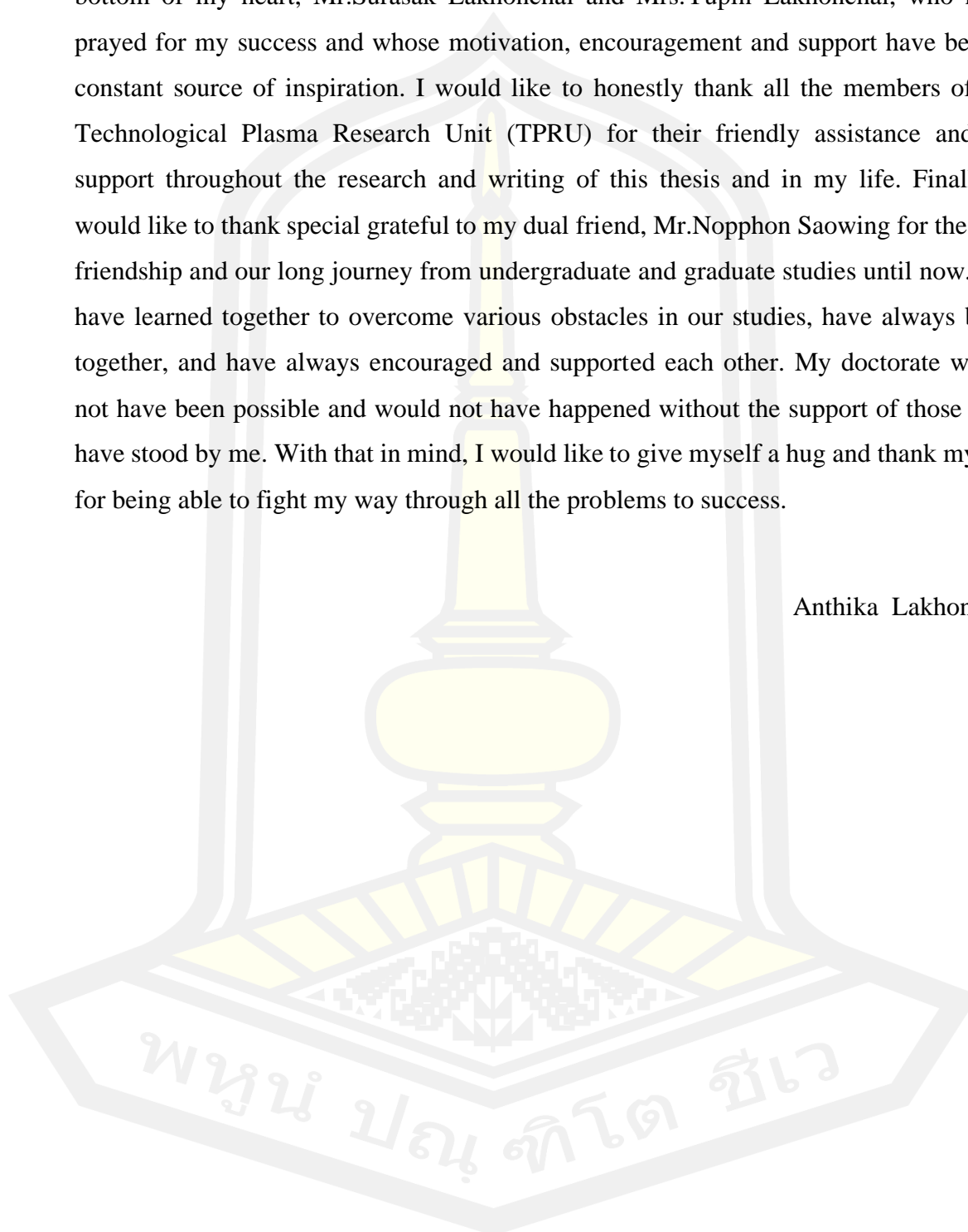
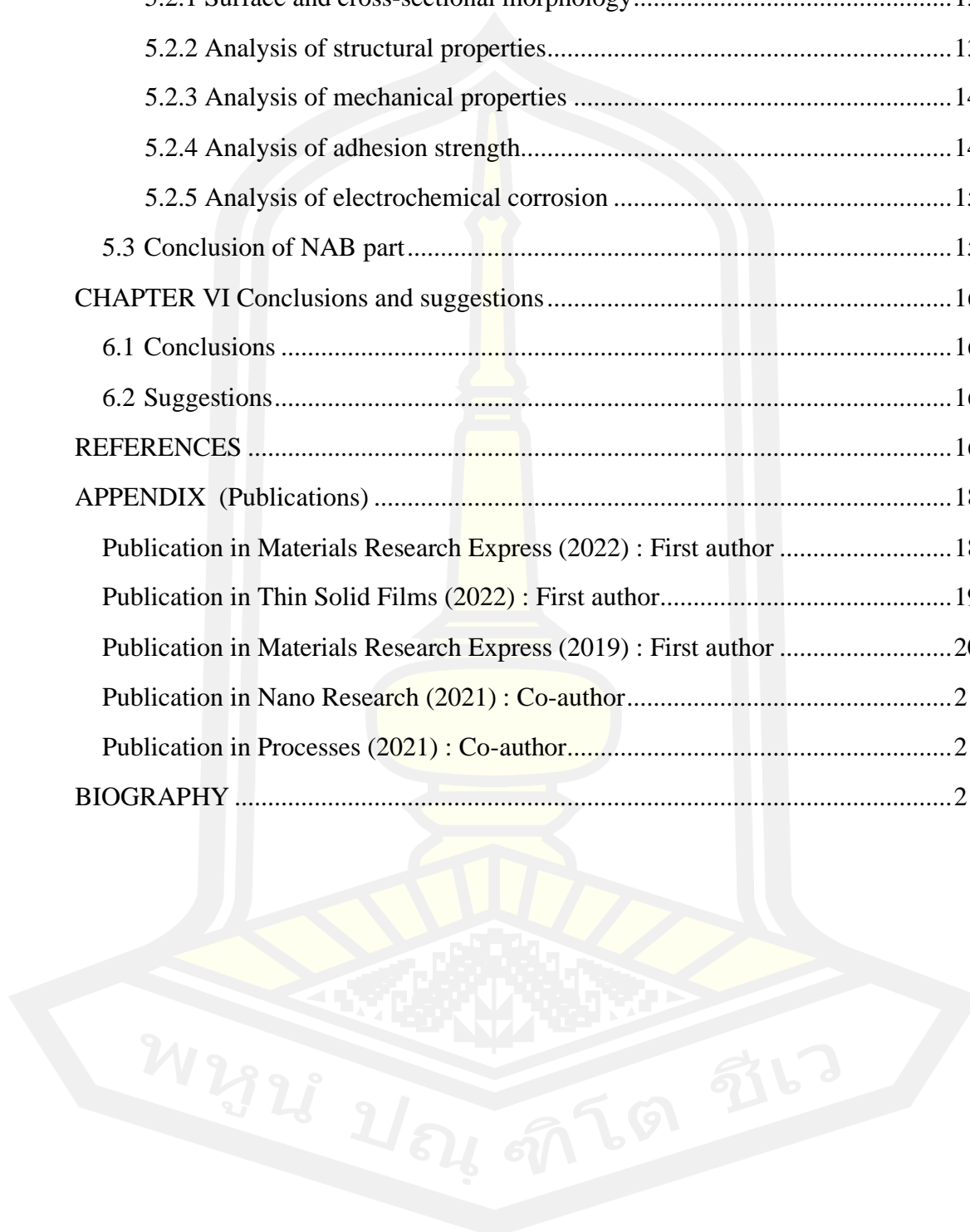


TABLE OF CONTENTS

	Page
ABSTRACT.....	D
ACKNOWLEDGEMENTS.....	F
TABLE OF CONTENTS.....	H
LIST OF FIGURES.....	K
LIST OF TABLES.....	R
LIST OF ABBREVIATIONS.....	T
CHAPTER I Introduction.....	1
1.1 Background and motivation.....	1
1.2 Research objectives.....	6
1.3 Research scope.....	6
1.4 Anticipated outcomes.....	8
1.5 Research timeline.....	8
1.6 The location of the research.....	9
1.7 Outline of the thesis.....	9
CHAPTER II Literature reviews and theoretical background.....	11
2.1 Literature reviews.....	11
2.2 Chromium-plated and nickel aluminum bronze substrates.....	15
2.3 Structure and classification of amorphous carbon.....	19
2.4 Hydrogenated amorphous carbon films.....	26
2.4.1 a-C:H films on metal alloys with the interlayers.....	27
2.4.2 Multilayer a-C:H films.....	28
2.5 Preparation of a-C:H film using RF-PECVD method.....	30
2.5.1 PECVD process.....	30
2.5.2 Process parameters.....	33
2.6 Preparation of interlayer using magnetron sputtering method.....	37

CHAPTER III Experimental procedure.....	39
3.1 Hybrid RF-PECVD/MS system	40
3.1.1 Vacuum system	44
3.1.2 Magnetron source	47
3.1.3 Bottom electrode	49
3.1.4 Vacuum control system	51
3.2 Thin-film deposition process	55
3.2.1 Substrate preparation	55
3.2.2 Argon-hydrogen plasma cleaning process	60
3.2.3 Deposition process	62
CHAPTER IV Results and discussion (Part : Chrome plating).....	69
4.1 Results of silicon-based interlayers	69
4.1.1 Thickness and deposition rate	70
4.1.2 Analysis of the structural properties	74
4.1.3 Mechanical properties analysis	82
4.2 Results of a-C:H films	86
4.2.1 Film thickness and deposition rate	86
4.2.2 Structural properties analysis	87
4.3 Results of a-C:H with interlayers	91
4.3.1 Surface and cross-sectional morphology.....	93
4.3.2 Structural properties	96
4.3.3 Mechanical properties	103
4.3.4 Adhesion strength analysis	106
4.3.5 Electrochemical corrosion analysis	110
4.4 Conclusion of chrome plating	114
CHAPTER V Results and discussion (Part : NAB).....	118
5.1 Coating layer characterizations	118
5.1.1 Morphology, thickness and deposition rate of the coating layers	119
5.1.2 Structural properties	122

5.2 Multilayer characterizations	134
5.2.1 Surface and cross-sectional morphology.....	136
5.2.2 Analysis of structural properties.....	139
5.2.3 Analysis of mechanical properties	145
5.2.4 Analysis of adhesion strength.....	148
5.2.5 Analysis of electrochemical corrosion	151
5.3 Conclusion of NAB part.....	156
CHAPTER VI Conclusions and suggestions.....	160
6.1 Conclusions	160
6.2 Suggestions.....	163
REFERENCES	164
APPENDIX (Publications)	183
Publication in Materials Research Express (2022) : First author	184
Publication in Thin Solid Films (2022) : First author.....	198
Publication in Materials Research Express (2019) : First author	205
Publication in Nano Research (2021) : Co-author.....	216
Publication in Processes (2021) : Co-author.....	217
BIOGRAPHY	218



LIST OF FIGURES

Figure 2.1	The distribution schematic of the density of carbon valence electrons in the s and p_x state.	19
Figure 2.2	Scheme of (a) the electron states redistribution, (b) the hybridization of s and p orbitals of the electron distributions, + and – denote the signs of the wave functions, (c) the overlap of p orbital with covalent π and σ bonding [10].	21
Figure 2.3	Structures of all carbon allotropes [69], [70].	23
Figure 2.4	Ternary phase diagram of amorphous carbon films [4].	24
Figure 2.5	Surface characteristics of (a) the AISI 4140 steel polished, (b) DLC without interlayer on steel, and (c) DLC with a-SiC _x :H adhesion interlayer on steel [74].	27
Figure 2.6	Residual stress of the DLC films with and without metals interlayer [76].	28
Figure 2.7	Schematic illustration of the mechanism of low residual stress in a multilayer DLC film [52].	29
Figure 2.8	The hardness of a-C:H films as a function of RF power [87].	32
Figure 2.9	Ion energy distribution in (a) conventional PECVD and (b) magnetic confinement PECVD [4].	33
Figure 2.10	Deposition rate of a-C:H film prepared by PECVD method with different precursor gases [4].	35
Figure 3.1	Flowchart of the experimental procedure.	39
Figure 3.2	A photo of a hybrid RF-PECVD/MS system used for a-C:H with silicon-based interlayer deposition.	41
Figure 3.3	A schematic diagram of the hybrid RF-PECVD/MS system used for a-C:H with silicon-based interlayer deposition.	42
Figure 3.4	A drawing of the hybrid RF-PECVD/MS system used for a-C:H with silicon-based interlayer deposition.	43
Figure 3.5	The drawing of the vacuum chamber, including the magnetron source and the bottom electrode.	46
Figure 3.6	The cross-section diagram of the magnetron source.	48

Figure 3.7	The schematic diagram of the magnetic holder; the outer magnets (south pole) are shown in green colour, while an inner magnet (north pole) is shown in blue.	48
Figure 3.8	The drawing of all components of the bottom electrode.	50
Figure 3.9	The schematic diagram shows the control panel of the hybrid RF-PECVD/MS system.	51
Figure 3.10	A photo of the National Instruments (PXIe-1062Q).	52
Figure 3.11	The panel of NI PXIe-8102 module [100].	52
Figure 3.12	Brooks 0254 instrument for mass flow controller.	53
Figure 3.13	A hardware diagram of the NI PXI-2564 for pneumatic valves.	54
Figure 3.14	A photo of the ultrasonic cleaner for substrate cleaning.	55
Figure 3.15	A photo of the silicon wafer substrates with the size of (a) $10 \times 10 \text{ mm}^2$, and (b) $20 \times 20 \text{ mm}^2$	57
Figure 3.16	A photo of the chromium-plated substrate (a) front view and (b) side view.	58
Figure 3.17	A photo of (a) unpolished and (b) polished NAB substrate.	59
Figure 3.18	The SiC sandpapers with grit sizes of 100, 200, 600, 800, 1000, 1500, 2000, 2500, 3000, 4000, and 5000.	59
Figure 3.19	The alumina powder with particle size of $0.5 \mu\text{m}$ and $0.05 \mu\text{m}$ used for suspension in DI water.	60
Figure 3.20	A photo of the (a) chromium-plated substrates and Si wafer (b) NAB substrates and Si wafer were placed onto the stainless-steel plate.	61
Figure 3.21	A photo of Ar- H_2 plasma during the cleaning process of (a) chromium-plated substrates and Si wafer (b) NAB substrates and Si wafer.	62
Figure 3.22	A Photo of silicon target (a) front view, and (b) side view.	63
Figure 3.23	A photo of plasma during the deposition process of (a) a-Si, (b) a-Si:N, (c) a-Si:H, and (d) a-Si _x C _y :H interlayers	64
Figure 3.24	A photo of C ₂ H ₂ -Ar- H_2 plasma during the deposition process.	65
Figure 3.25	A schematic diagram and photo of loading samples, plasma cleaning, interlayer coating and a-C:H coating process.	66

Figure 3.26	A photo of the plasma during the deposition process of (a) a-Si interlayer, (b) DLC film, and (c) Si-doped DLC film.	68
Figure 3.27	A schematic diagram and photo of loading samples, plasma cleaning, interlayer coating, Si-doped DLC coating and DLC coating process for NAB substrate.	68
Figure 4.1	Schematic model of four silicon-based interlayers on a silicon substrate (not to scale).	70
Figure 4.2	Photo of a-Si, a-Si:N, a-Si:H, and a-Si _x C _y :H interlayers deposited on a silicon substrate.	70
Figure 4.3	FESEM cross-sectional images of (a) a-Si, (b) a-Si:N, (c) a-Si:H, and (d) a-Si _x C _y :H interlayers on silicon substrate.	72
Figure 4.4	Deposition rate using different silicon-based interlayers.	73
Figure 4.5	Typical XPS spectra of a wide scan for a-Si, a-Si:N, a-Si:H and a-Si _x C _y :H interlayers.	75
Figure 4.6	Deconvoluted XPS spectra for Si2p of (a) a-Si, (b) a-Si:N, (c) a-Si:H, and (d) a-Si _x C _y :H interlayers. The black, red, blue, and other solid lines represent the experimental data, the fitted curve, the Shirley background, and the deconvolution of the individual peaks, respectively.	76
Figure 4.7	Deconvoluted XPS spectra for (a) N1s of a-Si:N interlayer and (b) C1s of a-Si _x C _y :H interlayer. The black, red, blue, and other solid lines represent the experimental data, the fitted curve, the Shirley background, and the deconvolution of the individual peaks, respectively.	77
Figure 4.8	XRR curve of the experimental data (black curve) and simulation data (red curve) of the different silicon-based interlayers.	81
Figure 4.9	Fitted results of thickness (orange bar) and density (green bar) of a-Si, a-Si:N, a-Si:H, and a-Si _x C _y :H interlayers.	81
Figure 4.10	Loading and unloading curves of chromium-plated substrate and different silicon-based interlayers.	83
Figure 4.11	Hardness and elastic modulus of chromium-plated substrate and a-Si, a-Si:N, a-Si:H, and a-Si _x C _y :H interlayers.	84

Figure 4.12	A photo of a-C:H film on a silicon substrate.....	86
Figure 4.13	Cross-sectional FESEM image of a-C:H film.....	87
Figure 4.14	XRR curve of experimental data (black curve) and simulation data (red curve) for a-C:H films.	88
Figure 4.15	Raman spectra of a-C:H films. The black and red lines show the experimental data and the fitted curve, respectively. The green, blue, and magenta lines correspond to the deconvolution of the X, D and G peaks, respectively.	90
Figure 4.16	The schematic model of a-C:H film with and without silicon-based interlayers (not to scale).....	91
Figure 4.17	A photo of a-C:H film deposited with (a) a-Si, (b) a-Si:N, (c) a-Si:H, and (d) a-Si _x C _y :H interlayers on substrate holder.....	92
Figure 4.18	A photo of an a-C:H film deposited with (a) a-Si, (b) a-Si:N, (c) a-Si:H, and (d) a-Si _x C _y :H interlayers on silicon and chromium-plated substrate.	92
Figure 4.19	A photo of an a-C:H film deposited on a chromium-plated substrate.	93
Figure 4.20	Surface morphologies (left) and cross-sectional microstructures (right) of a-C:H films with (a), (b) a-Si; (c), (d) a-Si:N; (e), (f) a-Si:H; and (g), (h) a-Si _x C _y :H interlayers deposited on a silicon substrate.	95
Figure 4.21	Raman spectra of a-C:H films deposited with a-Si, a-Si:N, a-Si:H, and a-Si _x C _y :H interlayers on (a) silicon and (b) chromium-plated substrate. The black and red lines show the experimental data and the fitted curve, respectively. The green, blue, and magenta lines correspond to the deconvolution of the X, D and G peaks, respectively.	97
Figure 4.22	Typical XPS spectra of a wide scan for a-C:H films with a-Si, a-Si:N, a-Si:H, and a-Si _x C _y :H interlayers.	99
Figure 4.23	Deconvoluted XPS spectra for C1s of a-C:H films with a-Si, a-Si:N, a-Si:H, and a-Si _x C _y :H interlayers. The black, red, blue, and other solid lines represent the experimental data, the fitted curve,	

	the Shirley background, and the deconvolution of the individual peaks, respectively.	101
Figure 4.24	(a) Loading and unloading curves and (b) hardness of the a-C:H film with different silicon-based interlayers in dynamic mode.	104
Figure 4.25	(a) Loading and unloading curves and (b) hardness depth profile of the a-C:H film with different silicon-based interlayers in ESP mode.	105
Figure 4.26	Principle of scratch testing with critical load (L_{c1} , L_{c2} and L_{c3}).	106
Figure 4.27	Morphology of scratch marks with L_{c1} , L_{c2} , and L_{c3} for a-C:H films with (a) a-Si, (b) a-Si:N, (c) a-Si:H, and (d) a-Si _x C _y :H interlayers deposited on a chromium-plated substrate.	108
Figure 4.28	Critical load values of L_{c1} , L_{c2} and L_{c3} for a-C:H films with a-Si, a-Si:N, a-Si:H, and a-Si _x C _y :H interlayers deposited on a chromium-plated substrate.	109
Figure 4.29	(a) Potentiodynamic polarization curves and (b) corrosion current density (orange bar) and porosity (green bar) of the a-C:H films with different silicon-based interlayers and uncoated chromium-plated substrate in 3.5 wt% NaCl solution.	112
Figure 5.1	The schematic model of the a-Si interlayer, the DLC film and the Si-doped DLC film on silicon substrate (not to scale).	119
Figure 5.2	Surface morphologies (left) and cross-sectional microstructures (right) of (a), (b) a-Si interlayer; (c), (d) DLC film; and (e), (f) Si-doped DLC film deposited on silicon substrate.	121
Figure 5.3	XRR curves of experimental data (black curve) and simulation data (red curve) for a-Si interlayers, DLC and Si-doped DLC films.	124
Figure 5.4	Fitted results for the thickness (orange bar) and density (green bar) of a-Si interlayers, DLC and Si-doped DLC films.	124
Figure 5.5	Typical XPS spectra of a wide scan for a-Si interlayer.	126
Figure 5.6	Deconvoluted XPS spectra for Si2p of the a-Si interlayer. The black, red, blue, and other solid lines represent the experimental data, the fitted curve, the Shirley background, and the deconvolution of the individual peaks, respectively.	126

Figure 5.7	Typical XPS spectra of a wide scan for DLC and Si-doped DLC films.	129
Figure 5.8	Comparison of high-resolution XPS spectra of the C1s peak of DLC and Si-doped DLC films.	129
Figure 5.9	Deconvoluted XPS spectra for C1s of DLC and Si-doped DLC films. The black, red, blue, and other solid lines represent the experimental data, the fitted curve, the Shirley background, and the deconvolution of each peak, respectively.	130
Figure 5.10	Raman spectra of DLC and Si-doped DLC films deposited on a silicon substrate. The black and red lines show the experimental data and the fitted curve, respectively. The green, blue, and magenta lines correspond to the deconvolution of the X, D and G peaks.	133
Figure 5.11	Schematic model of a multilayer DLC with 1, 3, and 5 stacks (not to scale).	135
Figure 5.12	Photo of multilayer DLC with 1 stack, 3 stacks, and 5 stacks on substrate holder.	135
Figure 5.13	Photo of multilayer DLC with 1 stack, 3 stacks, and 5 stacks on (a) silicon and (b) NAB substrates.	136
Figure 5.14	Surface morphologies of multilayer DLC with (a) 1 stack and (b) 3 stacks that deposited on silicon substrate.	137
Figure 5.15	(a) schematic model and (b) corresponding cross-sectional microstructures of multilayer DLC with 1 stack.	138
Figure 5.16	(a) schematic model and (b) corresponding cross-sectional microstructures of multilayer DLC with 3 stacks.	139
Figure 5.17	Typical XPS spectra of a wide scan for multilayer DLC with 1 stack, 3 stacks, and 5 stacks.	140
Figure 5.18	Deconvoluted XPS spectra for the C1s peak of multilayer DLC with 1 stack, 3 stacks and 5 stacks. The black, red, blue, and other solid lines represent the experimental data, the fitted curve, the Shirley background, and the deconvolution of each peak, respectively.	141

- Figure 5.19** Raman spectra of multilayer DLC films with 1 stack, 3 stacks, and 5 stacks deposited on a silicon substrate. The black and red lines show the experimental data and the fitted curve, respectively. The green, blue, and magenta lines correspond to the deconvolution of the X, D and G peaks..... 144
- Figure 5.20** Loading and unloading curves of (a) NAB and (b) a-Si interlayer..... 146
- Figure 5.21** Loading and unloading curves of multilayers DLC with 1 stack, 3 stacks and 5 stacks. 147
- Figure 5.22** Hardness and elastic modulus of NAB, a-Si interlayer, and multilayers DLC with 1 stack, 3 stacks and 5 stacks..... 147
- Figure 5.23** Morphology of scratch marks of Lc_1 , Lc_2 and Lc_3 for DLC multilayers with 1 stack, 3 stacks and 5 stacks deposited on a NAB. 150
- Figure 5.24** Critical load values of Lc_1 , Lc_2 and Lc_3 for DLC multilayers with 1 stack, 3 stacks and 5 stacks deposited on a NAB. 150
- Figure 5.25** Potentiodynamic polarization curves of NAB, a-Si interlayer, and 1 stack, 3 stacks and 5 stacks of multilayer DLC in 3.5 wt% NaCl solution..... 153
- Figure 5.26** Corrosion current density of NAB, a-Si interlayer, and 1 stack, 3 stacks and 5 stacks of multilayer DLC. 154
- Figure 5.27** Photo of (a) NAB, (b) a-Si interlayer, and (c) 1 stack, (d) 3 stacks, and (e) 5 stacks of multilayer DLC after corrosion measurement..... 155

LIST OF TABLES

Table 1.1	Characterization techniques and corresponding film properties.....	7
Table 1.2	Schedule of this research.....	8
Table 2.1	The characteristic of the diamond, graphite, and different DLC types [73].....	26
Table 2.2	Comparisons for the properties of plasma excitation using DC, low-frequency (60 Hz), and RF (13.56 MHz) power source [89].	36
Table 3.1	The parameters used for argon-hydrogen plasma cleaning process.....	61
Table 3.2	The parameters used for different silicon-based interlayer coating process.....	64
Table 3.3	The parameters used for a-C:H coating process.	65
Table 3.4	The parameters used for the deposition of the a-Si interlayer, the DLC and the Si-doped DLC.....	67
Table 4.1	Film thickness and deposition rate of all silicon-based interlayers.....	73
Table 4.2	The fitted results of bond type, binding energy, FWHM and content deconvoluted from the XPS spectra of a-Si, a-Si:N, a-Si:H, and a-Si _x C _y :H interlayers.	78
Table 4.3	Hardness, elastic modulus and penetration depth of a chromium-plated substrate, a-Si, a-Si:N, a-Si:H and a-Si _x C _y :H interlayers.....	85
Table 4.4	The fitted results of peak positions and FWHM of X, D, and G peaks and I_D/I_G from the Raman spectra of a-C:H films with a-Si, a-Si:N, a-Si:H, and a-Si _x C _y :H interlayers deposited on a silicon substrate.....	97
Table 4.5	The fitted results of peak positions and FWHM of X, D, and G peaks and I_D/I_G from the Raman spectra of a-C:H film with a-Si, a-Si:N, a-Si:H, and a-Si _x C _y :H interlayers deposited on a chromium-plated substrate.	98
Table 4.6	The fitted results of bonding type, binding energy, FWHM, and content deconvoluted from the C1s XPS spectra of a-C:H films with different silicon-based interlayers deposited on a silicon substrate.....	102

Table 4.7	Hardness, elastic modulus, and penetration depth of a chromium-plated substrate and a-C:H film with a-Si, a-Si:N, a-Si:H and a-Si _x C _y :H interlayers.....	104
Table 4.8	Critical load values (Lc ₁ , Lc ₂ , and Lc ₃) for a-C:H films with a-Si, a-Si:N, a-Si:H, and a-Si _x C _y :H interlayers.	109
Table 4.9	Electrochemical results from polarization curves for uncoated and coated substrates.	113
Table 5.1	Film thickness and deposition rate of all silicon-based interlayers.....	120
Table 5.2	The fitted results for the bond type, binding energy, FWHM, and deconvoluted content from the Si2p-XPS spectra of a-Si deposited on a silicon substrate.....	127
Table 5.3	The fitted results of bond type, binding energy, FWHM, and content deconvoluted from the C1s XPS spectra of DLC and Si-doped DLC deposited on a silicon substrate.....	131
Table 5.4	The fitted results of the peak positions and FWHM of the X, D, and G peaks and I _D /I _G from the Raman spectra of DLC and Si-doped DLC films deposited on a silicon substrate.....	133
Table 5.5	The fitted results of bond type, binding energy, FWHM, and content deconvoluted from the C1s XPS spectra of multilayer DLC with 1 stack, 3 stacks and 5 stacks deposited on a silicon substrate.	142
Table 5.6	The fitted results of peak positions and FWHM of X, D and G peaks and I _D /I _G from the Raman spectra of multilayer DLC with 1 stack, 3 stacks and 5 stacks deposited on silicon substrate.	144
Table 5.7	Hardness, elastic modulus, and penetration depth of multilayer DLC with 1 stack, 3 stacks and 5 stacks that deposited on a silicon substrate.	148
Table 5.8	Critical load values (Lc ₁ , Lc ₂ , and Lc ₃) for DLC multilayers with 1 stack, 3 stacks and 5 stacks.	151
Table 5.9	Electrochemical results of polarization curves of NAB, a-Si interlayer, and 1 stack, 3 stacks and 5 stacks of multilayer DLC....	154

LIST OF ABBREVIATIONS

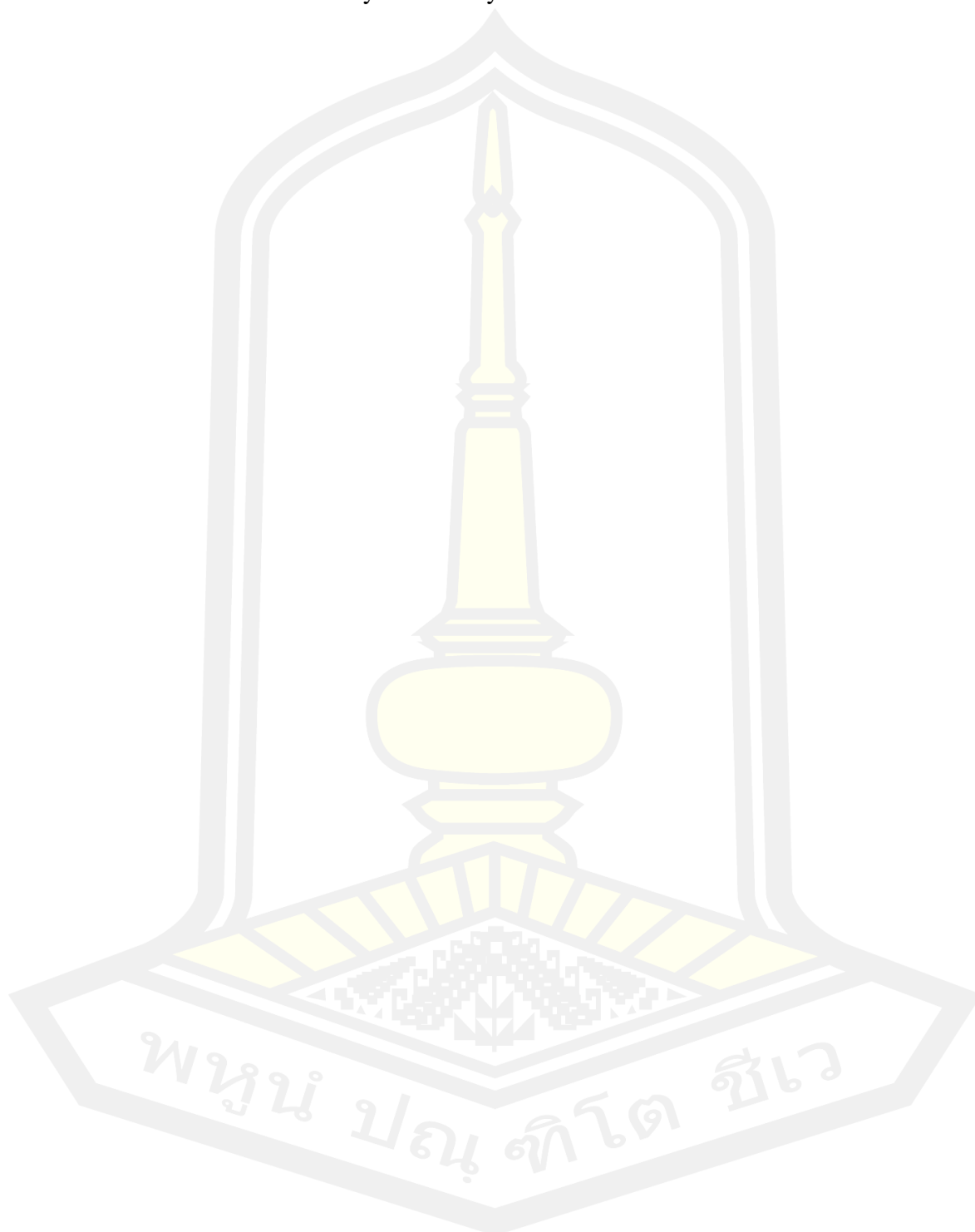
a-C	Amorphous carbon
a-C:H	Hydrogenated amorphous carbon
Ar	Argon
C	Carbon
Cr	Chromium
COF	Coefficient of friction
C ₂ H ₂	Acetylene
DC	Direct current
DLC	Diamond-like carbon
E _{corr}	Corrosion potential
FWHM	Full width at half-maximum
H	Hydrogen
HiPIMS	High-power impulse magnetron sputtering
I _{corr}	Corrosion current
i _{corr}	Corrosion current density
I _D	Intensity of the D peak
I _G	Intensity of the G peak
I _D /I _G ratio	The intensity ratio of D and G bands
MS	Magnetron sputtering
NAB	Nickel aluminum bronze
PECVD	Plasma enhanced chemical vapor deposition
PEEK	Polyether ether ketone
RF	Radio frequency
sccm	Standard cubic centimeters per minute
SE	Spectroscopic ellipsometry
SEM	Scanning electron microscope/microscopy
Si	Silicon
ta-C	Tetrahedral amorphous carbon
ta-C:H	Hydrogenated tetrahedral amorphous carbon

XPS

X-ray Photoelectron Spectroscopy

XRR

X-ray reflectivity



CHAPTER I

Introduction

1.1 Background and motivation

Thin-film coating technology has been used in industrial applications such as microelectronic devices, automotive parts, metal surface coating, food packaging, and medical instruments and tools industries. The thin-film coating aims to enhance the material surface's properties because the thin films have some unique characteristics due to their structure [1]–[3]. The thin-film coating has been used as a protective layer in the surface coating and automotive parts industries to enhance the hardness and anti-corrosion properties and reduce the friction coefficient and wear rate. The protective thin-film coating significantly improves durability and extends the lifetimes of materials used in the abrasive and corrosive environments. A long time ago, several researchers attempted to investigate the enhancement of the surface coating technology with the thin film, especially the diamond-like carbon film or DLC film.

DLC film, as an amorphous carbon material, has attracted much attention in the surface coating industry due to the combined properties of diamond and graphite. DLC films have unique and diverse properties, such as mechanical properties that can increase hardness, tribological properties that can reduce friction coefficient of the material surface, resulting in a low wear rate and improving performance and service life. The DLC film also offers excellent chemical inertness leading to high corrosion resistance [4]–[7]. The DLC film's outstanding properties result in applications in various industries, such as the magnetic data storage industry for the protective coating layer of magnetic storage disks and their read/write heads. In the automotive parts industry, the DLC is coated onto the piston ring and cylinder block to extend its service life and reduce the wear rate of continuously abrasive conditions. In the food packaging industry, the DLC film is applied to coat on to the PET bottle, fresh and dry food packaging due to the high atomic density of DLC film, so it acts as a gas diffusion barrier and then prolongs the shelf-life of food [8], [9]. These properties are mainly determined by sp^2 and sp^3 carbon hybridization, and hydrogen content of the

DLC film structure [4], [10]. The difference of sp^2 , sp^3 , and hydrogen content defines the following four types of DLC films; (i) tetrahedral amorphous carbon (ta-C), (ii) tetrahedral hydrogenated amorphous carbon (ta-C:H), (iii) amorphous carbon (a-C) and (iv) hydrogenated amorphous carbon (a-C:H) [10]. The sp^3 and sp^2 hybridization of DLC confer many of the beneficial properties of diamond and graphite such as high hardness, low friction coefficient, low wear rate, and high corrosion resistance. The a-C:H film consists of sp^3 carbon content of 0–50%, hydrogen content of 5–60%, density of 1.0–2.5 g/cm³, and hardness of 10–30 GPa (less than a diamond of 100 GPa); however, the friction coefficient of a-C:H film (< 0.1) lower than diamond [10]–[12]. In addition, the properties of a-C:H film can adjust by the deposition method and process parameters; therefore, the a-C:H film has been widely applied and satisfies the need for specific applications.

However, the major drawback of DLC's application is the poor adhesion to the substrate, especially to the ferrous alloy substrate. Due to the high internal compressive stress, mismatch in the chemical bonding, and incompatibility of thermal expansion coefficients between the DLC film (2.3 $\mu\text{m}/\text{m.K}$) and substrates such as AISI 52100 hardened steel (11.5 $\mu\text{m}/\text{m.K}$) and chromium (4.9 $\mu\text{m}/\text{m.K}$), which leads to delamination and failure [13]–[18]. Therefore, the deposition of DLC film directly on ferrous alloy limits its industrial applications and the film's thickness. Several previous research has solved this problem; it was summarized into four methods. The first method is metal-doped into the diamond-like carbon network structure (metal-doped DLC); this method can directly reduce the internal stress and improve the film's adhesive and structural properties. The second method is the interlayer's growth on the substrate before DLC deposition; the atom of the interlayer can create strong chemical bonding at the interface between the substrate and DLC film. The third method is the plasma surface treatment on the substrate and interlayer to increase surface energy and dangling bond. The last method, the construction of the multilayer structure deposition between the soft and hard layers, which is a feasible approach to reduce internal stress, and also enhances the adhesion and film thickness. M. Nöthe *et al.* (2001) [19] and Z.-H. Xie *et al.* (2007) [20] reported that the silicon-based interlayer coating could generate more robust and more chemical bonds at the interface than metal-doped DLC and plasma surface treatment [17], [18], [21]–[23].

Although the multilayer design is a suitable method for DLC coating with a required thickness of more than 1 μm . M. Cui *et al.* (2015) [24] reported that the multilayer design can coat the DLC film with a thickness of about 8.0 μm , while the DLC single layer limits the thickness to a range between 1 and 3 μm . However, the silicon transition layer was also needed improve the adhesive properties. Therefore, it can be generalized that the interlayers are necessary for DLC coatings with single and multiple layers. In recent decades, DLC coatings have attracted much attention in research and development for coating on various types of metal substrates. F. Cemin *et al.* (2016) [25] and S. Delfani-Abbariki *et al.* (2018) [26] reported the improvement of DLC adhesion on a steel substrate using a silicon-based interlayer. H. Cao *et al.* (2021) [27] deposited multilayer Ti-doped DLC films on an aluminum alloy and reported that the mechanical and adhesive properties of the films depend on the thickness of the Ti interlayer. Y. Lu *et al.* (2019) [28] investigated the improvement of tribological and mechanical properties of a copper substrate by multilayer DLC coating. S.S. Hadinata *et al.* (2013) [29] investigated and compared the DLC coatings on different materials such as stainless steel, carbon steel and brass in terms of their electrochemical behaviour. S.E. Mousavi *et al.* (2021) [30] recently investigated the DLC films coated with chromium carbide adhesive layers to enhance the mechanical properties, tribological behaviour, and corrosion performance of nickel-aluminum bronze alloys (NAB). All these literature reviews show that DLC films are being investigated and receiving attention as protective coatings on several types of substrates, especially metallic and alloy materials, to enhance mechanical and tribological properties and corrosion protection. However, according to our literature review, there are no studies on DLC protective coatings on chromium-plated substrates. For the materials of NAB, there was only one investigation, and that was in the form of single-layer DLC.

A chrome plating is a chromium layer that is electroplated onto a substrate (metal, alloy, plastic, etc). Chromium (Cr) is a metal element with hard, brittle, high corrosion resistance, and blue-white colour. The chromium gains much attention to coat on the metal and plastic surface for decorative, shiny, anti-scratch, and anti-rust properties [31]–[33]. The electroplating method has been widely used for chromium coating. The electroplated layer of chromium is often referred to as chrome.

Chrome plating is mainly used for bathtub faucets, showers, and bathroom fixtures. There are two types of chromed layer: decorative chrome plating and hard chrome plating. The decorative chrome plating with a thin layer (~1 μm thick) of chromium has the purpose of improving the shiny luster or mirror-like shine, aesthetic appeal, and as a protective coating that is easy to clean, making it desirable for various consumer products. While the hard chrome plating is thicker than decorative chrome and the goal of hard chrome is to increase the corrosion and wear resistance of equipment components in many industrial applications. Although the decorative chrome plating gives the corrosion resistance in most environments, it tends to form the microscopic cracks at the grain boundary due to stress, which leads to the corrosion at the grain boundary [34], [35]. These cracks form a pattern that intertwines with and sometimes reaches the base metal. A corrosive liquid or gas may penetrate the base substrates. Some studies have shown that the use of DLC coatings instead of chrome plating could improve the mechanical, tribological, and corrosive properties of the material [36], [37]. However, besides this substitution, it is also possible to use the DLC coating directly on a chromium layer, maintaining the esthetics and bright properties of the chromium layer. In addition, the DLC coating can solve the corrosion problem of the chromium layer and also improve the mechanical and tribological properties of the base substrates. Therefore, their service life will be prolonged even if they are used near the coast. Although the color of chrome plating changes from blond to shiny black after coating, they can be used for decorative applications to enhance the product value.

Besides, the nickel aluminum bronze as an alloy material mainly consists of copper, aluminum, nickel, and iron, which show an excellent combination of mechanical and corrosion resistance properties. The NAB material most widely used in the marine parts such as water end entry valves and fittings, tubing, ship propellers, and oil rig equipment in the shipbuilding industry and offshore oil/gas petrochemical industries [38], [39]. The oxide layer of both aluminum and copper identifies the corrosion resistance of NAB. However, after prolonged exposure times to seawater and under conditions where seawater flows at high velocity or turbulence, the protective oxide layer may be damaged, reducing corrosion resistance [40]. DLC coating is one of the ways to protect the NAB material. The excellent chemical

inertness of DLC film can improve the corrosion resistance of the coated substrates. Moreover, the mechanical and tribological properties of the substrate surface also improve. For the application of corrosion resistance, the multilayer DLC coating is more suitable than a single layer because of the higher thickness and the larger number of interfaces.

Therefore, the aim of this work is to improve the corrosion resistance and mechanical properties of chrome plating and nickel aluminum bronze by coating the a-C:H film with the silicon-based interlayer for adhesion enhancement. This thesis was divided into 2 parts; (i) chromium-plated substrate and (ii) NAB substrate. For the chromium-plated substrate, the four different types of amorphous silicon (a-Si), amorphous silicon nitride (a-Si:N), hydrogenated amorphous silicon (a-Si:H) and hydrogenated amorphous silicon carbide (a-Si_xC_y:H) were deposited as interlayers by direct current magnetron sputtering (DCMS), while the a-C:H films were deposited by radio frequency plasma enhanced chemical vapor deposition (RF-PECVD) under the same conditions. The DLC film with different silicon-based interlayers in the form of a single layer is studied because the focus is on improving the adhesive and corrosive properties. While the NAB substrate focuses on the mechanical and corrosive properties, the multilayer DLC is selected. The multilayer DLC films were designed and fabricated to be studied in terms of deposition period or stack (1 stack, 3 stacks and 5 stacks) with the same controlled of the total thickness for NAB. The a-Si film was used as an adhesive layer while the DLC and silicon doped DLC (Si-doped DLC) films were used as the hard and soft layer. A combination of DCMS and RF-PECVD method was used to deposit the Si-doped DLC film. The effect of different silicon-based interlayers for chrome plating and deposition stack for NAB will be systematically investigated and described using the characterization of field emission-secondary electron microscopy (FESEM), X-ray photoelectron spectroscopy (XPS), X-ray reflectivity (XRR), Raman spectroscopy, nanoindentation, micro-scratching, and electrochemical corrosion measurements in terms of morphology, structural, mechanical properties, adhesive properties, and corrosion resistance. The ultra-low friction coefficient and high corrosion resistance of a-C:H film has an excellent potential to improve the lifetimes, energy-saving, diminish the expenses, and satisfy the use of marine parts.

1.2 Research objectives

The objectives of this thesis are split into two points as follows.

1. To improve adhesive properties of a-C:H film on chrome plating and nickel aluminum bronze using the silicon-based interlayer prepared by the DCMS method.
2. To enhance the mechanical properties and corrosion resistance of chrome plating and nickel aluminum bronze by coating the a-C:H and multilayer DLC films based on the RF-PECVD method.

1.3 Research scope

This research focuses on the deposition of a-C:H and multilayer DLC films based on RF-PECVD method, and the silicon-based interlayer based on the DCMS method. The research scope for chromium-plating and nickel-aluminum bronze parts were given as follows.

1. The chrome plating and nickel aluminum bronze are used as the substrate for mechanical, corrosion and adhesion measurement.
2. The p-type silicon substrate is used for morphology and structural properties measurement.
3. The p-type silicon with copper backing plate (2 inches diameter and 0.125 inch thick, 99.999% purity) is used as the sputtering target.
4. The DC power supply is used to drive the magnetron sputtering source for interlayer coating.
5. The radio frequency of 13.56 MHz is used as the power source for a-C:H coating.
6. The importance deposition parameters were given by:
 - Base pressure
 - Distance between the target and substrate
 - Gas flow rate
 - Sputtering power
 - RF power
 - Deposition time

7. Analytical techniques

- Surface and cross-sectional morphology by:
 - FESEM
- Structural properties by:
 - XRR
 - XPS
 - Raman spectroscopy
- Adhesive properties by:
 - Micro-scratching
- Mechanical properties by:
 - Nanoindentation test
- Corrosive resistance properties by:
 - Electrochemical corrosion test (3.5 wt% NaCl solution)

Characterization techniques used to identify the film properties such as morphology, structural, adhesive, mechanical and corrosion resistance are summarized in Table 1.1.

Table 1.1 Characterization techniques and corresponding film properties.

Techniques	Film properties
Field emission-secondary electron microscopy	Surface and cross-sectional morphologies
X-ray reflectivity	Density, thickness
X-ray photoelectron spectroscopy	Chemical bonding, element content
Raman spectroscopy	I_D/I_G ratio
Micro-scratching	Critical load, morphology of scratch marks
Nanoindentation test	Hardness, elastic modulus
Electrochemical corrosion test	Corrosion current density, corrosion potential, porosity

Activities	2019		Summer	2020		Summer	2021	
	1	2		1	2		1	2
First draft manuscript paper								
Submit manuscript paper								
Writing the thesis chapter 4-5								
Thesis defense examination								

1.6 The location of the research

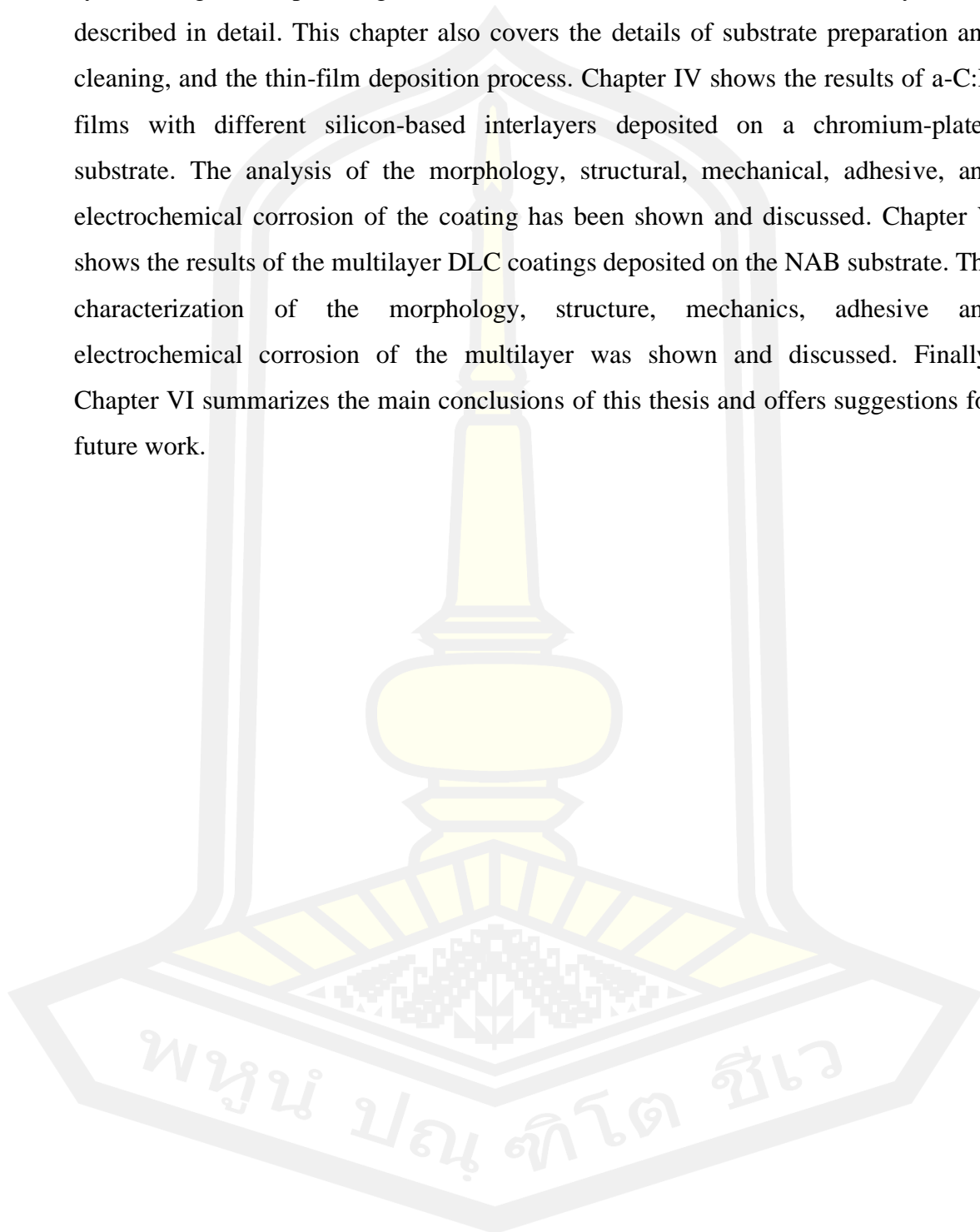
The main places for doing this research are located as follows.

- Technological Plasma Research Unit (TPRU), Department of Physics, Faculty of Science, Mahasarakham University (MSU), Maha Sarakham, Thailand.
- Department of Physics, Faculty of Science, Khon Kaen University (KKU), Khon Kaen, Thailand.
- Beamline 3.2a and 3.2b, Synchrotron Light Research Institute (SLRI) Public Organization, Nakhon Ratchasima, Thailand.

1.7 Outline of the thesis

This thesis is divided into six chapters that relate to the general research process. Chapter I covers the background and motivation of this thesis, thin-film coating technology for industrial applications, different types, and properties of DLC films, previous work, problems of DLC adhesion, objectives and scope of the research. Anticipated outcomes of this research are clearly pointed out. Chapter II presents the theoretical background and literature reviews on DLC films, the problems with the adhesive properties of DLC to metal substrates, and the approach used to solve the problem. The disadvantages and problems of using chromium-plating and NAB substrates in seawater or corrosive conditions are highlighted. Chapter III explains the methods of interlayer coating by magnetron sputtering and DLC coating

by RF-PECVD. The hybrid RF-PECVD/MS system, which consists of the vacuum system, magnetron sputtering source, bottom electrode, and vacuum control system, is described in detail. This chapter also covers the details of substrate preparation and cleaning, and the thin-film deposition process. Chapter IV shows the results of a-C:H films with different silicon-based interlayers deposited on a chromium-plated substrate. The analysis of the morphology, structural, mechanical, adhesive, and electrochemical corrosion of the coating has been shown and discussed. Chapter V shows the results of the multilayer DLC coatings deposited on the NAB substrate. The characterization of the morphology, structure, mechanics, adhesive and electrochemical corrosion of the multilayer was shown and discussed. Finally, Chapter VI summarizes the main conclusions of this thesis and offers suggestions for future work.



CHAPTER II

Literature reviews and theoretical background

In this chapter, the theoretical background regarding the DLC film, the principle of the RF-PECVD method, the magnetron sputtering, and the analytical techniques are given in detail. This chapter consists of the following six issues as follows: (i) literature review, (ii) chromium-plated and nickel-aluminum bronze substrates, (iii) amorphous carbon, (iv) hydrogenated amorphous carbon films, (v) preparation of a-C:H film using RF-PECVD method, and (vi) preparation of interlayer using magnetron sputtering technique.

2.1 Literature reviews

As is well-known, the diamond-like carbon film has mostly been investigated in the scientific community and industry due to its excellent properties such as high hardness and elastic modulus, low coefficient of friction, good biocompatibility, good anti-corrosion, and high wear resistance. DLC film is commonly applied as a protective coating in the microelectronic device, magnetic data storage, biomedical component, automotive parts, food packaging, and marine part, etc. [41]. Moreover, a critical review by Mahmud *et al.* (2015) [22] reported the DLC can be used as a dry solid lubricant in the part that cannot be lubricated by wet lubricants such as biological, food processing, and chemical pump applications. Most of all, the ultimate goal of DLC coating on substrates is to increase their lifetime. Despite the DLC film being studied and developed for more than two decades, many restriction problems remain unresolved for the practical application. Recently, the deposition of DLC film on ferrous and ferrous alloy substrate has attracted great interest because their mechanical, tribology, and anti-corrosion properties can be improved significantly. Li *et al.* (2019) [23] has reported that the thick DLC film often fails to protect the substrate material due to the coatings tend to delaminate after a critical thickness is reached. In general, thick films can achieve high performance in a wide range of applications. However, Cui *et al.* (2015) [24] concluded that the DLC film's thickness

is limited by the high internal stress, mismatch of the chemical bonding, and incompatibility of thermal expansion coefficients. These factors result in DLC film's poor adhesion on substrates, causing films to delaminate and peel off, reducing industrial applications [41]. The DLC film can present the desired property if the adhesion between the substrate and coating materials is strong enough. On the ferrous and ferrous alloy substrate, the weakly bonded carbon at the DLC film/substrate interface usually leads to a spontaneous separation of the DLC film from the substrates. Thus, the substrates request assistance from the third party of the intermediate layer or interlayer to improve the adhesion [38].

The adhesion is the interaction of chemical bonding with atoms and molecules at the interface between two surfaces. The strength of the interfacial chemical bonding has a significant influence on the adhesion [41]. The DLC films can be coated over the adhesion supported interlayer, so the interlayer should be appropriately selected. The interlayer materials must be strongly attached to the substrate and coating film. Boeira *et al.* (2018) [17] and Crespi *et al.* (2019) [42] recapitulated that interlayers can be classified into two main groups. The first group is pure metallic interlayer, such as Ti, Cr, W, Al, and Mo. Sometimes the compound metallic interlayer can be added by the N and C to create the metallic nitrides and carbides such as TiN, CrN, and WC prepared by the PVD methods. The second group is nonmetals, and semiconductor materials such as N, C, B, F, and Si-containing interlayers. They can be implanted and deposited by the nitriding/carburizing techniques and PECVD/PVD processes [17], [42]. Silicon and chromium-based interlayers are frequently used as the interlayer of DLC films. Furthermore, the SiN_x and $\text{SiN}_x\text{:H}$ are very reassuring as the interlayer because they have not only given the high adhesion and wear resistance but also significantly improved the corrosion resistance and the stability of DLC films [41], [43]. Yang *et al.* (2019) [44] investigated the effect of silicon-based interlayer on the microstructure, adhesion, in vitro corrosion resistance, and tribological behaviour of DLC film coated on titanium substrate. They found that the DLC with interlayer shows the high critical load, low friction coefficient, and good in vitro corrosion resistance compared with the DLC without interlayer. Azzi *et al.* (2010) [45] studied the corrosion performance and mechanical stability of DLC films on the medical grade 316L stainless steel substrate in the context of their biomedical applications in

which the DLC prepared using RF-PECVD. They also investigated the effect of the amorphous hydrogenated silicon-based materials such as a-Si, a-SiN_x, a-SiC_x, a-SiC_xN_y, and a nitride interlayer to optimize its adhesion strength. The nitride interlayer was created using the plasma nitriding process. The substrate was exposed in the pure nitrogen plasma, while the silicon-based interlayer was prepared by the gas precursor of silane (SiH₄). They reported that the a-SiN_x interlayer shows the significant improvement of adhesion. Moreover, it was still found to significantly increase the corrosion resistance of medical grade 316L stainless steel and substantially improve this coating system's mechanical stability in the simulated body fluid environment. Boeira *et al.* were published a series of research work about the process parameters of the silicon-containing interlayer preparation on the adhesion of DLC film deposited on ferrous alloy substrates [17], [18], [42], [46], [47]. They used hexamethyldisiloxane (HMDSO), tetramethylsilane (TMS), and tetraethoxysilane (TEOS) as the liquid precursors. The results showed that the high deposition temperature of at least 300 °C is still needed to provide adequate adhesion, which will adversely affect the substrates with a low melting point. In addition, the oxygen in the liquid precursors resulting in low adhesion. The nitrogen and hydrogen plasma treatments are necessary to reduce the oxygen in the interlayer structure. Chen *et al.* (2015) [48] were investigated the effect of difference Si, SiN_x, and CN_x interlayer prepared using magnetron sputtering on the performance of DLC films on Si substrate. They found that the DLC deposited on the SiN_x interlayer shown the highest uniform surface micrograph and least I_D/I_G ratio. The highest full wave at full width at half-maximum (FWHM) is observed, suggesting the lowest disordering among all the samples. While the DLC film without interlayer shows significant stress due to the interdiffusion of C atoms into the Si substrate and leads to the stress accumulation on the surface. The addition of an interlayer can decrease the internal stress and improve the DLC's adhesion on various substrates. It is promising which can push forward the DLC films for a wide variety of industrial applications.

Silicon-containing interlayers can be prepared using gaseous, liquids, and solids as a source of silicon atoms. However, poison gases such as SiF₄ and SiH₄ were often used in which high safety processes are required. Vaporized liquids such as TMS, HMDSO, and TEOS need a high substrate temperature to provide adequate

adhesion. Moreover, some precursor contains oxygen, which results in a significantly degrade of interface bonding between the interlayer and substrate or DLC film. In comparison, magnetron sputtering could be a potentially beneficial technique for applying silicon based thin-film coatings on metal substrates. The advantages of the magnetron sputtering technique are nontoxic and non-dangerous of sputtering gas. Therefore, in this work, the magnetron sputtering technique is an excellent choice for the deposition of the silicon-based interlayer. Plasma enhanced chemical vapor deposition is a technique that can extend the applicability of the method for various precursors, reactive organic and inorganic materials as well as inert materials. In thin-film processes for microelectronic applications, radio frequency (RF) glow discharges are used almost exclusively. Practically all plasma etching and deposition processes in thin-film technology utilize RF rather than dc or low-frequency glow discharges. The reasons for this are severalfold. Electrons gain sufficient energy during oscillation in the alternating field to ionize molecules during impact collisions. Therefore, unlike low-frequency plasmas, the discharge can be sustained even with low secondary electron yield. Electron oscillations also enhance ionization efficiency so that low pressures can be invoked. Finally, since surfaces in contact with plasma are bombarded with electrons and positive ions on alternate half cycles of the RF, insulators can be used as electrode materials.

Chrome plating is the chromium deposition obtained by electrolysis, which is of great importance in the field of decorative and industrial coatings. However, chrome plating containing minute cracks resulting in corrosive substance may penetrate into the cracks [49]. NAB is a metallic alloy widely applied for ship valves and marine components. While displaying a good combination of corrosion resistance and strength, NAB is still apt to different forms of corrosion, such as stagnant seawater corrosion, selective phase corrosion, and cavitation erosion [50], [51]. Therefore, if these metallic alloys are to be used in the saltwater or under the corrosive circumstances, the solution to avoid the problem of samples is to process the high corrosion resistant DLC films on the top of the interlayer and specimens.

A few research works have been investigated on the anti-corrosion property of a-C:H film on the chrome plating and NAB in seawater. Most research is focused on the mechanical and tribology properties for the engine component in the mechanical

industry. Another interesting way to enhance the corrosion and other DLC properties is the design of the multilayer structure. Cui *et al.* (2015) [24] investigated the corrosion and tribocorrosion properties of multilayer DLC film on steel substrate compared with the steel substrate and single layer DLC on a steel substrate. The results show that the multilayer DLC film is a superior protective material for improving corrosion and wear performance due to the lower corrosion current density compared to the substrate and single layer DLC film leading to extremely low wear rate under NaCl conditions. In general, the multilayers achieved by periodically alternating deposition of hard and soft of DLC layers; the hard DLC layer produces large elastoplastic deformation, while the soft DLC layer can alleviate the high stress of the hard layer [23]. Wang *et al.* (2013) [52] described that the hard layer's residual stress is the tensile stress, whereas that for the soft layer is compressive stress. Thus, the directions of strains occurring in soft and hard layers are opposite. The adhesion strength between these layers is sufficient; the stress does not cause the soft and hard layer peeling off each other. Therefore, an in-house hybrid RF-PECVD system is mainly used for the silicon-based interlayer coating and non-conductive materials, especially the a-C:H film to improve the corrosion resistance of chrome plating and NAB. Further studies will be conducted on a multilayer DLC film to enhance the superior anti-corrosion property.

2.2 Chromium-plated and nickel aluminum bronze substrates

The main substrates used in the thesis for DLC's deposition with silicon-based interlayer and multilayer DLC films are the chrome plating and NAB. These substrates are coated with DLC films to enhance the anti-corrosion property of components used under seawater conditions. The chrome plating was coated on consumer products such as the faucet, part of a marine boat, furniture, household, appliances, etc. that require esthetic, brightness, and corrosion resistance [53]. In the oil, petroleum, and chemicals industry, the chrome plating was used for interior and exterior coating of highly strained parts and interior coating of transport pipes [54]. While the NAB material is extensively used in the marine parts such as water valves, ship propellers, fittings, tubing, and oil rig equipment in the shipbuilding industry and

offshore oil/gas petrochemical industries due to its excellent anti-corrosion property [38]. However, it is necessary to enhance the anti-corrosion property of these substrates under advanced usability conditions. Thus, to overcome this drawback, the DLC coating's multifunction is considered an excellent choice as a protective layer coating to enhance the corrosion resistance.

Chromium is the metal in the transition metal category, which was first discovered by the France chemist Nicolas Louis Vauquelin in 1780. He accidentally discovered while experimenting with extracting a material known as Siberian red lead or also known as the mineral crocoite (PbCrO_4) [55]. The detail of chromium reveals that it is a blue-white metal that is hard, brittle, and good corrosion resistance. Chromium can be polished to be a very lustrous surface and is often coated to other metals to form a protective coating layer. Also, chromium can be added or doped into steel to improve the hardness. The chrome plating is the material thin layer of chromium material that is coated onto the object surface of other metal such as aluminum, brass, stainless steel, copper, or plastic. This coatings' objective is to increase the bulk material's surface properties, usually referred to as a substrate. The chromium coating offers several benefits that can improve equipment performance. It can enhance amongst other features, decorative, scratch resistance, adhesion, wettability, and reduces friction coefficient, reduces wear and damage from corrosion, reduces erosion, etc. In general, the chromed layer was coated on the surface using the electroplating method, and the chromed layer on the surface is often referred to as chrome or chrome plating. Chrome plating conducts the brightness, blue-colour, and mirror-like of the surface. The chrome plating is classified into two types: (i) hard chrome plating and (ii) decorative chrome plating.

The hard chrome plating is thicker than decorative chrome plating, and a typical thickness of hard chrome plating is in the range of 10–200 μm . The hard chrome layer is directly coated on the bare metal surface to achieve the unique properties due to the thick layer of chromium. The hardness of this is in the range of 46–74 R.C. depending on the electroplating condition. This hard chromium-plated layer can enhance the hardness, durability, corrosion resistance, and wear resistance of metal components for more effective machinery use. The hard chromium-plated

applications are the hydraulic rods, thread guides, mold surfaces, and piston rings [56].

The decorative chrome plating is commonly coated on top of either copper or nickel layer as the sub-layer. These sub-layers incline to protect the substrates from the micro-cracking chrome plating. The typical thickness for the decorative chromium-plated layer is in the range of 0.5–2 μm , and the total thickness of including the sub-layers and chromium-plated layer is typically 10 μm [56]. Decorative chrome plating provides a surface to a glossy, mirror-like shine, aesthetic appeal, smooth, and protective coating appearance desirable for various consumer products. Its smooth surface of the chromium-plated layer does not trap the dust particles and dirt. Therefore, the products are easy to clean and can keep on shining for long-term use. Decorative chrome plating can protect the products against wear and rust when products get exposed to the corrosive condition. For consumer products like the faucet, household, furniture, musical instruments, and car parts, the decorative chrome plating can increase products' perceived value and attractiveness.

The corrosion resistance of hard and decorative chrome plating depends on forming a thin layer of the oxide film, which protects it from further oxidation. The oxide film is sometimes called passive film. Also, the poor wettability of chrome plating protects easy access of corrosive liquid [57]. Even though the decorative chrome plating achieves the wear and corrosion resistance in environments but sometimes it tends to occur the microscopic cracks, which leads to corrosion and wear.

The aluminum bronze materials are the alloy metal of the copper-based alloys containing approximately 5–11% of aluminum [58]. Since 1850 of the first production of aluminum bronze, there is developed in elemental additions to improve the mechanical and corrosion resistance properties [39]. The binary system of early aluminum bronze consists of copper and aluminum, with aluminum content ranging from 5–11%. The increase of aluminum to about 8–9% results in higher strength, which is ascribable to a hard face-centered cubic (fcc) phase, improving their properties. In addition, some materials such as iron, nickel, silicon, and manganese can be added into aluminum bronze. All aluminum bronzes offer the best combination of mechanical and corrosion resistance properties, depending on their metallurgical

structure and composition. Consequently, these aluminum bronzes produce wide properties that are beneficial to a diverse range of industries. The other alloying elements also adjust the properties and modify the microstructure. Iron acts as a grain refiner and increases tensile strength, while the nickel enhances the properties of yield strength and corrosion resistance. Both of nickel and manganese adjust the microstructure stabilizers [38].

The nickel aluminum bronze has been used in various aerospace, architecture, marine part, offshore oil/gas and petrochemical, and desalination and water condenser systems applications. NAB is widely used in marine applications, particularly as the valves and fittings, valve stems, pump casings, pump shafts, ship propellers, etc. The NAB's corrosion resistance relies on forming the oxide layer in both copper (Cu_2O) and aluminum oxides (Al_2O_3), which perhaps about 900 to 1000 nm thick of the oxide layer. The oxide layers of nickel and iron also tend to occur after longer exposure times in the seawater. More oxygen concentration leads to a more protective oxide layer. These oxide layers act as a protective barrier and can self-repairing even in the very low oxygen levels in the seawater environment. While the alumina film (Al_2O_3) has high hardness, it creates higher resistance to erosion and abrasion. The oxide layer on the NAB surface achieves corrosion protection resulting in corrosion resistance. In general, at the recommended value of 4.3 m/s velocity, the oxide layer has an initial thickness of ~ 0.001 mm. The thickness will increase with time resulting in a steady corrosion rate of ~ 0.05 mm per year [38]. Moreover, under seawater conditions flowing at high speed and intermittent or with a high degree of turbulence, and oxygen is present enough, the protective oxide layer has time to repair itself. However, if the seawater's flow rate is persistent high or turbulent, the protective oxide layer unable to self-repair. Then shear stresses can be created, which may be degraded of the protective oxide layers, locally uncover the unprotected bare metal, and cause higher corrosion when the protective oxide layer formation rate is lower than the corrosion rate [38], [59]. If NAB's surfaces of or chrome plating get the corrosion, that can reduce the product's lifetime. Changing these products frequently is also not undesirable because of the high cost involved [60].

2.3 Structure and classification of amorphous carbon

Amorphous carbon is a non-crystalline solid forming based on the chemical element of carbon allotropic. The carbon is the sixth element in the periodic table, and it is one of the fourth most abundant species behind hydrogen, helium, and oxygen [61]. The isotopes of carbon have three: ^{12}C , ^{13}C , and ^{14}C , and the ^{12}C and ^{13}C are the stable isotopes. Most of Earth's carbon (~98.89%) occurs as the ^{12}C isotope contains six protons and six neutrons that the two electrons closed the inner shell, and the four electrons closed the outer shell acting as a valence electron [62], [63]. The electron states of carbon can be classified by the principal quantum number of $n = 1, 2$ and by the angular momentum values of s orbital for $n = 1, 2$ with two states of spin directions and p orbital for $n = 2$ with six states corresponding to the three possible orientations of p_x , p_y , and p_z with two spins. The ground state of a carbon atom consists of two core electrons in the $1s$ orbital and four valence electrons in the $2s$ and $2p$ orbital with corresponding to $1s^2, 2s^2, 2p^2$. The electron density distribution for s and p state is represented in Figure 2.1 [10].

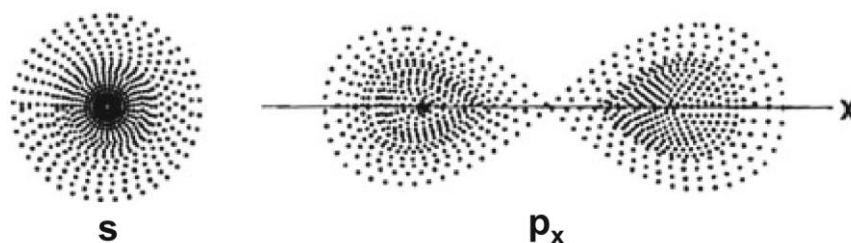
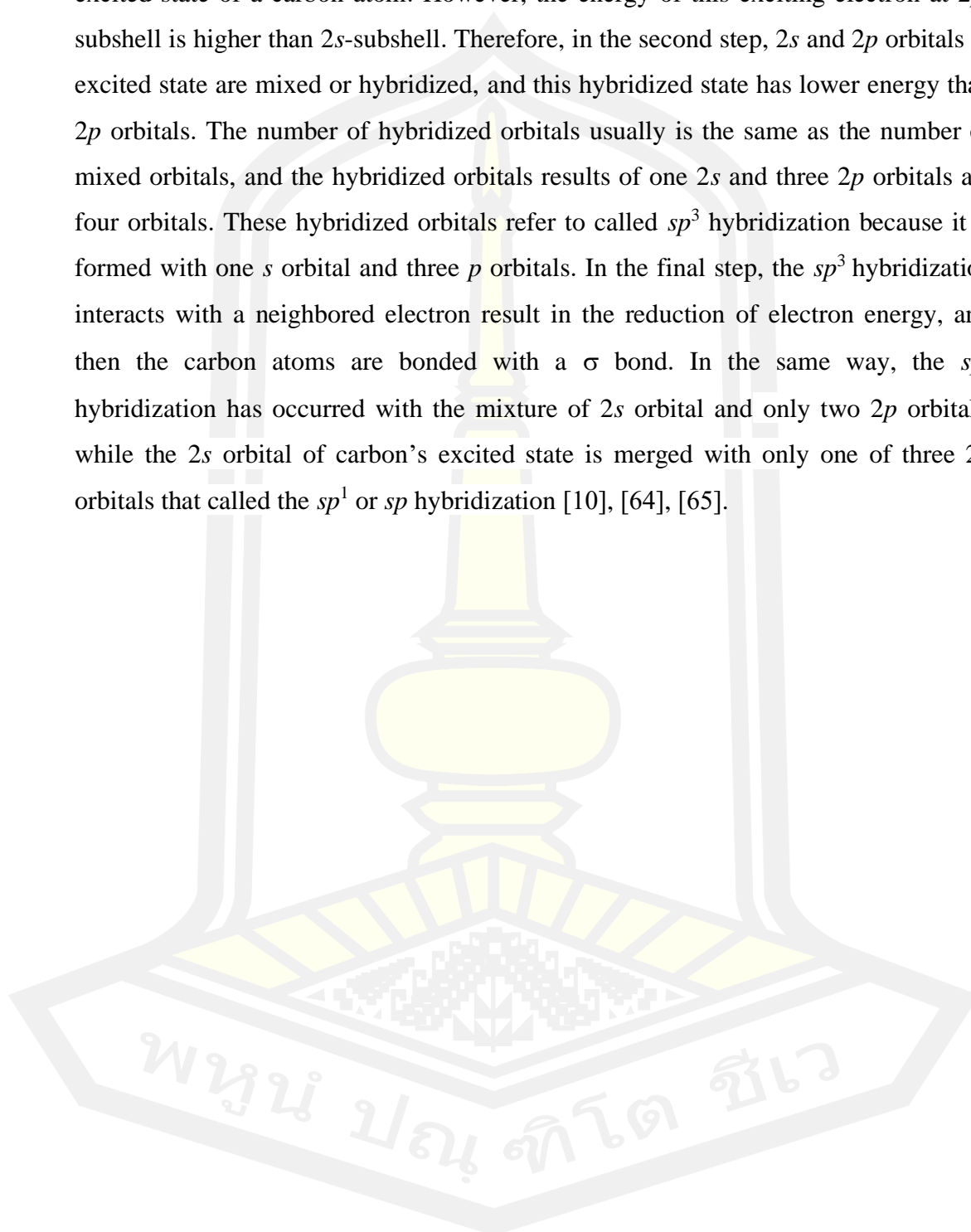


Figure 2.1 The distribution schematic of the density of carbon valence electrons in the s and p_x state.

The carbon compound's structure is based on the covalent bonding of pi (π) bond and sigma (σ) bond by the overlap of localized electron distributions of neighboring atoms. The bonding can be mixed or hybridized by the redistribution of carbon's valence electron. As shown in Figure 2.2 (a), the redistribution of electron states may be separate as three sequences. In the first step, in the ground state of a carbon atom ($1s^2, 2s^2, 2p^2$), the one-electron in $2s$ orbital is excited from the ground

state and transferred to $2p$ orbital with the excitation energy of 2.4 eV and lead to the excited state of a carbon atom. However, the energy of this exciting electron at $2p$ -subshell is higher than $2s$ -subshell. Therefore, in the second step, $2s$ and $2p$ orbitals of excited state are mixed or hybridized, and this hybridized state has lower energy than $2p$ orbitals. The number of hybridized orbitals usually is the same as the number of mixed orbitals, and the hybridized orbitals results of one $2s$ and three $2p$ orbitals are four orbitals. These hybridized orbitals refer to called sp^3 hybridization because it is formed with one s orbital and three p orbitals. In the final step, the sp^3 hybridization interacts with a neighbored electron result in the reduction of electron energy, and then the carbon atoms are bonded with a σ bond. In the same way, the sp^2 hybridization has occurred with the mixture of $2s$ orbital and only two $2p$ orbitals, while the $2s$ orbital of carbon's excited state is merged with only one of three $2p$ orbitals that called the sp^1 or sp hybridization [10], [64], [65].



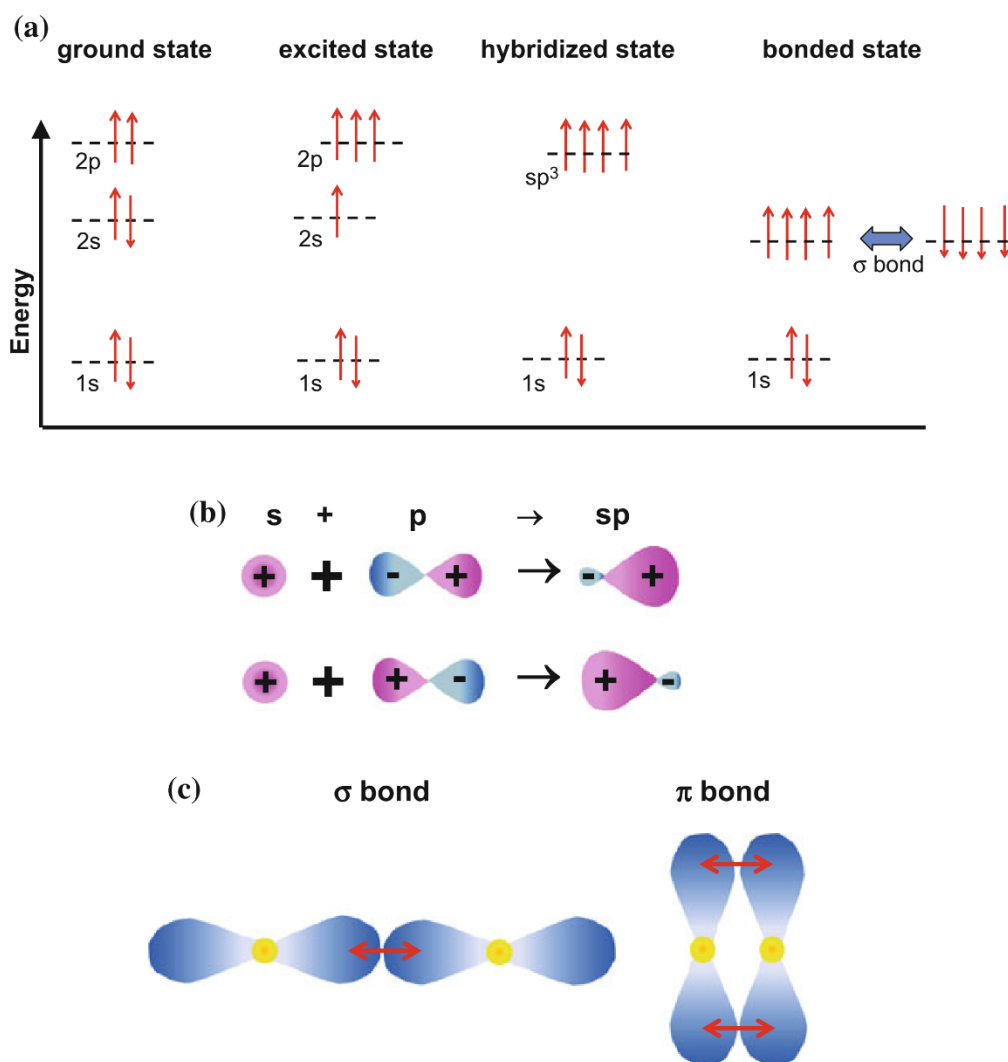
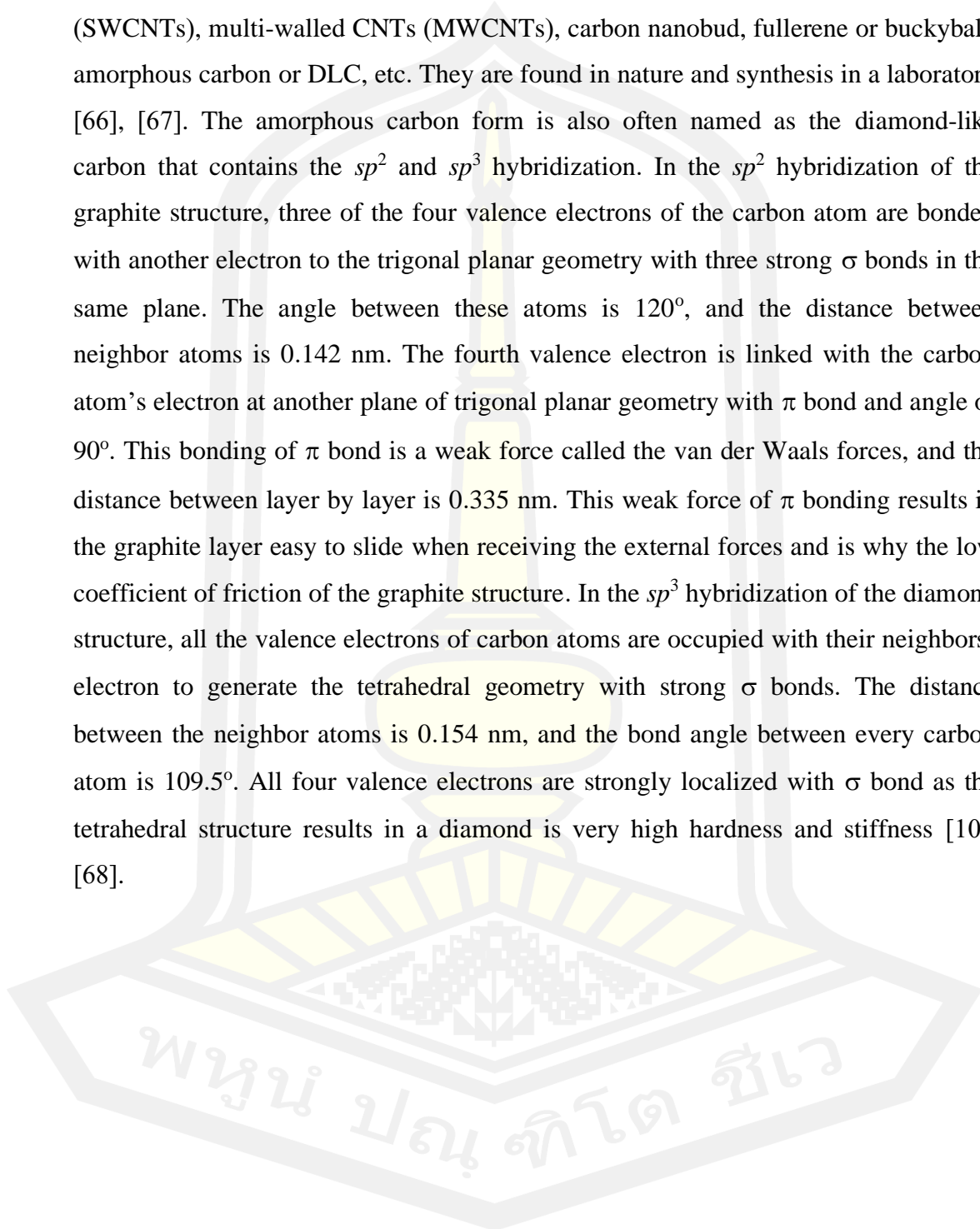


Figure 2.2 Scheme of (a) the electron states redistribution, (b) the hybridization of s and p orbitals of the electron distributions, + and - denote the signs of the wave functions, (c) the overlap of p orbital with covalent π and σ bonding [10].

Figure 2.2 (b) represents the schematic example of the redistribution of s and p orbital by the hybridization, + and - denote the signs of wave functions. The s (+) orbital hybrid with the p (-) orbital and s (+) orbital hybrid with the p (+) orbital resulting in a different shape. The electron clouds overlap directly between the atom's p orbital, leading to a strong bond or σ bond. While the π bond is formed with sideways or side by side overlap oriented of p orbitals leading to a weak bond, as shown in Figure 2.2 (c).

As shown in Figure 2.3, most carbon allotropic forms are crystalline and amorphous, such as diamond, graphite, graphene, single-walled carbon nanotubes (SWCNTs), multi-walled CNTs (MWCNTs), carbon nanobud, fullerene or buckyball, amorphous carbon or DLC, etc. They are found in nature and synthesis in a laboratory [66], [67]. The amorphous carbon form is also often named as the diamond-like carbon that contains the sp^2 and sp^3 hybridization. In the sp^2 hybridization of the graphite structure, three of the four valence electrons of the carbon atom are bonded with another electron to the trigonal planar geometry with three strong σ bonds in the same plane. The angle between these atoms is 120° , and the distance between neighbor atoms is 0.142 nm. The fourth valence electron is linked with the carbon atom's electron at another plane of trigonal planar geometry with π bond and angle of 90° . This bonding of π bond is a weak force called the van der Waals forces, and the distance between layer by layer is 0.335 nm. This weak force of π bonding results in the graphite layer easy to slide when receiving the external forces and is why the low coefficient of friction of the graphite structure. In the sp^3 hybridization of the diamond structure, all the valence electrons of carbon atoms are occupied with their neighbors' electron to generate the tetrahedral geometry with strong σ bonds. The distance between the neighbor atoms is 0.154 nm, and the bond angle between every carbon atom is 109.5° . All four valence electrons are strongly localized with σ bond as the tetrahedral structure results in a diamond is very high hardness and stiffness [10], [68].



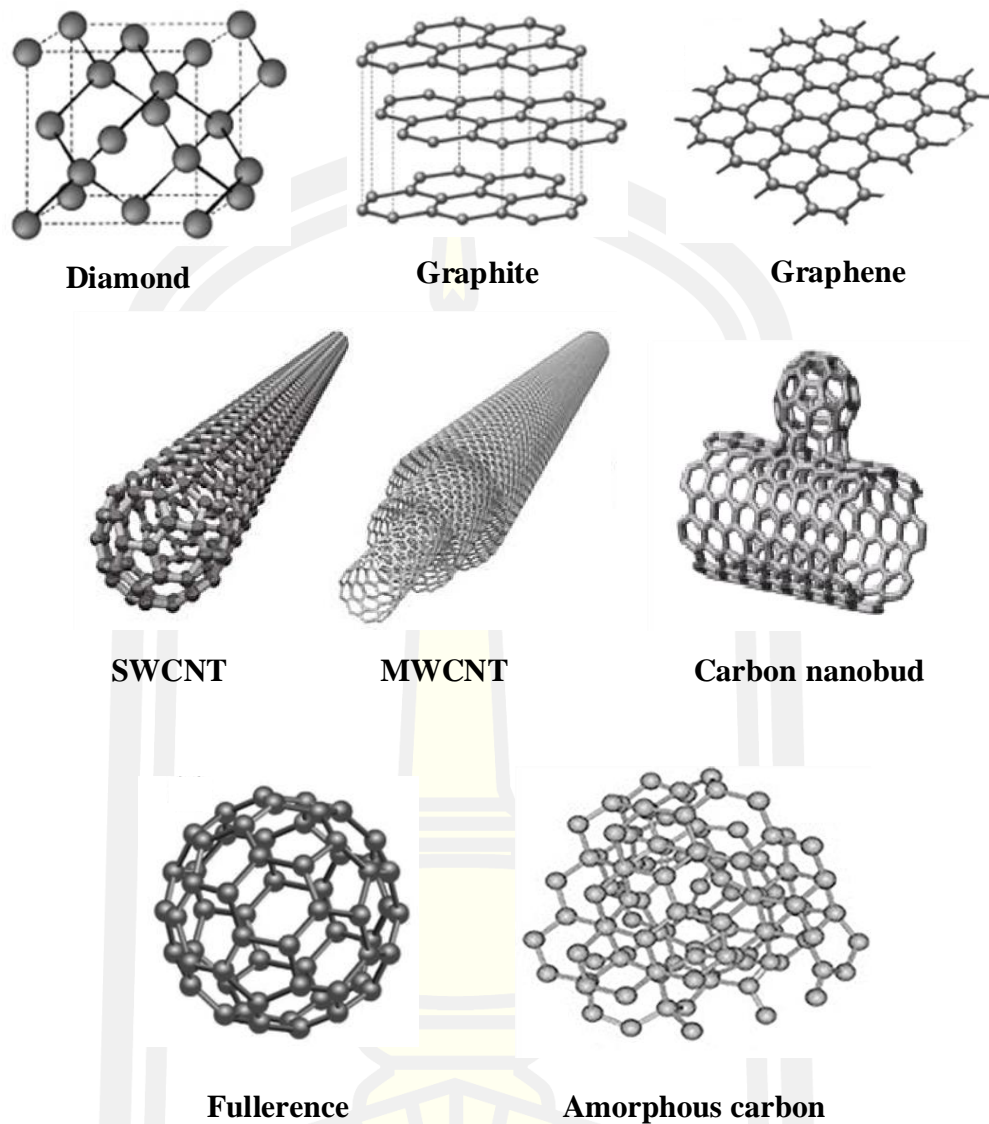


Figure 2.3 Structures of all carbon allotropes [69], [70].

Aisenberg and Chabot [71] have first discovered amorphous carbon films for over five decades, which prepared the diamond-like carbon films by the ion beam deposition method. After that, amorphous carbon films have been continuously developed until now. DLC is one of the amorphous carbon forms with a metastable state containing a significant fraction of sp^3 , sp^2 hybridizations, and sometimes with or without hydrogen content. Generally, the sp^3 , sp^2 fractions, and hydrogen content represent the fundamental characteristics of amorphous carbon films. The variety of

sp^3 and sp^2 hybridizations and hydrogen content result in the different types of DLC structures and properties. Hence, the different types of DLC can be classified by the position of C- sp^3 , C- sp^2 , and H in the ternary phase diagram by Robertson (2002) [4], as shown in Figure 2.4, as first reported by Jacob and Moller (1993) [72].

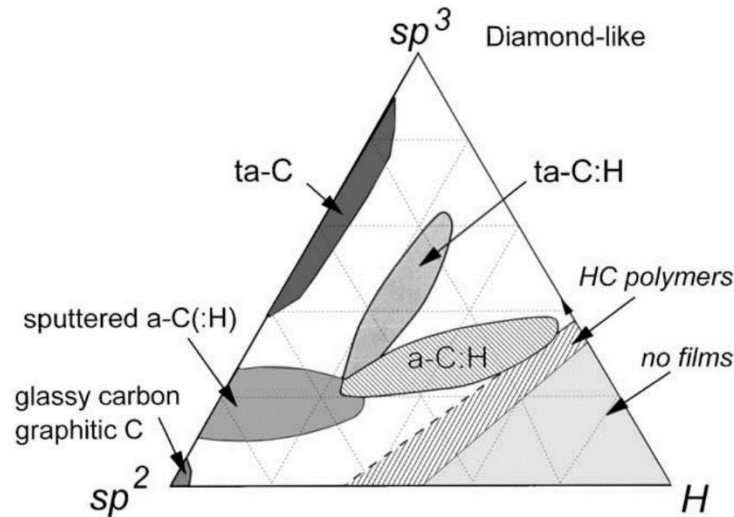


Figure 2.4 Ternary phase diagram of amorphous carbon films [4].

As indicated in Figure 2.4, the ternary phase diagram consists of three main regions using the quantitative measurement of three phases: C- sp^3 , C- sp^2 , and H concentration. Jacob and Moller compared and summarized the published data of the composition of amorphous carbon films. For the determination of C- sp^3 /C- sp^2 ratio, the infrared (IR) analysis, electron energy loss spectroscopy (EELS), and nuclear magnetic resonance (NMR) have been used. While the hydrogen content has been measured by the ion beam analysis (IBA) and combustion analysis (Co) in the literature. These data of the ternary phase diagram are normalized to the atomic fraction of 100 at% [72]. The first region lies in the lower left-hand corner in which the glassy carbon is located. It is not DLC films with the sp^2 rich usually prepared by the pyrolysis of hydrocarbon polymers or by an evaporation method. Up to the left corner, the conventional sputtering was used to prepare the higher sp^3 a-C film with or without hydrogen. This method can extend the sp^2 bond towards the sp^3 bond. The a-

C film with higher sp^3 fraction ($> 80\%$) denoted as the ta-C, which can produce with the filtered cathodic vacuum arc (FCVA), unbalanced magnetron sputtering, and pulse laser deposition (PLD). the lower right-hand corner. This region is closed to the hydrogen-rich in which the amorphous carbon films can not be formed a C-C network. The third region lies in the middle of the ternary phase diagram, the a-C:H and ta-C:H films is a combination of C- sp^3 , C- sp^2 , and H fraction. The PECVD method can synthesis the a-C:H film by the hydrocarbon precursor gas, and the ta-C:H can be achieved by adjusting the process parameters of the PECVD process. Furthermore, the electron cyclotron resonance (ECR), magnetron sputtering and inductively coupled plasma can be generated high-density plasma to produce the high sp^3 fraction of ta-C:H films [4], [10], [72].

Therefore, the DLC films can be classified by the C- sp^3 , C- sp^2 , and H content into four main types described below in detail. The characteristic of different DLC types compared with diamond and graphite is shown in Table 2.1.

- (i) Amorphous carbon (a-C) is the hydrogen-free DLC film, consist of 0–5% C- sp^3 , less than 1% hydrogen content, and 10–20 GPa hardness.
- (ii) Hydrogenated amorphous carbon (a-C:H) is the DLC film with hydrogen, consist of 40–60% C- sp^3 , 20–60% hydrogen content, and 10–20 GPa hardness.
- (iii) Tetrahedral amorphous carbon (ta-C) is the hydrogen-free DLC film, consist of 80–88% C- sp^3 , 20–60% hydrogen content, and 50–80 GPa hardness.
- (iv) Tetrahedral hydrogenated amorphous carbon (ta-C:H) is the DLC film with hydrogen, consist of 70% C- sp^3 , 30% hydrogen content, and 50 GPa hardness.

Table 2.1 The characteristic of the diamond, graphite, and different DLC types [73].

	sp^3 (%)	Hydrogen content (%)	Density (g/cm^3)	Hardness (GPa)	Young's modulus (GPa)
Diamond	0	0	2.267	0.2–2	10
Graphite	100	0	3.515	100	1000
a-C	0–5	<1	1.9–2.2	10–20	100–200
a-C:H soft	60	40–60	1.2–1.6	<10	100–300
a-C:H hard	40	20–40	1.6–2.2	10–20	100–300
ta-C	80–88	0	3.1–3.3	50–80	300–500
ta-C:H	70	30	2.4	50	300

2.4 Hydrogenated amorphous carbon films

The hydrogenated amorphous carbon films belong to the class of materials called diamond-like carbon. As is well known, the a-C:H films are formed by the cross-linking of the amorphous carbon network, which has a lower sp^3 content (maybe up to 60%) and the presence of a fraction of hydrogen atoms bonded to the carbon network in the range of 20–60%. The a-C:H films have attracted much attention to many industries due to their unique properties, a-C:H films can be coated on various substrates to protect the surface substrate material. However, it has limited tribological applications to deposit a-C:H films on the alloy steels when the film's thickness reaches the critical value. Therefore, this topic gives the feasible approach to enhancing the adhesion, increasing film thickness, and reducing residual stresses by adding an interlayer or multilayer between substrate and DLC films.

2.4.1 a-C:H films on metal alloys with the interlayers

Most a-C:H applications were synthesized onto tool steel substrates. Problems associated with the surface roughness and poor adhesion due to the high internal compressive stress have limited their use in tribological applications. Several techniques, including optimization of the process parameters, can reduce these limitations. One method of improving film to substrate adhesion has been through the deposition of interlayers. Cemin *et al.* (2005) [74] used the a-SiC_x:H interlayer for the steel substrate, the a-C:H coated on steel substrate without interlayer showed the spontaneous delamination of the DLC film from the steel surface after the deposition process. This spontaneous cracking is characteristic of seriously stressed films that break down in contact with the atmosphere and temperature shock. When the interlayer was grown on the steel substrate, the a-C:H films can completely adhere to the steel surface, as seen in Figure 2.5.



Figure 2.5 Surface characteristics of (a) the AISI 4140 steel polished, (b) DLC without interlayer on steel, and (c) DLC with a-SiC_x:H adhesion interlayer on steel [74].

The process parameters of the interlayer coating also affect on the a-C:H' adhesion. Bonetti *et al.* (2006) [75] reported the influence of self-bias voltage on the DLC growth with silicon interlayer on Ti6Al4V substrate. The addition of a silicon interlayer successfully reduced the films's intrinsic stress and the self-bias voltage resulting in the different stress and structural property of the films. Jeon *et al.* (2007) [76] studied the effect of different metals (Cr, Ni and Ti) interlayers on the tribological property. The result shows that the residual stress of a-C:H decrease with the addition of the metals interlayer, as seen in Figure 2.6. In addition, the friction

coefficient of a-C:H films with metals interlayer is lower than without interlayer. The interlayer's thickness should be appropriated because more thickness may induce residual stress and crack formation between the interlayer's innermost and outermost.

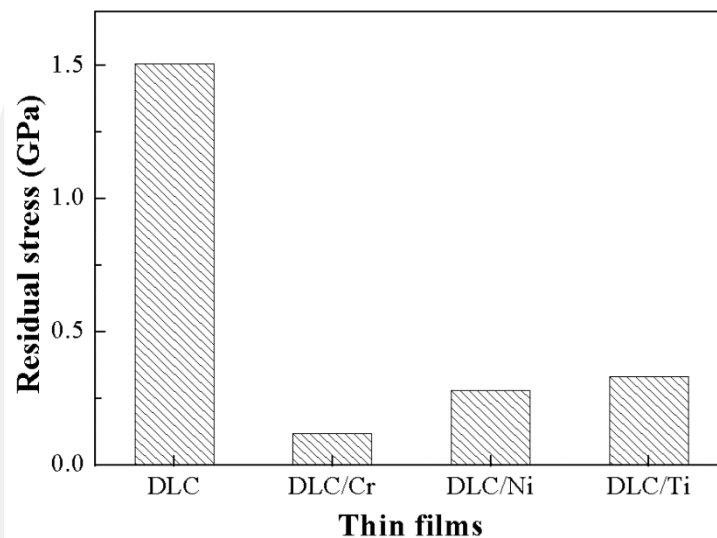


Figure 2.6 Residual stress of the DLC films with and without metals interlayer [76].

2.4.2 Multilayer a-C:H films

DLC films' thickness is an essential parameter because the thicker DLC coating provides excellent corrosion resistance, ultrahigh load-bearing capacity, and high wear resistance. In general, thick films can achieve better anticorrosion due to prevent corrosion penetration. However, the residual stress, mismatch of thermal expansion coefficient, and the chemical bonding limit the film thickness at only 1–3 μm . Ye *et al.* (2018) [77] investigated the anticorrosion and tribological behaviours in seawater of thin and thick DLC films prepared by an unbalanced magnetron sputtering technique on 304L stainless steel. The Cr interlayer was used to improve the adhesion force between DLC films and the substrates. The thicknesses of thin and thick DLC films are about 449 nm and 1.76 μm , respectively. The result shows that film thickness is significantly affected on the properties of the DLC film. The corrosion test, the thick DLC film, presents the lower corrosion current density and

higher impedance than the thin DLC film corresponding to the excellent anti-corrosion property. However, the thickness of the DLC film with interlayer remained less than 2 nm.

Recently, the multilayer DLC film design has drawn much attention in various applications. Many literature pieces have defined that the multilayer DLC film consists of the alternating hard and soft DLC layer could interestingly reduce stress, leading to an increase in the film thickness up to 50 μm [23], [52]. In research cases of Wang *et al.* (2013) [52] showed that the deposition of $\text{Si}_x\text{-DLC}/\text{Si}_y\text{-DLC}$ multilayer prepared by the PECVD method in which the SiH_4 gas was used to regulate the soft and hard DLC layer and transition layer. The total thickness of $\text{Si}_x\text{-DLC}/\text{Si}_y\text{-DLC}$ multilayer is about 52.2 μm . The multilayer residual stress with 52.2 μm thick (-0.05 GPa) is lower than pure DLC with 1 μm thick (-0.45 GPa). The describes of the low residual stress with multilayer coating is shown in the schematic in Figure 2.7. The residual stress for the $\text{Si}_x\text{-DLC}$ film is compressive stress, while the $\text{Si}_y\text{-DLC}$ and DLC films are tensile stress. Arrow direction indicated the characterize of stress. Therefore, the directions of strains occurring in $\text{Si}_x\text{-DLC}$ and $\text{Si}_y\text{-DLC}$ are opposite. Thus, the residual stress reduction in this approach is successfully achieved.

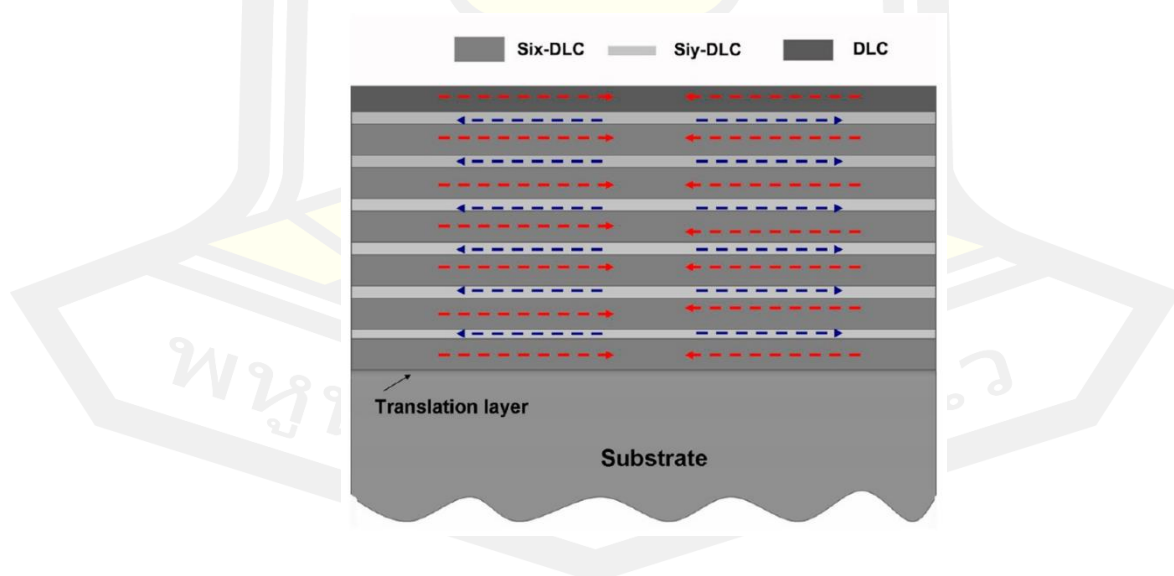


Figure 2.7 Schematic illustration of the mechanism of low residual stress in a multilayer DLC film [52].

2.5 Preparation of a-C:H film using RF-PECVD method

Hydrogenated amorphous carbon can be deposited by various techniques such as plasma immersion ion implantation (PIII) via the hydrocarbon and inert gases [78], reactive magnetron sputtering via the graphite target and hydrogen or hydrocarbon gases [79], [80], and plasma-enhanced chemical vapor deposition (PECVD) via the hydrocarbon gas [81]. The conventional CVD or thermal CVD process, external energy like a heating source is required to excite atoms and molecules (precursor). This process relies on thermal energy in which precursor gas was flown over the substrates, and the growth of thin films on the surface occurs due to the chemical reaction in the vapor phase. The PECVD is a well-known technique for preparation of a-C:H films at low temperatures. The electrical discharge utilized for plasma will promote the CVD processes by enhancing the chemical reaction rates of the precursors.

2.5.1 PECVD process

The electrical discharge is often driven at the DC, low frequency (<1 MHz), radio frequency (1–500 MHz, commonly 13.56 MHz), and microwave (0.5–10 GHz, commonly 2.45 GHz). The harmonic of 13.56 MHz frequency is a popular choice and set aside for medical and industrial applications [82]. The RF discharge is suitable for the insulating film deposition, especially the DLC film. In 1976, Holland and Ojha [83] reported that DLC film's high resistivity would limit the film growth rate due to the accumulated charges on the film surface. The radio-frequency glow discharge can overcome this problem by supplying the electrons to neutralize the ions. The plasma will be generated between the parallel electrodes or the chamber wall. One of the electrodes is connected to the RF power supply in which the substrate is mounted, and the other one is typically connected to the earth's ground. In RF plasma, the electrons can respond with the radio frequency better than ions due to the electron mass lower than ion. Therefore, the electrons move with much higher velocity (mobility) than ions. The plasma sheath will be generated near the surface of the RF power electrode with high ion density. This area is formed of the positive space charge barrier for the incoming electrons. Thus, the plasma creates a positive voltage

with regards to the electrodes, which equilibrium the average ion and electron current to the wall. The plasma sheath performs as the diode's characteristic, in order to balance the electrode voltage with the DC self-bias voltage and their peak RF voltage. The RF voltage is distributed between the electrodes' plasma sheath of both, just like in a capacitive divider that according to their inverse capacitance. Therefore, the voltage of DC self-bias changes inversely with the surface area of the electrode. The smaller electrode has a smaller capacitance. Thus the self-bias voltage is generated higher than the larger electrode, as shown in equation 2.1 [4], and the smaller electrode is usually acting as the substrate holder. The negative voltage of a plasma sheath will increase the high acceleration of positive ion to enhance the sp^3 bonding on the substrate.

$$\frac{V_1}{V_2} = \left(\frac{A_2}{A_1} \right)^2 \quad 2.1$$

The common precursor of hydrocarbon gasses used for a-C:H formation is the methane (CH_4), acetylene (C_2H_2), benzene (C_6H_6), ethylene (C_2H_4), propane (C_3H_8), butane (C_4H_{10}), etc. In addition, silane (SiH_4) has been used in the precursor mixtures for the doped-DLC. The operating pressure is essential for a-C:H deposition due to the ion energy may be reduced by the collision when accelerated across the plasma sheath. Robertson reported that the ions are only about 10% of film-forming flux at 50 mtorr pressure. Ryu *at al.* (2000) [84] reported when the deposition pressure increase results in decreased deposition rate due to the enhanced scattering of film-forming species at higher deposition pressure. The ions' mean free path is associated with the operating pressure expressed as Equation 2.2. In the PECVD system, the mean free path of ions and the energy transfer to the substrate are related to the pressure. The sheath thickness decreases while the ion mean path decreases with the increasing pressure [84].

$$\lambda = \frac{kT}{\sqrt{2\pi}d^2P} \quad 2.2$$

The plasma density, ion energy, and electron temperature are strongly affected to the properties of the DLC film. At low RF power input, the plasma density is relatively low in the range of 10^9 – 10^{10} cm^3 . However, the plasma density can increase with the RF power input increase while the electron temperature is only a slightly varying function of RF-power gain [85]. Moreover, increasing the critical RF input power results in a high DC self-bias (sheath voltage), the DLC structure has more graphite-like due to the too high ion energy. Therefore, the enhance of plasma density by increasing the RF power result in the limited application of this process [86]. Mahanti *et al.* (2014) [87] reported the hardness of a-C:H film depends on the RF power. The films' hardness increases from 13.45 to 15.90 GPa with the increasing of RF power in the range of 30–60 W, as shown in Figure 2.8.

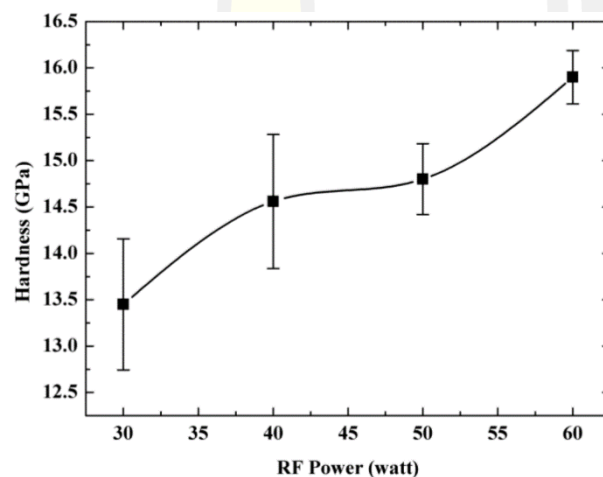


Figure 2.8 The hardness of a-C:H films as a function of RF power [87].

In addition, the high plasma density can be assisted with the magnetic field to confine the plasma and then enhance plasma density effectively. The magnetic plasma confinement will reduce the residual contamination from the chamber walls, prevent the film deposition on the chamber walls, and also can provide a more uniform electric field [86]. This configuration allows a capacitively coupled plasma system to generate the plasma stability at the very low operating pressure (5×10^{-4} torr). In this situation, the ion mean free path exceeds the plasma sheath thickness,

and the ion energy now becomes a narrow distribution at high ion energy, as shown in Figure 2.9.

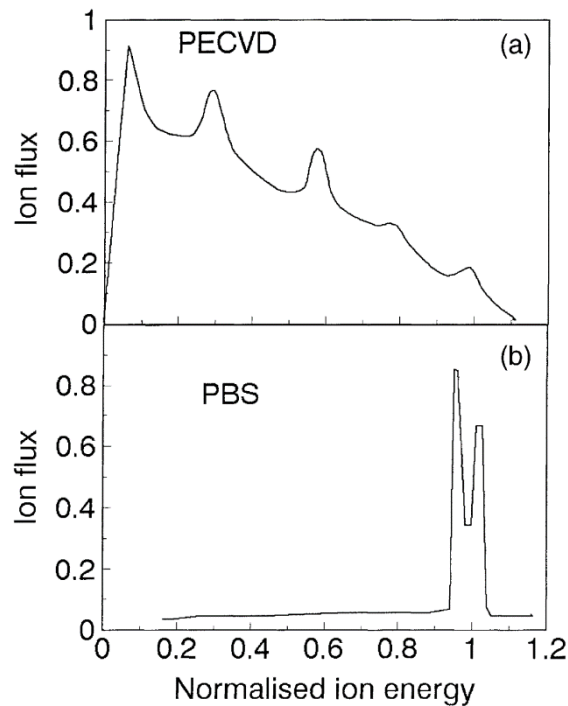


Figure 2.9 Ion energy distribution in (a) conventional PECVD and (b) magnetic confinement PECVD [4].

2.5.2 Process parameters

The properties of a-C:H films depend on the deposition parameters such as the precursor gas, frequency of power supply, substrate temperature, operating pressure, gases flow rate, and deposition time. These parameters influence the structural, mechanical, tribological, anti-corrosion property of a-C:H films.

Precursor gases effect

The difference of precursor gases on the growth of a-C:H films significantly affects their properties, especially the deposition rate. The precursor gas of a-C:H deposition consists of the carbon and hydrogen, which is often referred to as

hydrocarbon gas. The hydrocarbon gases such as methane (CH_4), ethane (C_2H_6), propane (C_3H_8), ethylene (C_2H_4), butane (C_4H_{10}), pentane (C_5H_{12}), hexane (C_6H_{14}), cyclohexane (C_6H_{12}), acetylene (C_2H_2), and benzene (C_6H_6) can be used to deposit a-C:H films. As shown in Figure 2.10, the growth rate of a-C:H film prepared based on the PECVD technique strongly depends on precursor gases. The difference in precursor gas has different ionization energy due to chemical bonding. The molecular species (C_xH_y) are reflected by the composition of the hydrocarbon ions (C_mH_n^*) and radicals (C_mH_n^+). In Figure 2.10, it can be seen that the deposition rate decreases roughly exponentially with the higher ionization energy and lower carbon content. The highest deposition rate can be achieved by the benzene gas (C_6H_6), due to the hydrogen per carbon (H/C) ratio of benzene gas is one, and ionization energy is 9.2 eV, which lower than other gases. For mechanical properties, the maximize in hardness can be accomplished by minimizing the incorporation of hydrogen. However, the energy per carbon atom in the benzene discharge can be much smaller even if the ion energy is assumed to be the same at the same value of pressure. It is well known that the a-C:H films properties rely on the ion energy per carbon atom. The ion energy of a carbon atom can accelerate by the bias voltage. The required bias voltage of a benzene ion (C_6H_n^+) is more than acetylene ion (C_2H_n^+) due to the benzene ion having six carbons atom while the acetylene has two. The benzene ion, therefore, requires a high bias voltage to reach the desired energy per atom. Thus, the acetylene gas is usually selected because they are the smallest H/C ratio and lowest ionization energy with high energy per carbon atom [4], [10].

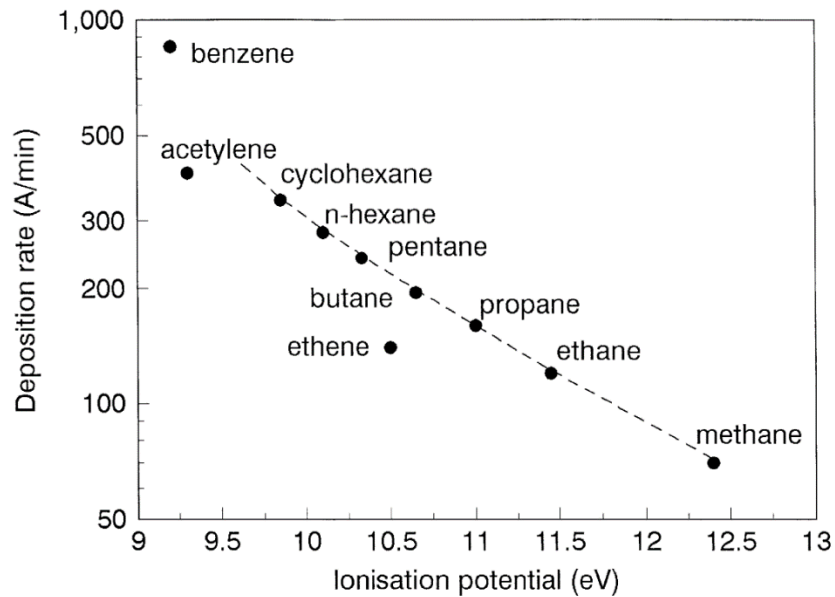


Figure 2.10 Deposition rate of a-C:H film prepared by PECVD method with different precursor gases [4].

Frequency effect

For the RF-PECVD system, the plasma density (n_p) is around 10^9 – 10^{10} cm^3 , the permittivity of free space (ϵ_0) is 8.85×10^{-12} F/m, electric charge (e) is 1.6×10^{-19} C, and the electron mass is 9.1×10^{-31} kg. Thus, the plasma frequency for the electrons is 895 MHz. While the frequency of methane (CH_4^+) and benzene (C_6H_6^+) ions are 5.4 MHz and 2.37 MHz, respectively. The responsibility of electron and ion to the input frequency is different. The acceleration of ions is based on the input frequency, which affects the plasma frequency ($f_{p,e}$) of the electrons and ($f_{p,i}$) ions. The plasma frequency is expressed as Equation 2.3 [10], [88].

$$f_p = \frac{1}{2\pi} \sqrt{\frac{e^2 n_p}{m \epsilon_0}} \quad 2.3$$

In case the plasma frequency more than the input frequency ($f_p > f$), the particles follow nearly immediately. With the RF frequency of 13.56 MHz, the plasma frequency is less than the input frequency ($f_p < f$). The particles can hardly follow the fast field oscillations. It means that the ions at a frequency above 10 MHz only slightly oscillate and at a frequency below 1 MHz keep pace with the changing field [10].

Many input frequencies of power sources are used to deposit the a-C:H films, including the DC, low-frequency (LF) (1–100 Hz), mid-frequency (30–100 kHz), RF (1–100 MHz), and microwave (1–30 GHz). The low-frequency has not been widely adopted in depositing thin films. However, the generated plasma by low frequency has a relatively higher electron temperature than radio frequency (13.56 MHz), resulting in the growth mechanism. Moreover, the molecular excitation energy using an RF source is lost more than using DC and low-frequency sources. The low-frequency and RF power sources are possible to deposit the dielectric film. The effect of input frequency on the plasma parameters and thin-film processes is summarized in Table 2.2 [89].

Table 2.2 Comparisons for the properties of plasma excitation using DC, low-frequency (60 Hz), and RF (13.56 MHz) power source [89].

Parameters	DC	LF	RF
Power frequency	0	60 Hz	13.56 MHz
Discharge pattern	Continuous	Discrete	Continuous
Ionization mode	γ -mode	γ -mode	α/γ -mode
Metal deposition	Possible	Possible	Possible
Dielectric deposition	Difficult	Possible	Possible
Plasma parameters	Similar in DC to RF		
Deposition rate	Higher in RF and DC than LF		
Energy loss	Higher in RF in DC and RF		

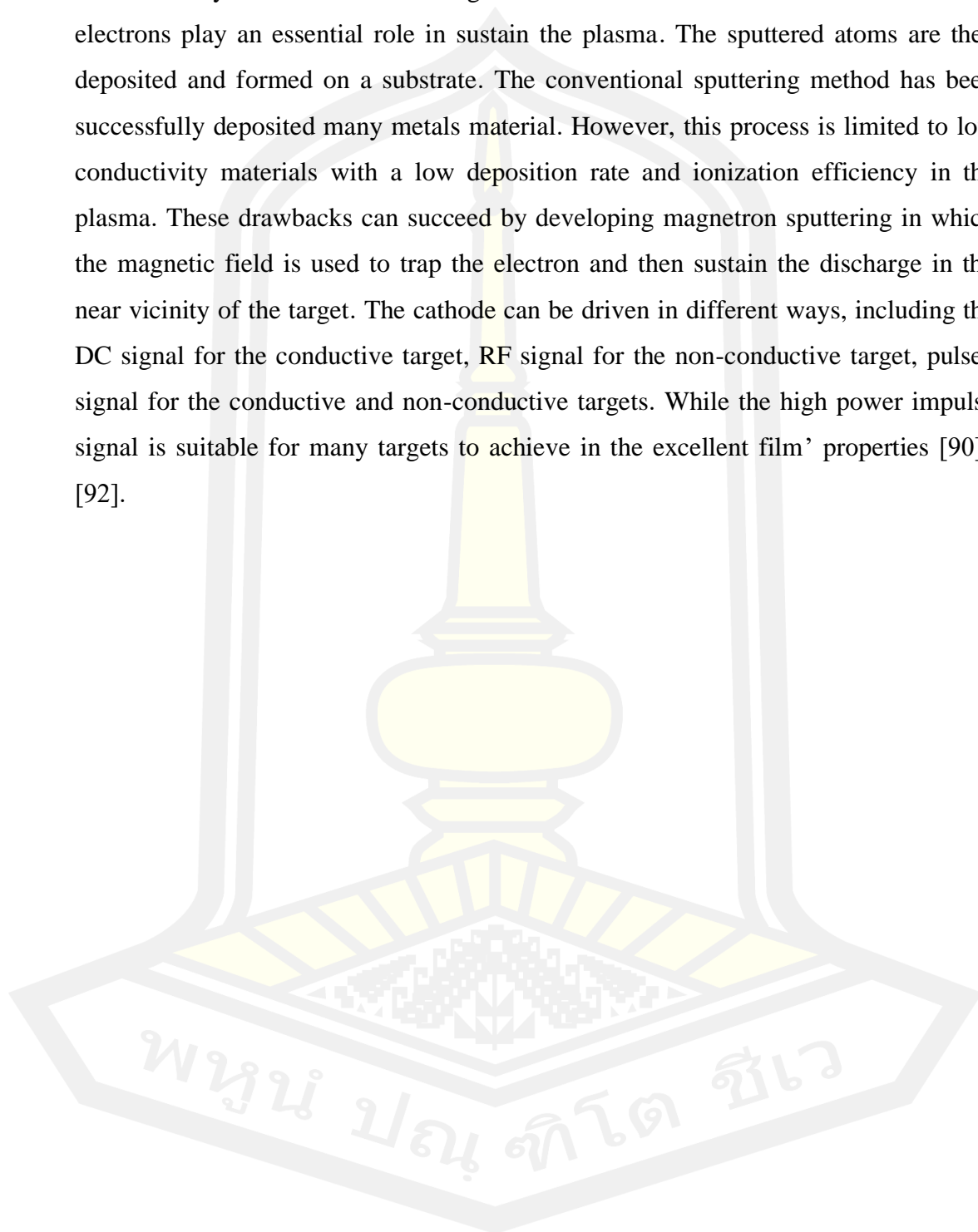
2.6 Preparation of interlayer using magnetron sputtering method

Various techniques with different sources can prepare silicon-containing interlayer. The liquid source required a high substrate temperature. The oxygen-containing in the vapor phase results in the failure adhesion. The gaseous of silicon required the high safety process, and the gas composition may contain the other atoms that result in difficulty controlling the film's properties. While the magnetron sputtering technique commonly used the solid source as the silicon target. It is easier to control film properties by adjusting the process parameters. This technique can produce the difference silicon-based interlayer such as a-Si, a-Si:N, a-Si:H, and a-Si_xC_y:H films by introducing the reactive gases such as nitrogen hydrogen, hydrocarbon gases. In addition, it can be used to produce the Si-doped DLC in the multilayer DLC film. Moreover, the process parameters are used to achieve good adhesive properties in DLC deposition.

Magnetron sputtering technique has developed rapidly over the two decades following the increasing industrial demand for high-quality functional films. This magnetron sputtering is a vacuum coating process. It is classified into the physical vapor deposition (PVD) like the pulsed laser deposition and thermal evaporation. Magnetron process can deposit a thin film of metals, alloys, insulators, and other material. The sputtering process's physical meaning is the ejection of atoms by the bombardment of a solid or liquid target by energetic particles, mostly ions [90].

The basic processes of sputtering are given as follows. As called the target, the precursor material is bombarded by the energetic ions of an inert gas such as argon, helium, neon, and krypton, which is accelerated with the negative voltage of the power source or power supply. The target material is referred to as the cathode since the target material is connected to the power supply's negative voltage. While the deposition chamber is also called the anode that is connected to the earth's ground. This negative voltage will generate the electric field to accelerate the energetic ion. The energetic ions are generated by the collision between the primary electron and inert gas and then create the secondary electron. The energetic ions with a positive charge will move toward the target material's cathode with the electric field. The energetic ions bombard and transfer the momentum to the target surface result in the

neutral atoms of the target source be dislodged. At the same time, this process emits the secondary electron from the target surface due to the ion bombardment. These electrons play an essential role in sustain the plasma. The sputtered atoms are then deposited and formed on a substrate. The conventional sputtering method has been successfully deposited many metals material. However, this process is limited to low conductivity materials with a low deposition rate and ionization efficiency in the plasma. These drawbacks can succeed by developing magnetron sputtering in which the magnetic field is used to trap the electron and then sustain the discharge in the near vicinity of the target. The cathode can be driven in different ways, including the DC signal for the conductive target, RF signal for the non-conductive target, pulsed signal for the conductive and non-conductive targets. While the high power impulse signal is suitable for many targets to achieve in the excellent film' properties [90]–[92].



CHAPTER III

Experimental procedure

The deposition and characterization of the a-C:H film with the silicon-based interlayer are described in this chapter. The chrome plating and nickel aluminum bronze are used as the substrate for adhesion and electrochemical corrosion testing, while the *p*-type silicon substrate is used for morphology and structural properties analysis. The experimental procedure is shown in Figure 3.1, and this chapter is divided into two sections and described in detail (i) the hybrid RF-PECVD/MS system, which consists of vacuum system, magnetron source, bottom electrode, and a vacuum control system. (ii) The thin-film deposition process is involved in substrate preparation, oxygen plasma cleaning process, and deposition process.

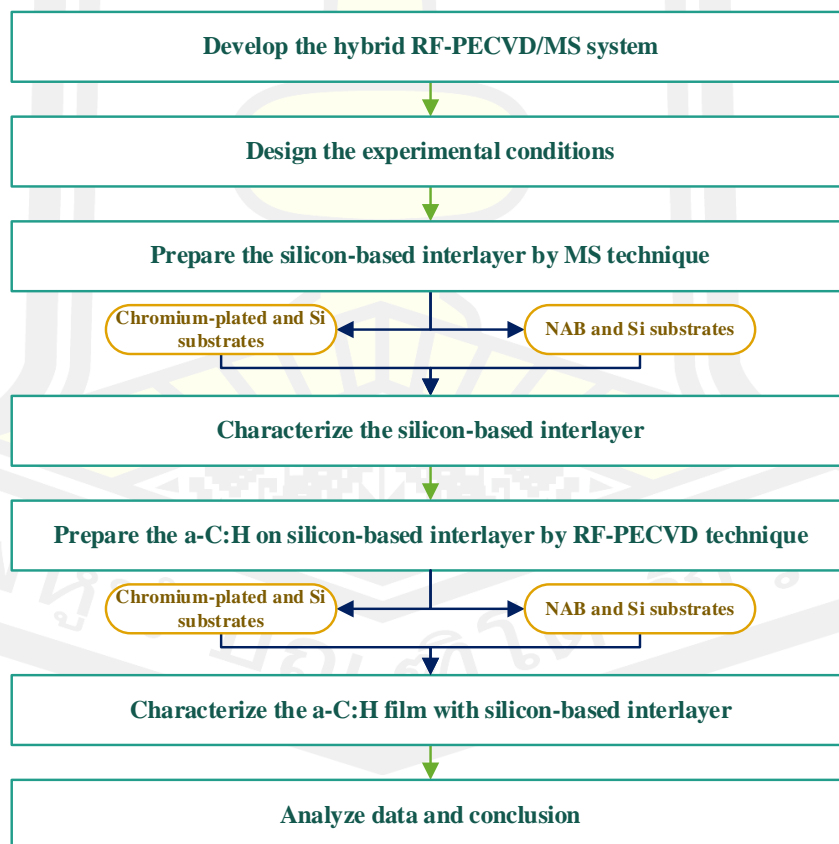


Figure 3.1 Flowchart of the experimental procedure.

3.1 Hybrid RF-PECVD/MS system

In this thesis, a novel hybrid deposition system is presented that uses a combination of radio frequency-plasma enhanced chemical vapor deposition (RF-PECVD) and magnetron sputtering (MS) techniques, which will be called the hybrid RF-PECVD/MS system. The a-C:H film with a silicon-based interlayer in which the silicon-based interlayer was deposited on the chromium-plating, NAB, and *p*-type silicon substrates using the MS technique, and then followed by the deposition of a-C:H film using the RF-PECVD method. The hybrid RF-PECVD/MS system used in this work is located at the technological plasma research unit, Mahasarakham University, Maha Sarakham, Thailand, as shown in Figure 3.2. The schematic diagram of all components, including the power supply, vacuum parts, gases flow controller, and system controller, is shown in Figure 3.3. The details of each part will be given on the topic of 3.1.1 to 3.1.4. Figure 3.4 shows a drawing of the hybrid RF-PECVD/MS system.

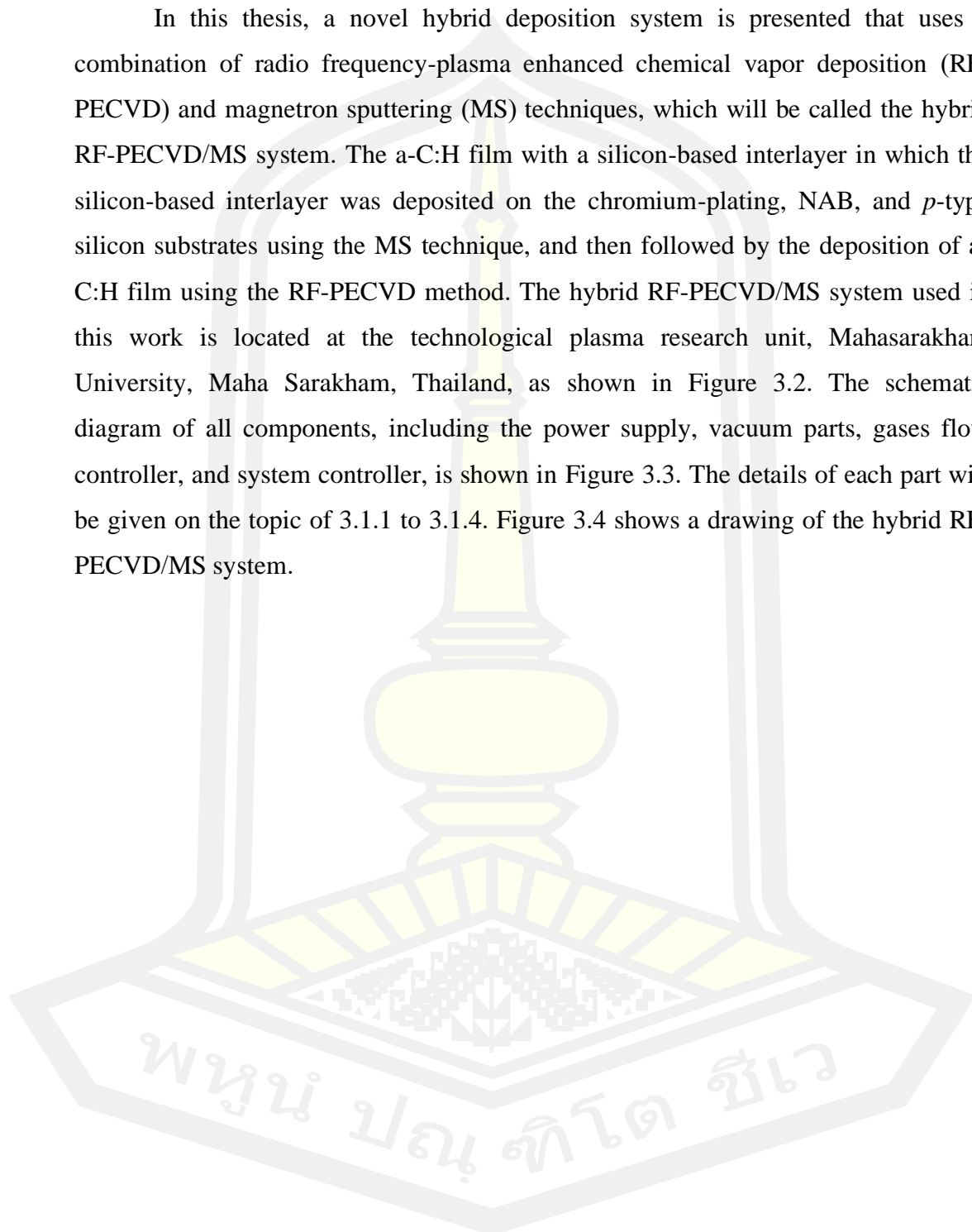




Figure 3.2 A photo of a hybrid RF-PECVD/MS system used for a-C:H with silicon-based interlayer deposition.

พหุบัณฑิต ชีวะ

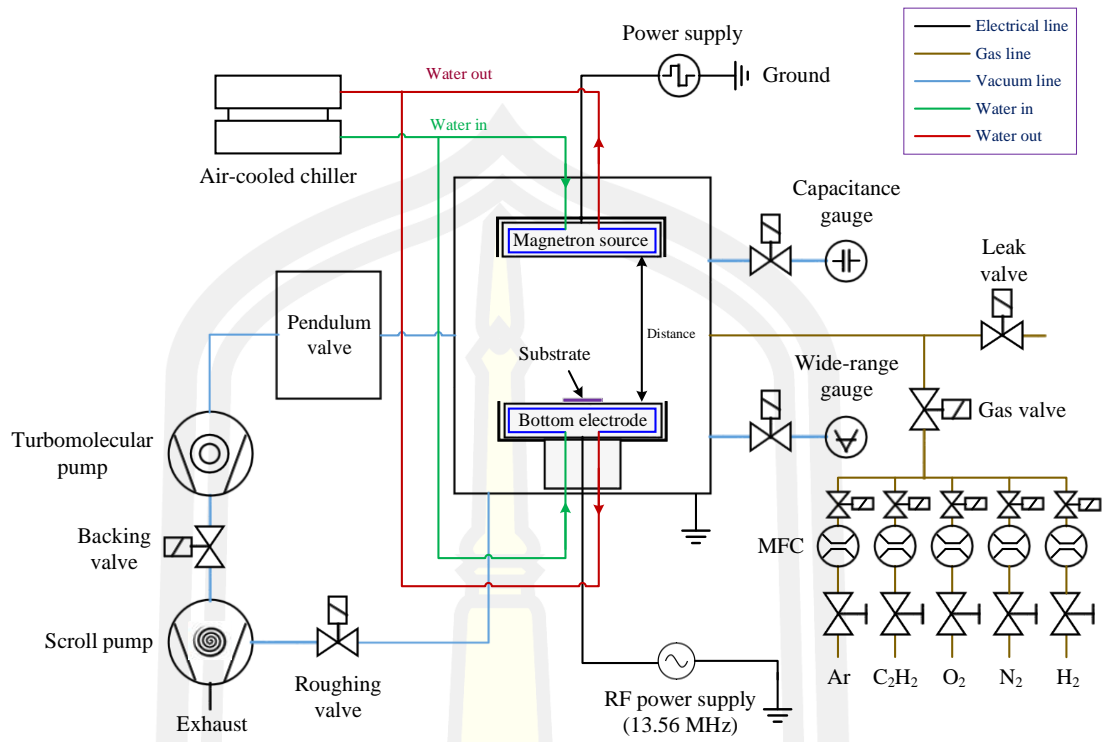


Figure 3.3 A schematic diagram of the hybrid RF-PECVD/MS system used for a-C:H with silicon-based interlayer deposition.

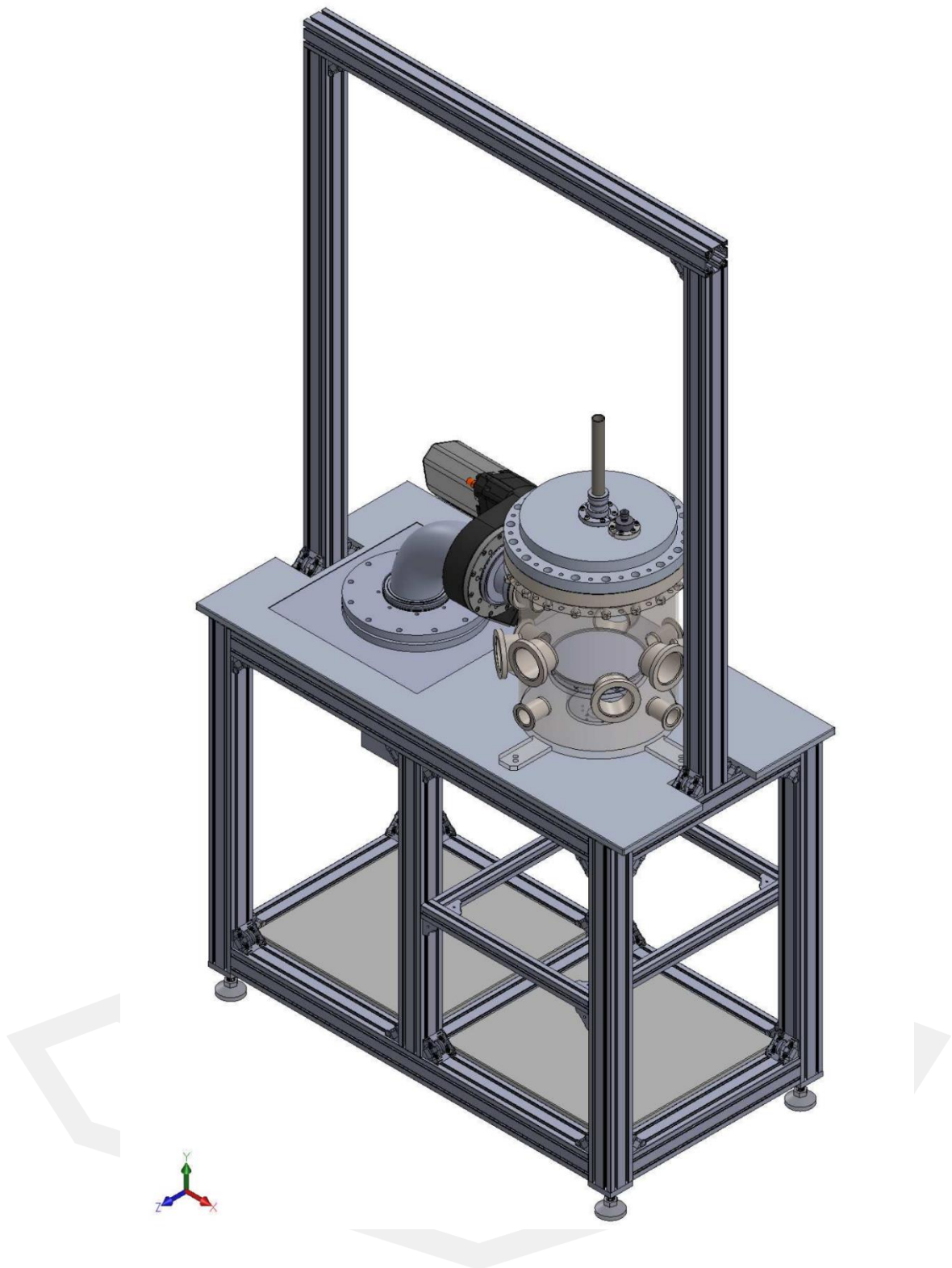
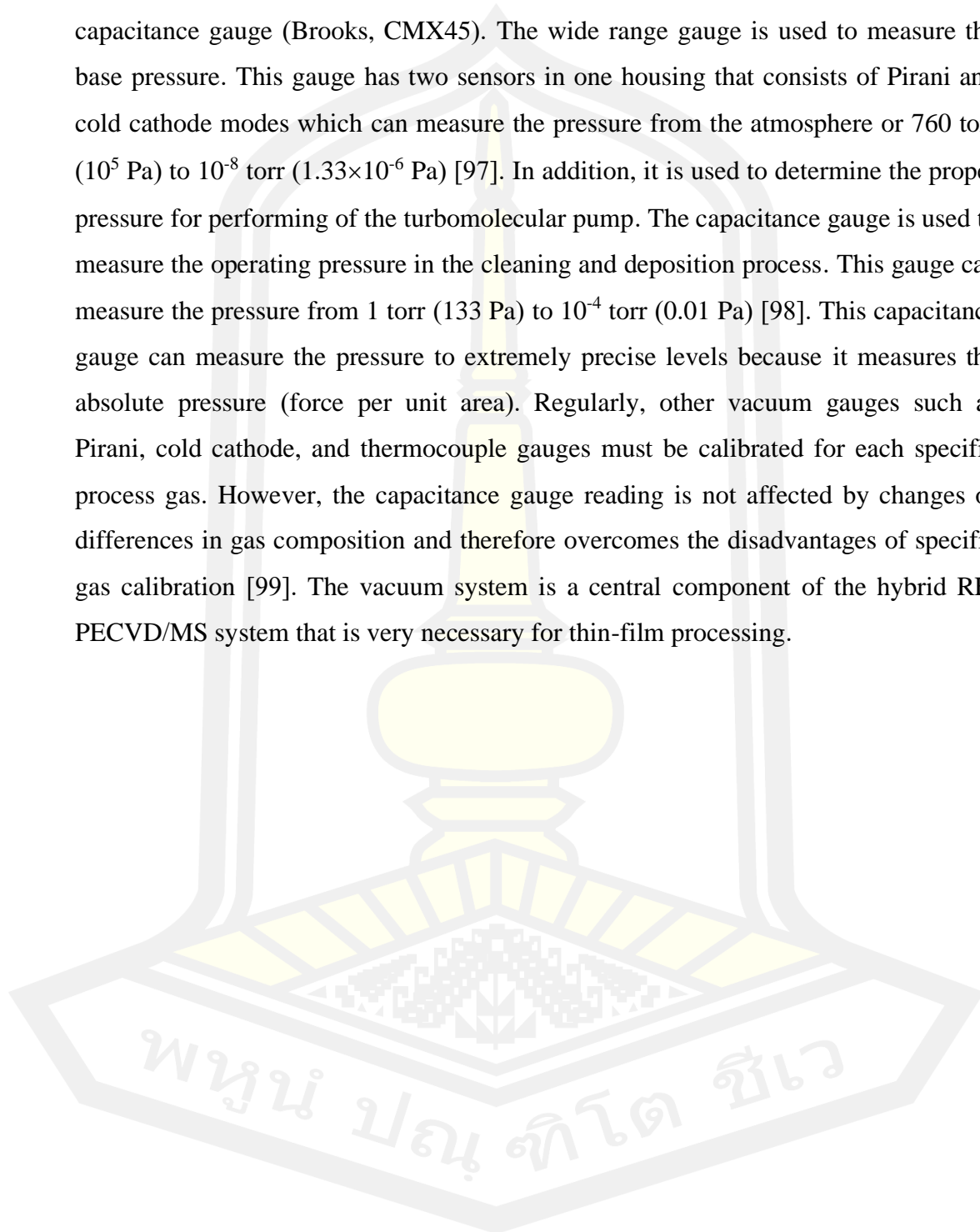


Figure 3.4 A drawing of the hybrid RF-PECVD/MS system used for a-C:H with silicon-based interlayer deposition.

3.1.1 Vacuum system

The vacuum system composes of the vacuum chamber, scroll pump, turbomolecular pump, control pendulum valve, wide range gauge, and capacitance gauge. The vacuum chamber was made of AISI 304 stainless steel cylinder with an inner diameter of about 295 mm and a height of 362 mm. The top of the vacuum chamber was installed with the magnetron source while the bottom of the vacuum chamber was installed with the bottom electrode, as shown in Figure 3.5. The details of the magnetron source and bottom electrode are given in the topics of 3.1.2 and 3.1.3. The distance between the magnetron source can be adjusted in the range of 80 mm to 200 mm. The pumping speed at the vacuum chamber can be controlled by the control pendulum valve (VAT, 65040-PHCP) for maintaining the operating pressure, which is installed between the chamber and the turbomolecular pump. In addition, the control pendulum valve was used together with a backing valve, and a roughing valve enable the venting process without breaking the vacuum pumps. The vacuum pump includes two pumps: (i) a scroll pump (Edwards, nXDS10i) and (ii) a turbomolecular pump (Pfeiffer, TC600). A scroll pump acts as a primary pump or backing pump for pressure above 5.25 mtorr (0.70 Pa) with the pumping speed of 3.17 l/s to achieve the pressure for turbomolecular pump operation. The scroll pump is the dry vacuum pump that uses two Archimedean spirals shape to pump or compress the gases, which one of the Archimedean spirals is fixed, while the other one orbits eccentrically without rotating. The gas enters the opening between two Archimedean spirals, and the volume between the spirals is expanded and eventually sealed off and transported the gases away [93], [94]. This scroll pump was connected to the turbomolecular pump and vacuum chamber to serve as the backing and roughing pump, respectively. A turbomolecular pump acts as a secondary pump or high vacuum pump for the base pressure of this hybrid system about 1×10^{-5} torr (1.33×10^{-3} Pa) with the pumping speed of 920 l/s. It was connected to the side of the vacuum chamber through the control pendulum valve. The turbomolecular pump works by transferring kinetic energy to gas molecules using high speed rotating, angled blades that propel the gas at high speeds [93], [95], [96]. The rotating speed of the Pfeiffer-TC600 model is 660 Hz that a typical ultimate pressure of 7.5×10^{-9} torr (1×10^{-6} Pa) can be achieved.

Two types of gauge pressure monitored the vacuum pressures in the vacuum chamber comprise of the wide range gauge (Pfeiffer, PKR361) and the capacitance gauge (Brooks, CMX45). The wide range gauge is used to measure the base pressure. This gauge has two sensors in one housing that consists of Pirani and cold cathode modes which can measure the pressure from the atmosphere or 760 torr (10^5 Pa) to 10^{-8} torr (1.33×10^{-6} Pa) [97]. In addition, it is used to determine the proper pressure for performing of the turbomolecular pump. The capacitance gauge is used to measure the operating pressure in the cleaning and deposition process. This gauge can measure the pressure from 1 torr (133 Pa) to 10^{-4} torr (0.01 Pa) [98]. This capacitance gauge can measure the pressure to extremely precise levels because it measures the absolute pressure (force per unit area). Regularly, other vacuum gauges such as Pirani, cold cathode, and thermocouple gauges must be calibrated for each specific process gas. However, the capacitance gauge reading is not affected by changes or differences in gas composition and therefore overcomes the disadvantages of specific gas calibration [99]. The vacuum system is a central component of the hybrid RF-PECVD/MS system that is very necessary for thin-film processing.



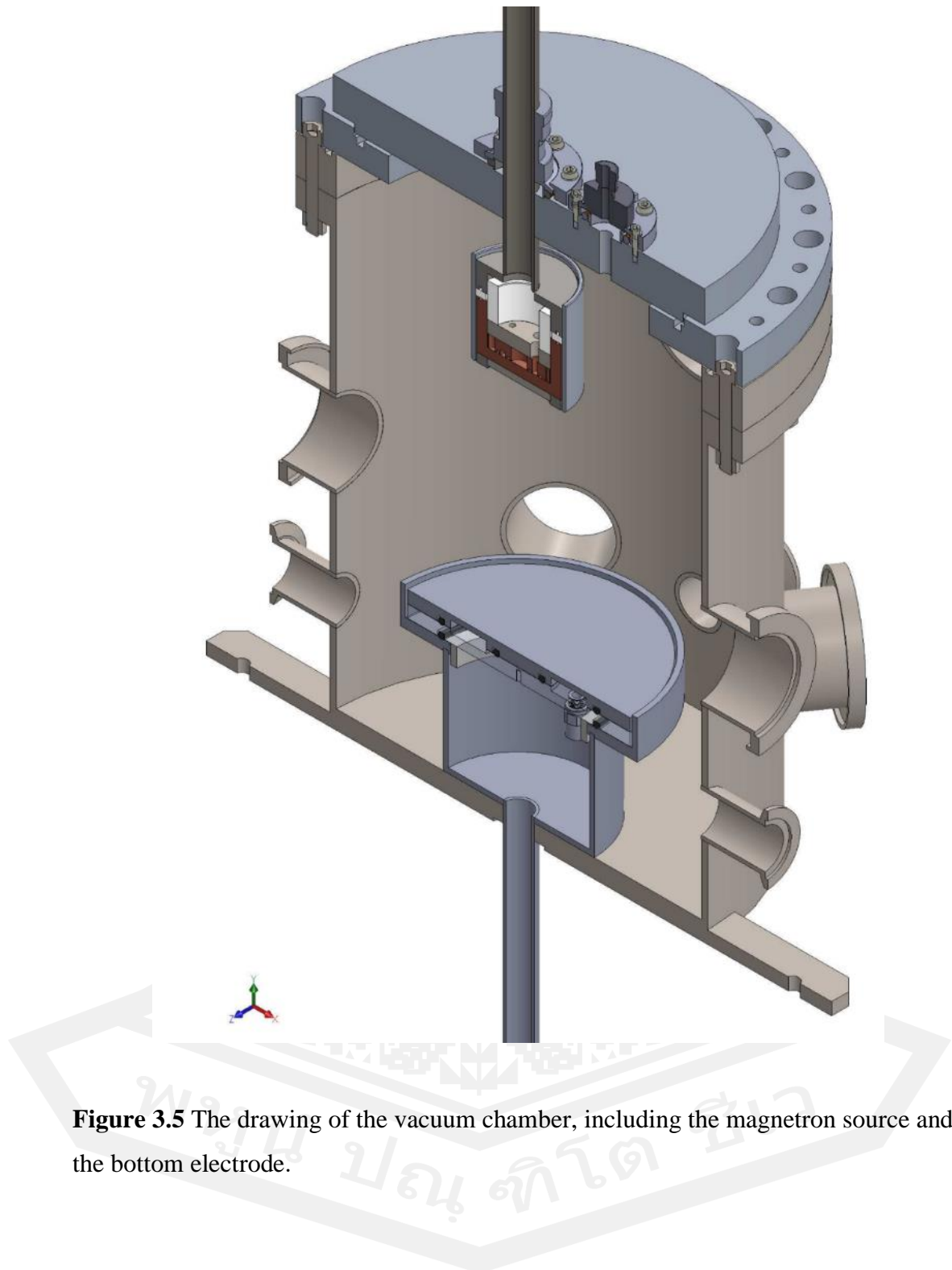


Figure 3.5 The drawing of the vacuum chamber, including the magnetron source and the bottom electrode.

3.1.2 Magnetron source

The drawing of the magnetron source's cross-section is shown in Figure 3.6, corresponding to the diameter and height of 71.30 mm and 60.50 mm, respectively. The magnetron source's outermost is the cylindrical aluminum tube, which is grounded to prevent the sputtering effect on the target's edge. A stainless-steel clamp is used to hold the target to be close to the cathode. The cathode or power electrode acting as the magnetic holder consists of the one-sided hollow cylinder copper block (68 mm in diameter and 30 mm in height) and the copper plate (50.25 mm in diameter and 10 mm in thickness). The cylindrical permanent magnets are arranged in sockets inside the magnetic holder, as seen in Figure 3.7. The outer sockets contain 24 magnets with a 5 mm diameter, while the inner socket consists of one magnet with a diameter of 12 mm. The permanent magnets are stacked inside these sockets in which the pole of outer magnets and inner magnet be opposite to generate an unbalanced magnetic field configuration. The cooling water system with a temperature range of 15–18 °C is connected inside the magnetic holder to cool the target and permanent magnets during the deposition process.

The next component is the stainless-steel plate (~ 50.85 mm in diameter and 10 mm in thickness) with external thread used to attach the magnetic holder. This component is locked with the inner thread of the copper block. The Teflon hollow cylinder (inner diameter of 33 mm, an outer diameter of 50.85 mm, and height of 28 mm) and Teflon ring (inner diameter of 53 mm, an outer diameter of 70 mm, and thickness of 5 mm) have employed the insulator to separate the cathode from the body of the anode. The anode body is made from the stainless steel and used to attach the anode through a Teflon hollow cylinder. For this configuration of the magnetron source, the cathode is driven to a negative voltage power supply while the anode and the vessel wall are grounded. The DC, pulsed DC (Advanced energy, DC pinnacle plus), and the HiPIMS supplies can be employed to deliver the electrical power to the magnetron source.

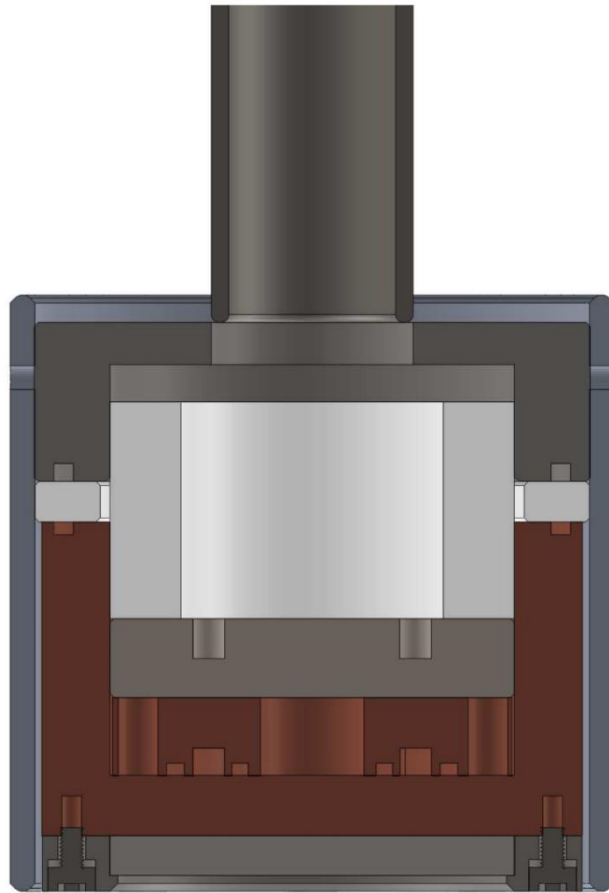


Figure 3.6 The cross-section diagram of the magnetron source.

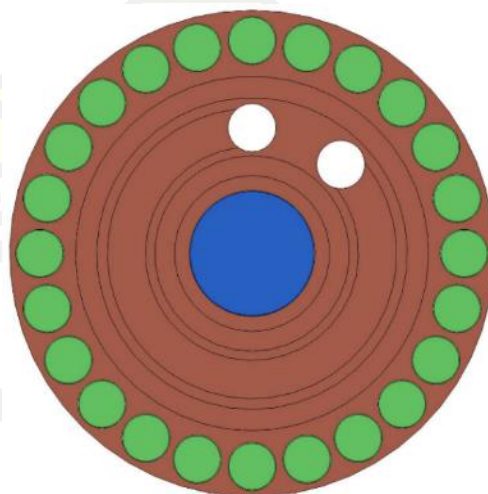


Figure 3.7 The schematic diagram of the magnetic holder; the outer magnets (south pole) are shown in green colour, while an inner magnet (north pole) is shown in blue.

3.1.3 Bottom electrode

The bottom electrode is used as the power electrode for generating the hydrocarbon plasma and is used as the substrate holder. The overall size of the bottom electrode is 191 mm in diameter and 115 mm in height. It is divided into 4 components, as shown in the schematic diagram in Figure 3.8. The first part is the main power electrode with a 180 mm diameter and 10 mm thickness. The frontside of this part is a flat planar to support the substrates, while the backside is gouged out as a groove for the cooling water. The second part is the sub-electrode with the same size as the main power electrode, sandwiched into the main power electrode to seal the water with the O-ring. Two of the tube fitting in the backside of this part are connected to the water inlet and outlet ports. The third part is a Teflon ring used as an insulator to keep the less gap distance between the power electrode and the ground shield. The O-ring with an inner diameter of 120 mm and a thickness of 5 mm is used as the insulator to separate the power electrode from the ground shield. The last part is the ground shield, which consists of a hollow cylinder and a 1-inch pipe. This pipe was fixed at the bottom of the vacuum chamber. The ground shield and the power electrode are locked together by the polyether ether ketone (PEEK) hexagon head screws acting as the insulator separator. The bottom electrode is connected to the matching box or matching network (AT-10, Seren IPS Inc.) and the automatic matching network controller (MC2, Seren IPS Inc.). The matching network is used to reduce the reflected power for achieving the maximum power dissipation in the discharge between the power and bottom electrodes. The RF generator or RF power supply (R1001, Seren IPS Inc.) of the fixed frequency at 13.56 MHz can provide power up to 1000 W. This RF power supply can be used in continuous mode and pulse mode. For RF on in pulse mode, the duty cycle and pulse frequency can be adjusted from 1–100% and 1–10 kHz, respectively.

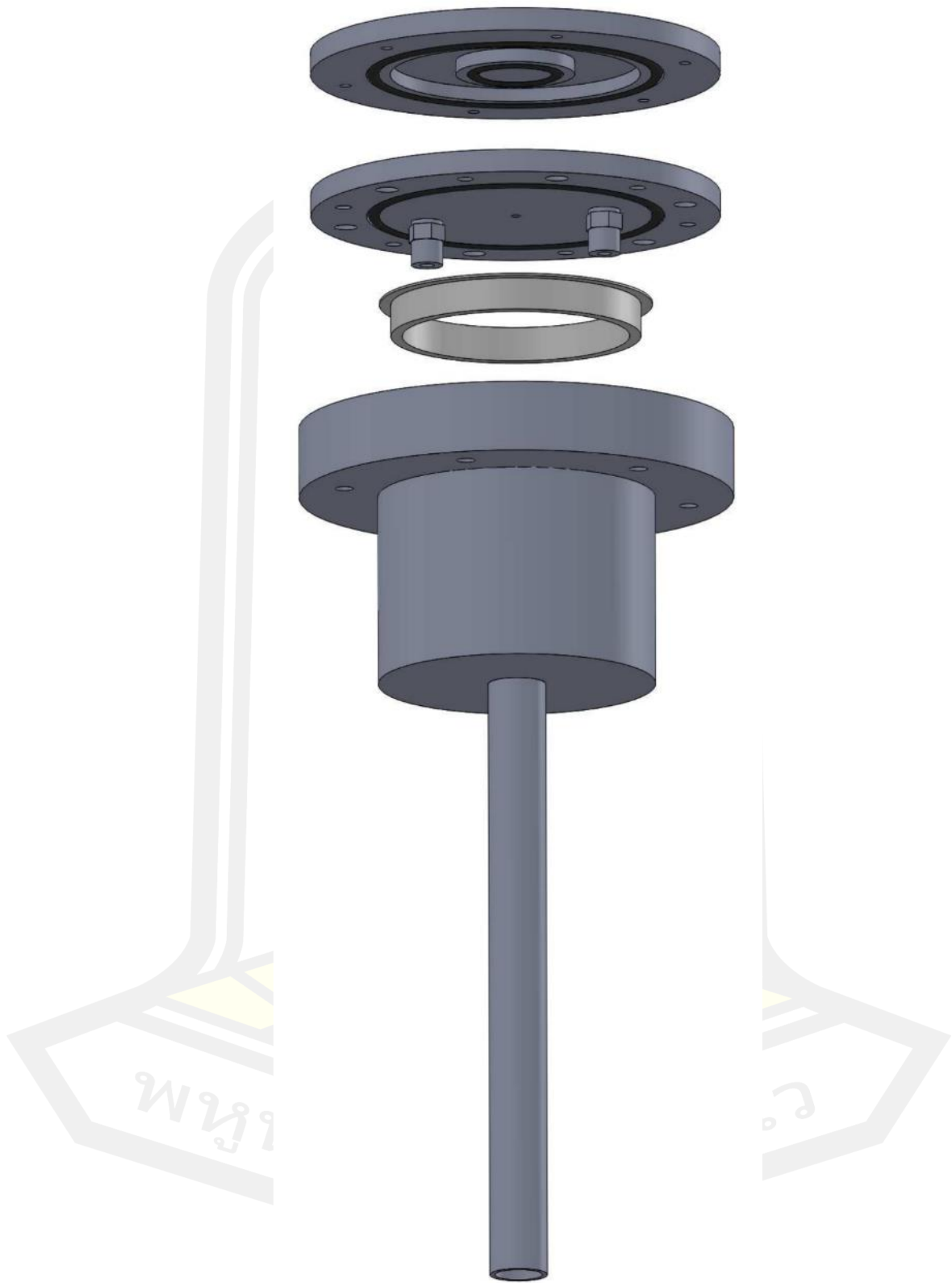


Figure 3.8 The drawing of all components of the bottom electrode.

3.1.4 Vacuum control system

A control panel, as seen in Figure 3.9 is used to regulate the hybrid RF-PECVD/MS system. This control system was developed using many advanced functions in LabVIEW program. It is used together with the National Instrument (PXIe-1062Q), as seen in Figure 3.10. The National Instrument system controller unit was installed with the main module NI PXIe-8102, the module NI PXIe-6124 (S-Series), the module NI PXI-2564, and the module NI PXI-6733.

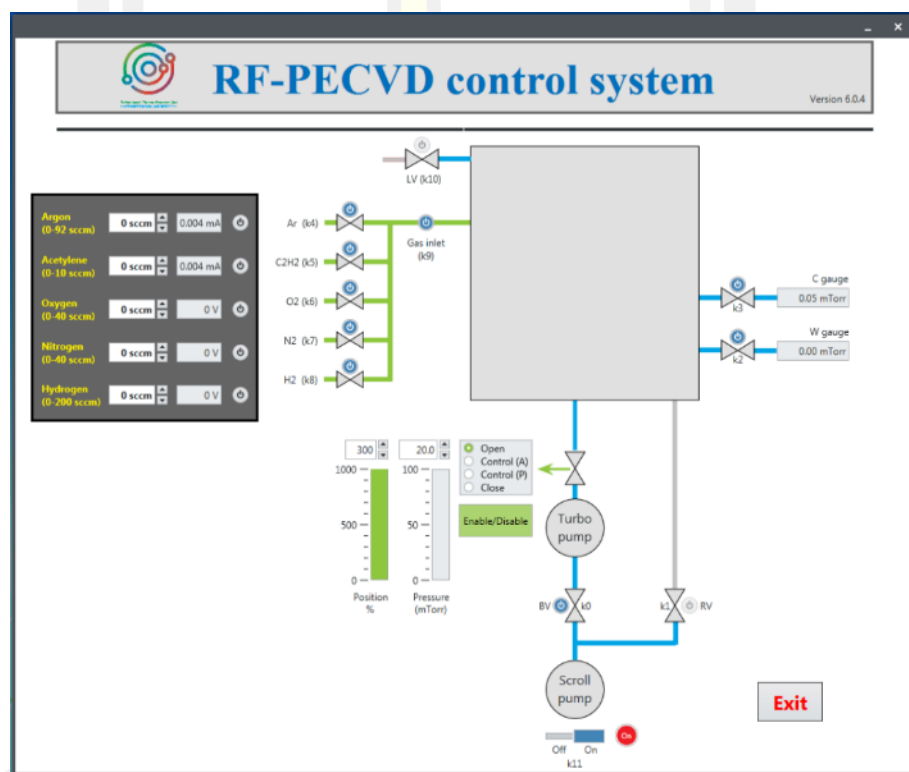


Figure 3.9 The schematic diagram shows the control panel of the hybrid RF-PECVD/MS system.



Figure 3.10 A photo of the National Instruments (PXIe-1062Q).

The NI PXIe-8102 module (see Figure 3.11) consists of a DVI-I port connected to the monitor, and the DVI-to-HDMI adapter was used to connect the monitor's HDMI port. The USB port was used to support USB devices such as a mouse and keyboard to control the NI-PXIe unit and an external flash drive for saving the data. The Ethernet port was connected to the Lane line for online data access and online system control.



Figure 3.11 The panel of NI PXIe-8102 module [100].

The flow rate of Ar and C₂H₂ gases can be controlled using the instrument BROOKS 0254, as shown in Figure 3.12. The flow rates of Ar and C₂H₂ gases were calibrated for the mass flow controllers of Ar (Brooks, GF040) and C₂H₂ (Brooks, GF040) corresponding to the flow rate range of 0–92 and 0–10 sccm, respectively, with Ar gas was connected to channel 1 and C₂H₂ gas was connected to channel 2 of the instrument BROOKS 0254. The BROOKS 0254 instrument was used as a power supply with 24 VDC for mass flow controllers and was used for setpoint control and flow rate display. For Ar and C₂H₂ gases, the current signal is used to control the setpoint controller for the model of Ar and C₂H₂. The current signal in the range of 4–20 mA from the BROOKS 0254 instrument was converted to the flow rate in the range of 0–92 sccm for Ar and 0–10 sccm for C₂H₂. The flow rate of O₂, N₂, and H₂ gases can be controlled by the analogue output card (NI PXI-6733). The flow rates of these gases were calibrated for the mass flow controllers of Ar (Brooks, GF040), C₂H₂ (Brooks, GF040), O₂ (Brooks, GF040), N₂ (Brooks, GF040), and H₂ (Brooks, GF040) according to the flow range of 0–40 sccm, 0–40 sccm, and 0–200 sccm, respectively. For O₂, N₂, and H₂ gases, the voltage signal from the analogue output card was used to control the setpoint controller. The voltage signal in the range of 0–5 VDC from the analogue output card was converted to the flow rate in the range of 0–40 sccm for O₂, 0–40 sccm for N₂ and 0–200 for H₂. Also, the external power supply of 24 VDC was used to drive the mass flow controllers of O₂, N₂ and H₂ gases.



Figure 3.12 Brooks 0254 instrument for mass flow controller.

The pneumatic valves including the backing valve (k0), the roughing valve (k1), the wide range gauge (k2), the capacitance gauge (k3), the individual gas inputs for Ar (k4), C₂H₂ (k5), O₂ (k6), N₂ (k7) and H₂ (k8), the main gas inlet (k9) and the leakage valve (k10) are controlled by the relay module card (NI PXI-2564) with 16 channels (CH0–CH15). The relay module card with channels 0–9 was used for switches k0–k9, respectively. The external power supply of 24 VDC was connected to the load (solenoid valve) as shown the diagram in Figure 3.13 to control the relay (closing the relay and opening the relay). When the relay is closed, the relay switch (COM0-COM10) is connected to the load (CH0–CH10) (close the relay) and then the valve is opened. For example, to close the relay of channel 1 (roughing valve), the relay switch of channel 1 is controlled by the LabVIEW diagram, whereupon this entry closes the relay between CH1 and COM1 and the pneumatic valve is opened. In case of opening the relay, the relay switch (COM0-COM10) is disconnected (open relay) and the valve was closed.

In addition, this vacuum control system can be used to open and close (on/off) the scroll pump switch and control the position of the pendulum valve to adjust the operating pressure.

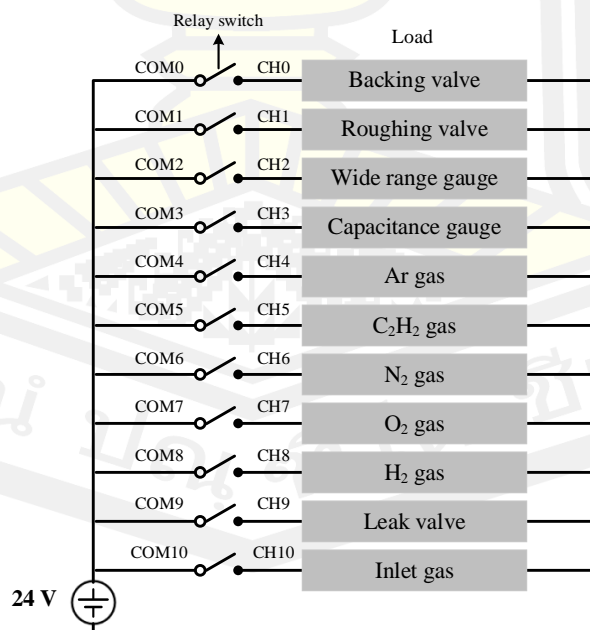


Figure 3.13 A hardware diagram of the NI PXI-2564 for pneumatic valves.

3.2 Thin-film deposition process

In this thesis, the experimental details have been divided into two parts, for the chromium-plated substrate and the NAB substrate. For this topic, the substrate preparation and chemical solution cleaning process of silicon wafers, chromium-plated and NAB substrates are described in detail. Then the thin-film deposition processes, including plasma cleaning and thin-film deposition of chromium-plated and NAB parts, are explained in detail.

3.2.1 Substrate preparation

In this study, the mirror-polished p-type silicon wafer, chromium-plated, and NAB pellets were used as the substrates for the a-C:H film with silicon-based interlayer coating. The ultrasonic cleaner with a frequency of 40 kHz (UC-5180L), as shown in Figure 3.14, was used to remove the contamination of oils and organic residuals that appear on the substrates. The details of each step used for the cleaning and preparation of substrates before coating are given below.



Figure 3.14 A photo of the ultrasonic cleaner for substrate cleaning.

Preparation of silicon wafer

The silicon wafers of 76 mm in diameter and 0.05 mm thickness were cut into two rectangular sizes of $10 \times 10 \text{ mm}^2$ and $20 \times 20 \text{ mm}^2$, as shown in Figure 3.15, by using the diamond-head ballpoint cutter. These sizes are suitable for all analytical techniques. The cleaning process of silicon wafers are given as follows;

1. The silicon wafer was placed into the glass container, then pour acetone and put the glass container in the ultrasonic bath. The silicon wafer was first cleaned with ultrasonic agitation. This setup time for this step is about 10 minutes.
2. Remove the acetone into the waste bottle and then pour the methanol into the ultrasonic bath.
3. The silicon wafer was second cleaned with ultrasonic agitation by the methanol for 10 minutes to remove the acetone and then repeat this step one time.
4. Remove the methanol into the waste bottle and then pour the deionized water into the ultrasonic bath.
5. The silicon wafer was third cleaned with ultrasonic agitation by the deionized water for 10 minutes to remove the acetone and then repeat this step two times.
6. In the last step, the silicon wafer was dried with dry air follow blow with warm air to get rid of moisture.

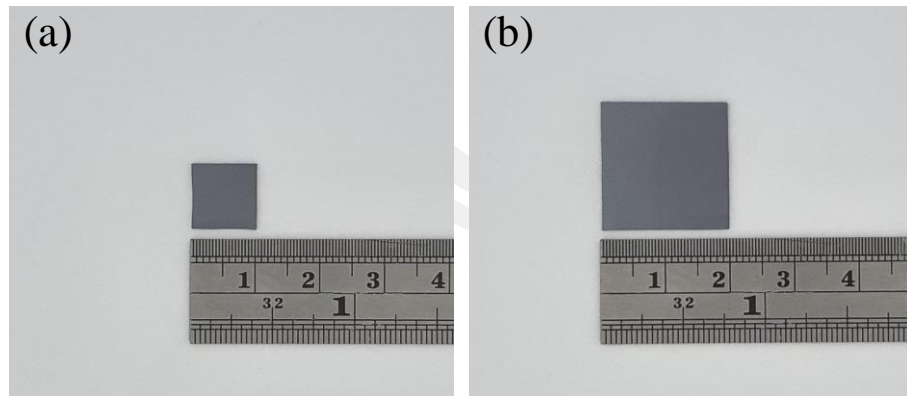


Figure 3.15 A photo of the silicon wafer substrates with the size of (a) $10 \times 10 \text{ mm}^2$, and (b) $20 \times 20 \text{ mm}^2$.

Preparation of the chrome plating and NAB

The chromium-plated substrate, as shown in Figure 3.16, was electroplated onto the brass substrate. The electroplating process was performed on a brass sample with a diameter of 20 mm and a height of 4 mm. A thick nickel layer was electroplated for corrosion resistance, followed by a thin chromium layer for decorative purposes. The nickel-plated brass was prepared from a solution bath of nickel chloride, nickel sulphate, and boric acid with a DC voltage of -5 V and an immersion time of 8 minutes. The coating thickness of the nickel was adjusted to about $5 \mu\text{m}$. Then the chromium coating was prepared from a chromate solution (chromium sulphate) with a DC voltage of -7 V and an immersion time of 2.5 minutes. The coating thickness of the chromium was adjusted to about $0.5 \mu\text{m}$. It is used to increase the reflectivity of nickel coating on a substrate. Therefore, in this work, chromium-plated substrate means nickel-chromium plating, in which nickel and chromium were electrodeposited to form a two-layer surface on a brass substrate. The chemical cleaning of the chrome-plated substrate follows the same procedure as the cleaning of silicon wafers (see above).

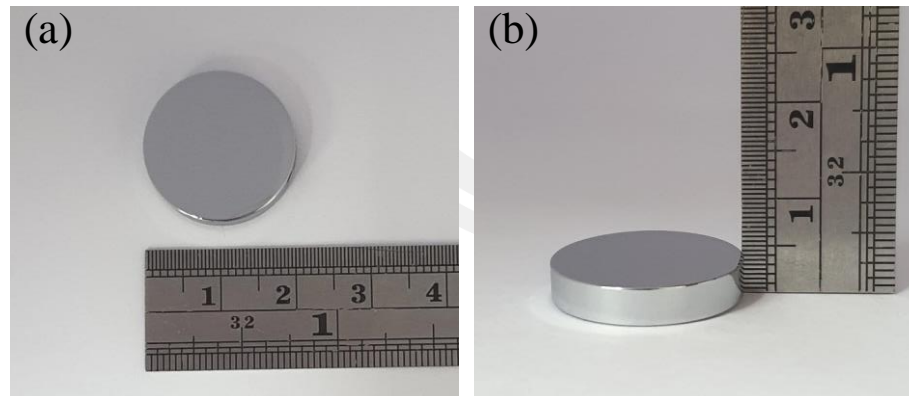


Figure 3.16 A photo of the chromium-plated substrate (a) front view and (b) side view.

The unpolished and polished NAB substrates, as shown in Figure 3.17, were machined from the NAB rod and prepared by grinding and polishing. The cylindrical NAB bulk was lathed into the same size as the chrome plating. The NAB was a single side mirror-polished to reduce the surface roughness using the standard metallographic method. The silicon carbide (SiC) sandpapers (Grit size of 100, 200, 600, 800, 1000, 1500, 2000, 2500, 3000, 4000, and 5000) as shown in Figure 3.18 were used for grinding process and then the alumina powder suspension in DI water as shown in Figure 3.19 (Grain size of $0.5\ \mu\text{m}$ and $0.05\ \mu\text{m}$) were used for polishing process. This step is necessary to accomplish a suitable surface roughness about 100 nm observed by the surface profilometer. After polishing, the NAB substrate was thoroughly rinsed with DI water to remove the alumina suspension and then immersed in a methanol solution. The cleaning process of the NAB substrate is described below, where only methanol solution was used to clean the NAB substrate.

1. The methanol solution was poured into the glass container and then the NAB substrate was placed in the glass container.
2. The NAB substrate was cleaned with ultrasonic agitation. The setup time for this step is about 10 minutes.
3. Finally, the substrates were suddenly dried with microfiber wiper and then blown out with warm air to remove the moisture.

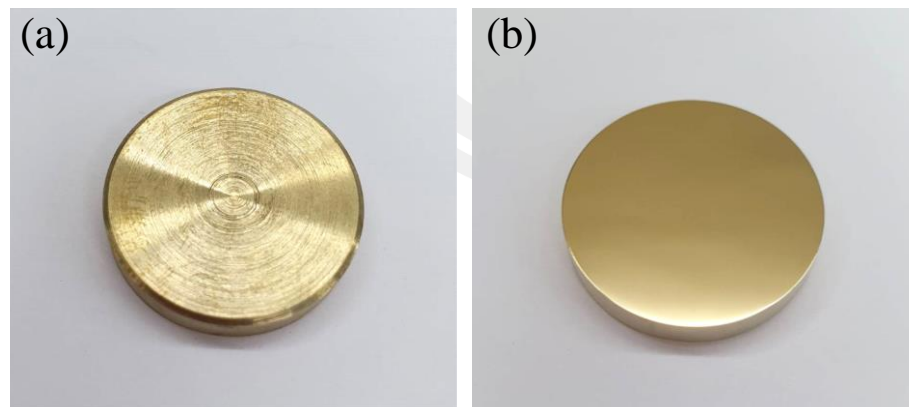


Figure 3.17 A photo of (a) unpolished and (b) polished NAB substrate.



Figure 3.18 The SiC sandpapers with grit sizes of 100, 200, 600, 800, 1000, 1500, 2000, 2500, 3000, 4000, and 5000.

พหุบัณฑิต ชีวะ



Figure 3.19 The alumina powder with particle size of 0.5 μm and 0.05 μm used for suspension in DI water.

3.2.2 Argon-hydrogen plasma cleaning process

Before the deposition procedure, the chamber and the substrate holder were thoroughly cleaned with a cleanroom wiper wetted with methanol to remove any loosely attached flakes of previously deposited materials repeatedly. Then the chamber was cleaned by a dry cleanroom wiper. Afterward, the substrates which were pre-cleaning by the ultrasonic process will be loaded into the deposition chamber. These substrates were placed on the stainless-steel plate that serves as the substrate holder as shown in Figure 3.20 (a) for the chromium-plated substrate and (b) for the NAB substrate. Then the substrate holder with the substrates was placed on the bottom electrode. The substrate holder was cooled using the cold water circulated in the center of the bottom electrode. In the next step, the deposition chamber was pumped down to a base pressure of about 10^{-3} Pa for about 60 minutes using the turbomolecular and scroll pumps. The plasma cleaning process is necessary to remove the scrupulous contamination and oxide layer on the top of the substrate surface. The substrates were physical and chemical cleaning by the bombardment of the mixture

argon and hydrogen plasma. The RF power of 300 W was used to generate the Ar-H₂ plasma. During the plasma cleaning, the argon, and hydrogen flow rates of 10 sccm with operating pressure of 0.1 Pa, and the processing time of 10 min were controlled to achieve the ultra-high cleaning substrate. The other parameters are shown in Table 3.1. and the photo for argon-hydrogen plasma during the cleaning process for chromium-plated and NAB substrates is shown in Figure 3.21.

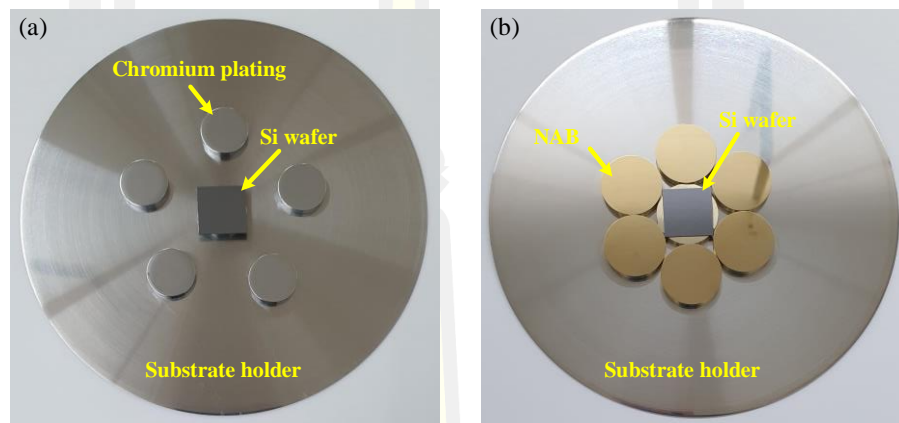


Figure 3.20 A photo of the (a) chromium-plated substrates and Si wafer (b) NAB substrates and Si wafer were placed onto the stainless-steel plate.

Table 3.1 The parameters used for argon-hydrogen plasma cleaning process.

	Cleaning parameters
RF power (W)	300
DC self-bias voltage (V)	~600–800
Argon flow rate (sccm)	10
Hydrogen flow rate (sccm)	10
Operating pressure (Pa)	~6.67
Valve position (%)	100
Cleaning time (minutes)	10

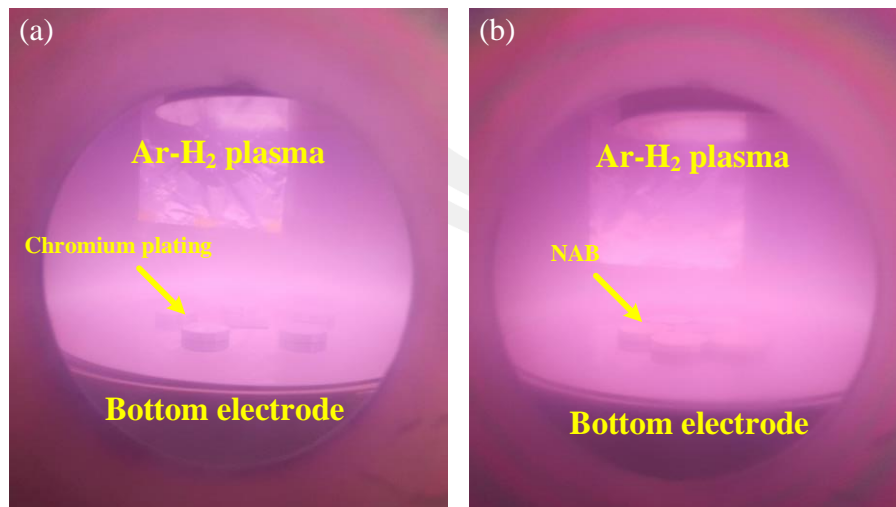


Figure 3.21 A photo of Ar-H₂ plasma during the cleaning process of (a) chromium-plated substrates and Si wafer (b) NAB substrates and Si wafer.

3.2.3 Deposition process

The deposition process is divided into two parts for chromium-plated and NAB substrate. The deposition processes including the interlayer coating and a-C:H coating operated via the hybrid RF-PECVD/MS system are given in detail below. For chromium-plated part, the a-C:H layer was regulated for the same condition while the different silicon-based interlayer coating was studied. For NAB part, the amorphous silicon interlayer was regulated for the same condition while the deposition period (stack) of the multilayer was studied. Multilayer DLC films were deposited using the DLC film (DLC) as the hard layer, and silicon doped DLC film (Si-doped DLC) as the soft layer.

Deposition process for chromium-plated part

The hybrid RF-PECVD/MS system was used to prepare a two-step process of a-C:H films with a silicon-based interlayer. In the first process, the silicon-based interlayer was deposited using the magnetron sputtering technique. The magnetron source is used to deposit the silicon-based interlayer via the pure silicon target of 2 inches (Kurt J Lesker Company) as shown in Figure 3.22. In the second process, the a-C:H layer following was deposited using the RF-PECVD technique. For different silicon-based interlayer, the a-Si, a-Si:N, a-Si:H, and a-Si_xC_y:H were deposited using different process parameters, the magnetron source with the pure silicon target was installed on the top of the vacuum chamber. The Pinnacle Plus power supply was employed to deliver the DC power to the magnetron source with the power of 100 W. During the silicon-based interlayer deposition, inert argon gas was fed into the vacuum chamber as the sputtering gas with a flow rate of 20 sccm and the bottom electrode was connected to the ground. The operating pressure of about 6.67 Pa for four interlayers was kept constant to control the deposition condition. For a-Si interlayer, argon gas was only used to film deposition. While the a-Si:N, a-Si:H, and a-Si_xC_y:H interlayers were deposited using reactive gases of nitrogen, hydrogen, and acetylene, respectively. The process parameters of different silicon-based interlayers for deposition were concluded in Table 3.2. The photo of plasma during the deposition process of a-Si, a-Si:N, a-Si:H, and a-Si_xC_y:H interlayers was shown in Figure 3.23.

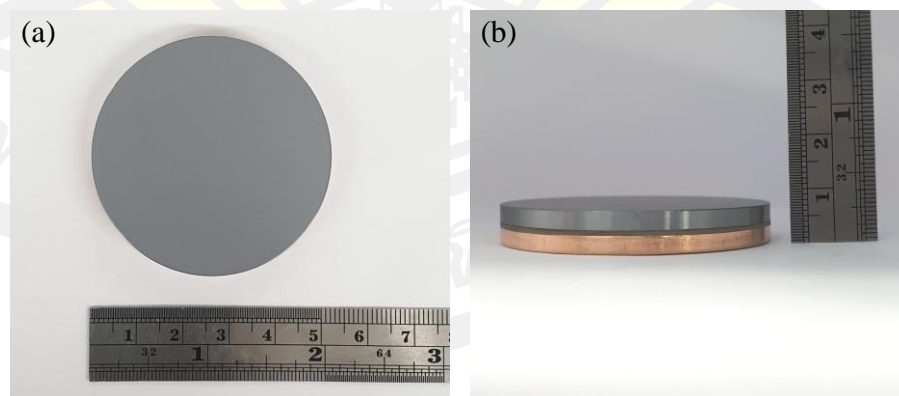
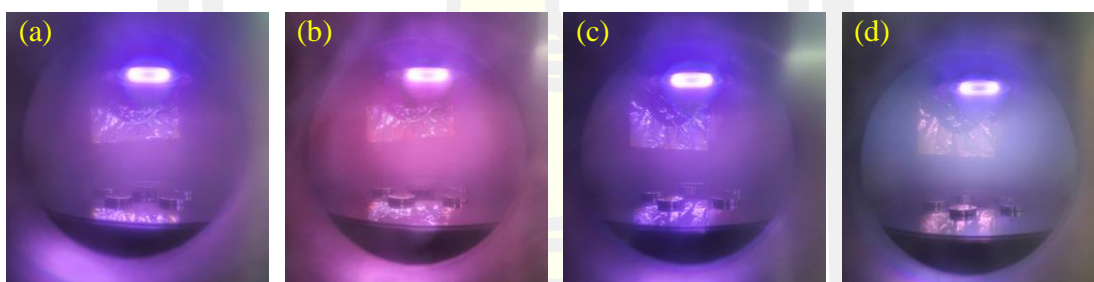


Figure 3.22 A Photo of silicon target (a) front view, and (b) side view.

Table 3.2 The parameters used for different silicon-based interlayer coating process.

Parameters	Interlayers			
	a-Si	a-Si:N	a-Si:H	a-Si _x C _y :H
DC power (W)	100			
Argon flow rate (sccm)	20			
Hydrogen flow rate (sccm)	-	2	-	-
Nitrogen flow rate (sccm)	-	-	2	-
Acetylene flow rate (sccm)	-	-	-	1
Operating pressure (Pa)	~6.67			
Valve position (%)	118	121	120	119

**Figure 3.23** A photo of plasma during the deposition process of (a) a-Si, (b) a-Si:N, (c) a-Si:H, and (d) a-Si_xC_y:H interlayers

In the deposition of a-C:H film, the best condition of a-C:H was chosen to deposit. The acetylene gas was used as a hydrocarbon precursor, and the hydrogen and argon gases were utilized for the stability of the operating pressure and sustain of the plasma. The operating pressure for the a-C:H coating was kept at 0.93 Pa, and the flow rate of acetylene, argon and hydrogen remained the same at 10 sccm. The RF power of 300 W was used to generate the C₂H₂-Ar-H₂ plasma. Figure 3.24 shows the photo of C₂H₂-Ar-H₂ plasma during the deposition process. The process parameters of a-C:H coating were concluded in Table 3.3. Figure 3.25 concludes the experimental

procedure for chromium-plated substrate with the schematic diagram and a corresponding photo of the process for loading samples, plasma cleaning, interlayer coating and a-C:H coating.

Table 3.3 The parameters used for a-C:H coating process.

Parameters	a-C:H film
RF power (W)	300
DC self-bias voltage (V)	~800–1000
Argon flow rate (sccm)	10
Hydrogen flow rate (sccm)	10
Acetylene flow rate (sccm)	10
Operating pressure (Pa)	~0.93
Valve position (%)	1000

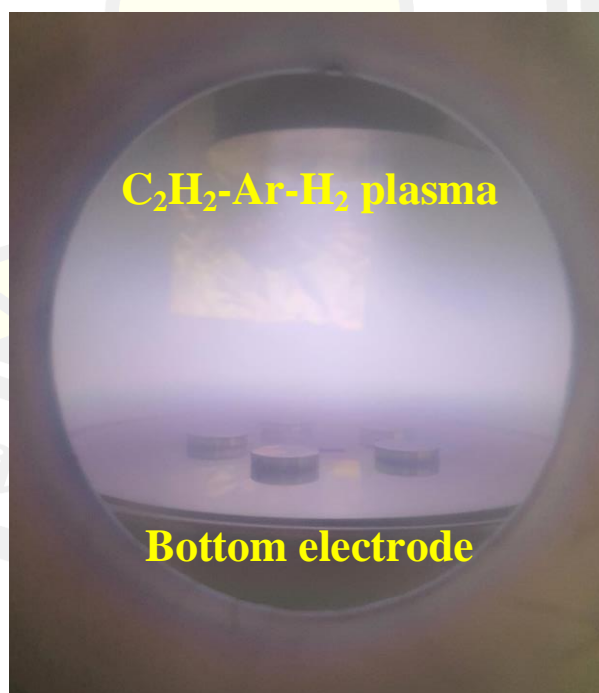


Figure 3.24 A photo of C_2H_2 -Ar- H_2 plasma during the deposition process.

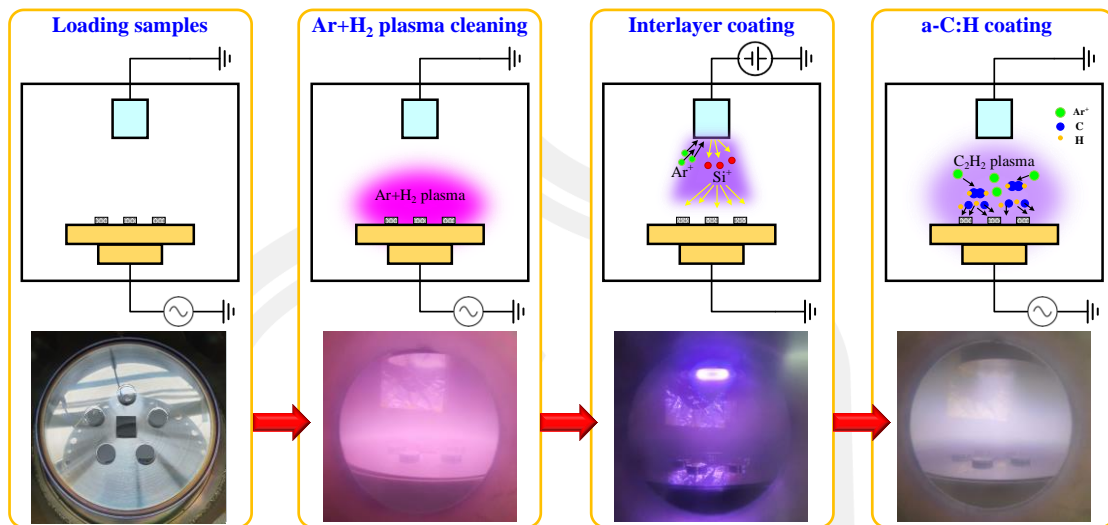


Figure 3.25 A schematic diagram and photo of loading samples, plasma cleaning, interlayer coating and a-C:H coating process.

Deposition process for NAB part

In this part, the multilayer DLC films were deposited on an alloyed NAB substrate. The amorphous silicon film (a-Si) was used as an interlayer. The DLC film and the silicon doped DLC film (Si-doped DLC) were used as hard and soft layers, respectively. The deposition period of 1 stack, 3 stacks and 5 stacks were investigated. For the example of 1-stack deposition, the a-Si interlayer was deposited by magnetron sputtering technique after the plasma cleaning process. Then the layer of Si-doped DLC was deposited using a combination of magnetron sputtering and RF-PECVD. During RF-PECVD discharge, the magnetron sputtering source generates the silicon atoms that can be doped into the DLC structure. Finally, the DLC layer was deposited on the a-Si layer using the RF-PECVD. In the deposition of 3 and 5 stacks, the Si-doped DLC and DLC layers following were deposited until the completion of the number of layers. For the deposition of a-Si interlayers, an argon gas flow of 20 sccm with an operating pressure of 6.67 Pa was used to generate a plasma with a DC power of 100 W. During the deposition of the interlayers, the bottom electrode was connected to the ground with the substrates. While argon, hydrogen and acetylene were used for DLC deposition at a flow rate of 10 sccm with

a controlled operating pressure of 0.93 Pa. The C₂H₂-Ar-H₂ plasma was generated at a power of RF of 300 W. For Si-doped DLC deposition, magnetron sputtering source was operated in parallel with the RF plasma. Therefore, the same parameters were used for the Si-doped DLC deposition as for the DLC deposition. The DC power of 100 W was used for magnetron sputtering discharge. The process parameters of the interlayer, DLC and Si-doped DLC coating are summarized in Table 3.4. Figure 3.26 shows the photo of the plasma during the deposition of the a-Si interlayer, the DLC and the Si-doped DLC. Figure 3.27 concludes the experimental procedure for NAB substrate with the schematic diagram and a corresponding photo of the process for loading samples, plasma cleaning, interlayer coating, Si-doped DLC coating and DLC coating.

Table 3.4 The parameters used for the deposition of the a-Si interlayer, the DLC and the Si-doped DLC.

Parameters	Interlayer	DLC	Si-doped DLC
RF power (W)	-	300	300
DC power (W)	100	-	100
Argon flow rate (sccm)	20	10	10
Hydrogen flow rate (sccm)	-	10	10
Acetylene flow rate (sccm)	-	-	10
Operating pressure (Pa)	~6.67	~0.93	~0.93
Valve position (%)	118	1000	1000

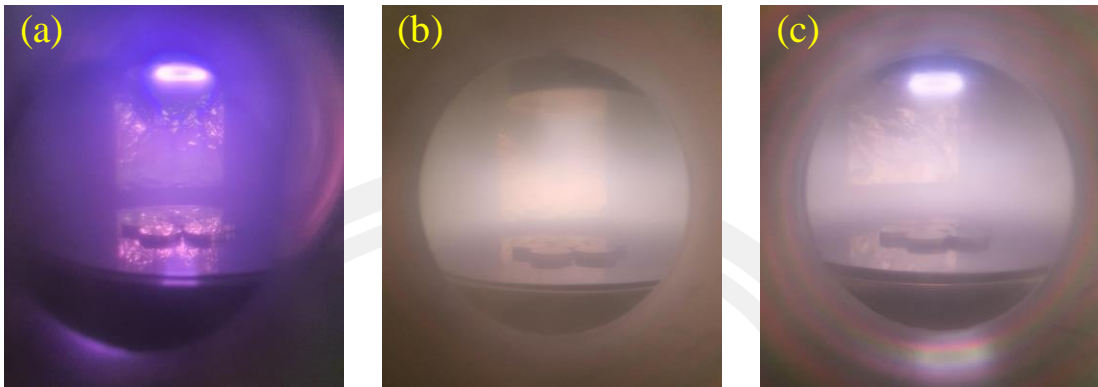


Figure 3.26 A photo of the plasma during the deposition process of (a) a-Si interlayer, (b) DLC film, and (c) Si-doped DLC film.

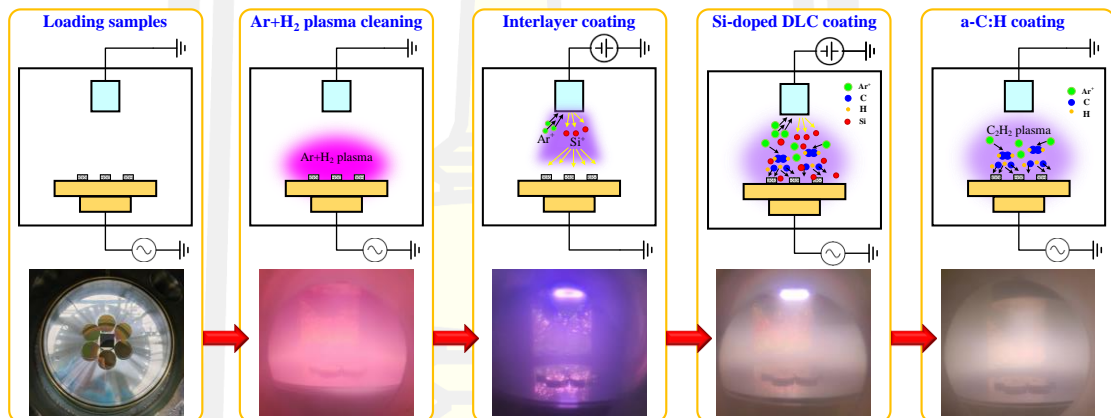


Figure 3.27 A schematic diagram and photo of loading samples, plasma cleaning, interlayer coating, Si-doped DLC coating and DLC coating process for NAB substrate.

CHAPTER IV

Results and discussion (Part : Chrome plating)

The chapter IV deals with the results and discussion of a-C:H films deposited on chromium-plated and silicon substrates with different silicon-based interlayers. This chapter is divided into three sections. In the first section, the deposition rate, structural properties, and mechanical properties of the silicon-based interlayers were investigated. In this part, the film thickness and chemical bonding of different silicon-based interlayers deposited on a silicon substrate were measured, while the effect of the different interlayers deposited on a chromium-plated substrate on hardness was evaluated. The second section investigated the deposition rate and structural properties of a-C:H films deposited on a silicon substrate in terms of film thickness, film density, and D and G peak parameters for sp^2 vibrations of a-C:H films. In the third section, the surface and cross-sectional morphology, structural properties, mechanical properties, adhesion strength, and electrochemical corrosion resistance of a-C:H films deposited with different silicon-based interlayers were analysed and discussed.

4.1 Results of silicon-based interlayers

Four types of amorphous silicon films including a-Si, a-Si:N, a-Si:H, and a-Si_xC_y:H were used as interlayers for the a-C:H coating. These interlayers were deposited on a silicon substrate with the same deposition time of 30 minutes using the DC magnetron sputtering method. The model of four interlayers on a silicon substrate is shown in Figure 4.1. A photo of the a-Si, a-Si:N, a-Si:H, and a-Si_xC_y:H interlayers deposited on the silicon substrates is shown in Figure 4.2. The different colour of the films corresponds to the different types of dopants, thickness and density in the films. To determine the deposition rate for the control of the same thickness, the film thickness was measured using a field emission secondary electron microscope (FESEM). Then, the microstructure and density of these interlayers with the same thickness of about 50 nm were characterized by X-ray photoelectron spectroscopy

(XPS) and X-ray reflectivity (XRR), respectively. For the mechanical properties, the interlayers with 300 nm thick were deposited on a chromium-plated substrate and then the hardness and elastic modulus were observed using nanoindentation techniques.



Figure 4.1 Schematic model of four silicon-based interlayers on a silicon substrate (not to scale).

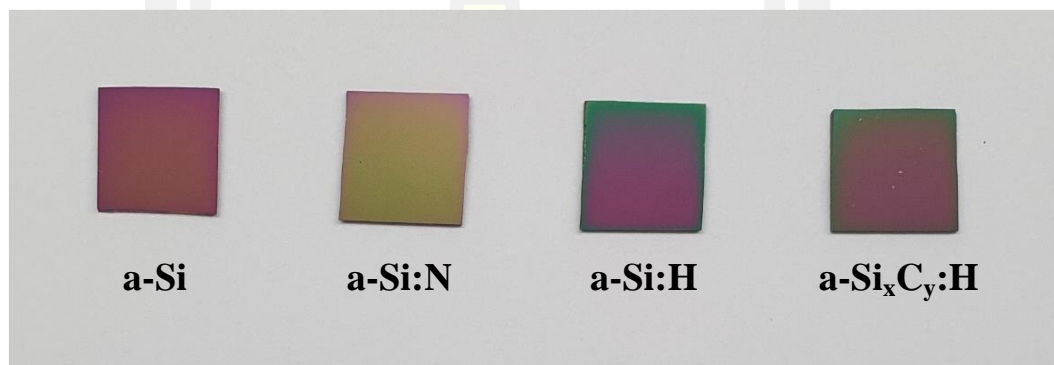
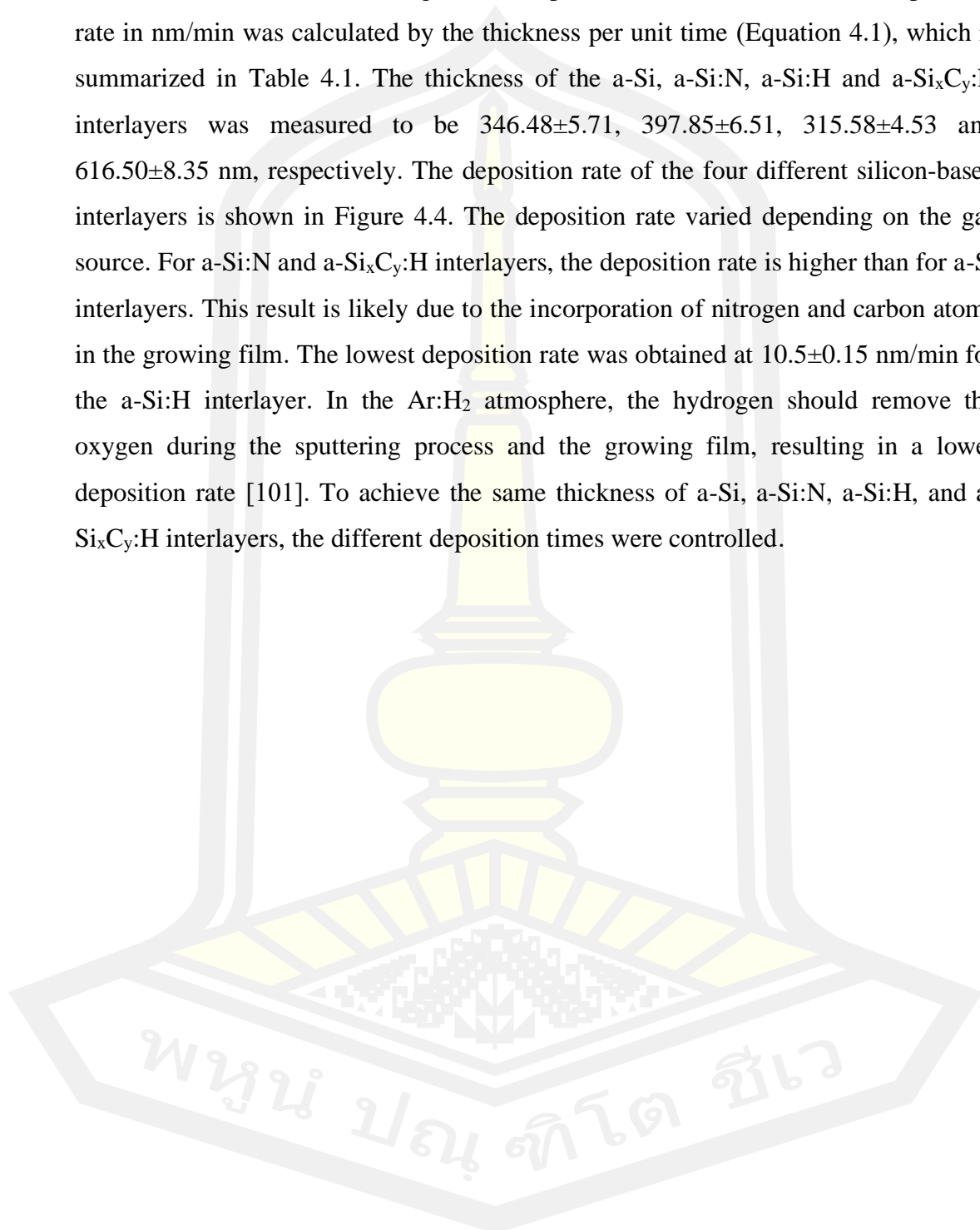


Figure 4.2 Photo of a-Si, a-Si:N, a-Si:H, and a-Si_xC_y:H interlayers deposited on a silicon substrate.

4.1.1 Thickness and deposition rate

The use of different precursor gasses for different silicon-based interlayers directly affected the deposition rate. Therefore, to investigate the effects of different silicon-based interlayers on the properties of a-C:H films, the same film thickness is controlled with the same deposition time of 30 minutes and an operating pressure of 50 mtorr. To determine the film thickness, the deposited a-Si, a-Si:N, a-Si:H and a-Si_xC_y:H interlayers were characterized by FESEM (TESCAN, MIRA3 model) at an accelerating voltage of 20 kV and a magnification of 80 kx in backscattered electron (BSE) mode. Figure 4.3 shows the microscopic cross-sectional images of all the

interlayers. The layer thickness was measured using the Image J program based on two FESEM cross-sectional images with 20 positions each, while the static deposition rate in nm/min was calculated by the thickness per unit time (Equation 4.1), which is summarized in Table 4.1. The thickness of the a-Si, a-Si:N, a-Si:H and a-Si_xC_y:H interlayers was measured to be 346.48±5.71, 397.85±6.51, 315.58±4.53 and 616.50±8.35 nm, respectively. The deposition rate of the four different silicon-based interlayers is shown in Figure 4.4. The deposition rate varied depending on the gas source. For a-Si:N and a-Si_xC_y:H interlayers, the deposition rate is higher than for a-Si interlayers. This result is likely due to the incorporation of nitrogen and carbon atoms in the growing film. The lowest deposition rate was obtained at 10.5±0.15 nm/min for the a-Si:H interlayer. In the Ar:H₂ atmosphere, the hydrogen should remove the oxygen during the sputtering process and the growing film, resulting in a lower deposition rate [101]. To achieve the same thickness of a-Si, a-Si:N, a-Si:H, and a-Si_xC_y:H interlayers, the different deposition times were controlled.



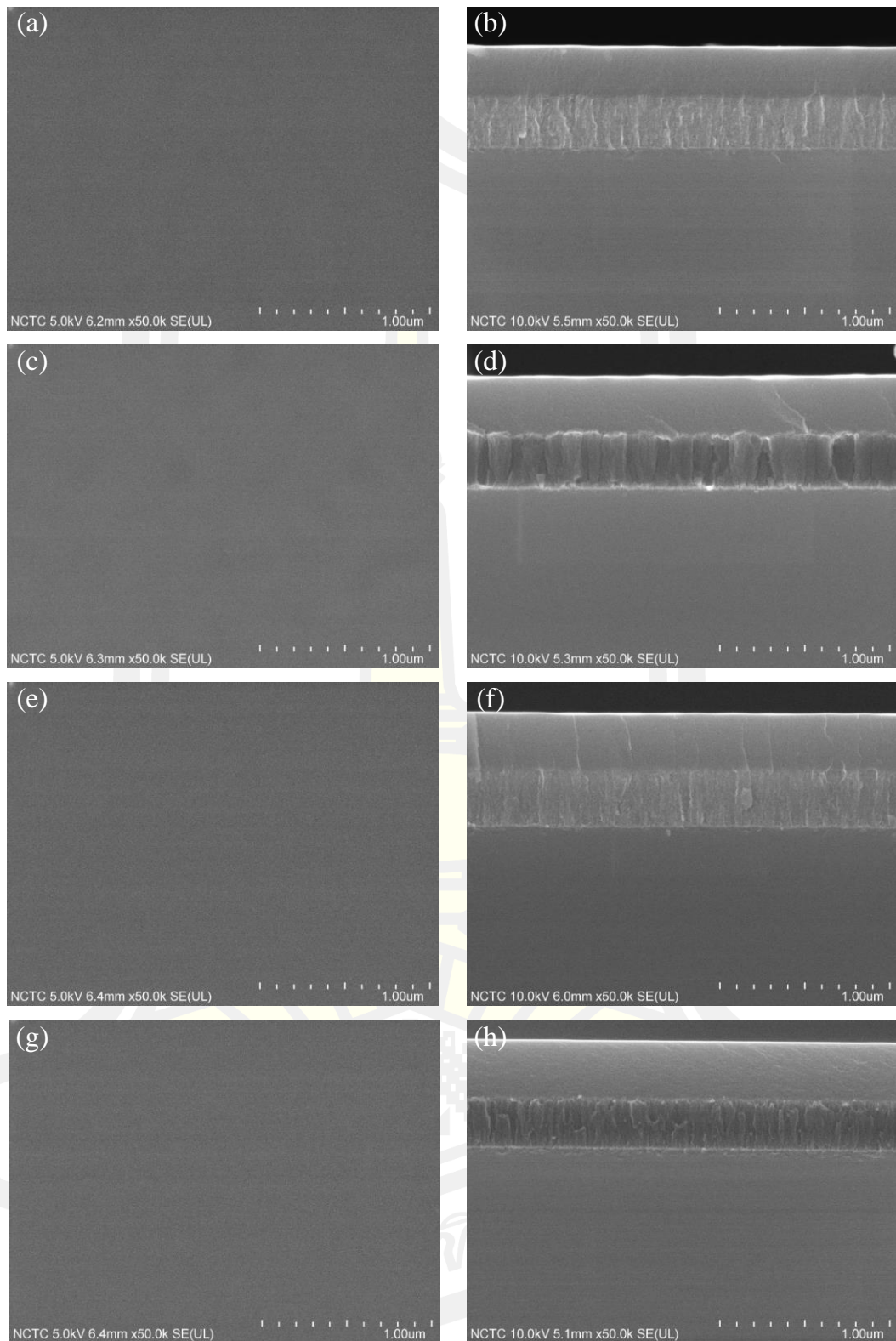


Figure 4.3 FESEM cross-sectional images of (a) a-Si, (b) a-Si:N, (c) a-Si:H, and (d) a-Si_xC_y:H interlayers on silicon substrate.

$$\text{Deposition rate (nm/min)} = \frac{\text{Film thickness (nm)}}{\text{Deposition time (min)}} \quad 4.1$$

Table 4.1 Film thickness and deposition rate of all silicon-based interlayers.

Interlayers	Film thickness (nm)	Deposition rate (nm/min)
a-Si	346.48±5.71	11.5±0.19
a-Si:N	397.85±6.51	13.3±0.22
a-Si:H	315.58±4.53	10.5±0.15
a-Si _x C _y :H	616.50±8.35	20.6±0.28

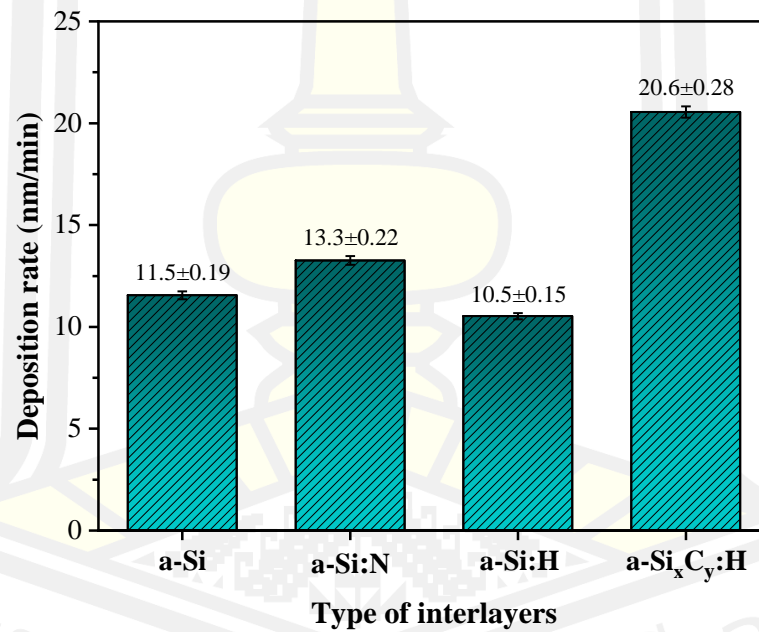


Figure 4.4 Deposition rate using different silicon-based interlayers.

4.1.2 Analysis of the structural properties

For the characterization of the microstructure and film density, the different a-Si, a-Si:N, a-Si:H, and a-Si_xC_y:H interlayers were prepared on the silicon substrate with a layer thickness of about 50 nm. The chemical state of the different interlayers, including a-Si, a-Si:N, a-Si:H, and a-Si_xC_y:H, was investigated by X-ray photoelectron spectroscopy measurements. XPS measurements were performed using a PHI5000 Versa Probe II, ULVAC-PHI, Japan, at the joint research facility SUT-NANOTEC-SLRI, Synchrotron Light Research Institute (SLRI), Thailand. Monochromatic Al-K_α X-rays (1,486.6 eV) was used as the excitation source. All binding energies of the samples were calibrated with the C1s peak at 284.8 eV. For a wide scan, the binding energy range of 0–700 eV was used with a step size of 1 eV. The Si2p, C1s, N1s, and O1s fine scans were performed with the binding energy range of 95–108, 280–290, 394–404, and 529–537 eV, respectively, and a step size of 0.05 eV. The results of the wide-scan XPS spectra for the four silicon-based interlayers, shown in Figure 4.5, mainly contain three peaks at ~102 eV, ~153 eV, and ~532 eV, corresponding to the silicon (Si2p and Si2s) and oxygen (O1s) peaks, respectively [102]. In addition, the peak at ~397 eV of the a-Si:N sample corresponds to nitrogen (N1s) and the peak at ~285 eV of the a-Si_xC_y:H sample corresponds to carbon (C1s), which are dominant compared to the other samples and are associated with the doping gases [102]. The silicon peaks originate from the silicon target, which serves as the main precursor material for silicon-based interlayer deposition. The oxygen-rich peaks should be originated from the residual gas in the vacuum chamber during the deposition process and the adsorption process during the measurement [103], [104].

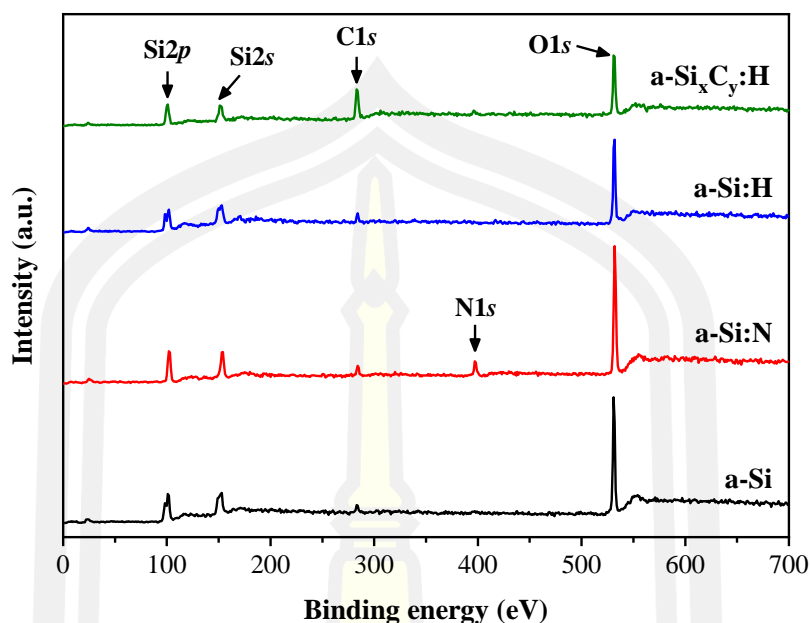


Figure 4.5 Typical XPS spectra of a wide scan for a-Si, a-Si:N, a-Si:H and a-Si_xC_y:H interlayers.

Fitting of the Si2*p* peak for all samples, the N1*s* peak for a-Si:N, and the C1*s* peak for a-Si_xC_y:H was performed using the Gaussian function of Origin software, and backgrounds were fitted using the Shirley method. The deconvoluted XPS spectra for Si2*p* of all interlayers are shown in Figure 4.6. It can be seen that the Si2*p* spectrum was decomposed into six peaks located at binding energies of ~99.3, ~100.0, ~100.6, ~101.4±0.08, ~102.5±0.10, and ~103.5±0.10 eV. These peaks were observed in the functional group of Si2*p*, Si₂O, SiO, Si₂O₃ and SiO₂ and are in agreement with those in other works [105]–[107]. The Si2*p* spectrum was found to contain two spin splitting peaks, which may be overlapping spin-orbit components leading to an asymmetric peak shape. The silicon dioxide and suboxides, including Si₂O, SiO, Si₂O₃ and SiO₂, correspond to oxidation states +1, +2, +3, and +4, respectively [108]. In the a-Si:N interlayer, the nitrogen dopant atoms are not bonded to the silicon atoms, but are located between the silicon network, which is consistent with the XPS spectra of the N1*s* peak, as shown in Figure 4.7 (a). In addition, the a-Si_xC_y:H interlayer also shows the Si–C peak with a binding energy of ~100.3 eV, as

shown in Figure 4.6 (d), indicating that the carbon dopant can be bound to the silicon core atoms [103], [109]. In addition, Figure 4.7 (b) shows the C1s spectra of the a-Si_xC_y:H interlayer that was deconvoluted into four components centered at 283.2, 284.1, 284.9 and 286.4 eV, corresponding to C–Si, C=C, C–C, and C–O, respectively [110], [111]. The results show that the carbon atom is bonded to silicon, which is consistent with the results of the Si2p peak. Moreover, the carbon atom of acetylene gas also binds to its atom to form C=C and C–C bonds, and it binds to the remaining oxygen moiety to form a C–O bond. The fitting results of all peaks such as bond type, binding energy, FWHM and content are summarized in Table 4.2.

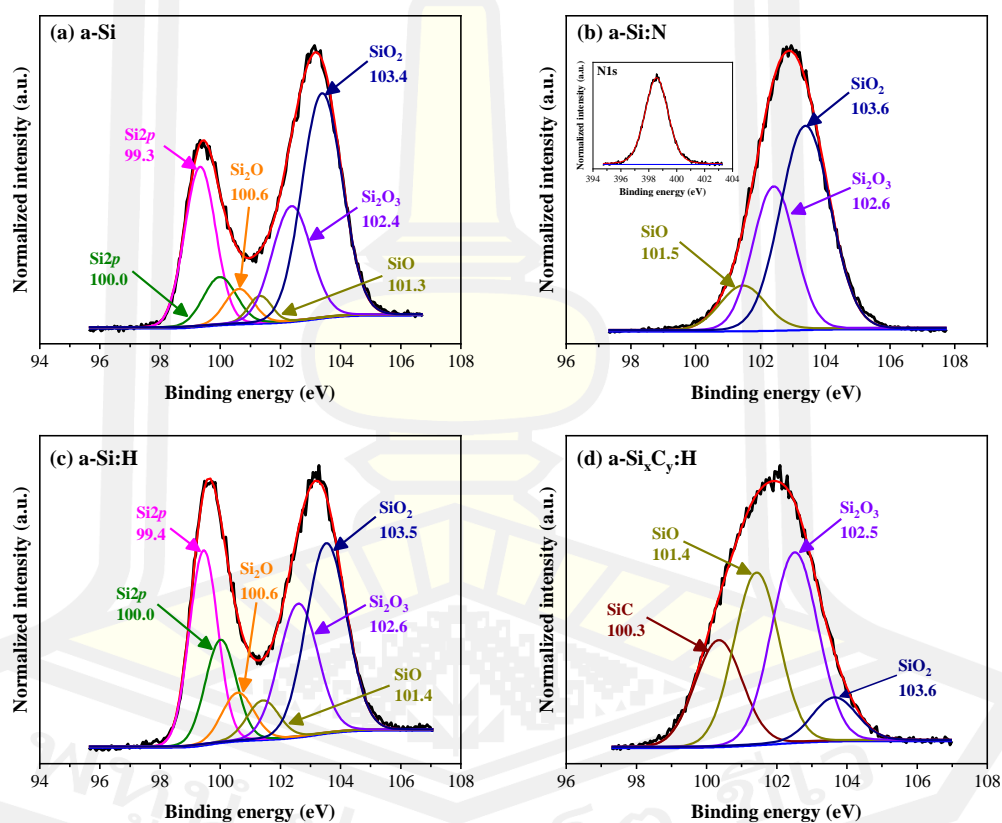


Figure 4.6 Deconvoluted XPS spectra for Si2p of (a) a-Si, (b) a-Si:N, (c) a-Si:H, and (d) a-Si_xC_y:H interlayers. The black, red, blue, and other solid lines represent the experimental data, the fitted curve, the Shirley background, and the deconvolution of the individual peaks, respectively.

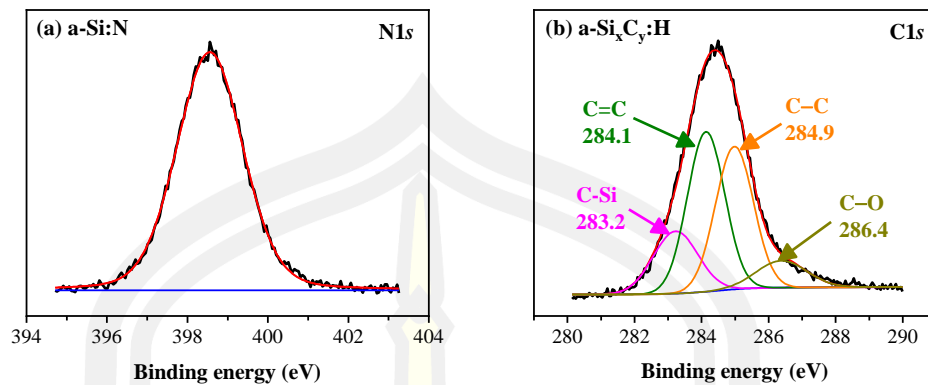


Figure 4.7 Deconvoluted XPS spectra for (a) N1s of a-Si:N interlayer and (b) C1s of a-Si_xC_y:H interlayer. The black, red, blue, and other solid lines represent the experimental data, the fitted curve, the Shirley background, and the deconvolution of the individual peaks, respectively.



Table 4.2 The fitted results of bond type, binding energy, FWHM and content deconvoluted from the XPS spectra of a-Si, a-Si:N, a-Si:H, and a-Si_xC_y:H interlayers.

Interlayers	Peak designation	Bonding	Chemical information		
			Binding energy (eV)	FWHM (eV)	Content (%)
a-Si	Si2p	Si2p	99.3	1.21	22.88
		Si2p	100.0	1.28	7.16
		Si ₂ O	100.6	1.11	4.53
		SiO	101.3	0.90	2.83
		Si ₂ O ₃	102.4	1.51	20.63
		SiO ₂	103.4	1.58	41.96
a-Si:N	Si2p	SiO	101.5	1.56	14.31
		Si ₂ O ₃	102.6	1.55	46.49
		SiO ₂	103.6	1.69	39.20
	N1s	N1s	398.56	1.94	100
a-Si:H	Si2p	Si2p	99.4	1.11	22.76
		Si2p	100.0	1.19	12.94
		Si ₂ O	100.6	1.23	6.20
		SiO	101.4	1.23	5.03
		Si ₂ O ₃	102.6	1.52	21.32
		SiO ₂	103.5	1.58	31.76
a-Si _x C _y :H	Si2p	Si-C	100.3	1.58	21.24
		SiO	101.4	1.51	33.05
		Si ₂ O ₃	102.5	1.56	37.60
		SiO ₂	103.6	1.49	8.11
	C1s	C-Si	283.2	1.58	17.99
		C=C	284.1	1.31	38.39
		C-C	285.0	1.33	34.87
		C-O	286.4	1.77	8.74

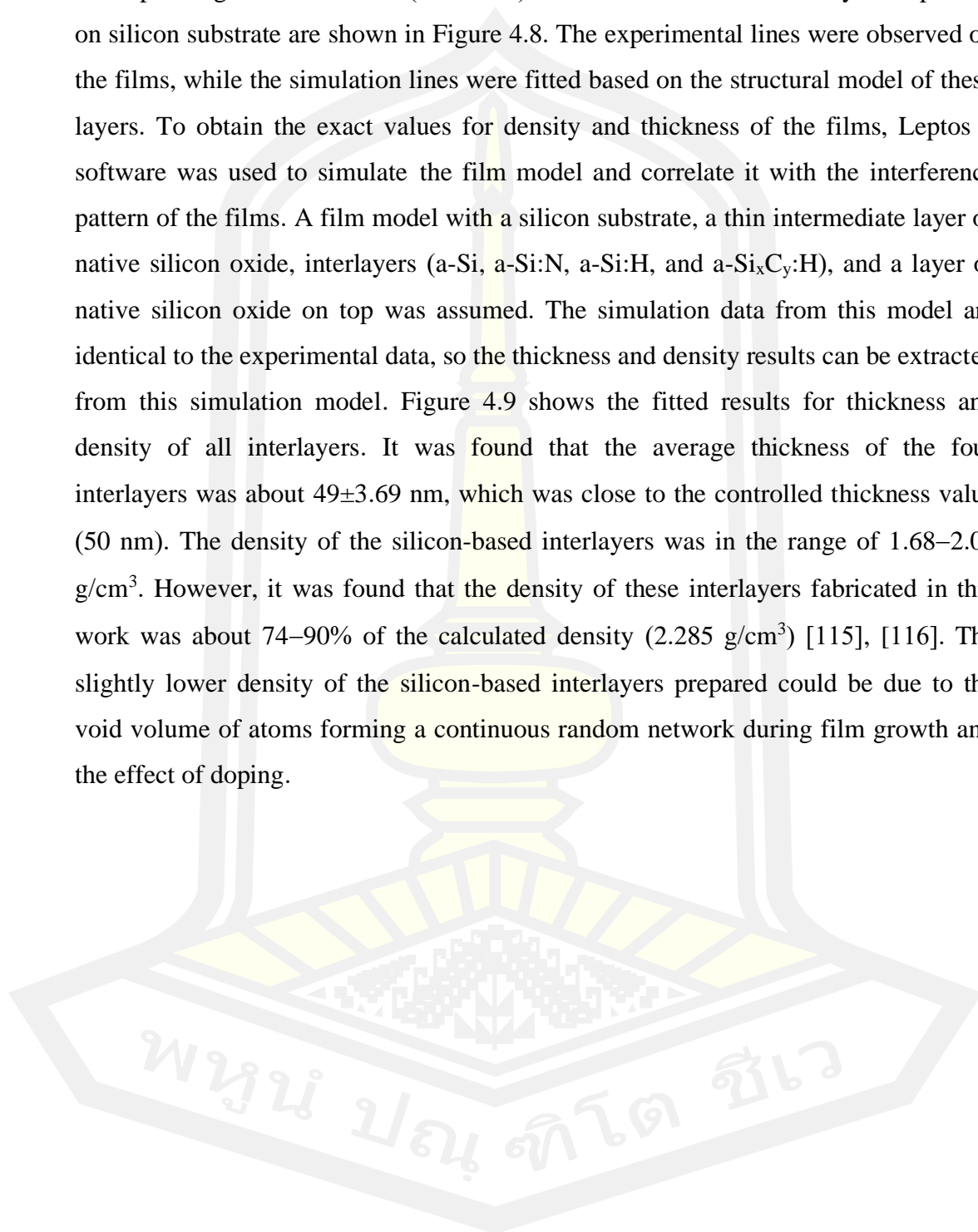
The physical properties such as density, thickness, and roughness of the thin film can be determined by X-ray reflectivity technique. The XRR technique is a nondestructive, powerful, and widely used scattering technique for determining the physical properties of thin-film coatings [112]. The film density of four silicon-based interlayers with a controlled thickness of 50 nm was determined using X-ray reflection by grazing-incidence (Bruker: D8 Advance Diffractometer model). An X-ray beam of Cu-K α radiation with a wavelength of 0.154 nm was used to impinge on the film surface, generated with an accelerating voltage and a cathode current of 40 kV and 40 mA, respectively. With an incident angle of 0–2 degrees and an increment angle of 0.005 degrees at an integration time of 1 s, the oscillations due to the reflection of air-film and film-substrate were observed. This interference pattern of oscillations was also called the Kiessig fringe, which consists of a critical angle (θ_c) and an interference fringe. The density (ρ) of the thin film was extracted from the critical angle for total electron reflection using Equation 4.2 [113], while the layer thickness was defined from the periodic oscillation of intensity, which can be simulated using the modified Bragg equation as shown in Equation 4.3 [114] as follows:

$$\rho \approx \frac{\theta_c^2}{\lambda^2 r_e} \quad 4.2$$

$$t = \frac{\lambda \sqrt{n_i + \Delta n^2}}{2\sqrt{\sin^2 \theta_i - \theta_c^2}} \quad 4.3$$

where λ is the wavelength of the X-rays, $r_e = 2.818 \times 10^{-15}$ m is the Thomson's classical electron radius, θ_i is the observed position of the maximum or minimum of the i -th interference fringe, and n_i is an integer, $\Delta n = 1/2$ and 0 for the maximum and minimum, respectively.

The XRR-Kiessig fringes of experimental data (black curve) and the corresponding simulation data (red curve) for four silicon-based interlayers deposited on silicon substrate are shown in Figure 4.8. The experimental lines were observed on the films, while the simulation lines were fitted based on the structural model of these layers. To obtain the exact values for density and thickness of the films, Leptos 7 software was used to simulate the film model and correlate it with the interference pattern of the films. A film model with a silicon substrate, a thin intermediate layer of native silicon oxide, interlayers (a-Si, a-Si:N, a-Si:H, and a-Si_xC_y:H), and a layer of native silicon oxide on top was assumed. The simulation data from this model are identical to the experimental data, so the thickness and density results can be extracted from this simulation model. Figure 4.9 shows the fitted results for thickness and density of all interlayers. It was found that the average thickness of the four interlayers was about 49 ± 3.69 nm, which was close to the controlled thickness value (50 nm). The density of the silicon-based interlayers was in the range of 1.68–2.05 g/cm³. However, it was found that the density of these interlayers fabricated in this work was about 74–90% of the calculated density (2.285 g/cm³) [115], [116]. The slightly lower density of the silicon-based interlayers prepared could be due to the void volume of atoms forming a continuous random network during film growth and the effect of doping.



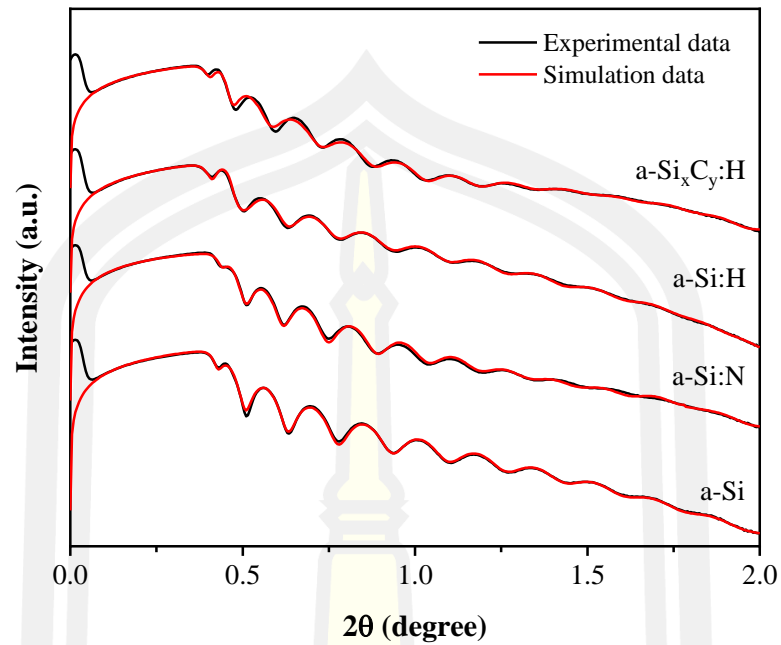


Figure 4.8 XRR curve of the experimental data (black curve) and simulation data (red curve) of the different silicon-based interlayers.

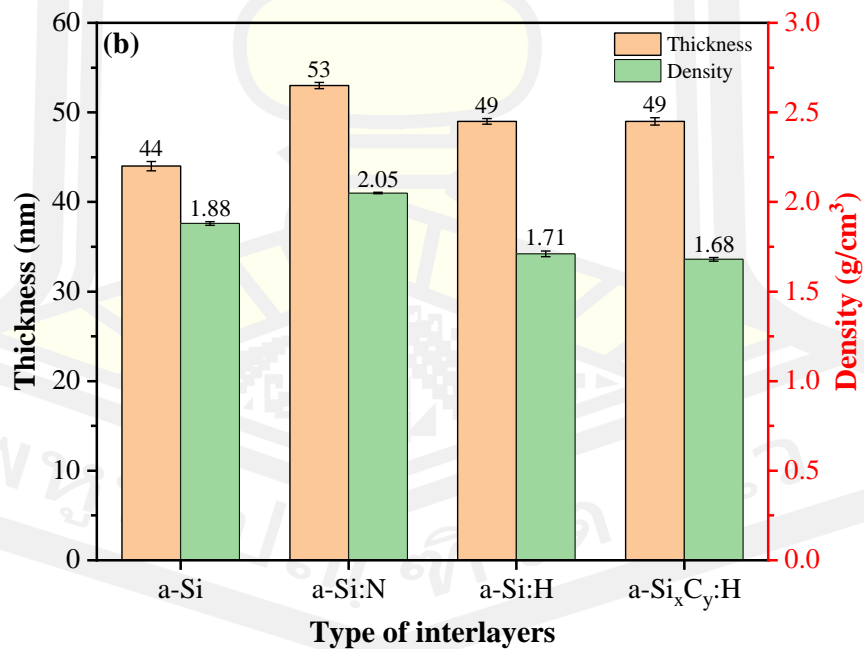


Figure 4.9 Fitted results of thickness (orange bar) and density (green bar) of a-Si, a-Si:N, a-Si:H, and a-Si_xC_y:H interlayers.

4.1.3 Mechanical properties analysis

The nanoindentation test is commonly used to evaluate the hardness and elastic modulus of nanoscale materials determined based on the method of Oliver and Pharr [117]. The hardness and elastic modulus of four silicon-based interlayers with a thickness of 300 nm and the chromium-plated substrates were measured using a nanoindentation test (Hysitron, TI Premier model). To determine the actual hardness value, repeated tests were performed five times on each sample using a pyramid-shaped Berkovich indenter at a different location. To reduce the effects of the chromium-plated substrate, the same low load of 250 μN was used for the dynamic mode so that the maximum indentation depth was less than 10% of the total coating thickness.

Figure 4.10 shows the loading and unloading curves of chromium-plated substrate and four silicon-based interlayers. The curve represents the penetration behaviour of the indenter on a substrate and the films. It became clear that the penetration depth of the sample was different at the same maximum load (250 μN). The penetration depth of the chromium-plated substrate is about 20.26 ± 0.29 nm, while the penetration depth of the a-Si, a-Si:N, a-Si:H and a-Si_xC_y:H interlayers is about 29.31 ± 0.92 , 46.26 ± 2.69 , 48.94 ± 2.87 , and 51.77 ± 2.66 nm, respectively. It can be seen that the penetration depth of four interlayers is 9.77, 15.42, 16.31 and 17.26% of the total film thickness (300 nm). The penetration depth higher than 10% for a-Si:N, a-Si:H and a-Si_xC_y:H samples corresponds to the higher hardness. Although the ultra-low applied load constant of 250 μN was employed to keep the penetration depth below 10%, the indenter can penetrate the film with different depths depending on the hardness.

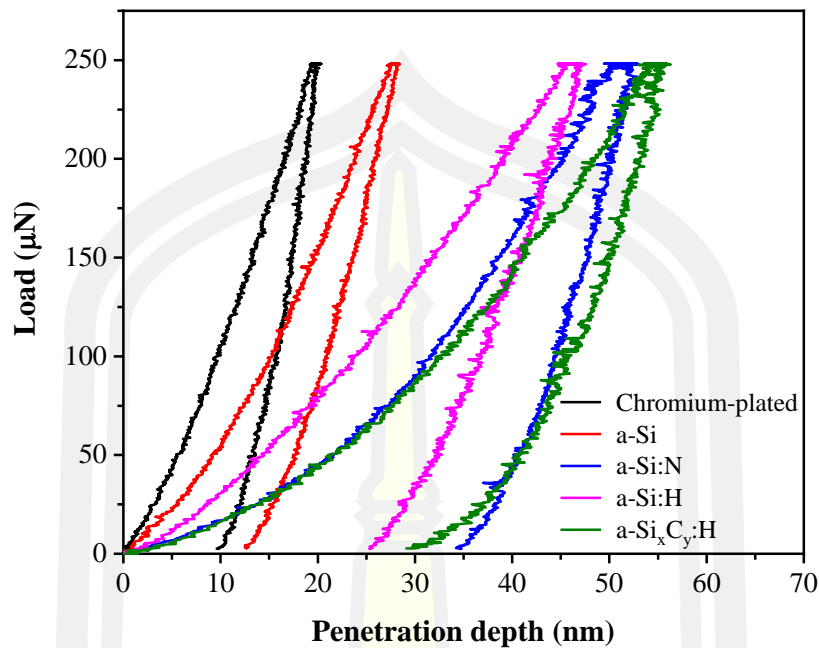


Figure 4.10 Loading and unloading curves of chromium-plated substrate and different silicon-based interlayers.

The hardness and elastic modulus of a substrate and the four interlayers are shown in Figure 4.11. The summarized results of the hardness, penetration depth, and elastic modulus of a chromium-plated substrate and the interlayers a-Si, a-Si:N, a-Si:H, and a-Si_xC_y:H are also shown in Table 4.3. As can be seen in Figure 4.11, the hardness and elastic modulus of four interlayers are lower than those of the substrate. This result shows that coating with only one interlayer is not sufficient to improve the mechanical properties of the substrate. At the same applied load, the highest hardness of 5.28 ± 0.24 GPa of the a-Si interlayer corresponds to the lowest penetration depth for all interlayers. For the a-Si interlayer, all silicon atoms are bonded to four adjacent silicon atoms (Si-Si bonds) to obtain an amorphous structure, and also bonded to residual oxygen atoms, as shown by the XPS results, which may result in lower hardness than other works. Another factor that may affect the lower hardness is the process parameters during deposition. Danesh *et al.* [118] show that the hardness of a-Si films prepared by DC magnetron sputtering is about 9.55 GPa, but a high substrate temperature of 300 °C is required. Moreover, a-Si:N, a-Si:H, and a-Si_xC_y:H

interlayers have lower hardness than a-Si interlayers. The introduction of nitrogen, hydrogen, and carbon atoms from doping gasses into the amorphous silicon structure can cause the Si-Si bonds to be broken [119]. However, the slightly different hardness of a-Si:N, a-Si:H, and a-Si_xC_y:H interlayers is difficult to compare and explain due to the different concentrations and process parameters for thin-film deposition. The elastic modulus of a material is the resistance to elastic deformation under an externally applied stress, which can be represented by the stress-strain ratio of the material. In Figure 4.11, the modulus of elasticity is varied in the same way as hardness. For all the interlayers, the a-Si interlayer exhibits the highest elastic modulus of 100.28 ± 4.33 GPa, indicating a high load carrying capacity of the film.

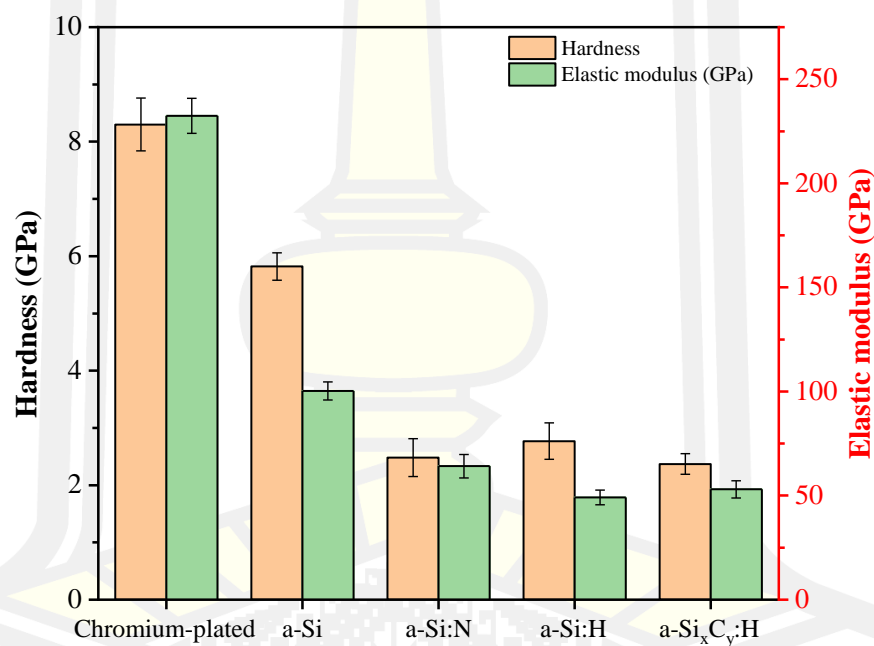
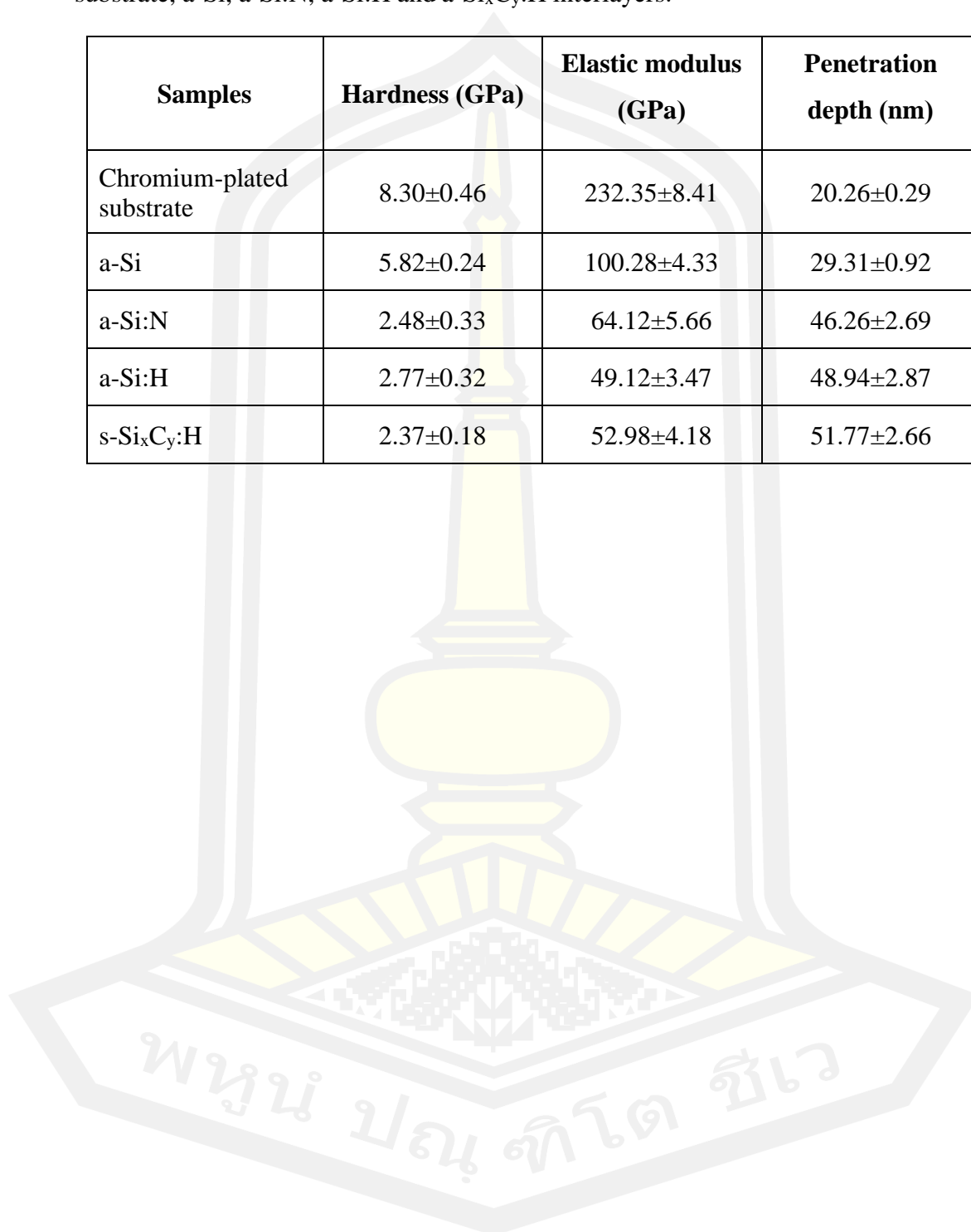


Figure 4.11 Hardness and elastic modulus of chromium-plated substrate and a-Si, a-Si:N, a-Si:H, and a-Si_xC_y:H interlayers.

Table 4.3 Hardness, elastic modulus and penetration depth of a chromium-plated substrate, a-Si, a-Si:N, a-Si:H and a-Si_xC_y:H interlayers.

Samples	Hardness (GPa)	Elastic modulus (GPa)	Penetration depth (nm)
Chromium-plated substrate	8.30±0.46	232.35±8.41	20.26±0.29
a-Si	5.82±0.24	100.28±4.33	29.31±0.92
a-Si:N	2.48±0.33	64.12±5.66	46.26±2.69
a-Si:H	2.77±0.32	49.12±3.47	48.94±2.87
s-Si _x C _y :H	2.37±0.18	52.98±4.18	51.77±2.66



4.2 Results of a-C:H films

The chromium-plated substrates with silicon-based interlayers were coated with a-C:H film to improve the mechanical and corrosive properties. To compare the effect of the interlayers, the process parameters of the a-C:H coating were controlled. First, the a-C:H film was deposited on a silicon substrate using the RF-PECVD method with a deposition time of 20 minutes, as shown in the photo in Figure 4.12. Then, the thickness of the a-C:H film was investigated by FESEM to determine the deposition rate. In addition, the a-C:H film with a controlled thickness of about 50 nm was characterized for density by XRR.

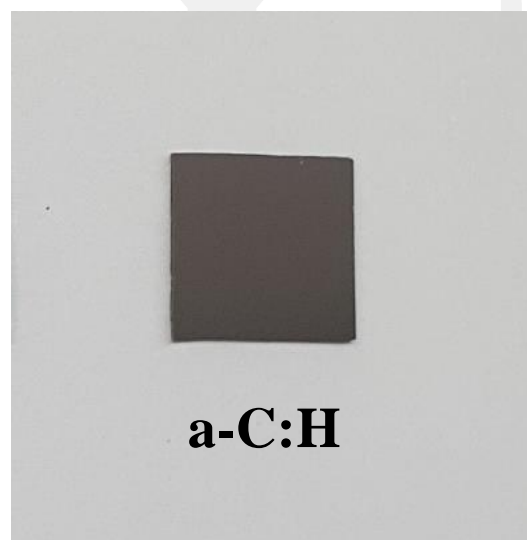


Figure 4.12 A photo of a-C:H film on a silicon substrate.

4.2.1 Film thickness and deposition rate

The FESEM cross-sectional image (TESCAN, MIRA3 model) with an accelerating voltage of 20 kV and a magnification of 80 kx in BSE mode was used to evaluate the actual thickness of the a-C:H film. Figure 4.13 shows the FESEM cross-sectional image of a-C:H film on a silicon substrate. The layer thickness was measured using the Image J program based on two FESEM cross-sectional images with 20 positions each. The result shows that the film thickness was 417.39 ± 5.64 nm

with a deposition time of 20 minutes. Accordingly, the deposition rate of the a-C:H film was 20.87 ± 0.28 nm/min, which can be used to control the thickness of the a-C:H layer later.

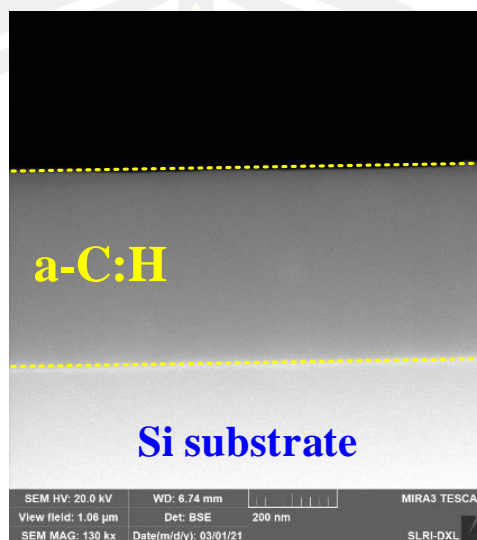


Figure 4.13 Cross-sectional FESEM image of a-C:H film.

4.2.2 Structural properties analysis

The XRR technique was used to investigate the physical properties such as density and thickness of the a-C:H layer. The deposited a-C:H film with a controlled thickness of about 50 nm was measured by XRR technique with grazing-incidence mode. The layer model with the silicon substrate, the thin native silicon oxide, and the carbon layer on the top was used to interpret the Kiessig fringes using Leptos 7 software. The XRR Kiessig fringes of the experimental data (black curve) and the corresponding simulation data (red curve) for the a-C:H sample are shown in Figure 4.14. It was found that the thickness of the a-C:H film is about 45 nm, which is close to the controlled thickness value (50 nm). In this work, it was found that the density of the a-C:H film deposited with RF-PECVD is about 2.15 g/cm^3 . This density value is in the range previously reported ($1.60\text{--}2.10 \text{ g/cm}^3$ for hydrogenated amorphous carbon films prepared by the RF-PECVD method [120]). Moreover, the

density of the a-C:H film can be improved by adjusting the process parameters, although the data are not shown in this work.

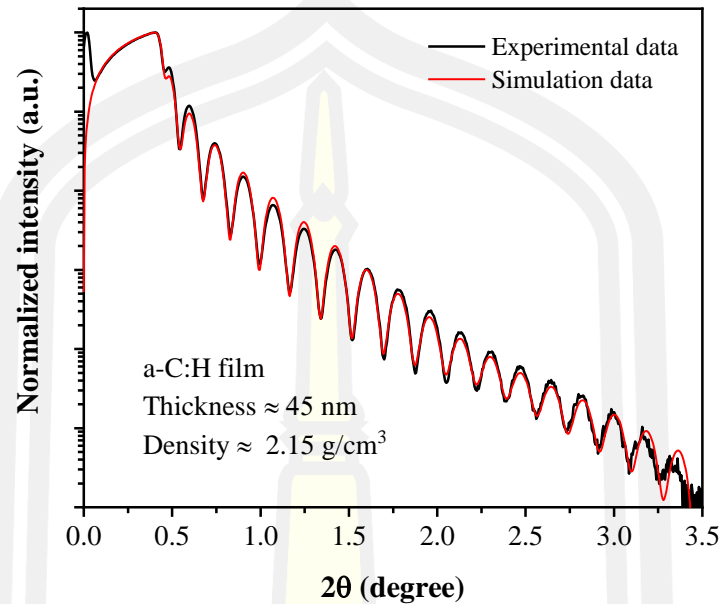
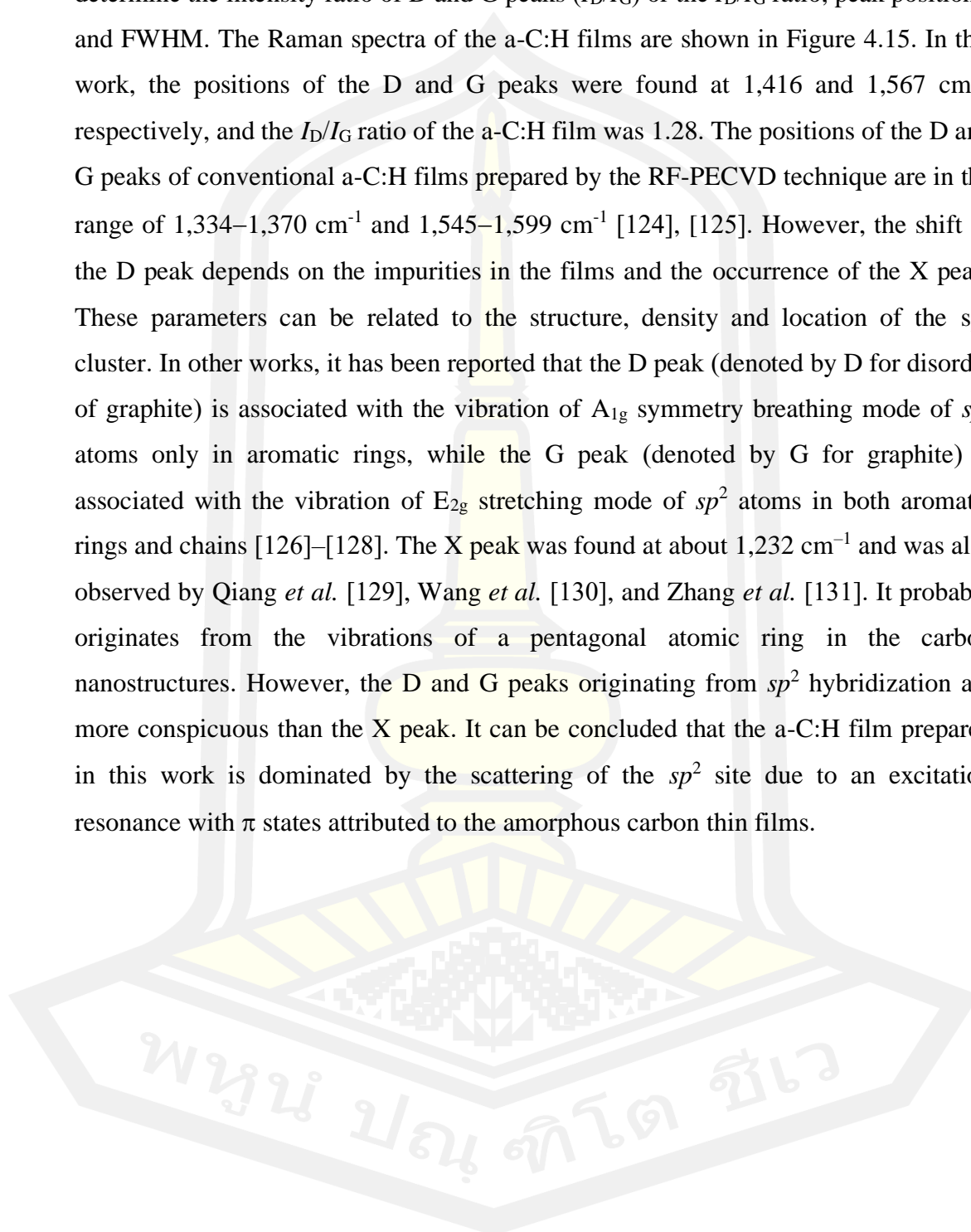


Figure 4.14 XRR curve of experimental data (black curve) and simulation data (red curve) for a-C:H films.

Raman spectroscopy is widely used to determine the structural and complementary information of DLC films because it detects the chemical bonds in carbon-based materials with a nondestructive method [121], [122]. In general, the Raman spectra of undoped amorphous carbon films with and without hydrogenation show two peaks, the D peak and the G peak. These peaks were usually excited by the oscillation of sp^2 hybridization in the carbon network [123]. In this work, the structure formation of the a-C:H thin films deposited on the silicon substrate with a thickness of about 50 nm was characterized by Raman spectroscopy (Bruker, Senterra model). The surface of the a-C:H films was excited using an Ar laser with a wavelength of 532 nm and a power of 12.5 mW. The scan range of the Raman spectra was between $50\text{--}2,700\text{ cm}^{-1}$ (0.5 cm^{-1} resolution) with an aperture size of 50 μm slit. The spectrum was a co-addition of 30 scans with a short exposure time (2 s) to avoid the effect of laser annealing, which could lead to a graphitized diamond-like sample. Three Raman spectra of the a-C:H samples from the different positions were averaged and

deconvoluted with the Gaussian function using Origin software (version 2018) to determine the intensity ratio of D and G peaks (I_D/I_G) or the I_D/I_G ratio, peak positions, and FWHM. The Raman spectra of the a-C:H films are shown in Figure 4.15. In this work, the positions of the D and G peaks were found at 1,416 and 1,567 cm^{-1} , respectively, and the I_D/I_G ratio of the a-C:H film was 1.28. The positions of the D and G peaks of conventional a-C:H films prepared by the RF-PECVD technique are in the range of 1,334–1,370 cm^{-1} and 1,545–1,599 cm^{-1} [124], [125]. However, the shift of the D peak depends on the impurities in the films and the occurrence of the X peak. These parameters can be related to the structure, density and location of the sp^2 cluster. In other works, it has been reported that the D peak (denoted by D for disorder of graphite) is associated with the vibration of A_{1g} symmetry breathing mode of sp^2 atoms only in aromatic rings, while the G peak (denoted by G for graphite) is associated with the vibration of E_{2g} stretching mode of sp^2 atoms in both aromatic rings and chains [126]–[128]. The X peak was found at about 1,232 cm^{-1} and was also observed by Qiang *et al.* [129], Wang *et al.* [130], and Zhang *et al.* [131]. It probably originates from the vibrations of a pentagonal atomic ring in the carbon nanostructures. However, the D and G peaks originating from sp^2 hybridization are more conspicuous than the X peak. It can be concluded that the a-C:H film prepared in this work is dominated by the scattering of the sp^2 site due to an excitation resonance with π states attributed to the amorphous carbon thin films.



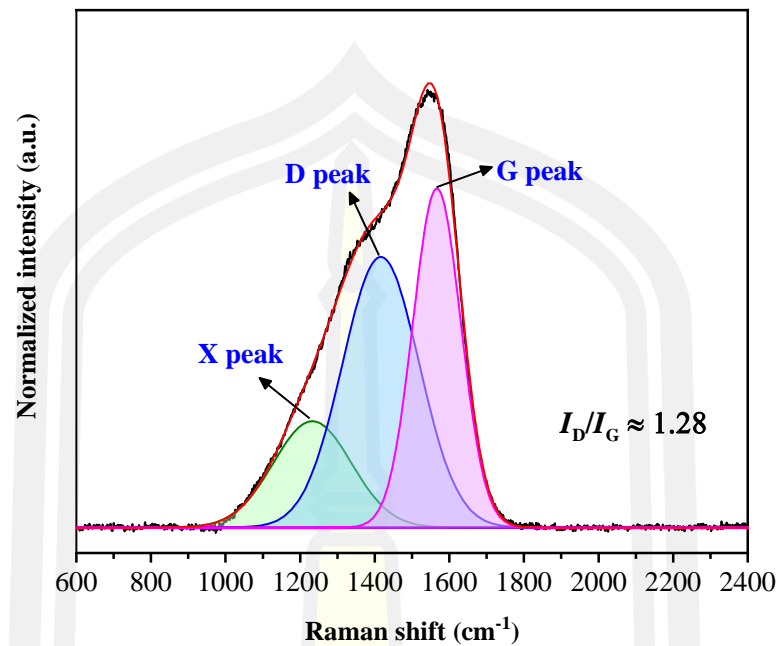
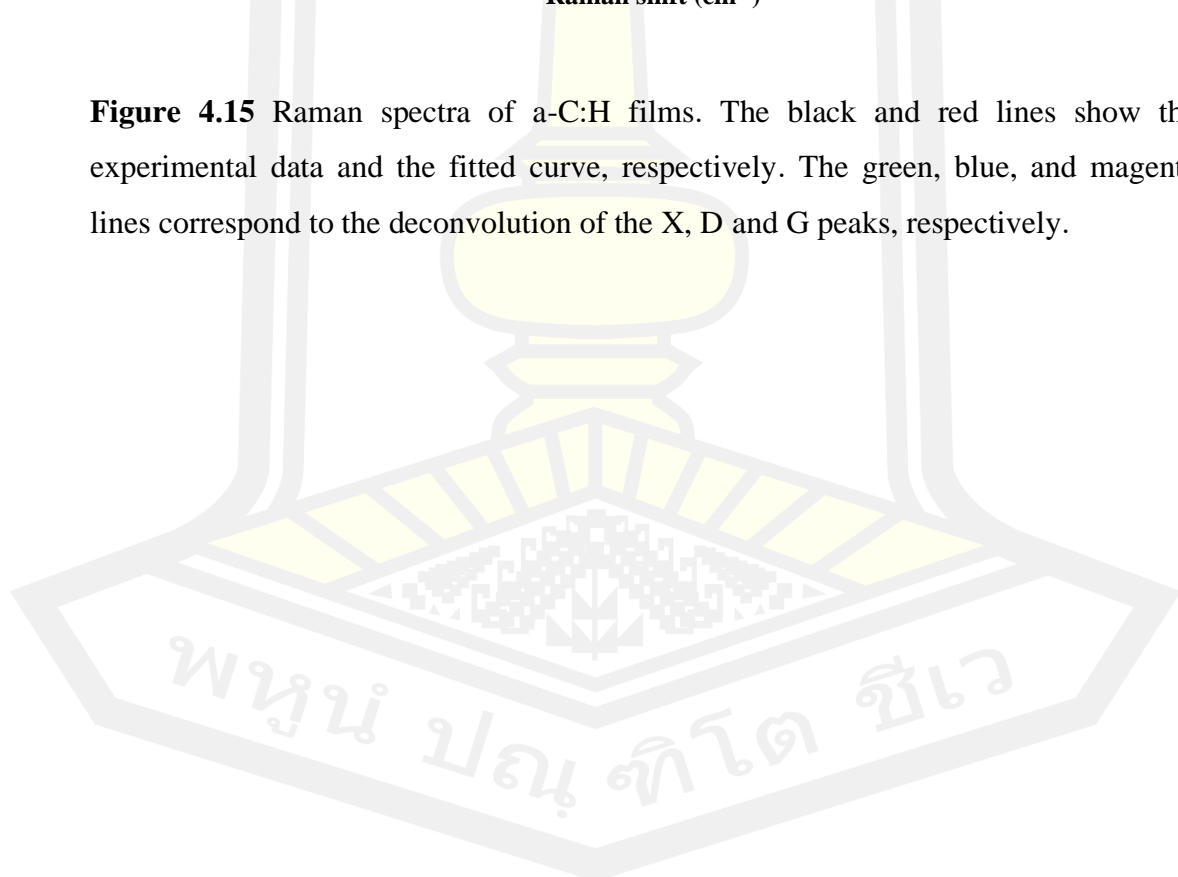


Figure 4.15 Raman spectra of a-C:H films. The black and red lines show the experimental data and the fitted curve, respectively. The green, blue, and magenta lines correspond to the deconvolution of the X, D and G peaks, respectively.



4.3 Results of a-C:H with interlayers

In this part, the a-C:H films with different silicon-based interlayers were deposited on chromium-plated and silicon substrates. The thickness of the silicon-based interlayers of a-Si, a-Si:N, a-Si:H, and a-Si_xC_y:H was set to about 300 nm. The a-C:H layer was also controlled at a thickness of 300 nm. In the first study of this part, the thickness of the a-C:H layer was controlled to about 600 nm, but the a-C:H films with the a-Si:N interlayer detached from the chromium-plated substrate as if deposited. Therefore, the thickness of the a-C:H layer was set to 300 nm to be compatible with all interlayers. Figure 4.16 shows the model of a-C:H layer deposition with different silicon-based interlayers and without an interlayer on a chromium-plated substrate. The different deposition times of the four interlayers and the a-C:H film were manipulated based on the deposition rate of each thin film to achieve a film thickness of 300 nm.

Figure 4.17 shows a photo of a-C:H films deposited with different silicon-based interlayers on substrate holder. Figure 4.18 shows a photo of a-C:H films deposited on silicon and chromium-plated substrates using a-Si, a-Si:N, a-Si:H and a-Si_xC_y:H films as the interlayers. It was found that the colour of the films on silicon substrates was dark brown or black and uniform. On chrome plating, the colour was not uniform with greenish-black and purplish-black, which is due to the height of the sample and the non-uniform coating of the interlayers. However, the films showed good adhesion to the substrates without cracking or peeling. In contrast, the a-C:H films deposited on a chromium-plated substrate without an interlayer can be seen to detach from the substrate, as shown in Figure 4.19. Thus, the a-C:H films deposited without an interlayer exhibit poor adhesion.

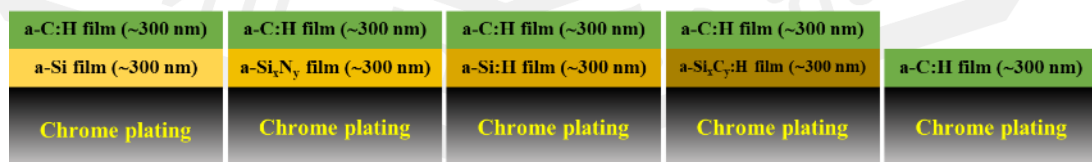


Figure 4.16 The schematic model of a-C:H film with and without silicon-based interlayers (not to scale).

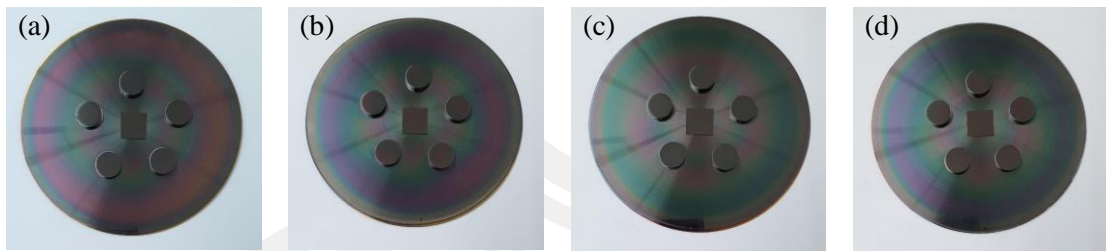


Figure 4.17 A photo of a-C:H film deposited with (a) a-Si, (b) a-Si:N, (c) a-Si:H, and (d) a-Si_xC_y:H interlayers on substrate holder.

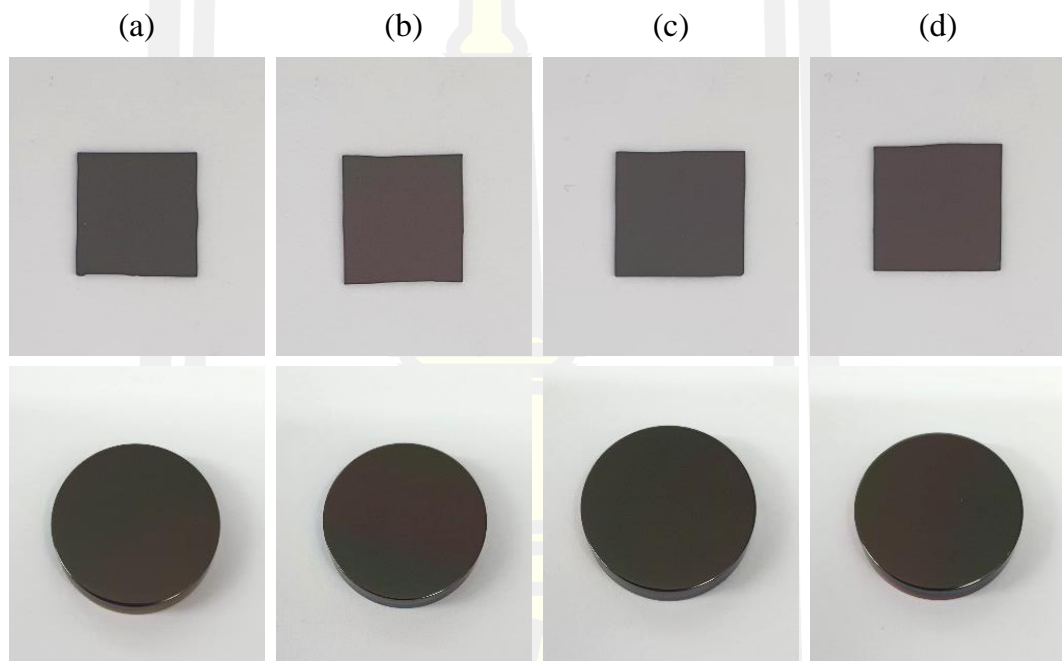


Figure 4.18 A photo of an a-C:H film deposited with (a) a-Si, (b) a-Si:N, (c) a-Si:H, and (d) a-Si_xC_y:H interlayers on silicon and chromium-plated substrate.



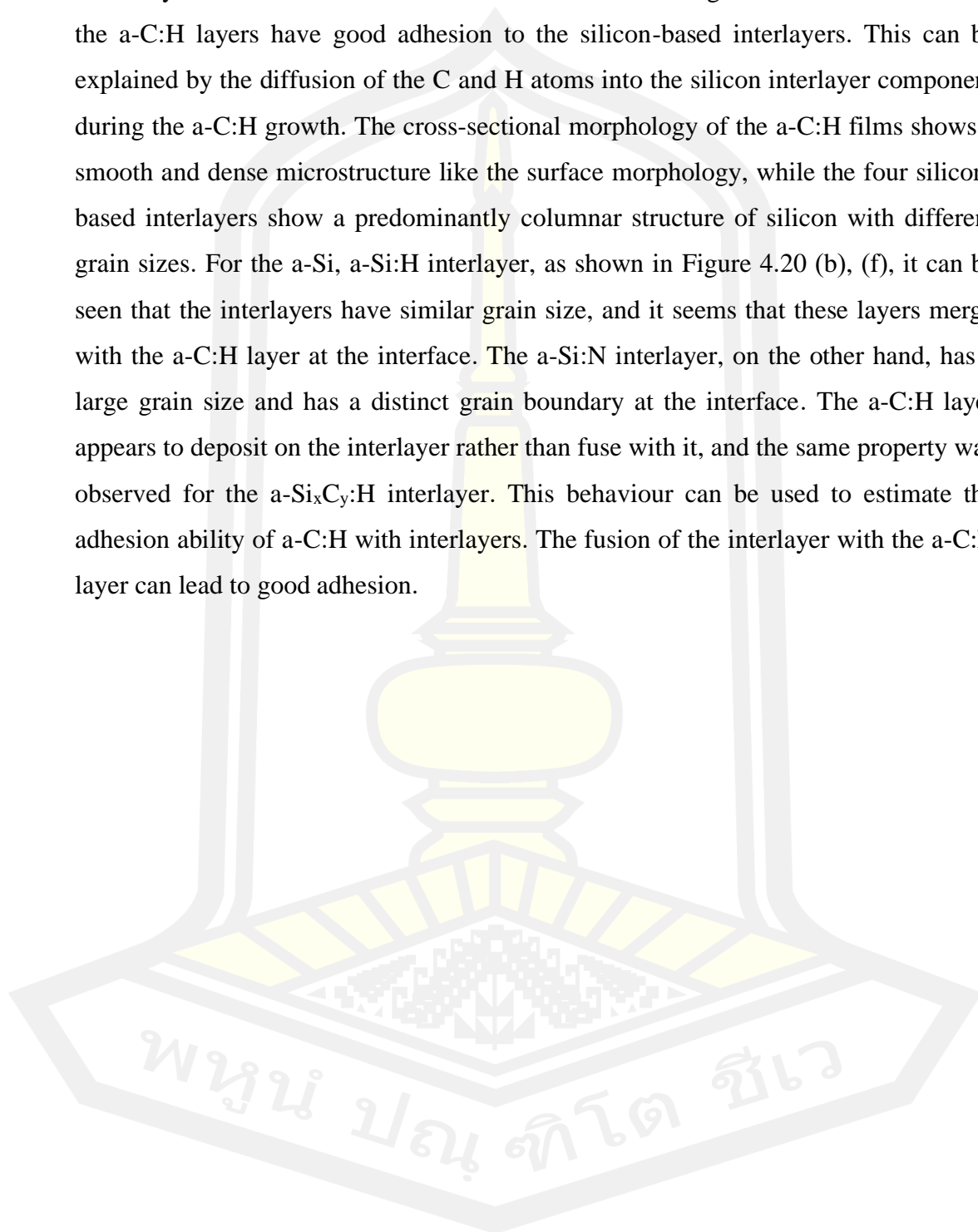
Figure 4.19 A photo of an a-C:H film deposited on a chromium-plated substrate.

The deposited a-C:H films with different silicon-based interlayers were characterized by FESEM, Raman spectroscopy, micro-scratching, nanoindentation and electrochemical tests. Surface and cross-sectional morphology, structural properties, adhesion strength, hardness, and corrosion resistance were observed.

4.3.1 Surface and cross-sectional morphology

The surface and cross-sectional images of the a-C:H films with different silicon interlayers were acquired using FESEM (HITACHI, model SU8030) to study their morphological properties. The FESEM images were measured at a magnification of 80 kx in secondary electron mode with an accelerating voltage of 5 kV for the surface morphology and 10 kV for the cross-sectional microstructures. Figure 4.20 shows the surface morphologies and corresponding cross-sectional images of the deposited a-C:H films with (a), (b) a-Si; (c), (d) a-Si:N; (e), (f) a-Si:H; and (g), (h) a-Si_xC_y:H interlayers. The surface morphology of all samples was detected on the top of the a-C:H layers. It can be seen that the surface morphology exhibits very homogeneous, smooth and dense microstructures without microparticle defects, as also reported by Song *et al.* [132] and Schlebrowski [133]. On the cross-sectional images, all samples consist of two different layers, with the a-C:H layer being about 317±12.99 nm thick and the interlayers having a thickness of about 306±14.23 nm. The average total thickness of a-C:H with interlayers is about 623±13.61 nm. The

cross-sectional morphology between the a-C:H layer and the interlayer shows a clear boundary at the interface without delamination and cracking. This result indicates that the a-C:H layers have good adhesion to the silicon-based interlayers. This can be explained by the diffusion of the C and H atoms into the silicon interlayer component during the a-C:H growth. The cross-sectional morphology of the a-C:H films shows a smooth and dense microstructure like the surface morphology, while the four silicon-based interlayers show a predominantly columnar structure of silicon with different grain sizes. For the a-Si, a-Si:H interlayer, as shown in Figure 4.20 (b), (f), it can be seen that the interlayers have similar grain size, and it seems that these layers merge with the a-C:H layer at the interface. The a-Si:N interlayer, on the other hand, has a large grain size and has a distinct grain boundary at the interface. The a-C:H layer appears to deposit on the interlayer rather than fuse with it, and the same property was observed for the a-Si_xC_y:H interlayer. This behaviour can be used to estimate the adhesion ability of a-C:H with interlayers. The fusion of the interlayer with the a-C:H layer can lead to good adhesion.



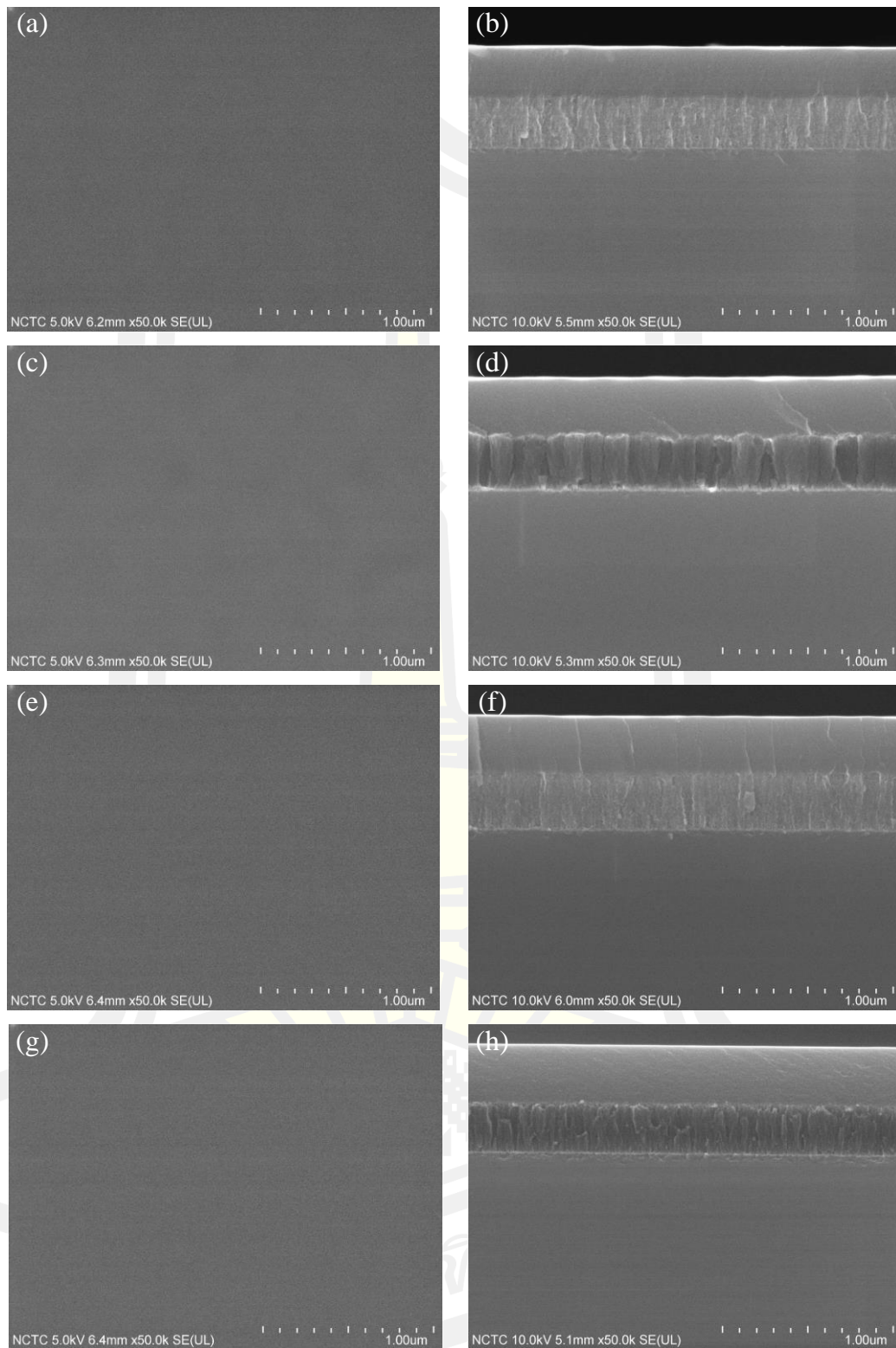


Figure 4.20 Surface morphologies (left) and cross-sectional microstructures (right) of a-C:H films with (a), (b) a-Si; (c), (d) a-Si:N; (e), (f) a-Si:H; and (g), (h) a-Si_xC_y:H interlayers deposited on a silicon substrate.

4.3.2 Structural properties

The structural properties of a-C:H deposited with four silicon-based interlayers were characterized by Raman spectroscopy and XPS. For Raman spectroscopy, the surface of the a-C:H films deposited on both silicon and chromium-plated substrates was excited using an Ar laser with a wavelength of 532 nm and a power of 5 mW. The scan range was between 50–2700 cm^{-1} (0.5 cm^{-1} resolution) with an aperture size of 50 μm slit. Each spectrum was a co-addition of 30 scans with an integration time (2 s). Three Raman spectra of the samples from the different positions were averaged and deconvoluted using Origin software (version 2018) with three Gaussian peaks to determine the I_D/I_G ratio, peak positions, and FWHM of the X, D, and G peaks.

The Raman spectra of a-C:H films with different silicon-based interlayers on silicon and chromium-plated substrates are shown in Figure 4.21. The fitted results such as peak position, FWHM and I_D/I_G ratio are listed in Table 4.4 and Table 4.5 for silicon substrates and chromium-plated substrates, respectively. The position of the D and G peaks were found centered in the range of 1,413–1,417 cm^{-1} and 1,562–1,569 cm^{-1} , respectively, in all samples. The position of the X peak was also found to be 1222–1225 cm^{-1} , resulting in a shift in the position of the D peak. The I_D/I_G ratio of a-C:H films on silicon and chromium-plated substrates was found in the range of 1.25–1.27, which corresponds to a similar value. The parameters such as the I_D/I_G ratio, peak position and FWHM of the X, D and G peaks have similar values since the same coating conditions were used. The physical significance of the X, D and G peaks is described in section 4.2.2. It can be concluded that the different silicon-based interlayers do not affect the structural properties of the a-C:H film.

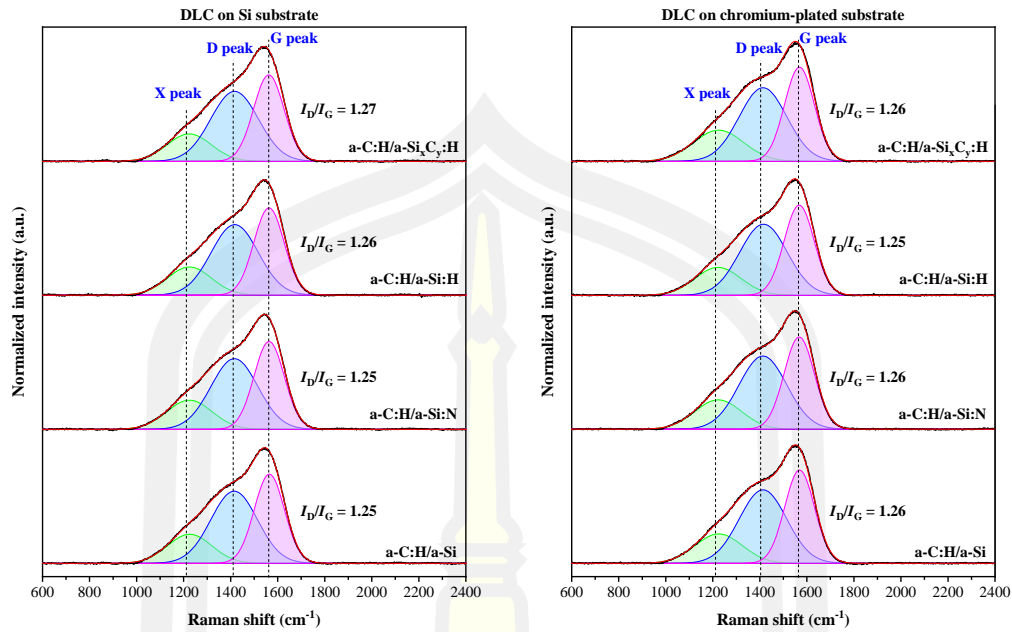


Figure 4.21 Raman spectra of a-C:H films deposited with a-Si, a-Si:N, a-Si:H, and a-Si_xC_y:H interlayers on (a) silicon and (b) chromium-plated substrate. The black and red lines show the experimental data and the fitted curve, respectively. The green, blue, and magenta lines correspond to the deconvolution of the X, D and G peaks, respectively.

Table 4.4 The fitted results of peak positions and FWHM of X, D, and G peaks and I_D/I_G from the Raman spectra of a-C:H films with a-Si, a-Si:N, a-Si:H, and a-Si_xC_y:H interlayers deposited on a silicon substrate.

Samples	X peak		D peak		G peak		I_D/I_G
	Position (cm ⁻¹)	FWHM (cm ⁻¹)	Position (cm ⁻¹)	FWHM (cm ⁻¹)	Position (cm ⁻¹)	FWHM (cm ⁻¹)	
a-C:H/a-Si	1,225	222	1,415	233	1,564	151	1.25
a-C:H/a-Si:N	1,225	227	1,416	235	1,563	151	1.25
a-C:H/a-Si:H	1,225	220	1,417	236	1,563	151	1.26
a-C:H/a-Si _x C _y :H	1,224	221	1,417	238	1,562	152	1.27

Table 4.5 The fitted results of peak positions and FWHM of X, D, and G peaks and I_D/I_G from the Raman spectra of a-C:H film with a-Si, a-Si:N, a-Si:H, and a-Si_xC_y:H interlayers deposited on a chromium-plated substrate.

Samples	X peak		D peak		G peak		I_D/I_G
	Position (cm ⁻¹)	FWHM (cm ⁻¹)	Position (cm ⁻¹)	FWHM (cm ⁻¹)	Position (cm ⁻¹)	FWHM (cm ⁻¹)	
a-C:H/a-Si	1,225	236	1,413	237	1,569	149	1.26
a-C:H/a-Si:N	1,223	233	1,413	239	1,567	151	1.26
a-C:H/a-Si:H	1,222	231	1,416	239	1,567	150	1.25
a-C:H/a-Si _x C _y :H	1,225	251	1,413	239	1,569	149	1.26

For XPS analysis, a-C:H films were prepared with different a-Si, a-Si:N, a-Si:H, and a-Si_xC_y:H interlayers on a silicon substrate with an average film thickness of 623±13.61 nm. The chemical state of the upper a-C:H layer was investigated using XPS measurement. XPS measurements were performed using a PHI5000 Versa Probe II, ULVAC-PHI, Japan, at the joint research facility SUT-NANOTEC-SLRI, Synchrotron Light Research Institute (SLRI), Thailand. Monochromatic Al-K_α X-ray (1,486.6 eV) was used as the excitation source. All binding energies of four samples were calibrated with the C1s peak at a binding energy of 284.8 eV. For a wide scan, the binding energy range of 0–600 eV was used with a step size of 1 eV. The C1s fine scan was performed with a binding energy range of 270–300 eV and a step size of 0.1 eV.

The results of the wide-scan XPS spectra for the a-C:H films with four silicon-based interlayers deposited on a silicon substrate are shown in Figure 4.22. From the results, the surface of the a-C:H films mainly contains two peaks at ~284.8 and ~532 eV, which correspond to the carbon (C1s) and oxygen (O1s) peaks, respectively [101], [134]. The minor O1s peak in all samples was attributed to the residual gas in the vacuum chamber during the deposition process and the surface with air exposure [134] during the XPS measurement. The carbon peaks originated

from the hydrocarbon gas of C_2H_2 , which was used as the main precursor gas for the deposition of hydrogenated amorphous carbon.

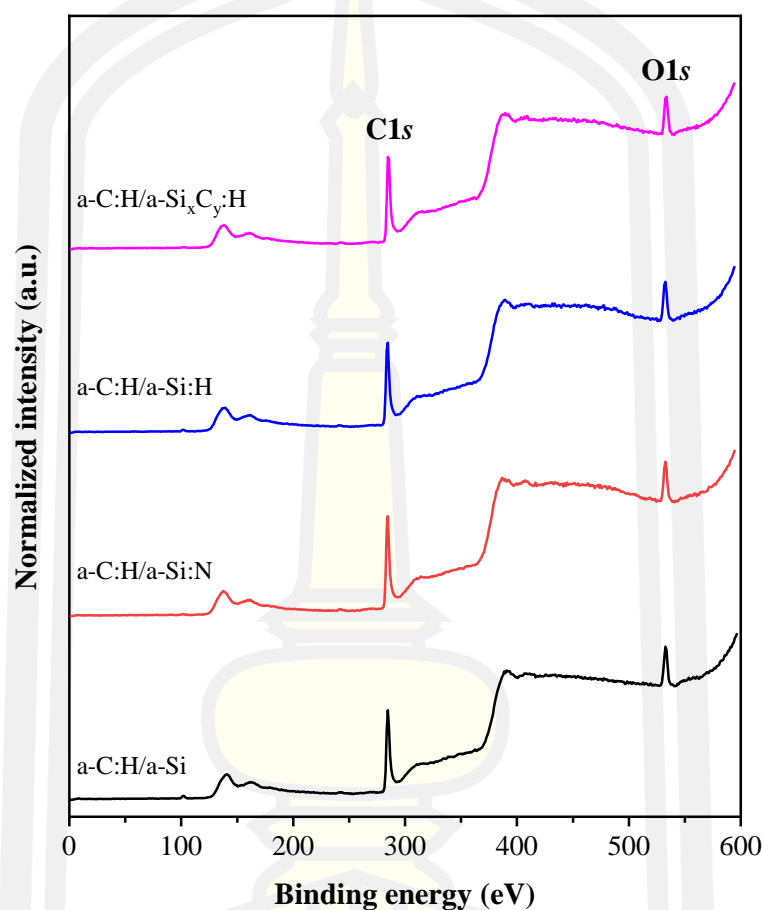
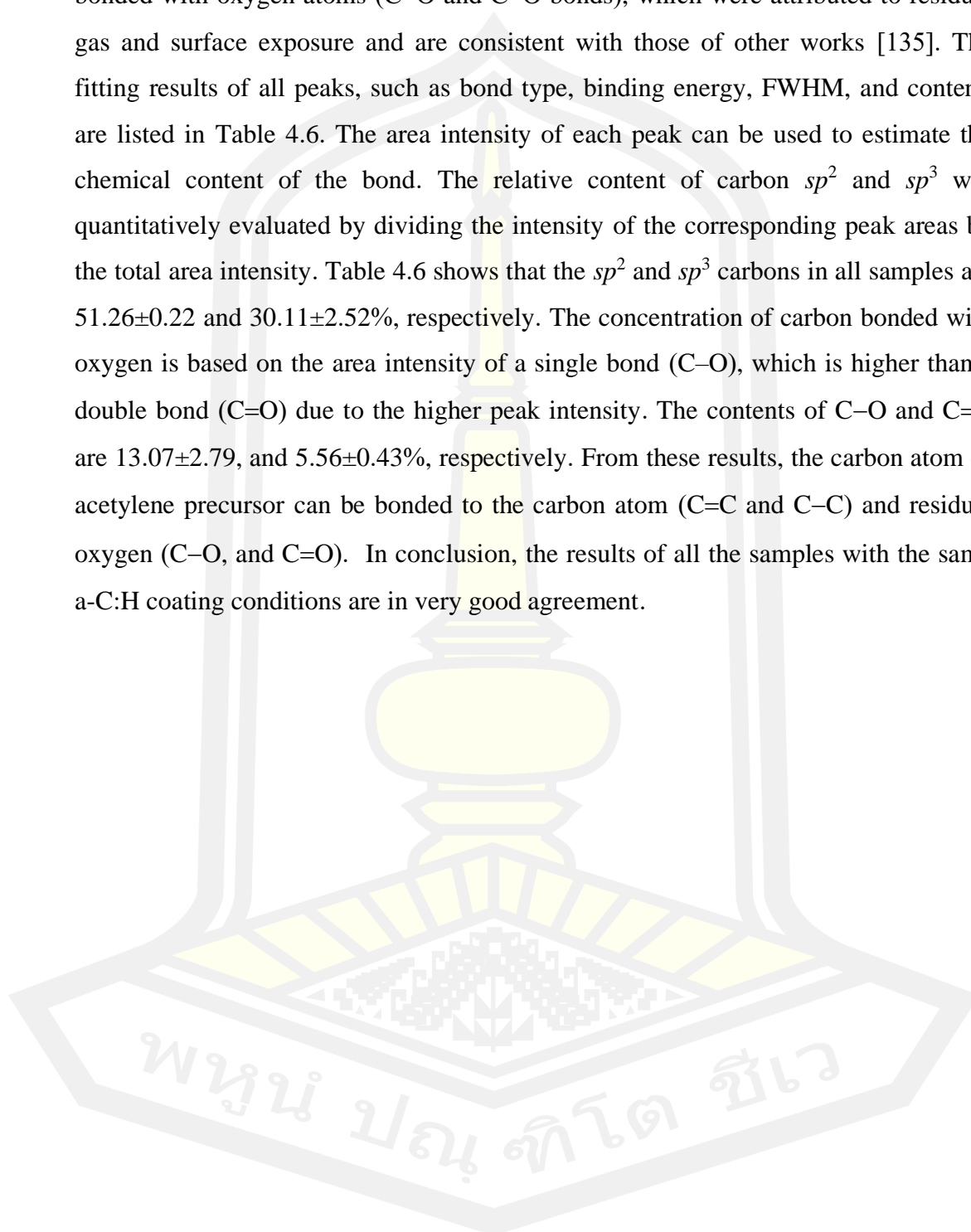


Figure 4.22 Typical XPS spectra of a wide scan for a-C:H films with a-Si, a-Si:N, a-Si:H, and a-Si_xC_y:H interlayers.

In addition, the high-resolution C1s main peak of all samples was deconvoluted into four Gaussian functions using Origin software. Backgrounds were subtracted using the Shirley method. The deconvoluted XPS spectra for C1s of all samples are shown in Figure 4.23. It can be seen that the C1s spectrum was decomposed into four peaks located at different binding energies. The first peak at about 284.1 eV and the second peak at about 285.1 eV were defined as C=C binding of sp^2 hybridization and C–C and C–H binding of sp^3 hybridization, respectively

[135]. The higher binding energies at about 286.4 and 288.4 eV represent carbon bonded with oxygen atoms (C–O and C=O bonds), which were attributed to residual gas and surface exposure and are consistent with those of other works [135]. The fitting results of all peaks, such as bond type, binding energy, FWHM, and content, are listed in Table 4.6. The area intensity of each peak can be used to estimate the chemical content of the bond. The relative content of carbon sp^2 and sp^3 was quantitatively evaluated by dividing the intensity of the corresponding peak areas by the total area intensity. Table 4.6 shows that the sp^2 and sp^3 carbons in all samples are 51.26 ± 0.22 and $30.11\pm 2.52\%$, respectively. The concentration of carbon bonded with oxygen is based on the area intensity of a single bond (C–O), which is higher than a double bond (C=O) due to the higher peak intensity. The contents of C–O and C=O are 13.07 ± 2.79 , and $5.56\pm 0.43\%$, respectively. From these results, the carbon atom of acetylene precursor can be bonded to the carbon atom (C=C and C–C) and residual oxygen (C–O, and C=O). In conclusion, the results of all the samples with the same a-C:H coating conditions are in very good agreement.



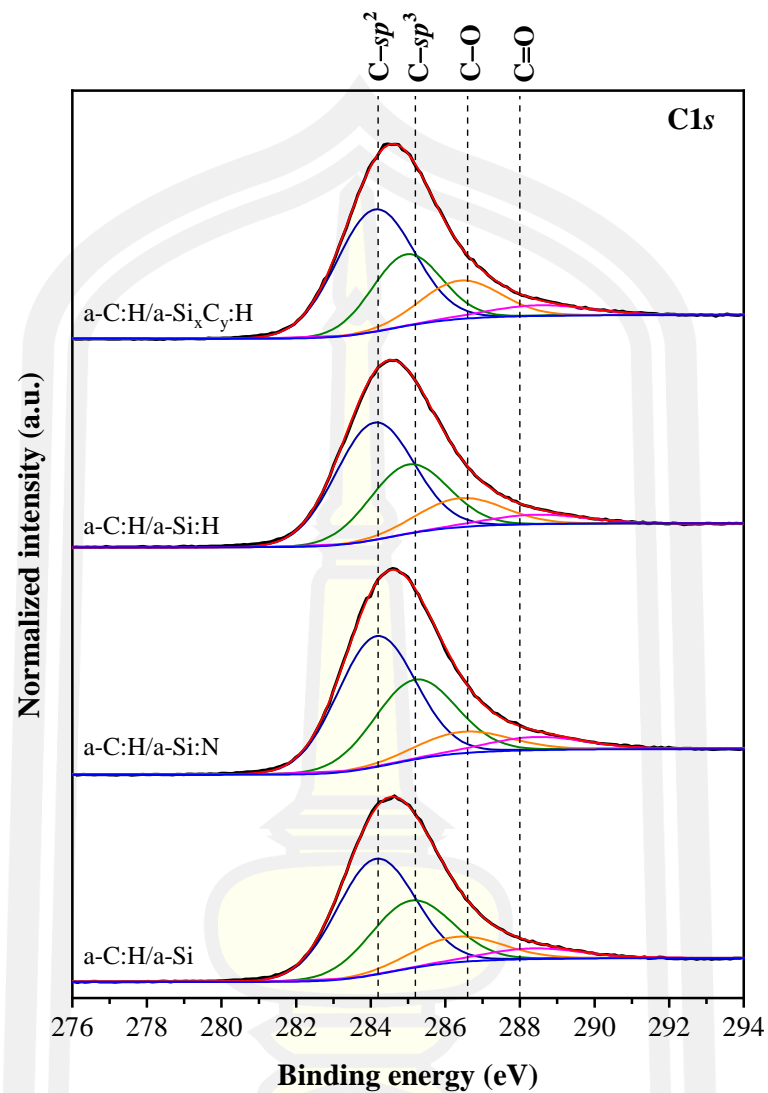


Figure 4.23 Deconvoluted XPS spectra for C1s of a-C:H films with a-Si, a-Si:N, a-Si:H, and a-Si_xC_y:H interlayers. The black, red, blue, and other solid lines represent the experimental data, the fitted curve, the Shirley background, and the deconvolution of the individual peaks, respectively.

Table 4.6 The fitted results of bonding type, binding energy, FWHM, and content deconvoluted from the C1s XPS spectra of a-C:H films with different silicon-based interlayers deposited on a silicon substrate.

Samples	Bonding	Chemical information		
		Binding energy (eV)	FWHM (eV)	Content (%)
a-C:H/a-Si	C- sp^2	284.1	2.47	51.08
	C- sp^3	285.1	2.55	30.81
	C-O	286.3	2.80	12.61
	C=O	288.3	2.97	5.50
a-C:H/a-Si:N	C- sp^2	284.1	2.44	51.54
	C- sp^3	285.2	2.55	32.78
	C-O	286.5	2.84	9.59
	C=O	288.4	3.00	6.10
a-C:H/a-Si:H	C- sp^2	284.1	2.45	51.08
	C- sp^3	285.0	2.45	30.11
	C-O	286.4	2.68	13.76
	C=O	288.4	3.03	5.04
a-C:H/a-Si _x C _y :H	C- sp^2	284.1	2.45	51.35
	C- sp^3	285.0	2.18	26.73
	C-O	286.4	2.48	16.31
	C=O	288.5	3.14	5.62

4.3.3 Mechanical properties

For the protective layer on the chromium-plated substrate, the hardness of the a-C:H films is one of the most important factors for tribological application. The mechanical properties of a-C:H films with a-Si, a-Si:N, a-Si:H and a-Si_xC_y:H interlayers with an average total thickness of nm were analysed by nanoindentation test and determined by the method of Oliver and Pharr [117]. In this work, the hardness of the film coating and the chromium-plated substrate was evaluated using nanoindentation (Fischer Scope, model HM2000). The pyramid-shaped Berkovich indenter was used with a maximum load of 3 mN and a 3-fold repeatability for the dynamic mode to keep the indentation depth below 10% of the total film thickness. A loading range of 2–60 mN for the enhanced stiffness procedure (ESP) was used to investigate the effect of indentation depth on hardness.

The loading and unloading curves of the a-C:H film with different silicon-based interlayers in dynamic mode are shown in Figure 4.24 (a), while the hardness in dynamic mode is shown in Figure 4.24 (b). The values of hardness, elastic modulus and penetration depth of the coated film and substrate are shown in Table 4.7. The results show that the a-C:H/a-Si:H samples have the lowest penetration depth of about 84 ± 10.04 nm, as shown in the blue line, and it is 13.48% of the average total film thickness (623 ± 13.61 nm). At the same load of 3 mN, the lowest penetration depth of the a-C:H/a-Si:H sample corresponds to a high hardness of about 20.98 ± 0.63 GPa, which is much higher than the other samples and the chromium-plated substrate. Moreover, with penetration depth of about 103 ± 6.19 nm (16.53% of the average total film thickness), the a-C:H/a-Si sample shows a slightly higher hardness of 10.92 ± 0.42 GPa than the chromium-plated substrate. In addition, a-C:H/a-Si:H and a-C:H/a-Si samples exhibit higher elastic modulus than a-C:H/a-Si:N and a-C:H/a-Si_xC_y:H samples. These results indicate that a-Si and a-Si:H interlayers are good supports for the formation of the a-C:H film on the chromium-plated substrate. While a-C:H/a-Si:N and a-C:H/a-Si_xC_y:H show higher penetration depth with lower hardness of about 9.39 ± 0.09 and 8.55 ± 0.14 GPa, respectively.

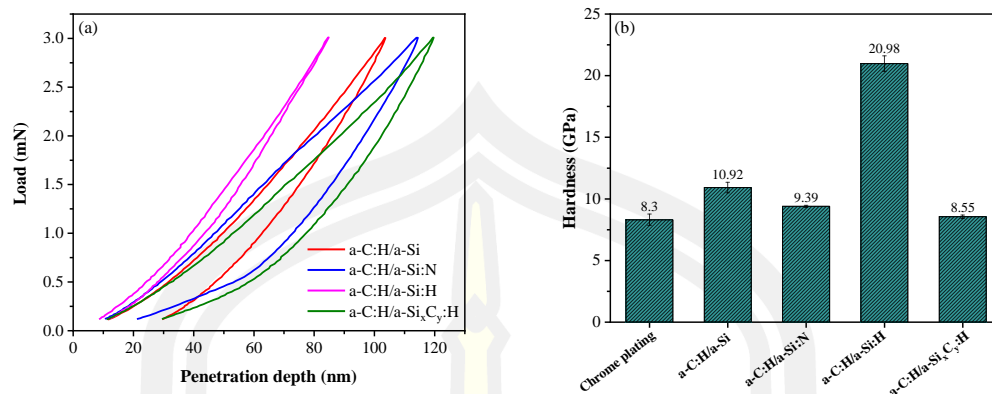


Figure 4.24 (a) Loading and unloading curves and (b) hardness of the a-C:H film with different silicon-based interlayers in dynamic mode.

Table 4.7 Hardness, elastic modulus, and penetration depth of a chromium-plated substrate and a-C:H film with a-Si, a-Si:N, a-Si:H and a-Si_xC_y:H interlayers.

Samples	Hardness (GPa)	Elastic modulus (GPa)	Penetration depth (nm)
Chromium-plated substrate	8.30±0.46	232.35±8.41	20.26±0.29
a-C:H/a-Si	10.92±0.42	79.98±7.67	103.44±6.19
a-C:H/a-Si:N	9.39±0.09	69.22±4.52	113.94±2.94
a-C:H/a-Si:H	20.98±0.63	104.23±8.72	84.65±10.04
a-C:H/a-Si _x C _y :H	8.55±0.14	66.44±1.20	119.41±2.26

In the ESP mode, the maximum load was increased from 2 to 60 mN, which was divided into 30 cycles of loading and subsequent unloading to a total film thickness of about 500-600 nm for coated samples and 38 cycles for a chromium-plated substrate. The repeatable loading and unloading curves of the film-coated samples and the chromium-plated substrate in the ESP measurement are shown in Figure 4.25. The results show the same trend as in the dynamic mode, that the curve of the a-C:H/a-Si:H and a-C:H/a-Si specimens show a lower penetration depth than

that of the other specimens and the substrate. Figure 4.25 (b) shows the hardness depth profile in ESP mode of the a-C:H film with different silicon-based interlayers compared to an uncoated chromium-plated substrate. It was found that the hardness decreases with increasing penetration depth (increasing load) and is close to the hardness value of the chromium-plated substrate. This behaviour is consistent with the Bückle's rule, which recommends that the penetration depth should not exceed 10% of the coating thickness to reduce the influence of the substrate [136]. It can be seen that when the penetration depth is less than 60 nm (10% of the total film thickness), the hardness depth profile is close to the dynamic mode. The random network of a-Si, a-Si:H and a-SiC in a-Si_xC_y:H and the nitrogen in the a-Si:N interlayers could deteriorate the bonding between C and Si and affect the structural and mechanical properties. Therefore, it can be concluded that the a-C:H coating with the a-Si and a-Si:H interlayers can improve the hardness of the chromium-plated substrate (8.48 ± 1.41 GPa), resulting in a longer application lifetime.

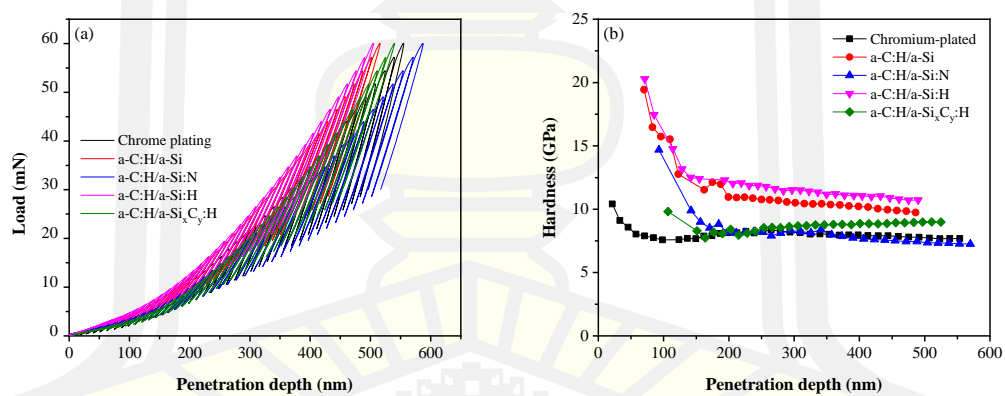


Figure 4.25 (a) Loading and unloading curves and (b) hardness depth profile of the a-C:H film with different silicon-based interlayers in ESP mode.

4.3.4 Adhesion strength analysis

Adhesion strength is a very important parameter for the properties of a-C:H films. The micro-scratch measurements can directly reveal the adhesive behaviour in terms of the value of critical load (L_c). For the a-C:H films with four silicon-based interlayers deposited on chromium-plated substrates, the adhesive properties were evaluated in terms of critical load using micro-scratch test (Fischer Scope, model HM2000) with 3 repetitions at different positions. According to the vertical load, the scratch test was performed in a progressive mode, continuously increasing from 0.5 to 50 N. To achieve the scratching behaviour, a scratching speed of 2 mm/min and a loading rate of 10 N/min were used. After the scratch test, the scratch behaviour was observed with the optical microscope to identify three types of critical loads as shown in Figure 4.26: The first critical load (L_{c1}) corresponds to the first signal of cohesive failure of a-C:H film in the form of spalling and cracking in the scratch track. The second critical load (L_{c2}) corresponds to the beginning of the adhesive failure of the delamination between the a-C:H layer and interlayer. Finally, the third critical load (L_{c3}) corresponds to the complete delamination of the coating from the scratch track and the complete removal of the interlayer from the substrate.

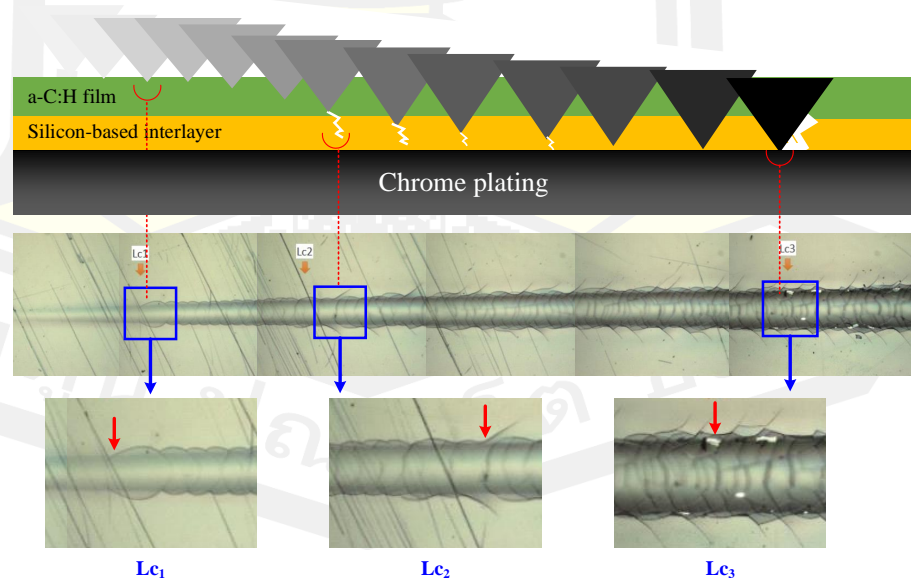


Figure 4.26 Principle of scratch testing with critical load (L_{c1} , L_{c2} and L_{c3}).

The deposited a-C:H film (~300 nm thick) on a chromium-plated substrate without an interlayer delaminates from the substrate after deposition, indicating very poor adhesion. This behaviour can be explained by the high residual stress of the films and the incompatibility at the interfacial adhesion between film and substrate [137]. The scratch behaviour with values of Lc_1 , Lc_2 and Lc_3 of a-C:H films with four different interlayers was determined and is shown in Figure 4.27. In general, the scratch behaviour includes three stages: the first stage is microcracking and partial ring cracking, the second stage is complete ring cracking, delamination, and spalling, and the last stage is substrate exposure [138]. Figure 4.27 (b) and (d) show that the a-C:H films with a-Si:N and a-Si_xC_y:H interlayers delaminate and spall from the substrate and that the films are obviously fractured at the edge of the scratch track, indicating a cohesive failure mode. Figure 4.27 (a) and (c) show higher critical load of the a-C:H films with a-Si and a-Si:H interlayers, indicating good adhesion between films and substrate. The a-C:H films with a-Si_xC_y:H interlayer have lower Lc_1 , Lc_2 and Lc_3 values than the other samples, as shown in Figure 4.28. This behaviour could be due to the strong bonding of Si–C, which can reduce the dangling bond at the interface, while the C1s peak in the XPS results indicates excessive carbon doping in the silicon network, leading to high internal stresses in the interlayer. The lowest value for the adhesion of the a-Si_xC_y:H interlayer coincides with the lowest hardness of the a-C:H/a-Si_xC_y:H sample. The adhesion strength of a-C:H films with a-Si:H interlayer is about 2.47 ± 0.09 , 5.67 ± 0.28 and 15.15 ± 1.16 N at Lc_1 , Lc_2 and Lc_3 , respectively, indicating the plastic deformation in the conformal cracking phase of a-C:H film, the adhesion strength between the a-C:H film and the a-Si:H interlayer and good adhesion strength between the a-C:H interlayer and the substrate. In the case of a-Si:H interlayer, during the deposition process, the residual oxygen in the silicon networks reduce (reducing the Si–O bonds) by the interaction between hydrogen and oxygen atoms. Moreover, the hydrogen atoms can remove the Cr–O bonds from the surface of the chromium plating. Therefore, the bonding of Cr–Si between the interface of chrome plating and a-Si:H interlayer, and Si–C between the interface of a-Si:H interlayer and a-C:H layer increase, which could promote the highest Lc_3 value. This behaviour could improve the resistance to adhesive failure (higher Lc_2

value) between the a-C:H layer and the a-Si:H interlayer with a strong bonding at the interface with respect to the a-Si interlayer. As for the Lc_1 value, the good adhesive strength (Lc_2) of the a-C:H/a-Si:H sample should promote the formation of the a-C:H film, which has a higher Lc_1 value than the a-C:H with a-Si interlayer, that indicating the plastic deformation in the conformal cracking phase.

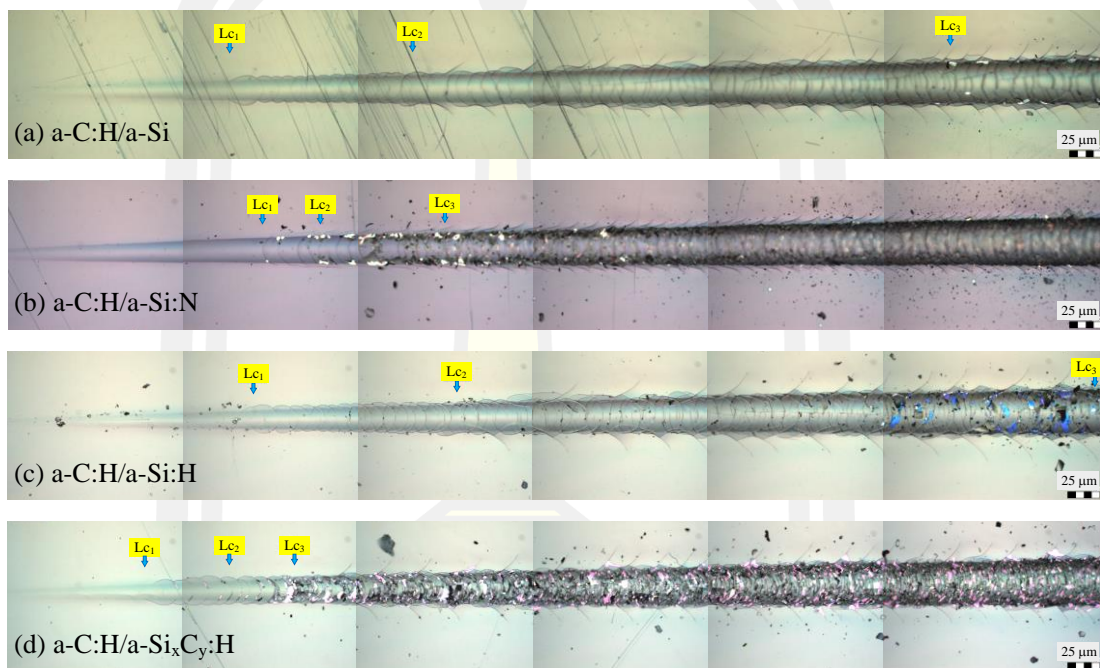


Figure 4.27 Morphology of scratch marks with Lc_1 , Lc_2 , and Lc_3 for a-C:H films with (a) a-Si, (b) a-Si:N, (c) a-Si:H, and (d) a-Si_xC_y:H interlayers deposited on a chromium-plated substrate.

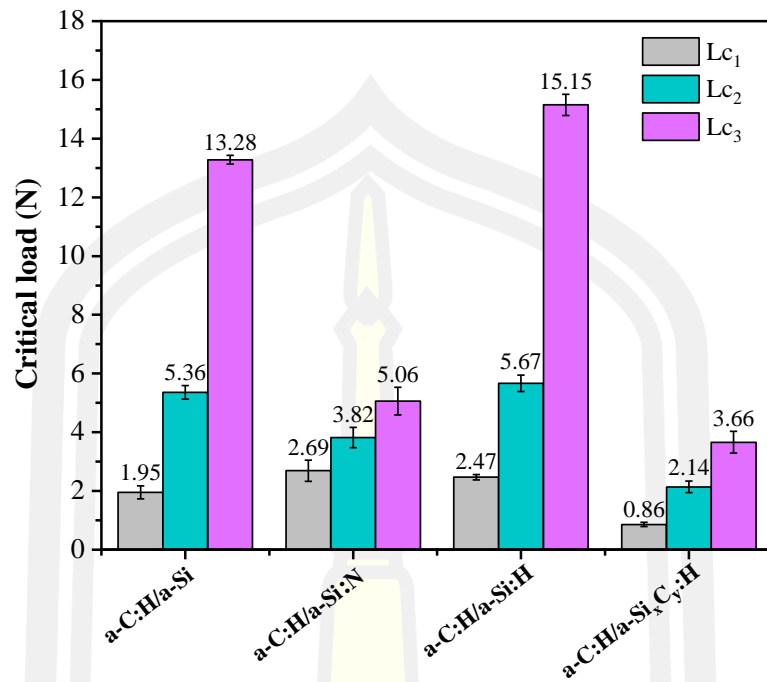


Figure 4.28 Critical load values of Lc₁, Lc₂ and Lc₃ for a-C:H films with a-Si, a-Si:N, a-Si:H, and a-Si_xC_y:H interlayers deposited on a chromium-plated substrate.

Table 4.8 Critical load values (Lc₁, Lc₂, and Lc₃) for a-C:H films with a-Si, a-Si:N, a-Si:H, and a-Si_xC_y:H interlayers.

Samples	Lc ₁ (N)	Lc ₂ (N)	Lc ₃ (N)
a-C:H/a-Si	1.95±0.22	5.36±0.23	13.28±0.15
a-C:H/a-Si:N	2.69±0.36	3.82±0.35	5.06±0.47
a-C:H/a-Si:H	2.47±0.09	5.67±0.28	15.15±1.16
a-C:H/a-Si _x C _y :H	0.86±0.07	2.14±0.2	3.66±0.37

4.3.5 Electrochemical corrosion analysis

The corrosion behaviour of the thin films deposited on the chromium-plated substrate was measured electrochemically to confirm the corrosion resistance of the a-C:H coating. The electrochemical corrosion measurement was carried out using the 3.5 wt% NaCl solution at room temperature. The samples were exposed to 3.5 wt% NaCl solution for 30 minutes. Polarization curves were obtained with an applied potential of -1000 to 1000 mV and a sampling rate of 1 mV/s. Electrochemical corrosion measurement is an efficient method with simple procedures and high sensitivity that reflects the lifetime and corrosion behaviour of bulk materials and thin films [139], [140]. The corrosion behaviour of the a-C:H coatings with different silicon-based interlayers compared to the bare chromium-plated substrate is shown in Figure 4.29 (a). The x-axis and y-axis intersections between the anodic and cathodic branches of the polarization curves were considered as the corrosion current density (i_{corr}) and corrosion potential (E_{corr}) [141], [142]. Lower corrosion current density and higher corrosion potential indicate lower corrosion rate and better corrosive properties [142], [143]. From Figure 4.29 (a), it can be seen that all a-C:H films with different silicon-based interlayers show a shift in corrosion potential to a more positive value compared to the uncoated substrate, indicating better corrosion resistance of the a-C:H film [144]. The coating layers require a higher applied potential for dissolution or corrosion than the substrate. The corrosion current density is $0.71 \mu\text{A}/\text{cm}^2$ for an uncoated substrate, which is higher than the coated samples. The a-C:H/a-Si:H sample has the lowest corrosion current density ($0.02 \mu\text{A}/\text{cm}^2$), indicating the lowest metal loss from the material and coating. Therefore, the lowest corrosion current density means the best corrosion resistance [143]. This result could be correlated with the hardness and adhesion strength of the a-C:H/a-Si:H coatings. Moreover, porous defects or pinholes in the films are one of the most important factors that can be associated with the corrosion behaviour. Porosity (P) was determined based on polarization resistance (R_p) using equation (1) [145],

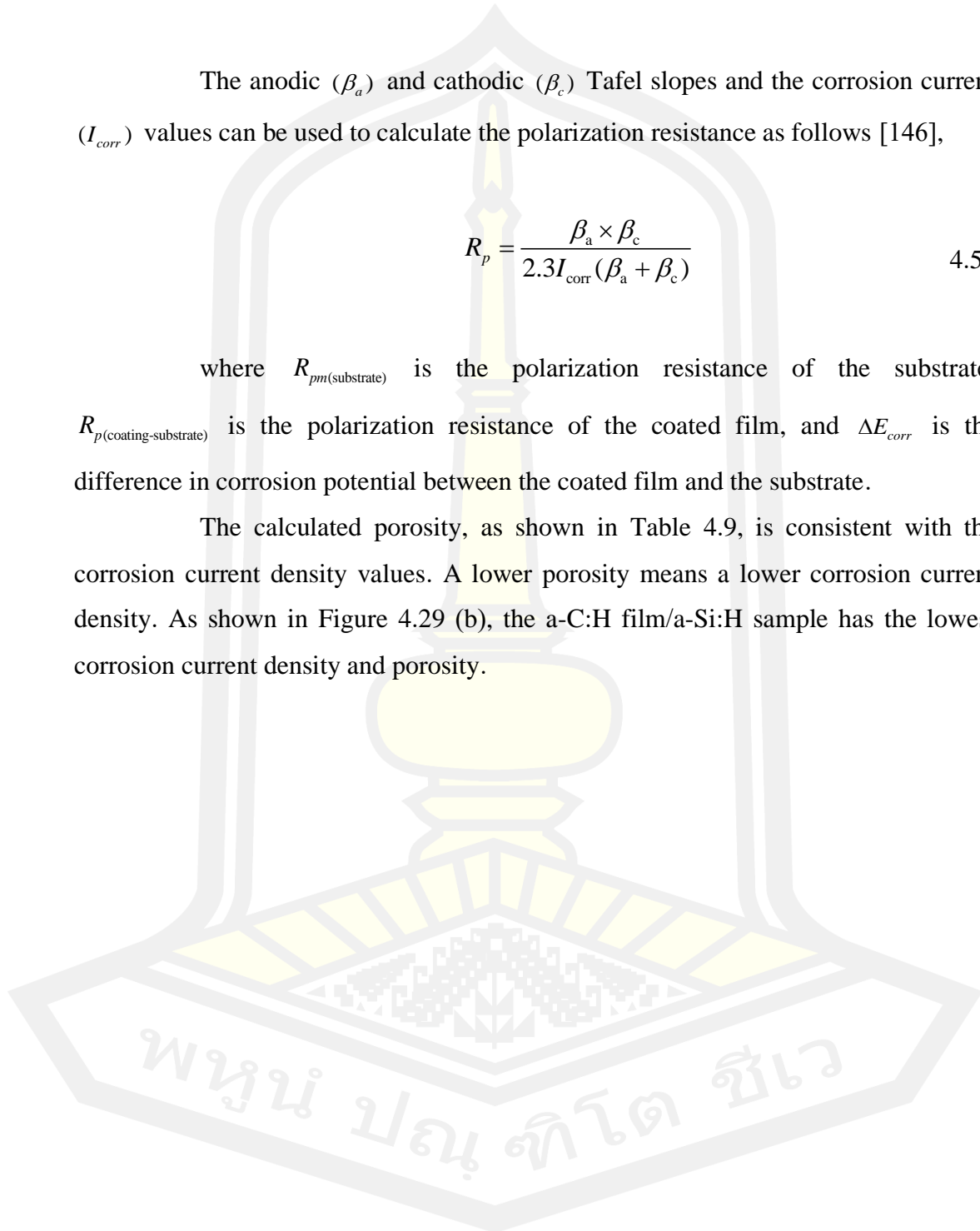
$$P = \frac{R_{pm(\text{substrate})}}{R_{p(\text{coating-substrate})}} \times 10^{-|\Delta E_{\text{corr}}/\beta_a|} \quad 4.4$$

The anodic (β_a) and cathodic (β_c) Tafel slopes and the corrosion current (I_{corr}) values can be used to calculate the polarization resistance as follows [146],

$$R_p = \frac{\beta_a \times \beta_c}{2.3 I_{\text{corr}} (\beta_a + \beta_c)} \quad 4.5$$

where $R_{pm(\text{substrate})}$ is the polarization resistance of the substrate, $R_{p(\text{coating-substrate})}$ is the polarization resistance of the coated film, and ΔE_{corr} is the difference in corrosion potential between the coated film and the substrate.

The calculated porosity, as shown in Table 4.9, is consistent with the corrosion current density values. A lower porosity means a lower corrosion current density. As shown in Figure 4.29 (b), the a-C:H film/a-Si:H sample has the lowest corrosion current density and porosity.



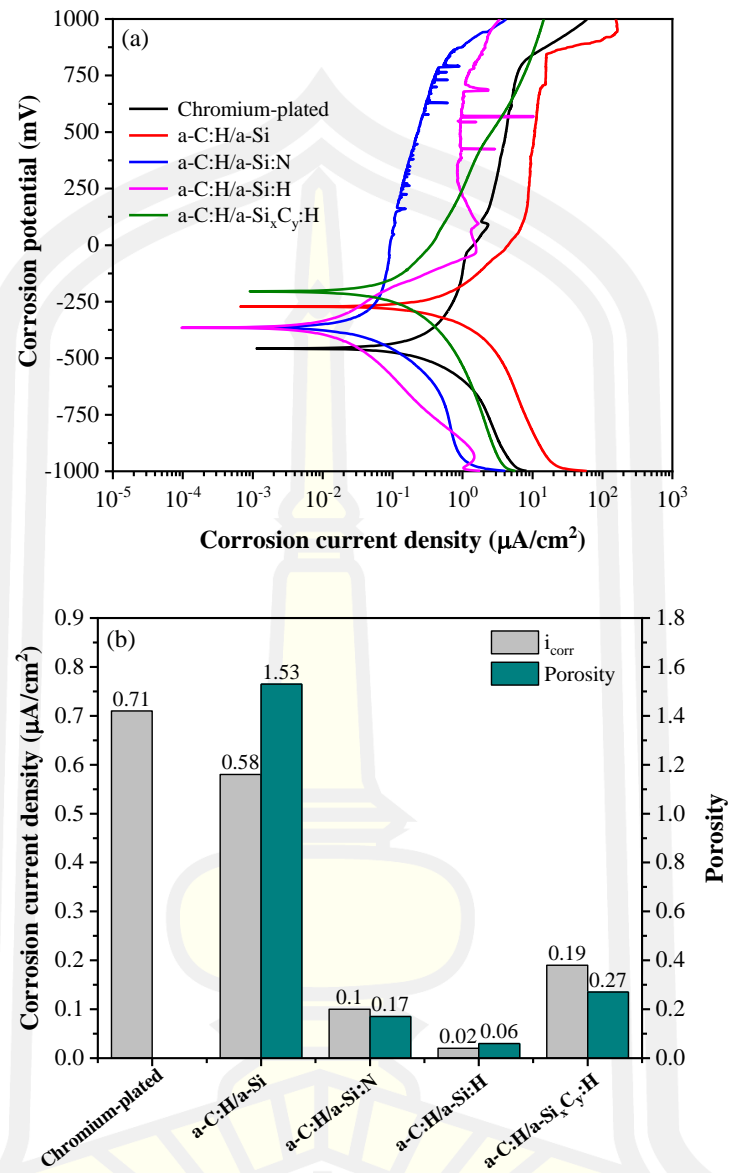
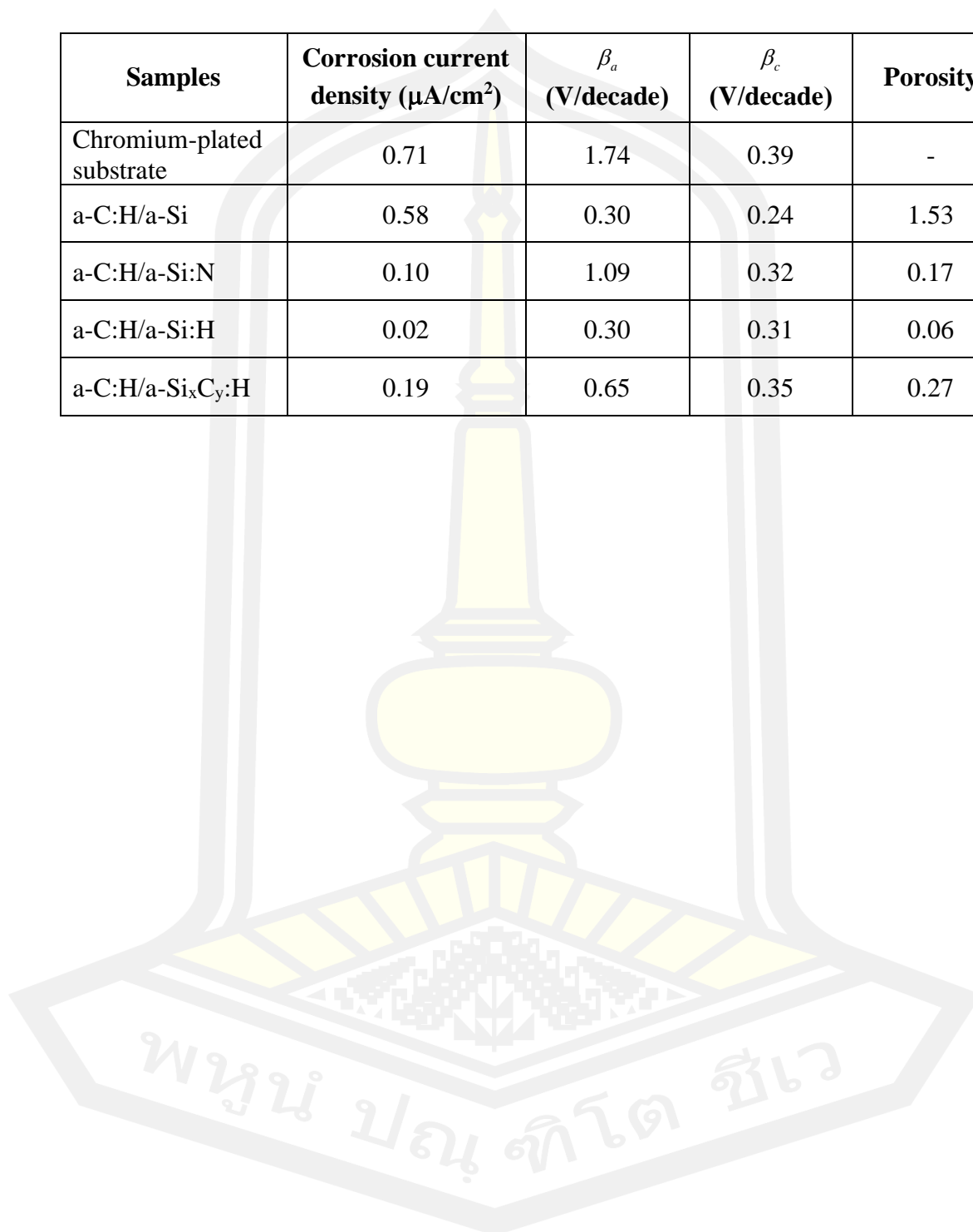


Figure 4.29 (a) Potentiodynamic polarization curves and (b) corrosion current density (orange bar) and porosity (green bar) of the a-C:H films with different silicon-based interlayers and uncoated chromium-plated substrate in 3.5 wt% NaCl solution.

Table 4.9 Electrochemical results from polarization curves for uncoated and coated substrates.

Samples	Corrosion current density ($\mu\text{A}/\text{cm}^2$)	β_a (V/decade)	β_c (V/decade)	Porosity
Chromium-plated substrate	0.71	1.74	0.39	-
a-C:H/a-Si	0.58	0.30	0.24	1.53
a-C:H/a-Si:N	0.10	1.09	0.32	0.17
a-C:H/a-Si:H	0.02	0.30	0.31	0.06
a-C:H/a-Si _x Cy:H	0.19	0.65	0.35	0.27



4.4 Conclusion of chrome plating

In this part, a-C:H films were prepared using a-Si, a-Si:N, a-Si:H, and a-Si_xC_y:H as interlayers to improve adhesion. The chromium-plated material was used as substrate for the surface properties improvement. All interlayers were deposited by the DC magnetron sputtering method, while the a-C:H films were deposited by the radio-frequency plasma-enhanced chemical vapor deposition method. For the deposition of the interlayers, the argon was used as the sputtering gas for a-Si deposition, while argon mixed with nitrogen, hydrogen, and acetylene was used as the reactive gas for a-Si:N, a-Si:H, and a-Si_xC_y:H deposition, respectively. For the deposition of a-C:H films, hydrocarbon gas from acetylene mixed with argon and hydrogen was used as precursor gas. The characterization of the interlayers and a-C:H films was systematically investigated.

The deposition rate of all interlayers (a-Si, a-Si:N, a-Si:H, and a-Si_xC_y:H) on silicon substrate was investigated using FESEM images to control the same film thickness. It was found that the different silicon-based interlayers have different deposition rate depending on the gas source. The XPS results show that all the interlayers on the silicon substrate with a thickness of about 50 nm contain the silicon (Si2*p* and Si2*s*) originated from the silicon target, which serves as the main precursor material for the silicon-based interlayer deposition. In addition, silicon dioxide and suboxides (Si2*p*, Si₂O, SiO, Si₂O₃, and SiO₂) were also found in the XPS spectra, mainly due to the residual gas in the vacuum chamber during the deposition process and the surface oxidation and adsorption process during the measurement. In the a-Si:N interlayer, the nitrogen dopant atoms are located between the silicon network, while the carbon dopant can be bonded to the silicon core atoms to form a Si-C bond for the a-Si_xC_y:H deposition. The XRR technique was used to investigate the physical properties of all the interlayers on a silicon substrate with a thickness of about 50 nm in terms of film density. It was found that the density of the silicon-based interlayers was in the range of 1.68–2.05 g/cm³, lower than the calculated density (2.285 g/cm³). This was attributed to the void volume of atoms forming a continuous random network during film growth and the effect of doping. However, the low hardness from the nanoindentation measurement of all the interlayers on the chromium-plated

substrate with a thickness of about 300 nm shows that the a-C:H film is very important for improving the mechanical properties of the chromium-plated substrate.

In a-C:H deposition, the deposition rate of the a-C:H film prepared with RF-PECVD is 20.87 ± 0.28 nm/min. The density of the a-C:H film on a silicon substrate with a thickness of about 45 nm was about 2.15 g/cm^3 , which is in the range reported in other works. For the structural properties of the a-C:H layer, Raman spectroscopy was used to determine the scattering of sp^2 hybridization in the amorphous carbon structure of the a-C:H film deposited on the silicon substrate. The positions of the D and G peaks in a-C:H films were found at $1,416$ and $1,567 \text{ cm}^{-1}$ of Raman shift with a relative intensity I_D/I_G of about 1.28. These peaks are associated with the vibration of A_{1g} symmetry breathing mode of sp^2 atoms only in the aromatic rings for disorder of graphite (D peak) and with the vibration of E_{2g} stretching mode of sp^2 atoms in both aromatic rings and chains for graphite (G peak). In addition, the X peak was found at about $1,232 \text{ cm}^{-1}$, which probably originates from the vibrations of a pentagonal atomic ring in the carbon nanostructures.

In the last section, a-C:H films deposited with four interlayers on both chromium-plated and silicon substrates were characterized in terms of morphology, structure, mechanical, adhesive properties, and corrosion resistance using FESEM, Raman spectroscopy, XPS, nanoindentation, micro-scratch, and electrochemical measurements. First, it was found that the a-C:H film with a thickness of about 300 nm deposited on a chromium-plated substrate without interlayer detaches from the substrate, while the a-C:H films deposited with interlayer show good adhesion to the substrates without cracking and detachment. The average total thickness of a-C:H with interlayers is about 623 ± 13.61 nm. The surface morphology shows very homogeneous, smooth, and dense microstructures without microparticle defects. The cross-sectional images between the a-C:H films and the interlayers show a clear boundary at the interface without delamination and cracking. For the a-Si and a-Si:H interlayers, it can be seen that the interlayers have similar grain size. It seems that these layers merge together with the a-C:H layer at the interface and have good adhesion, which can be confirmed by the critical load of the micro-scratch test. The Raman spectra of the a-C:H films on both silicon and the chromium-plated substrate clearly show the presence of D and G peaks with a relative intensity I_D/I_G of about

1.26, indicating the structure of the amorphous carbon films. It can be concluded that the a-C:H film prepared in this work is dominated by the scattering of the sp^2 site due to an excitation resonance with π states attributed to the amorphous carbon thin films. The XPS results show that the bonding of C- sp^2 and C- sp^3 hybridizations with the carbon content of all samples is about 51.26 ± 0.22 and $30.11\pm 2.52\%$, respectively. Moreover, C-O and C=O bonds are also found in the a-C:H structure, which originate from the residual oxygen and surface oxidation. Raman spectroscopy and XPS analysis show a similar result and confirm that the a-C:H films were deposited under the same conditions. The a-C:H/a-Si:H sample exhibits the highest hardness of about 20.98 ± 0.63 GPa with the lowest penetration depth, which is significantly higher than that of the other samples and the uncoated chromium-plated substrate (8.48 GPa). In addition, the a-C:H with a-Si:H interlayers exhibited higher Lc_1 , Lc_2 and Lc_3 values ($1.47\pm 5.67\pm 0.28$ and 15.15 ± 1.16 N) than the a-C:H/a-Si:N and a-C:H/a-Si_xC_y:H samples, indicating higher resistance to adhesive fracture between the a-C:H and the interlayer, and indicating the good adhesion strength of the interlayer with a chromium-plated substrate, which should promote the good corrosion resistance and high hardness of the film. This result indicates that a-Si and a-Si:H are good supporting interlayer for the formation of a-C:H film. On the other hand, the a-C:H films with a-Si:N and a-Si_xC_y interlayers with low critical load show delamination and detachment from the substrate and are obviously broken at the edge of the scratch track, indicating a cohesive failure mode. This behaviour could be due to the strong bonding of Si-C in the a-Si_xC_y:H interlayer, and the nitrogen in the silicon network of the a-Si:N interlayer could deteriorate the bonding between C and Si at the interface. The a-C:H films with a-Si:H interlayer exhibit the lowest corrosion current density with the lowest porosity, which is about 36 times lower than that of the uncoated chromium-plated substrate. The mixing with hydrogen gas could reduce the residual oxygen, which could reduce the Si-O bonding and improve the adhesion between the interlayer and the a-C:H film. Therefore, it can be concluded that the protective a-C:H coating with an a-Si:H interlayer has excellent potential to significantly improve the durability and extend the service life of materials used in abrasive and corrosive environments. In the a-Si_xC_y:H interlayer, the carbon dopant can be bonded to the

silicon atoms to form Si–C, which negatively affects the adhesive properties. This behaviour is probably due to the low dangling bond and high residual stress of the interlayer. Therefore, based on the adhesion strength, hardness, and corrosive properties, the a-C:H film with the a-Si:H interlayer can be very useful to meet the multifunctional applications of the chromium-plated products.



CHAPTER V

Results and discussion (Part : NAB)

Chapter V deals with the results and discussion of a-C:H multilayers deposited on both nickel-aluminum bronze and silicon substrates. In this chapter, the term “DLC” was used to represent the “a-C:H” in its general form. Multilayer DLC films were deposited using amorphous silicon (a-Si) film as the interlayer, DLC film as the hard layer, and silicon doped DLC film (Si-doped DLC) as the soft layer. The alloyed NAB was used as the main substrate for the study. Chapter V is divided into two sections. In the first part, the deposition rate and structural properties of the silicon interlayer, DLC and Si-doped DLC were investigated. In this part, the film thickness was determined using the FESEM technique to estimate the deposition rate, while the structural properties in terms of film density, chemical bonding, and microstructural features were analysed using XRR, XPS, and Raman spectroscopy techniques. In the second section, the surface and cross-sectional morphology, structural properties, mechanical properties, adhesion strength, and electrochemical corrosion resistance of the DLC multilayer films were fully investigated. The influence of the deposition period (stack) of the multilayer was investigated.

5.1 Coating layer characterizations

In this part, the a-Si film was used as an interlayer for DLC multilayer deposition. The a-Si interlayer was deposited using the DCMS method. The pure DLC film was deposited by the RF-PECVD method using acetylene gas mixed with argon and hydrogen, while the Si-doped DLC film was deposited by the hybrid DCMS and RF-PECVD method. The a-Si interlayer, DLC film and Si-doped DLC film were deposited with the same controlled deposition time of 20 minutes. The model of these films on a silicon substrate is shown in Figure 5.1. In the first study, the deposition rate of the a-Si interlayer, the DLC film, and the Si-doped DLC film were determined using FESEM techniques to control the film thickness. Then, the structural properties of the a-Si interlayer, DLC film and Si-doped DLC film with a controlled thickness

of about 50 nm were investigated using XRR, XPS, and Raman spectroscopy techniques.



Figure 5.1 The schematic model of the a-Si interlayer, the DLC film and the Si-doped DLC film on silicon substrate (not to scale).

5.1.1 Morphology, thickness and deposition rate of the coating layers

The surface and cross-sectional images of the a-Si interlayer, DLC film and Si-doped DLC film were performed using FESEM (HITACHI, model SU8030) to observe their morphological properties. The FESEM images were acquired at a magnification of 50 kx in secondary electron mode with an accelerating voltage of 10 kV for the surface morphologies and 5 kV for the cross-sectional microstructures. Figure 5.2 shows the surface morphologies (left figure) and the corresponding cross-sectional images (right figure) of (a), (b) a-Si interlayer; (c), (d) DLC film; and (e), (f) Si-doped DLC film deposited on silicon substrate. For the a-Si interlayer, the surface morphology is smooth and compact, with small grains, while the DLC and Si-doped DLC films have smooth and dense surface microstructures with homogeneous structures, like the general amorphous carbon film. The fractional FESEM cross-sectional images of the a-Si interlayer, the DLC film and the Si-doped DLC film are shown on the left in Figure 5.2. It can be seen that the a-Si film in Figure 5.2 (b) shows columnar growth with the substrate. The DLC and Si-doped DLC films exhibit smooth and dense microstructures as surface morphology. On the cross-sectional images, the thickness of all films was measured with two FESEM cross-sectional images using Image J program. Twenty measurements with different positions were used to determine the average thickness. Then, the static deposition rate in nm/min was calculated using Equation 4.1. The average thickness and deposition rate of the a-Si interlayer, DLC film, and Si-doped DLC film are summarized in Table 5.1. The

thickness of the a-Si interlayer, DLC film and Si-doped DLC film was measured to be about 252.67 ± 6.88 , 279.04 ± 3.11 and 463.07 ± 4.03 nm, corresponding to a deposition rate of 12.63 ± 0.34 , 13.95 ± 0.16 and 23.15 ± 0.20 nm/min, respectively. It was found that Si-doped DLC films have higher deposition rate than pure DLC films. This result is likely due to the drive by the magnetron discharge, which can provide an efficient additional source of precursor dissociation [147]. Moreover, the dopant of silicon atoms from the silicon target is also incorporated into the growing film. Therefore, the value of deposition rate for the a-Si interlayer, DLC film, and Si-doped DLC film was used to adjust the deposition time to control the film thickness.

Table 5.1 Film thickness and deposition rate of all silicon-based interlayers.

Samples	Film thickness (nm)	Deposition rate (nm/min)
a-Si	252.67 ± 6.88	12.63 ± 0.34
DLC	279.04 ± 3.11	13.95 ± 0.16
Si-doped DLC	463.07 ± 4.03	23.15 ± 0.20

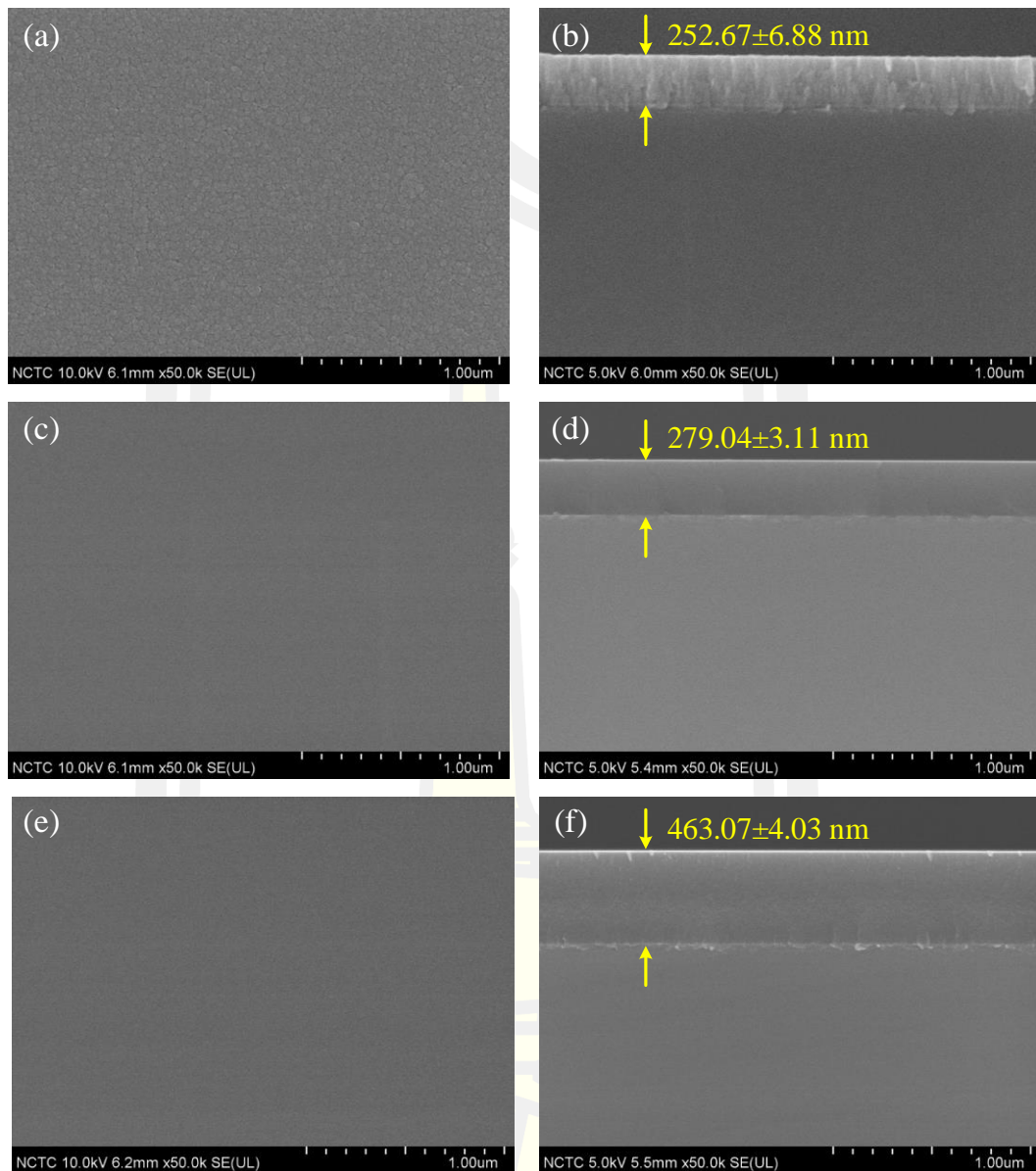


Figure 5.2 Surface morphologies (left) and cross-sectional microstructures (right) of (a), (b) a-Si interlayer; (c), (d) DLC film; and (e), (f) Si-doped DLC film deposited on silicon substrate.

5.1.2 Structural properties

In this section, the structural properties of the a-Si interlayer, DLC film, and Si-doped DLC film are described. The a-Si interlayer, DLC film and Si-doped DLC film were deposited with a control thickness of about 50 nm and characterized by XRR, XPS and Raman spectroscopy.

X-ray reflectivity is one of the most popular techniques for determining the density, thickness, and roughness of thin films [112], [148]. In this method, the thin film is examined non-destructively and the film thickness can be calculated to calculate the film thickness in the range of a few to 1000 nanometers depending on the resolution of the instrument. Single crystalline, polycrystalline and amorphous structure of thin films can be used for this measurement. It can also be used to study the layer structure of a single and multilayer film. In the XRR measurement, the observed diffraction peaks are correlated with the thickness of the measured layer.

The film density and thickness of a-Si interlayers, DLC and Si-doped DLC films with a controlled thickness of about 50 nm were determined using X-ray reflection by grazing-incidence (Bruker: D8 Advance Diffractometer model). The configuration of this equipment instrument allows the film thickness to be determined in the range of ~5 to ~150 nm. The film surface was excited with an X-ray beam of Cu-K_α radiation with a wavelength of 0.154 nm. This X-ray beam was generated with an accelerating voltage and a cathode current of 40 kV and 40 mA, respectively. The samples were irradiated with an X-ray beam with an angle of incidence of 0-4 degrees and an increment angle of 0.005 degrees with an integration time of 1 s. Then, the oscillation behaviour due to the reflection from air to film and film to substrate was detected and observed in the form of an interference pattern. This interference pattern of oscillations was also called the Kiessig fringe, which consists of a critical angle and an interference peak. The film density was extracted directly from the critical angle for total electron reflection using Equation 4.2 [113], while the film thickness was determined from the periodic oscillation of intensity, which can be simulated using the modified Bragg equation as shown in Equation 4.3 [114].

After the measurement procedure, the observed experimental data were fitted to the simulation curve based on the structural film model of these layers. To

obtain the accurate values for the density and thickness of the films, Leptos 7 software was used to simulate the film model and correlate it with the interference pattern of the films. For the a-Si interlayer, a film model consisting of a silicon substrate, a thin intermediate layer of native silicon oxide, a-Si interlayers, and a layer of native silicon oxide on top was assumed. For DLC and Si-doped DLC films, a silicon substrate, a thin intermediate layer of native silicon oxide, and a carbon layer on the top were used as the film model to interpret the Kiessig fringes.

The results of XRR-Kiessig fringes of the experimental data (black curve) and the corresponding simulation data (red curve) for a-Si interlayers, DLC, and Si-doped DLC films deposited on silicon substrate are shown in Figure 5.3. It can be seen that the simulation data of the corresponding model completely overlaps the experimental data. Therefore, the film thickness and density were extracted from the program as shown in Figure 5.4. It was found that the average thickness of the a-Si interlayer, DLC and Si-doped DLC films was about 51 ± 2.52 nm, which was close to the controlled thickness value of 50 nm. In the NAB part, it was found that the density of the a-Si interlayer was about 2.13 g/cm^3 , which was about 93% of the calculated density (2.285 g/cm^3) [115], [116]. It was found that the a-Si interlayer prepared in this part has a higher density than the a-Si interlayer prepared in the chromium-plated part (1.88 g/cm^3). This result may be due to the use of different target sputtering sources. Other factors such as deposition parameters, equipment accuracy, and impurities may also affect the layer deposition. For DLC and Si-doped DLC, the density is 1.98 and 1.86 g/cm^3 , respectively. The lower density of the carbon structure in the Si-doped DLC film is due to the effect of the silicon dopant in the carbon network. Most researchers report that sufficient and suitable silicon doping, and deposition conditions can generate the Si-C bond, which can increase the film density and sp^3 content in the DLC film. However, if the deposition conditions and the dopant cannot generate Si-C bond, the incorporation of silicon atoms into the DLC network will increase the disorder in the graphite clusters, resulting in higher thickness with lower film density. Therefore, the higher deposition rate of the Si-doped DLC film correlates with the low film density. Moreover, the increase of disordered graphite clusters in the Raman spectroscopy analysis will be seen in the next part.

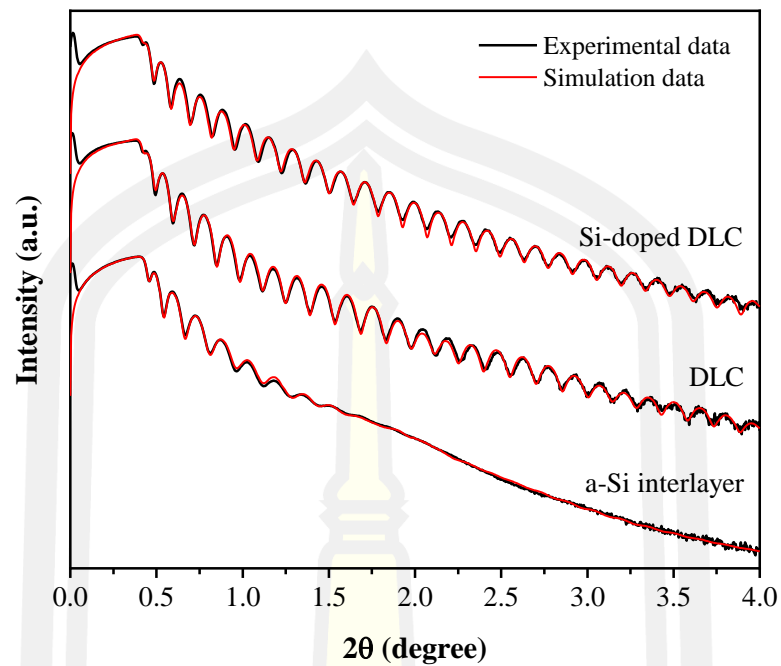


Figure 5.3 XRR curves of experimental data (black curve) and simulation data (red curve) for a-Si interlayers, DLC and Si-doped DLC films.

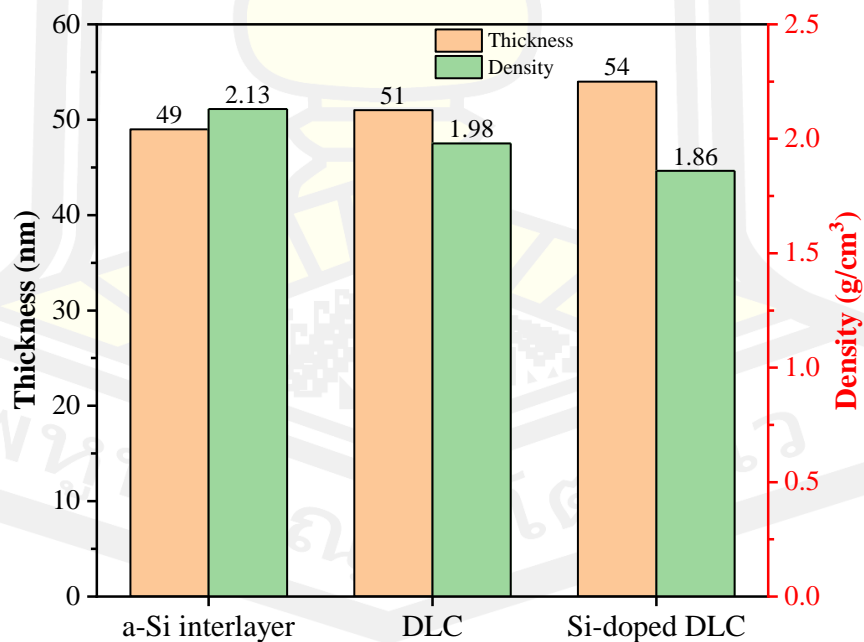


Figure 5.4 Fitted results for the thickness (orange bar) and density (green bar) of a-Si interlayers, DLC and Si-doped DLC films.

The chemical state of the a-Si interlayer, DLC film and Si-doped DLC film was investigated using XPS measurements performed with a PHI5000 Versa Probe II, ULVAC-PHI, Japan, at the joint research facility SUT-NANOTEC-SLRI, Synchrotron Light Research Institute (SLRI), Thailand. Monochromatic Al- K_{α} X-ray (1486.6 eV) was used as the excitation source. All binding energies of the samples were calibrated with the C1s peak at 284.8 eV. For a wide scan, the binding energy range of 0–1,400 eV was used with a step size of 1 eV. The Si2p fine scan was performed with the binding energy range around 96–107 eV for the a-Si interlayer, while the C1s and O1s fine scans for DLC and Si-doped DLC films were performed with the binding energy range around 280–290 and 529–537 eV, respectively, and a step size of 0.05 eV was used.

Figure 5.5 shows an XPS spectrum of the a-Si interlayer with a broad scan. It contains the silicon and oxygen rich peaks corresponding to the binding energy of ~102, ~153, ~532, and ~975 eV for Si2p, Si2s, O1s, and OKLL auger, respectively [102], [149], [150]. To identify the chemical state of the silicon in the a-Si interlayer, the fine scans of the Si2p peak were deconvoluted using the Gaussian function in Origin software, with background data subtracted using the Shirley method. The Si2p spectrum was decomposed into six peaks as shown in Figure 5.6, located at binding energies ~99.2, ~99.8 ~100.2, ~101.1, ~102.5, and ~103.5 eV. The peaks at ~99.2 and ~99.8 eV are from the two spin splitting peaks of Si2p, which could be overlapping spin-orbit components leading to an asymmetric peak shape. The other peaks are from the functional group of Si₂O, SiO, Si₂O₃, and SiO₂, which correspond to +1, +2, +3, and +4 oxidation states, respectively [105]–[108]. It can be seen that the silicon composition is sensitive to oxygen, as indicated by the dominant O1s peak in the wide scan. For the deposition and measurement process, the process chamber was evacuated to a vacuum pressure in the high and ultra-high vacuum range. Therefore, there is a possibility that the oxygen-rich peaks originated from the residual gas during surface exposure. The fitting results of the Si2p peaks such as bond type, binding energy, FWHM and content are listed in Table 5.2.

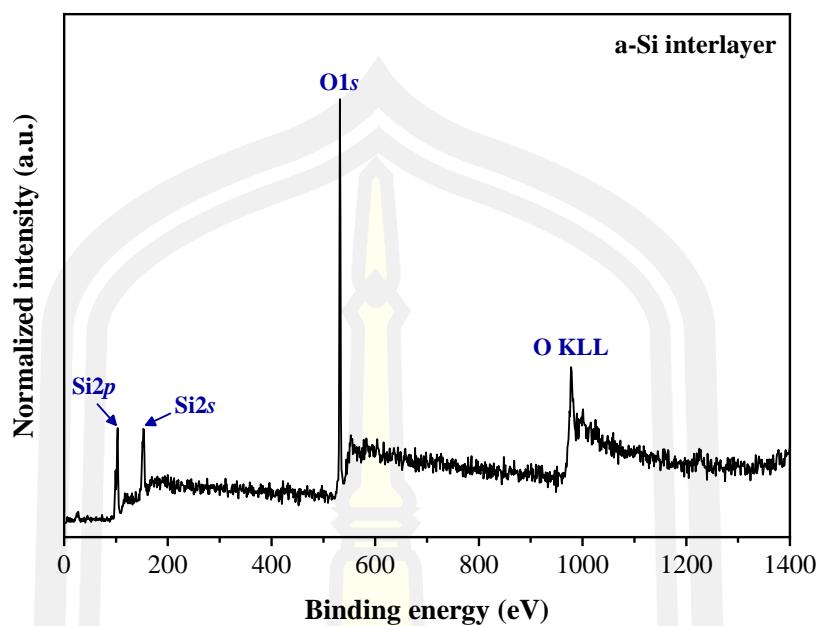


Figure 5.5 Typical XPS spectra of a wide scan for a-Si interlayer.

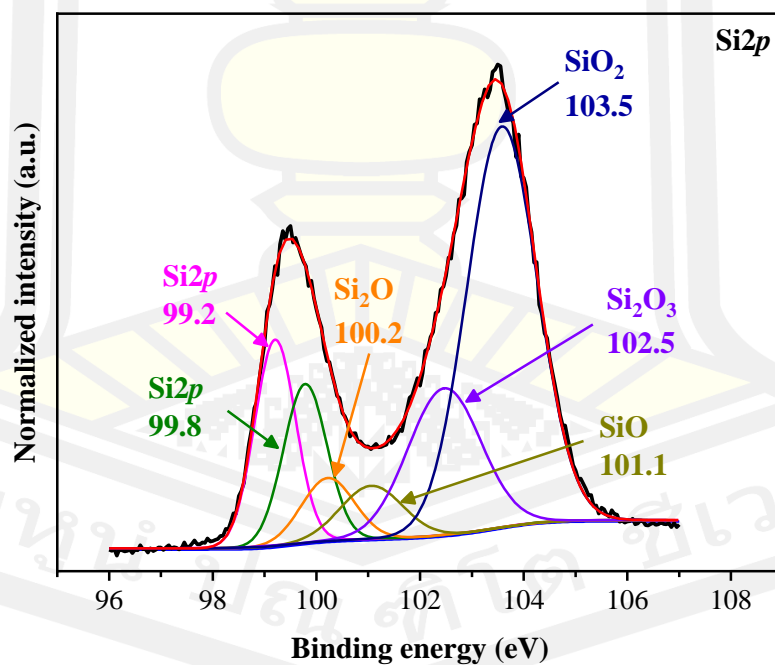


Figure 5.6 Deconvoluted XPS spectra for Si 2p of the a-Si interlayer. The black, red, blue, and other solid lines represent the experimental data, the fitted curve, the Shirley background, and the deconvolution of the individual peaks, respectively.

Table 5.2 The fitted results for the bond type, binding energy, FWHM, and deconvoluted content from the Si2*p*-XPS spectra of a-Si deposited on a silicon substrate.

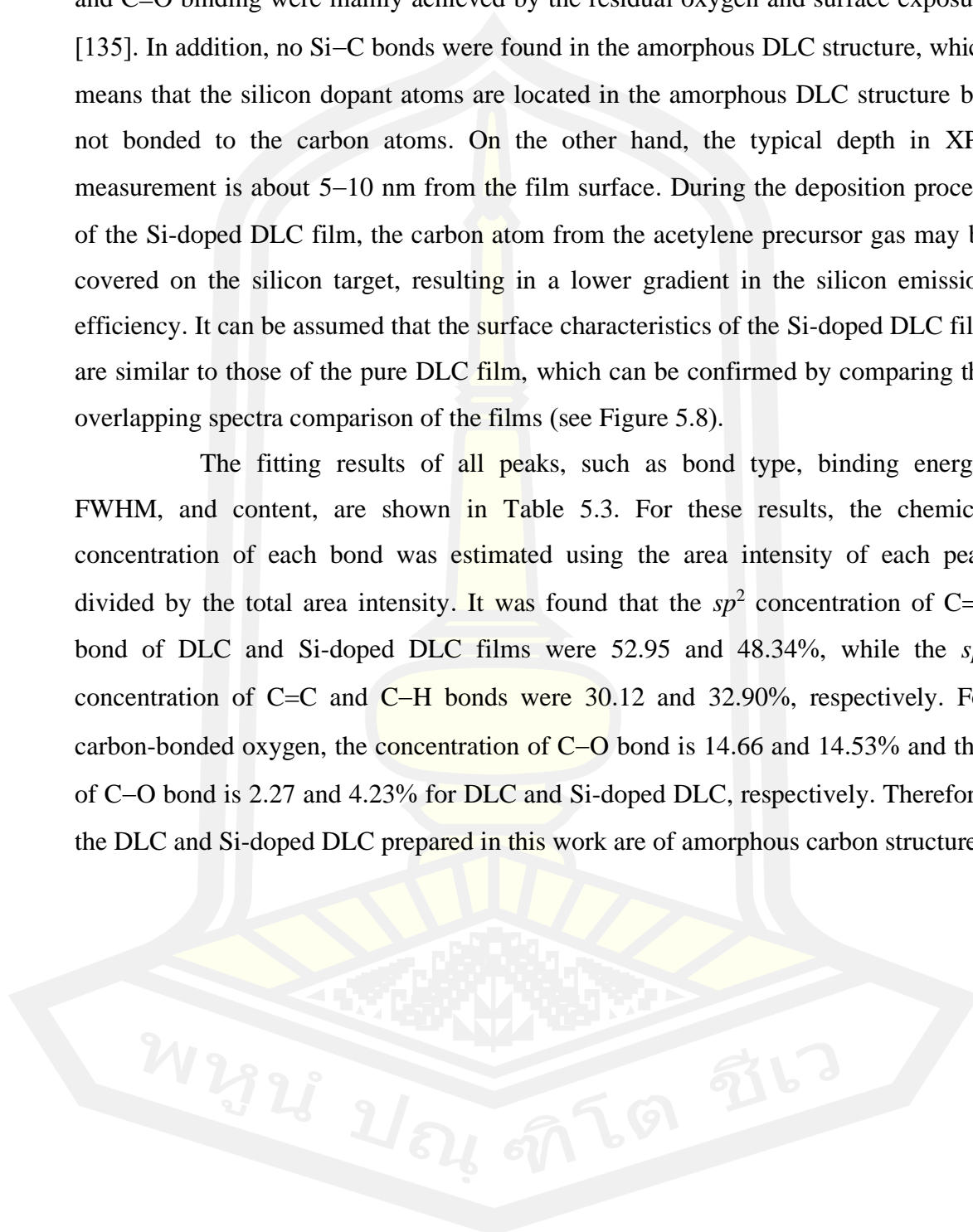
Sample	Peak designation	Bonding	Chemical information		
			Binding energy (eV)	FWHM (eV)	Content (%)
a-Si interlayer	Si2 <i>p</i>	Si2 <i>p</i>	99.2	0.93	13.87
		Si2 <i>p</i>	99.8	0.99	11.33
		Si ₂ O	100.2	1.19	5.40
		SiO	101.1	1.41	5.40
		Si ₂ O ₃	102.5	1.66	17.62
		SiO ₂	103.5	1.60	46.38

Figure 5.7 shows the XPS spectra of the DLC and Si-doped DLC films deposited on a silicon substrate with a broad scan. The result shows that the structure of both the DLC and Si-doped DLC films consists of two peaks of carbon and oxygen composition. These peaks are located at a binding energy of ~ 284.8 eV, and ~ 532 eV [101], [134]. The carbon peak, which dominates over the oxygen peak, indicates the main composition of carbon in the structure of the film. The oxygen composition, on the other hand, indicates to the residual gas in the vacuum chamber during the deposition process and the surface with air exposure [134]. For the Si-doped DLC film, the silicon peak is not found in the spectrum, which could indicate to the low concentration in the structure.

To confirm the structure of DLC and Si-doped DLC films, the high-resolution C1*s* main peak was analysed and compared. The C1*s* main peak was fitted using Gaussian functions, with the background subtracted using the Shirley method. It can be seen that the C1*s* peak was decomposed into four peaks as shown in Figure 5.9. These peaks at binding energy of ~ 284.6 , ~ 285.2 , ~ 286.4 , and ~ 288.8 eV correspond to C-*sp*² hybridization of C=C bond, C-*sp*² hybridization of C-C and

C–H bond, C–O, and C=O bond, respectively [135]. Most studies show that the C–O, and C=O binding were mainly achieved by the residual oxygen and surface exposure [135]. In addition, no Si–C bonds were found in the amorphous DLC structure, which means that the silicon dopant atoms are located in the amorphous DLC structure but not bonded to the carbon atoms. On the other hand, the typical depth in XPS measurement is about 5–10 nm from the film surface. During the deposition process of the Si-doped DLC film, the carbon atom from the acetylene precursor gas may be covered on the silicon target, resulting in a lower gradient in the silicon emission efficiency. It can be assumed that the surface characteristics of the Si-doped DLC film are similar to those of the pure DLC film, which can be confirmed by comparing the overlapping spectra comparison of the films (see Figure 5.8).

The fitting results of all peaks, such as bond type, binding energy, FWHM, and content, are shown in Table 5.3. For these results, the chemical concentration of each bond was estimated using the area intensity of each peak divided by the total area intensity. It was found that the sp^2 concentration of C=C bond of DLC and Si-doped DLC films were 52.95 and 48.34%, while the sp^3 concentration of C=C and C–H bonds were 30.12 and 32.90%, respectively. For carbon-bonded oxygen, the concentration of C–O bond is 14.66 and 14.53% and that of C–O bond is 2.27 and 4.23% for DLC and Si-doped DLC, respectively. Therefore, the DLC and Si-doped DLC prepared in this work are of amorphous carbon structure.



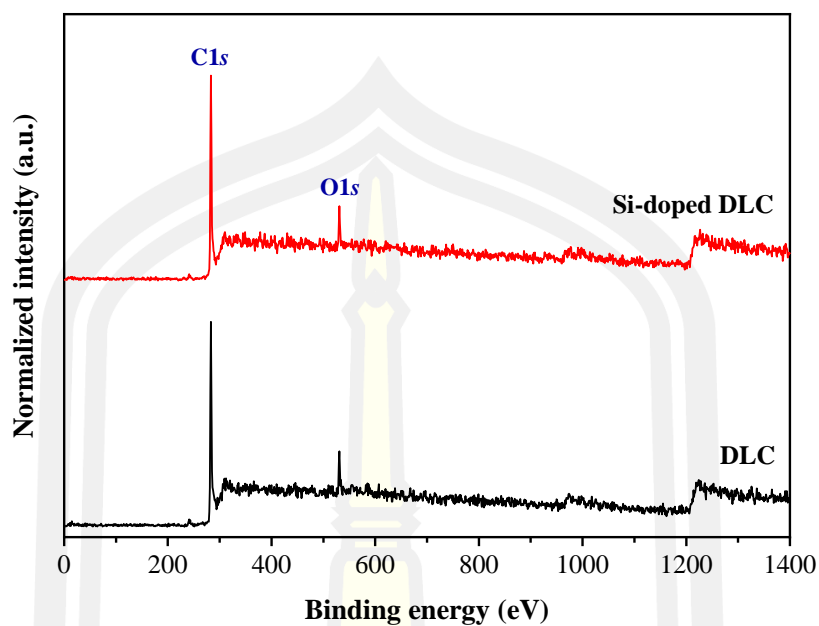


Figure 5.7 Typical XPS spectra of a wide scan for DLC and Si-doped DLC films.

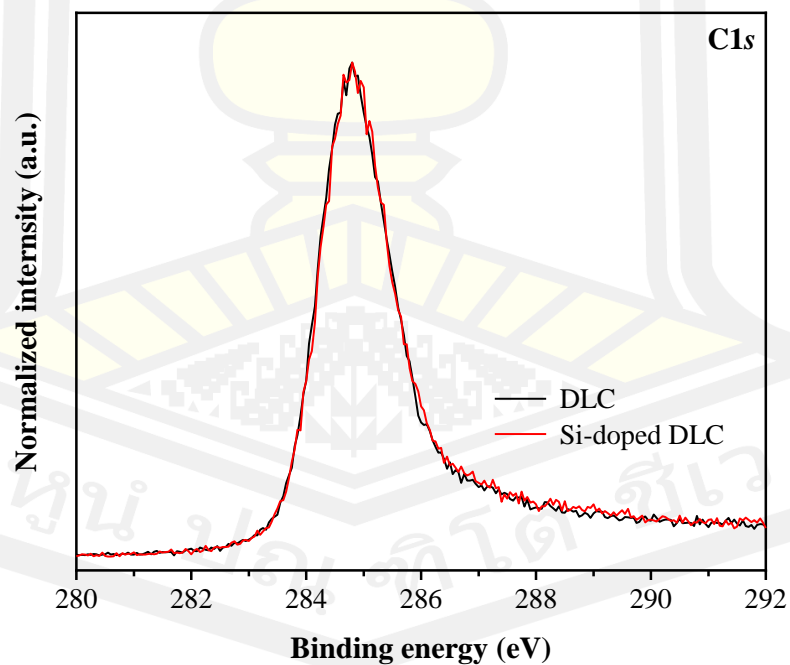


Figure 5.8 Comparison of high-resolution XPS spectra of the C1s peak of DLC and Si-doped DLC films.

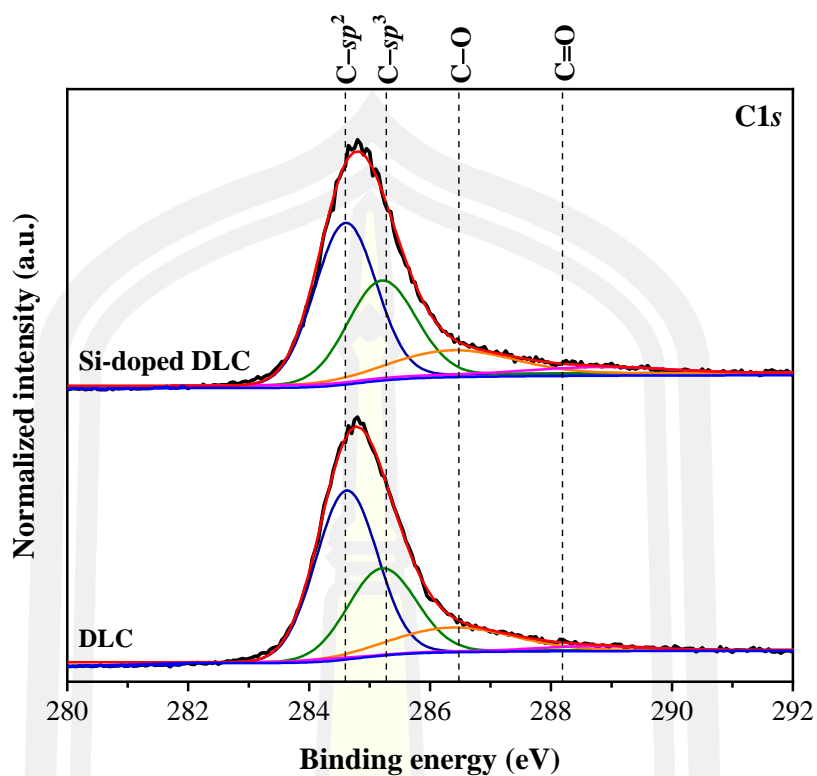


Figure 5.9 Deconvoluted XPS spectra for C1s of DLC and Si-doped DLC films. The black, red, blue, and other solid lines represent the experimental data, the fitted curve, the Shirley background, and the deconvolution of each peak, respectively.



Table 5.3 The fitted results of bond type, binding energy, FWHM, and content deconvoluted from the C1s XPS spectra of DLC and Si-doped DLC deposited on a silicon substrate.

Samples	Bonding	Chemical information		
		Binding energy (eV)	FWHM (eV)	Content (%)
DLC	C- sp^2	284.6	1.19	52.95
	C- sp^3	285.2	1.32	30.12
	C-O	286.4	2.32	14.66
	C=O	288.8	2.04	2.27
Si-doped DLC	C- sp^2	284.6	1.19	48.34
	C- sp^3	285.2	1.32	32.90
	C-O	286.4	2.32	14.53
	C=O	288.8	2.61	4.23

In addition, the structure of the DLC and Si-doped DLC films was characterized by Raman spectroscopy (Bruker, Senterra model). The surface of the DLC and Si-doped DLC films deposited on silicon substrate was excited using an Ar laser with a wavelength of 532 nm and a power of 12.5 mW. The scan range was between 50-2,700 cm^{-1} (0.5 cm^{-1} resolution) with an aperture size of 25 μm slit. Each spectrum was a co-addition of 2 scans with an integration time (20 s). Three Raman spectra of the samples from the different positions were averaged and deconvoluted with three Gaussian peaks using Origin software (version 2018) to determine the I_D/I_G ratio, peak positions, and FWHM of the X, D and G peaks.

The Raman spectra with deconvoluted lines of the DLC and Si-doped DLC films are shown in Figure 5.10 and the fitted results such as peak position, FWHM and I_D/I_G ratio are listed in Table 5.4. The Raman spectra of the films show three peaks: X, D, and G peaks. The X peak at about 1,222 and 1,241 cm^{-1} is from the

vibrations of a pentagonal atomic ring in the carbon nanostructures [129], [131]. The D and G peaks at about 1,417 and 1,422 cm^{-1} and 1,566 and 1,577 cm^{-1} are from vibrations of A_{1g} symmetry breathing mode of sp^2 atoms only in the aromatic rings and from the vibrations of E_{2g} stretching mode of sp^2 atoms in both aromatic rings and chains, respectively [126]–[128]. The I_D/I_G ratio of the DLC and Si-doped DLC films were 1.27 and 1.51, respectively. It can be seen that the I_D/I_G ratio of Si-doped DLC is higher than that of pure DLC. This behaviour indicates that the disorder of graphite or sp^2 clusters increase in the DLC structure increases due to the incorporation of silicon atoms. However, most researchers report that silicon doping in the amorphous structure leads to a decrease in I_D/I_G , which means that sp^3 bonding increases. In this context, silicon doping may replace some of the C–C bonds with Si–C bonds, which should decrease the average size of sp^2 clusters and increase the sp^3 bond. It should be mentioned that such behaviour has been reported in several researches [151]–[153]. On the other hand, Meškinis *et al.* reported that at low Si concentrations, the Si–C peak disappears in the C1s region of the XPS result, indicating that the silicon atoms were inserted into the DLC structure and not connected to the carbon atom. Thus, the incorporation of silicon atoms into the DLC film reduces the formation of sp^2 clusters, leading to an increase in disordered sp^2 clusters. In this work, it should be concluded that the silicon atoms are not bonded to the carbon atoms to form Si–C bond and the disorder of graphite was more pronounced in Si-doped DLC structure.



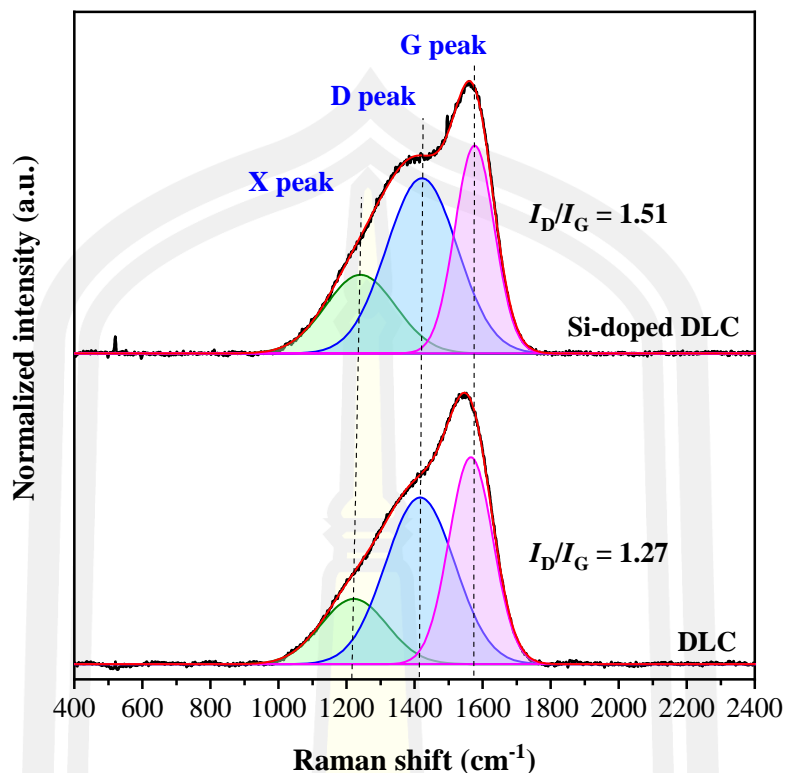


Figure 5.10 Raman spectra of DLC and Si-doped DLC films deposited on a silicon substrate. The black and red lines show the experimental data and the fitted curve, respectively. The green, blue, and magenta lines correspond to the deconvolution of the X, D and G peaks.

Table 5.4 The fitted results of the peak positions and FWHM of the X, D, and G peaks and I_D/I_G from the Raman spectra of DLC and Si-doped DLC films deposited on a silicon substrate.

Samples	X peak		D peak		G peak		I_D/I_G
	Position (cm ⁻¹)	FWHM (cm ⁻¹)	Position (cm ⁻¹)	FWHM (cm ⁻¹)	Position (cm ⁻¹)	FWHM (cm ⁻¹)	
DLC	1,222	228.30	1,417	239.05	1,566	151.86	1.27
Si-doped DLC	1,241	242.55	1,422	245.02	1,577	136.94	1.51

5.2 Multilayer characterizations

In this part, the multilayer DLC coating on the NAB was investigated, and the total coating thickness was adjusted to about 1 μm . For the NAB, the mechanical and corrosive properties need to be improved. Therefore, a multilayer design with a higher coating thickness than that of the chromium-plated substrate is required. The multilayer DLC was studied in terms of the stack or period of each layer where the interlayer was controlled. The thickness of the a-Si interlayer was kept at about 200 nm by adjusting the deposition time over the deposition rate to improve the adhesion strength. The thickness of the Si-doped DLC and DLC films was controlled to 300 and 500 nm, respectively, for 1 stack. The Si-doped DLC layer was used as a soft layer with lower thickness than the DLC layer, which has lower internal stress than the DLC layer. The soft layer is usually used to reduce the internal stress in the multilayer DLC film. Therefore, the lower thickness of the soft layer was used to maintain the properties of the DLC layer. In 3 stacks, the layer thickness of each Si-doped DLC and DLC film was split into 3 layers, with the thickness of Si-doped DLC being 100 nm and that of DLC being 166 nm. In the last embodiment, the layer thickness of each film was divided into 5 layers, where the thickness of the Si-doped DLC is 60 nm and the thickness of the DLC is 160 nm. The schematic model of the multilayer DLC with 1 stack, 3 stacks and 5 stacks on the NAB is shown in Figure 5.11. It can be seen that the total thickness of the multilayer DLC with 1 stack, 3 stacks and 5 stacks was set to about 1 μm to study the effects of the stacks. During deposition, the sample NAB with a diameter of ~ 25 mm and a height of ~ 5 mm and a silicon wafer with a size of 2×2 cm^2 were used as the substrate. The photo in Figure 5.12 shows the deposited multilayer DLC films with 1 stack, 3 stacks and 5 stacks on substrate holder. In Figure 5.13 (a), it was observed that the colour of the films on silicon substrates was dark brown or black and uniform for 1 stack and 3 stacks. In contrast, at 5 stacks, one layer of the film appears to peel off due to the film residue, but there is still a film layer remaining on the substrate. As can be seen in Figure 5.13 (b), the colour characteristics on NAB were uniform and black glossy with no peeling or cracking on the film, indicating good adhesion of the film to the substrate. After the deposition process, the morphologies and film thicknesses of the multilayer DLC

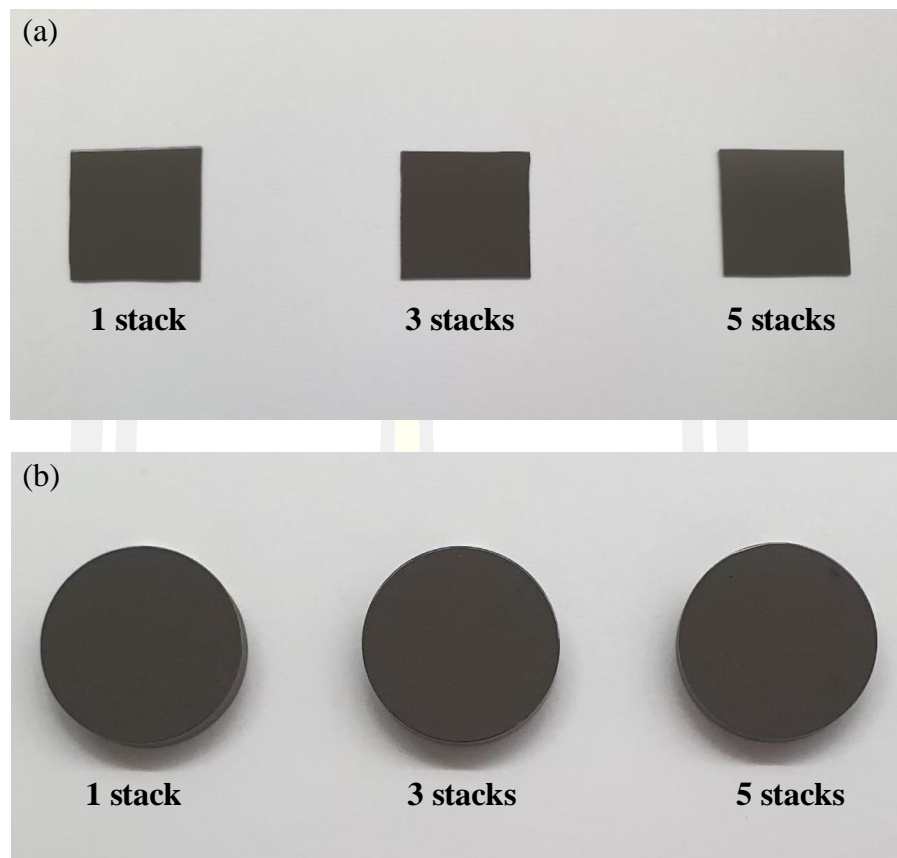


Figure 5.13 Photo of multilayer DLC with 1 stack, 3 stacks, and 5 stacks on (a) silicon and (b) NAB substrates.

5.2.1 Surface and cross-sectional morphology

The surface and cross-sectional morphology of the multilayer DLC films with 1 stack and 3 stacks deposited on a silicon substrate was analysed by FESEM (HITACHI, model SU8030). For the surface and cross-sectional images in FESEM, a magnification of 50 kx was used in secondary electron mode with an accelerating voltage of 5 kV for the surface morphology and 10 kV for the microstructures in the cross-section. The multilayer DLC with 5 stacks was not measured because the layer was peeled off after cutting the silicon substrate. Therefore, only the surface and cross-sectional morphology of multilayer DLC with 1 stack and 3 stacks are shown in this section.

Figure 5.14 shows the surface morphology of multilayer DLC with 1 stack and 3 stacks. It can be seen that the surface of the pure DLC layer has a dense and smooth surface.

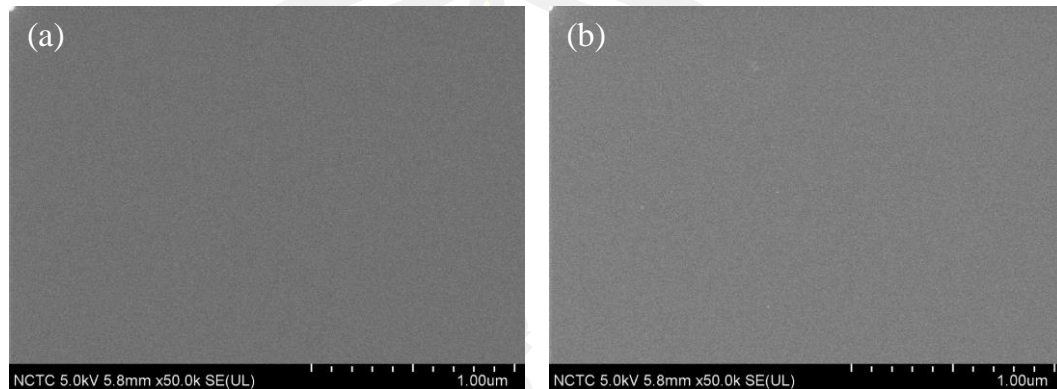


Figure 5.14 Surface morphologies of multilayer DLC with (a) 1 stack and (b) 3 stacks that deposited on silicon substrate.

Figure 5.15 and Figure 5.16 show the FESEM cross-sectional morphology of multilayer DLC deposited on silicon substrate (right figure) corresponding to the film model (left figure) for 1 stack and 3 stacks, respectively. For the 1 stack sample shown in Figure 5.15, the film consists of 3 layers, where the first layer is the a-Si interlayer, the second layer is the Si-doped DLC film, and the top layer is the DLC film. It is clear that the cross-sectional morphology of 1 stack of multilayer DLC films corresponds to the film model. The film thickness was measured with 20 measurements at different positions using Image J program. It was found that the average total thickness was $\sim 1,368 \pm 6.49$ nm, with the thickness of a-Si interlayer, Si-doped DLC film and DLC film being $\sim 183 \pm 3.82$, $\sim 405 \pm 7.16$, and $\sim 779 \pm 8.47$ nm, respectively. The higher film thickness than the controlled film thickness (~ 1 μm) may be due to the many factors, such as the carbon residue on the wall of the vacuum chamber during film deposition, which acts as an impurity and promotes the film growth. Other factors such as the flow rate of the precursor, which must fluctuate during the deposition process, and the self-annealing of the substrate can induce film

growth. The fractured FESEM cross-sectional image of the a-Si layer shows a smooth and compact morphology with small columnar grains growing perpendicular to the substrate. While the Si-doped DLC and DLC films show smooth and dense surface microstructures with amorphous structure. The different contrast between the Si-doped DLC and DLC layers indicates the difference in film density. With the low film density of the Si-doped DLC film, the dark region appears, while the high film density of the DLC film represents the bright region.

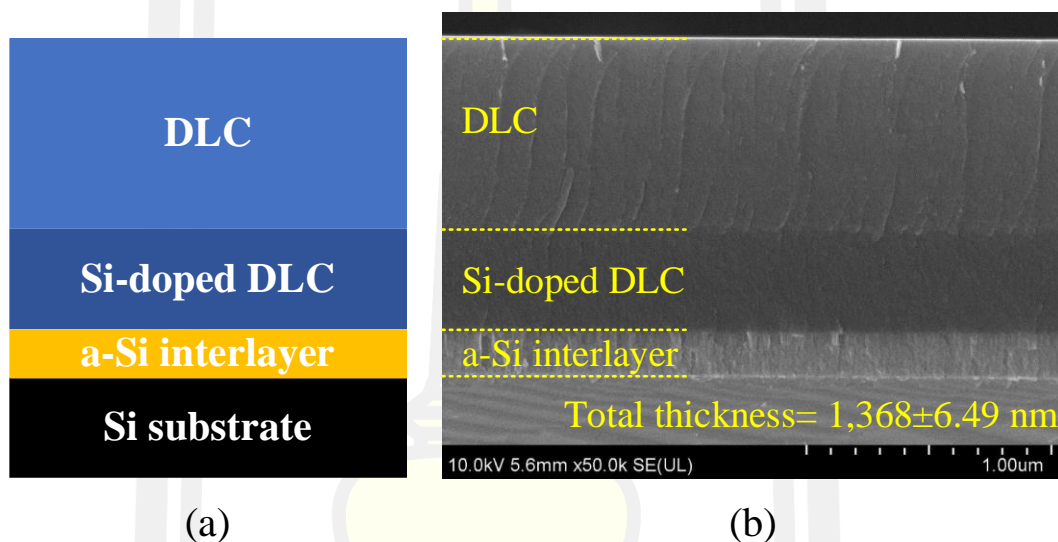


Figure 5.15 (a) schematic model and (b) corresponding cross-sectional microstructures of multilayer DLC with 1 stack.

For the sample with 3 stacks, as shown in Figure 5.16, the fractured FESEM cross-sectional image shows an unclear interface between the individual layers, which is due to the sample preparation for the measurement process. However, the overall average thickness is estimated to be $\sim 1,379 \pm 5.81$ nm. The average thickness of the a-Si interlayer is estimated to be $\sim 182 \pm 3.23$ nm based on the columnar structure. For the Si-doped DLC and DLC layer, the average thickness of the 3 layers is $\sim 114 \pm 4.26$ and $\sim 285 \pm 7.95$ nm, respectively. The Si-doped DLC and DLC layers also exhibit smooth and dense surface microstructures with amorphous structure and different contrast.

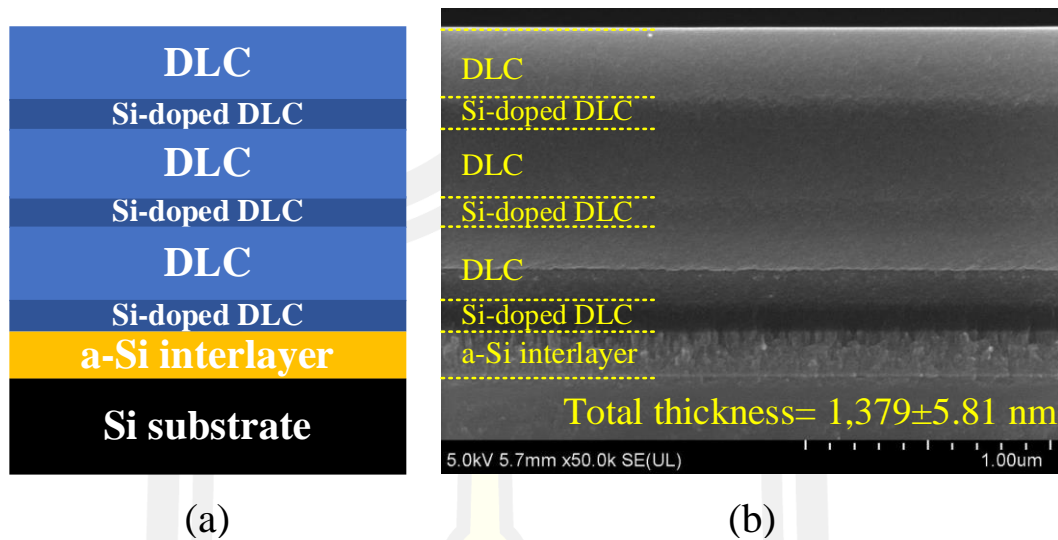


Figure 5.16 (a) schematic model and (b) corresponding cross-sectional microstructures of multilayer DLC with 3 stacks.

5.2.2 Analysis of structural properties

The surface of the multilayer DLC deposited on a silicon substrate was analysed for its structural properties using XPS and Raman spectroscopy techniques. The top surface of the multilayer DLC, i.e., the pure DLC, was acquired for the analysis. Therefore, it can be predicted that the structural properties are similar.

The upper DLC layer was also examined using the XPS technique. The same detail as in topic 5.1.2 is used for the XPS measurement. The result of the wide scan XPS spectra for the multilayer DLC deposited on a silicon substrate with 1 stack, 3 stacks and 5 stacks is shown in Figure 5.17. It can be seen that the surface of the top DLC layer consists of two peaks at ~ 284.8 eV, and ~ 532 eV, corresponding to the carbon ($C1s$) and oxygen ($O1s$) peaks, respectively [101], [134]. For 5 stacks sample, the XPS spectra can be measured when the film is peeled down to the DLC layer. However, it is difficult to confirm which layer has peeled off.

For the high-resolution $C1s$ spectra, the $C1s$ peak 1 stack, 3 stacks and 5 stacks was deconvoluted into four Gaussian functions using Origin software, and the backgrounds were subtracted using the Shirley method. The deconvoluted XPS

spectra for C1s of all samples are shown in Figure 5.18. The C1s spectrum was decomposed into four peaks located at different binding energies. These peaks at binding energy of $\sim 284.6 \pm 0.1$, $\sim 285.2 \pm 0.1$, ~ 286.4 , and ~ 288.8 eV correspond to C sp^2 hybridization of C=C bond, C- sp^2 hybridization of C-C and C-H bond, C-O, and C=O bond, respectively [135]. The fitting results of all peaks, such as bond type, binding energy, FWHM and content, are listed in Table 5.5. The sp^2 and sp^3 carbons of the three samples are 49.44 ± 0.62 and $34.40 \pm 1.07\%$, respectively. The concentration of C-O and C=O bonds in the DLC structure are 14.42 ± 0.60 and $1.74 \pm 0.15\%$, respectively. From these results, it can be concluded that the results of all samples with the same DLC coating conditions are in very good agreement.

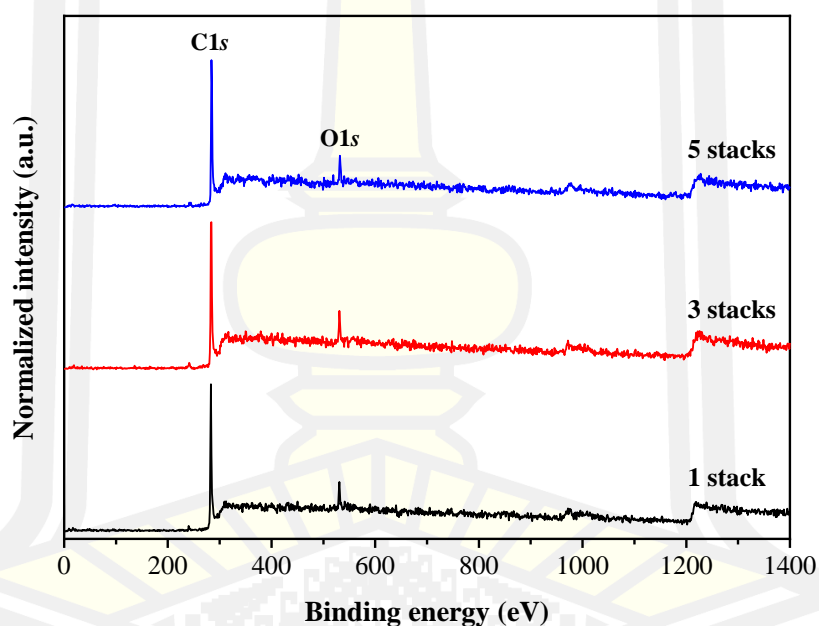


Figure 5.17 Typical XPS spectra of a wide scan for multilayer DLC with 1 stack, 3 stacks, and 5 stacks.

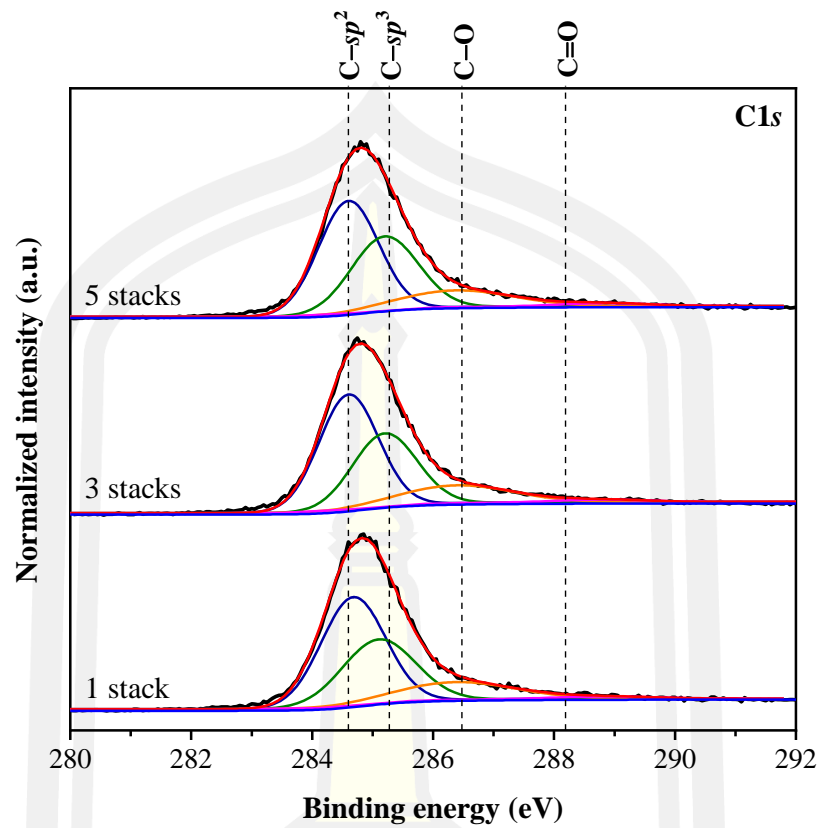


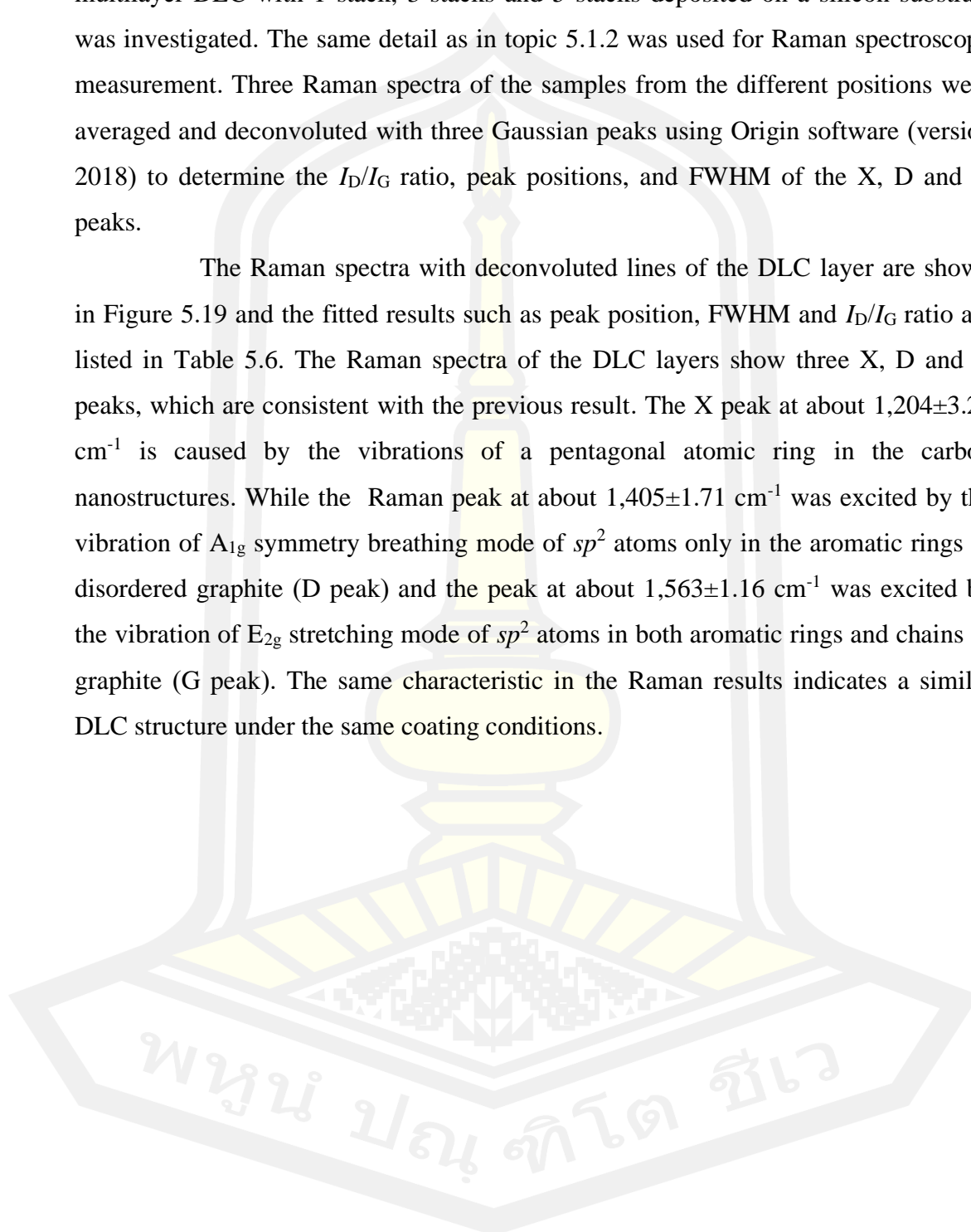
Figure 5.18 Deconvoluted XPS spectra for the C1s peak of multilayer DLC with 1 stack, 3 stacks and 5 stacks. The black, red, blue, and other solid lines represent the experimental data, the fitted curve, the Shirley background, and the deconvolution of each peak, respectively.

Table 5.5 The fitted results of bond type, binding energy, FWHM, and content deconvoluted from the C1s XPS spectra of multilayer DLC with 1 stack, 3 stacks and 5 stacks deposited on a silicon substrate.

Samples	Bonding	Chemical information		
		Binding energy (eV)	FWHM (eV)	Content (%)
1 stack	C- sp^2	284.7	1.14	49.87
	C- sp^3	285.1	1.22	33.51
	C-O	286.4	2.19	14.97
	C=O	288.8	1.74	1.65
3 stacks	C- sp^2	284.6	1.15	49.72
	C- sp^3	285.2	1.25	34.11
	C-O	286.4	2.17	14.53
	C=O	288.8	1.76	1.64
5 stacks	C- sp^2	284.6	1.17	48.73
	C- sp^3	285.2	1.30	35.58
	C-O	286.4	2.21	13.77
	C=O	288.8	1.70	1.91

For the Raman spectroscopy part, the surface of the top DLC layer of multilayer DLC with 1 stack, 3 stacks and 5 stacks deposited on a silicon substrate was investigated. The same detail as in topic 5.1.2 was used for Raman spectroscopy measurement. Three Raman spectra of the samples from the different positions were averaged and deconvoluted with three Gaussian peaks using Origin software (version 2018) to determine the I_D/I_G ratio, peak positions, and FWHM of the X, D and G peaks.

The Raman spectra with deconvoluted lines of the DLC layer are shown in Figure 5.19 and the fitted results such as peak position, FWHM and I_D/I_G ratio are listed in Table 5.6. The Raman spectra of the DLC layers show three X, D and G peaks, which are consistent with the previous result. The X peak at about $1,204 \pm 3.23 \text{ cm}^{-1}$ is caused by the vibrations of a pentagonal atomic ring in the carbon nanostructures. While the Raman peak at about $1,405 \pm 1.71 \text{ cm}^{-1}$ was excited by the vibration of A_{1g} symmetry breathing mode of sp^2 atoms only in the aromatic rings of disordered graphite (D peak) and the peak at about $1,563 \pm 1.16 \text{ cm}^{-1}$ was excited by the vibration of E_{2g} stretching mode of sp^2 atoms in both aromatic rings and chains of graphite (G peak). The same characteristic in the Raman results indicates a similar DLC structure under the same coating conditions.



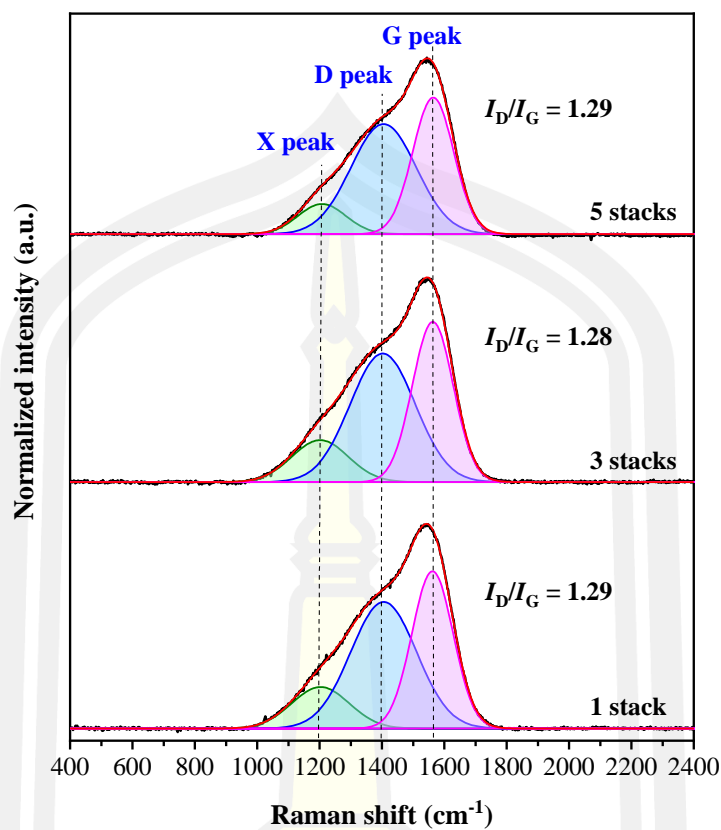


Figure 5.19 Raman spectra of multilayer DLC films with 1 stack, 3 stacks, and 5 stacks deposited on a silicon substrate. The black and red lines show the experimental data and the fitted curve, respectively. The green, blue, and magenta lines correspond to the deconvolution of the X, D and G peaks.

Table 5.6 The fitted results of peak positions and FWHM of X, D and G peaks and I_D/I_G from the Raman spectra of multilayer DLC with 1 stack, 3 stacks and 5 stacks deposited on silicon substrate.

Samples	X peak		D peak		G peak		I_D/I_G
	Position (cm ⁻¹)	FWHM (cm ⁻¹)	Position (cm ⁻¹)	FWHM (cm ⁻¹)	Position (cm ⁻¹)	FWHM (cm ⁻¹)	
1 stack	1,203	217.53	1,406	248.25	1,562	155.20	1.29
3 stacks	1,202	213.15	1,403	246.06	1,563	153.77	1.28
5 stacks	1,208	179.85	1,405	246.74	1,565	154.30	1.29

5.2.3 Analysis of mechanical properties

The nanoindentation test is mainly used to determine the mechanical properties in terms of hardness and elastic modulus of microscopic film materials. The NAB, the a-Si interlayer and the multilayer DLC with 1 stack, 3 stack and 5 stacks were analysed by nanoindentation test (Hysitron, TI Premier model) to confirm improvement of the properties of substrate NAB. The pyramid-shaped Berkovich indenter was used with 5-fold repeatability for dynamic mode at different positions. A maximum load of 7 mN was used for the bulk NAB. For the a-Si interlayer deposited on the substrate NAB with a thickness of $\sim 182.50 \pm 3.53$ nm, a maximum load of 500 μ N was used to keep the indentation depth below 10% of the film thickness. For the DLC multilayer with 1 stack, 3 stacks and 5 stacks with a thickness of about $\sim 1373.50 \pm 6.15$ nm, the higher maximum load of 7 mN was used to achieve a penetration depth of about 10% of the film thickness in the range of one micrometre.

The loading and unloading curves of the NAB, the a-Si interlayer and the multilayer DLC with 1 stack, 3 stacks and 5 stacks were plotted separately due to the different range in penetration depth. Figure 5.20 shows the loading and unloading curves of the NAB and the a-Si interlayer. The loading and unloading curves of the multilayer DLC with 1 stack, 3 stacks and 5 stacks are shown in Figure 5.21. The values of hardness, elastic modulus and penetration depth of the coated film and substrate are listed in Table 5.7. It was obvious that the area under the curve was larger than other deposited films that have high plastic deformation, which is a typical property of most metals and metal alloys. For the a-Si interlayer, the penetration depth was 50.61 ± 1.66 nm, which corresponds to 28% of film thickness, although the maximum load was very low, 500 μ N. Therefore, the effect of the NAB could be quite relevant during the measurement process. As shown in Figure 5.21, it was found that the penetration depth of the multilayer DLC increased from 160.65 ± 3.12 to 168.74 ± 2.08 nm when the number of stacks was increased from 1 stack to 5, indicating a decrease in hardness. The penetration depth of the multilayer DLC is 11.70–12.29% of the average total thickness ($\sim 1373.50 \pm 6.15$ nm), slightly more than 10% of the film thickness. The comparison of the hardness and elastic modulus of the NAB, a-Si interlayer, and multilayer DLC with 1 stack, 3 stacks and 5 stacks are

shown in Figure 5.22. It was found that the hardness of the multilayer DLC improved compared to the NAB. The hardness and elastic modulus of the NAB show the lowest hardness with the highest elastic modulus value of 3.71 ± 0.34 and 147.98 ± 10.91 GPa, respectively. Although the penetration depth is more than 10% of the film thickness, the hardness of the a-Si interlayer also shows a high value of about 5.43 ± 0.35 GPa, which is a good support for the multilayer formation of the NAB. On the other hand, the hardness of the DLC multilayer decreases slightly from 17.00 ± 0.88 to 15.57 ± 0.51 GPa when the DLC multilayer is increased from 1 stack to 5 stacks. It can be found that the hardness of the multilayer film increases by 4.58 times of the uncoated NAB. The modulus of elasticity of the multilayer DLC are slightly lower than those of the NAB and decrease with the number of stack increase. This is because the multilayer structure, in which the Si-doped DLC layer and the pure DLC layer are deposited alternately, corresponds to the substrate of the topmost DLC layer. This assumed substrate affects the performance of the top DLC layer due to differences in film thickness, residual stress, and hardness [23]. The low hardness of the 5-stack sample can be attributed to the effect of the soft layer (Si-doped DLC), as the thickness of the top DLC layer decreases with increasing number of film layers. The indenter penetrates closer to the soft layer. The change in hardness of multilayer DLC films can also be explained by the thickness of the top DLC layer. When the number of stacks is greater than 1, the thickness of the top DLC layer decreases rapidly, resulting in lower hardness.

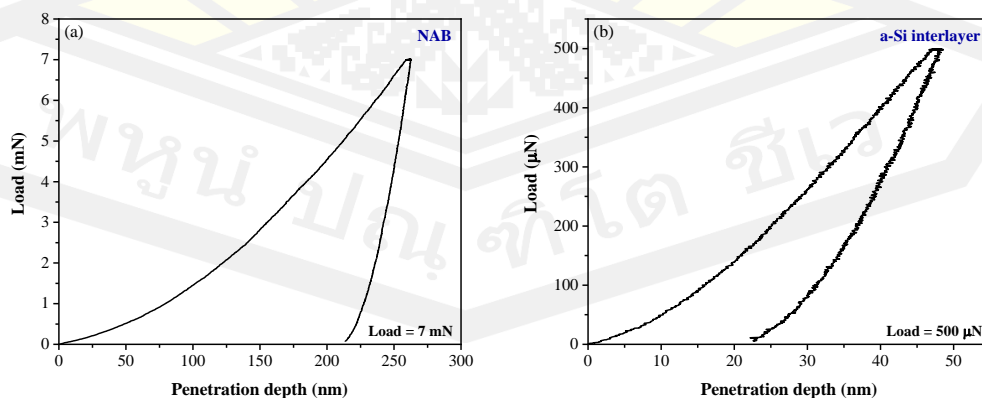


Figure 5.20 Loading and unloading curves of (a) NAB and (b) a-Si interlayer.

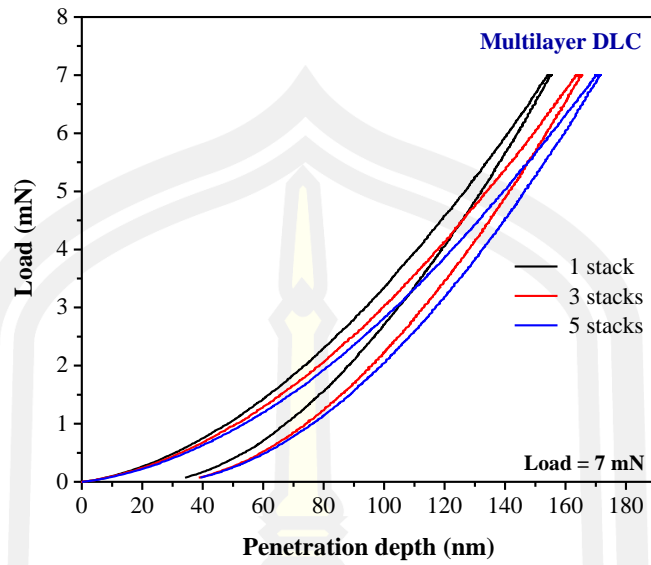


Figure 5.21 Loading and unloading curves of multilayers DLC with 1 stack, 3 stacks and 5 stacks.

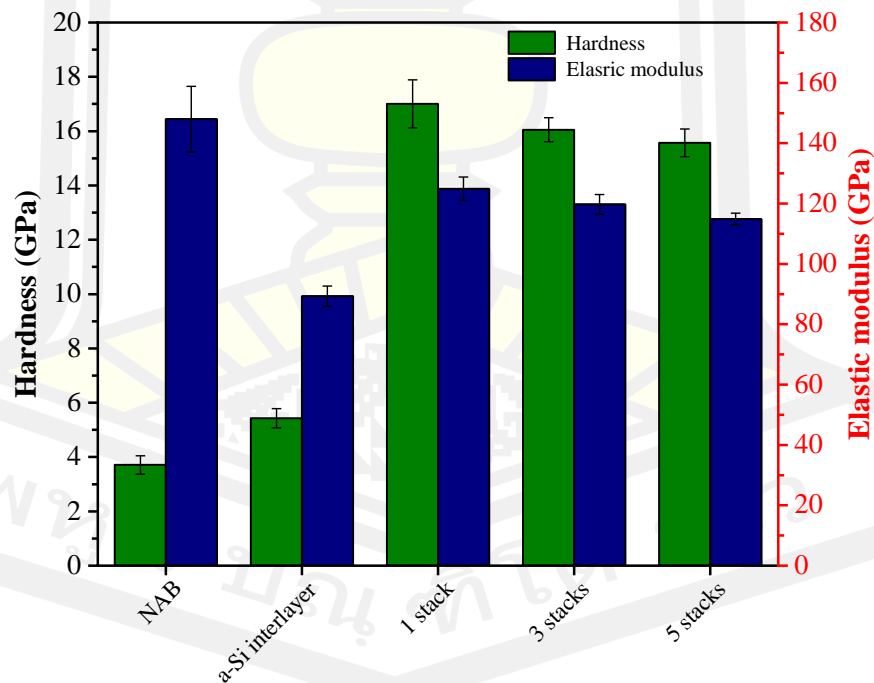


Figure 5.22 Hardness and elastic modulus of NAB, a-Si interlayer, and multilayers DLC with 1 stack, 3 stacks and 5 stacks.

Table 5.7 Hardness, elastic modulus, and penetration depth of multilayer DLC with 1 stack, 3 stacks and 5 stacks that deposited on a silicon substrate.

Samples	Hardness (GPa)	Elastic modulus (GPa)	Penetration depth (nm)
NAB	3.71±0.34	147.98±10.91	274.82±14.02
a-Si interlayer	5.43±0.35	89.30±3.33	50.61±1.66
1 stack	17.00±0.88	124.90±3.91	160.65±3.12
3 stacks	16.05±0.44	119.69±3.27	165.21±2.65
5 stacks	15.57±0.51	114.85±3.91	168.74±2.08

5.2.4 Analysis of adhesion strength

Important factors that determine the quality and durability of coatings are their cohesive and adhesive properties. The scratch test is an important tool for comparing the cohesive or adhesive properties of coatings or bulk materials. Good adhesive performance can support the properties of the film. When performing a progressive load test, the critical load is defined as the smallest load at which a detectable failure occurs. To determine the critical load, scratch marks from optical microscopy were used to identify the critical load based on scratch behaviour. For a thin-film coating on a substrate, the critical loads are divided into three types. The first critical load (Lc_1) corresponds to the first sign of cohesive failure in the form of spalling and cracking in the scratch track. The second critical load (Lc_2) corresponds to the beginning of the adhesive failure of the delamination of the film. Finally, the third critical load (Lc_3) corresponds to the complete delamination of the coating from the scratch track and the complete removal of the interlayer from the substrate. In addition, the critical load can be determined by monitoring the acoustic emission on the sample during scratching, which works very well for brittle and hard film coatings. In this technique, a typical diamond stylus or indenter with linear progressive loading is projected onto the surface of sample and slide. At higher load, further damage usually occurs due to detachment of the coating from the substrate by

spalling, buckling or chipping. The critical load is then determined based on the failure and delamination characteristics.

In this part, the micro-scratch test (Fischer Scope, model HM2000) was used to observe the adhesive behaviour of thin films with respect to the critical load value. The scratch marks of the optical microscope were used to identify three types of critical loads. The multilayer DLC films with 1 stack, 3 stacks and 5 stacks were analysed in progressive mode with a continuous increase from 0.5 to 50 N using a spherical Rockwell C indenter. A scratch speed of 2 mm/min, a scan load step of 0.5 N, and a load rate of 10 N/min were used with 3 repetitions at different positions.

The scratch behaviour with L_{c1} , L_{c2} and L_{c3} of multilayer DLC films with 1 stack, 3 stacks and 5 stacks was identified and is shown in Figure 5.23. The values of L_{c1} , L_{c2} and L_{c3} can be found in Figure 5.24 and Table 5.8. The scratch behaviour includes three stages: the first stage is microcracking and partial ring cracking, the second stage is complete ring cracking, delamination, and spalling, and the last stage is substrate exposure [138]. As can be seen in Figure 5.23, the multilayer DLC coating exhibits excellent scratch failure characteristics along the scratch. This means that the film shows favourable adhesion strength on NAB. In multilayers with 1 stack, it can be seen that the film delaminates and spalls from the edge of the scratch track, indicating a cohesive failure mode. This behaviour explains the high internal stresses in the thick DLC top layer. The scratch marks of 3 and 5 stacks show no evidence of delamination of the coatings, indicating good cohesive properties of the film. All of the multilayer DLC films have a first critical load greater than 4 N. The mean values of the three critical loads are slightly different, as shown in Figure 5.24, so the different multilayer DLC films are not considered to affect the adhesion value due to the overlap of the error bars of the measured data. However, the a-Si interlayer and multilayer design show good adhesion strength of the film on NAB for higher film thicknesses above 1 μm .

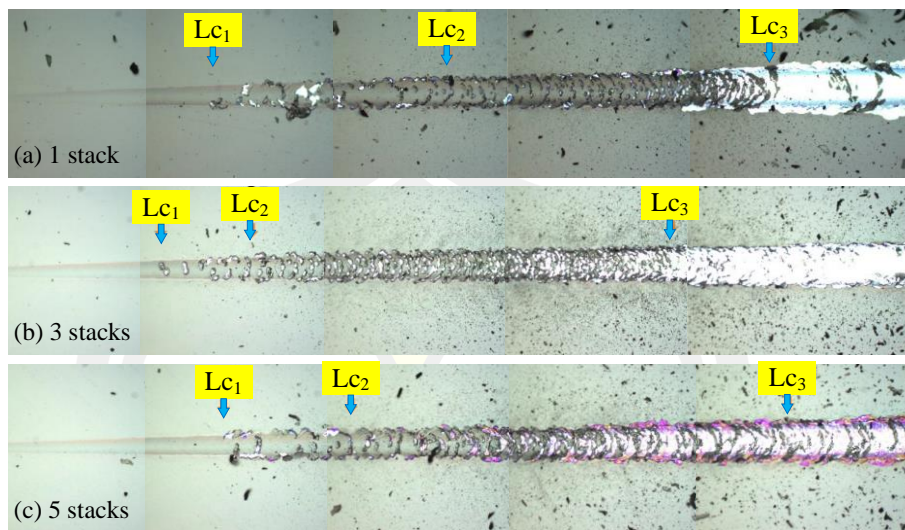


Figure 5.23 Morphology of scratch marks of Lc_1 , Lc_2 and Lc_3 for DLC multilayers with 1 stack, 3 stacks and 5 stacks deposited on a NAB.

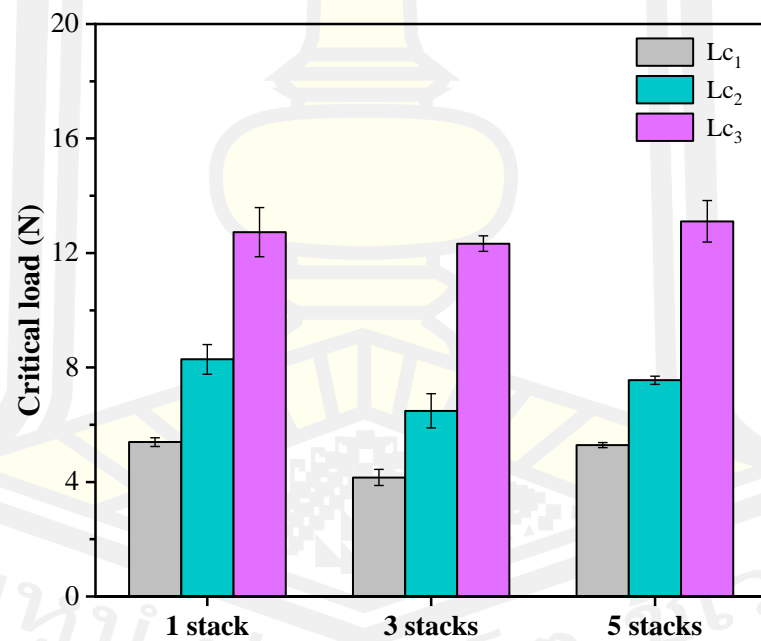


Figure 5.24 Critical load values of Lc_1 , Lc_2 and Lc_3 for DLC multilayers with 1 stack, 3 stacks and 5 stacks deposited on a NAB.

Table 5.8 Critical load values (L_{c1} , L_{c2} , and L_{c3}) for DLC multilayers with 1 stack, 3 stacks and 5 stacks.

Samples	L_{c1} (N)	L_{c2} (N)	L_{c3} (N)
1 stack	5.39 ± 0.15	8.28 ± 0.52	12.73 ± 0.86
3 stacks	4.16 ± 0.28	6.49 ± 0.59	12.33 ± 0.27
5 stacks	5.29 ± 0.09	7.55 ± 0.14	13.11 ± 0.73

5.2.5 Analysis of electrochemical corrosion

The corrosion protection of thin-film coatings has long been used to protect the substrate from corrosion. An electrochemical potentiodynamic measurement is used to obtain the electrochemical properties of a material. Electrochemical corrosion measurement is a proficient method with simple procedures and high sensitivity that reflects the chemical reactions of atomic, ionic, and molecular transport in solution that led to dissolution of the metal. This behaviour provides information about the lifetime and corrosion behaviour of bulk materials and thin films [139], [140]. In this work, the corrosion behaviour of the multilayer DLC film and a-Si interlayer deposited on NAB was measured electrochemically to confirm the corrosion resistance compared to uncoated NAB. For the electrochemical corrosion measurement, three-electrodes were immersed in a corrosion solution. The sample material or thin-film coating was used as the working electrode (WE), the saturated silver to silver chloride (Ag/AgCl) was used as the reference electrode (RE) serving as the standard, and a pure platinum rod was used as the counter electrode (CE). In the measurement, the Ag/AgCl and pure platinum rod electrodes were immersed in NaCl solution, while the thin-film sample and substrate were mounted between the metal plate and the O-ring for the surface contact with the solution and electrical connection. The electrochemical corrosion measurement was carried out using a 3.5 wt% NaCl solution in which 35 grams of NaCl powder was diluted in 1 litre of deionized water. The exposed area of the sample was controlled by the inner diameter of the O-ring (6 mm), which resulted in an exposed area of 0.2827 cm^2 . The

operating temperature during the measurement procedure was kept at room temperature and the samples were exposed to NaCl solution for 30 minutes. A potential of -1000 to 1000 mV with a sampling rate of 1 mV/s was applied to observe the polarisation curves.

The corrosion behaviour of the a-Si interlayer and 1, 3 and 5 stacks of multilayer DLC in 3.5 wt% NaCl solution compared to the bare NAB is shown in Figure 5.25. The corrosion parameters achieved from the Tafel extrapolation are listed in Table 5.9. The E_{corr} and i_{corr} are the corrosion current density and corrosion potential observed at the y-axis and x-axis intersections between the anodic and cathodic branches of the polarisation curves. Lower corrosion current density and higher corrosion potential indicate lower corrosion rate and better corrosion resistance [142], [143].

From Figure 5.25, it can be seen that the multilayer DLC coating with 1 stack, 3 stacks and 5 stacks exhibits a shift of the corrosion potential to a more positive region and the corrosion current density trend decreases compared to the uncoated substrate [144]. Thus, it was clear that the corrosion resistance of NAB was highly improved by the multilayer DLC coating. In particular, the 5 stacks sample shows a significant shift in the potentiodynamic polarization curves. The lowest corrosion current density means the best corrosion resistance [143]. From Table 5.9, the corrosion current density of NAB is $1.41 \mu\text{A}/\text{cm}^2$, while the a-Si interlayer ($0.92 \mu\text{A}/\text{cm}^2$) and the multilayer DLC coating ($0.02\text{--}0.83 \mu\text{A}/\text{cm}^2$) have lower values indicating a lower loss of composition of material and coating. It can be concluded that the corrosion current density of NAB up to $1.41 \mu\text{A}/\text{cm}^2$, is 70 times higher than that of 5 stacks of multilayer DLC coatings. The corrosion current density of all samples was plotted for comparison, as shown in Figure 5.26. This result shows that both the a-Si interlayer and multilayer DLC coating can reduce the corrosion current density. This result could be explained by the typical corrosion resistance of the thin-film coating.

In addition, the corrosion current density was found to decrease significantly with an increase in the number of film layers for multilayer DLC from 1 stack to 5 stacks. The improved corrosion protection mechanism of the multilayer structure can be explained by the increase of the interfacial area with the increase of

the number of layers [154]. When the top DLC layer is directly exposed to the corrosion solution, it is corroded first, while the bottom layer was protected. Therefore, the lower layer is protected until the collapse of the upper layer occurs. This behaviour leads to lateral propagation of the corrosion product in the plane of the interface. After the breakdown of the first layer, the second layer is exposed to the corrosion solution and this behaviour is repeated layer by layer until it penetrates through the coating and then into the substrate. In the case of 1 stack, the number of interfaces is less than for 3 stacks and 5 stacks, resulting in a high corrosion current density. The above results clearly show that multilayer DLC coating can positively affect the corrosion current density and effectively reduce the corrosion rate of NAB in a corrosive environment. The porosity analysis cannot be estimated due to the failure of anodic and cathodic Tafel slope.

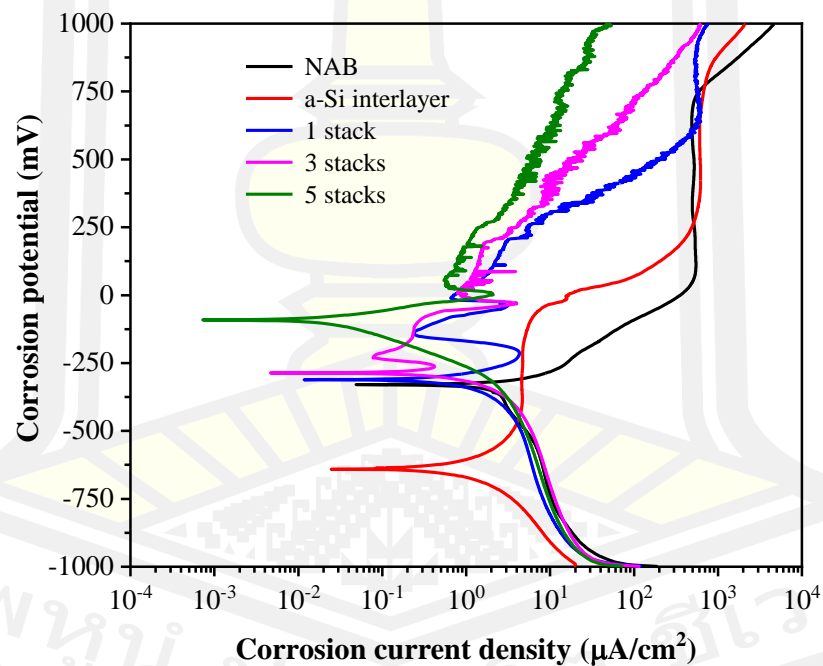


Figure 5.25 Potentiodynamic polarization curves of NAB, a-Si interlayer, and 1 stack, 3 stacks and 5 stacks of multilayer DLC in 3.5 wt% NaCl solution.

Table 5.9 Electrochemical results of polarization curves of NAB, a-Si interlayer, and 1 stack, 3 stacks and 5 stacks of multilayer DLC.

Samples	Corrosion potential (mV)	Corrosion current density ($\mu\text{A}/\text{cm}^2$)
NAB	-330	1.41
a-Si interlayer	-640	0.92
1 stack	-310	0.83
3 stacks	-285	0.22
5 stacks	-90	0.02

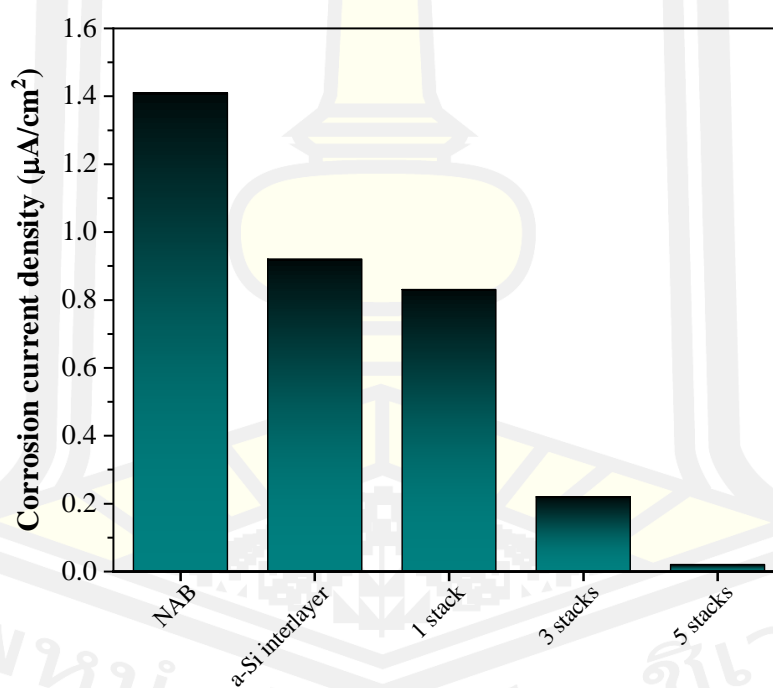


Figure 5.26 Corrosion current density of NAB, a-Si interlayer, and 1 stack, 3 stacks and 5 stacks of multilayer DLC.

Figure 5.27 shows a photo of NAB and an a-Si interlayer, a multilayer DLC with 1 stack, 3 stacks and 5 stacks applied to NAB after the corrosion test. It can be seen that the surface of NAB has clearly corroded areas. While the a-Si interlayer exhibits the corroded behaviour of the spot coverage of the surface test. The DLC multilayer with 1 stack shows the corroded behaviour revealed by the surface of the substrate. The DLC multilayers with 3 stacks and 5 stacks show a slightly different morphology. These behaviours observed on the surface correspond to the corrosion current density as shown above.

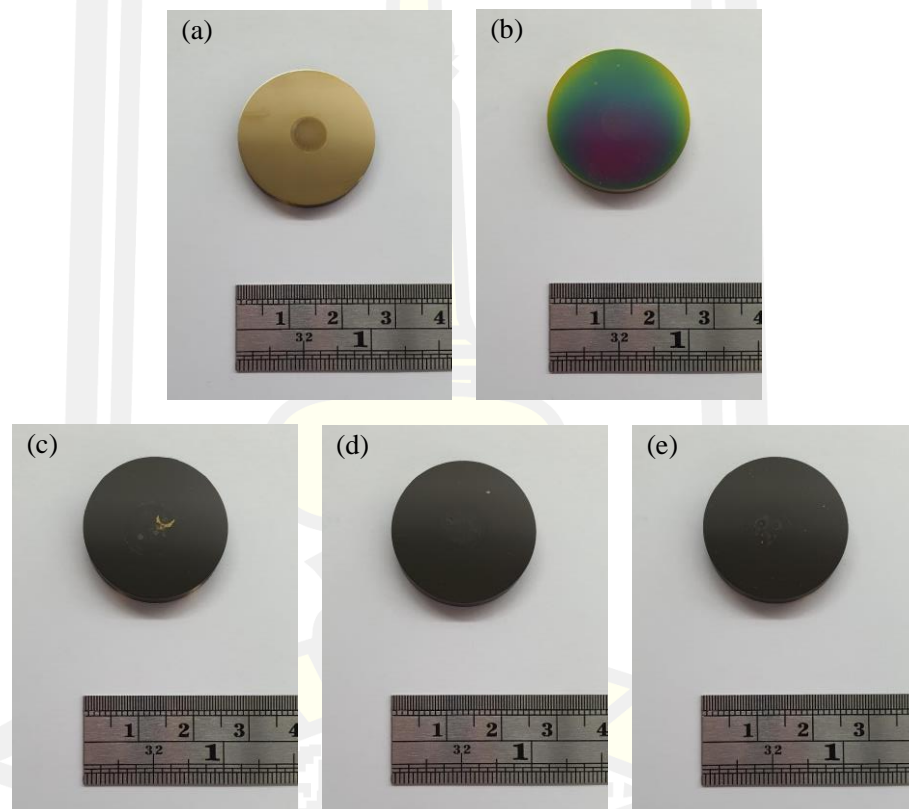


Figure 5.27 Photo of (a) NAB, (b) a-Si interlayer, and (c) 1 stack, (d) 3 stacks, and (e) 5 stacks of multilayer DLC after corrosion measurement.

5.3 Conclusion of NAB part

In this part, the multilayer DLC films were developed and fabricated, with the a-Si film serving as the adhesive layer. The nickel aluminum bronze was used as a substrate to improve the mechanical and corrosive resistance. The pure DLC film was used as a hard layer with high film density, while the Si-doped DLC film was used as a soft layer with low film density. The a-Si interlayer was prepared by the DC magnetron sputtering method. The DLC film was deposited using the radio-frequency plasma-enhanced chemical vapor deposition method. A combination of magnetron sputtering and radio frequency plasma-enhanced chemical vapor method was used to deposit the Si-doped DLC film. In a first study, the characterization of the individual a-Si interlayers, DLC and Si-doped DLC films was systematically investigated. In another study, the multilayer design was investigated in terms of deposition period or stack (1 stack, 3 stacks and 5 stacks) with a controlled film thickness of about 1.3 μm .

The film thickness and structural properties of the a-Si interlayer, DLC and Si-doped DLC films were investigated by FESEM, XRR, XPS and Raman spectroscopy. The deposition rates calculated from the thickness of the a-Si interlayer, DLC and Si-doped DLC film are 12.63 ± 0.34 , 13.95 ± 0.16 and 23.15 ± 0.20 nm/min, respectively, and these values were used to estimate the deposition time for each thickness. The higher deposition rate of Si-doped DLC compared to DLC is due to the discharge assistance from the magnetron sputtering source, which increases during the film growth in the deposition particles. The results of the XRR techniques show that the density of the a-Si interlayer, DLC, and Si-doped DLC film are about 2.13, 1.98, and 1.86 g/cm^3 , respectively, with an average thickness of 51 ± 2.52 nm. The a-Si interlayer has a high density of up to 93% of the calculated density, which is a good quality for the adhesive layer. In contrast, the density of Si-doped DLC is lower density than that of DLC, indicating the typical properties of the soft layer.

The XPS results of the a-Si interlayer show the silicon peak ($\text{Si}2p$ and $\text{Si}2s$) and the oxygen-rich peak originating from the silicon precursor during the deposition process and from the residual oxygen during surface exposure to air, respectively. The predominant silicon dioxide and suboxides of the Si_2O , SiO , Si_2O_3 and SiO_2 functional groups show the sensitivity of the silicon surface to air exposure. For the

DLC and Si-doped DLC films, the film structure consists of carbon and oxygen compositions. It was found that the C- sp^2 concentration of C=C bond for DLC and Si-doped DLC films were 52.95 and 48.34%, while the C- sp^3 concentration of C-C and C-H bonds were 30.12 and 32.90%, respectively. For carbon-bonded oxygen originating from residual oxygen and surface oxidation, the concentration of C-O and C=O bonds ranged from 14.53–14.66% and that of bonds was 2.27–4.23%, respectively for DLC and Si-doped DLC. It is surprising that the Si-C bonds were not found in the Si-doped DLC, which could be due to the low doping concentration during the co-deposition process.

Raman spectroscopy was used to identify the scattering of sp^2 hybridization in the amorphous carbon structure of DLC and Si-doped DLC films. The Raman spectra of these films show three peaks of X, D, and G in the range of 1,222 and 1,241 cm^{-1} , 1,417 and 1,422 cm^{-1} and 1,566 and 1,577 cm^{-1} , respectively. These peaks originate from the vibrations of a pentagonal atomic ring in the carbon nanostructures, the vibration of A_{1g} symmetry breathing mode of sp^2 atoms only in aromatic rings, and the vibration of E_{2g} stretching mode of sp^2 atoms in both aromatic rings and chains.

The I_D/I_G ratio of the Si-doped DLC film (1.51) is higher than that of the DLC film (1.27). This is due to the increase in disordered sp^2 clusters caused by the incorporation of silicon atoms into the amorphous carbon structure. From the results of XPS and Raman spectroscopy, it can be concluded that the silicon atoms are not connected to the carbon atoms to form Si-C bond, which leads to the increase of disordered graphite in the Si-doped DLC structure.

In the multilayer DLC section, the multilayer design of 1 stack, 3 stacks and 5 stacks was deposited on NAB and silicon substrates and characterized using FESEM, Raman spectroscopy, XPS, nanoindentation, micro-scratching, and electrochemical measurements to observe the morphology, structure, mechanical and adhesive properties, and corrosion resistance.

The surface morphology of the multilayer DLC exhibits a dense and smooth surface, while the overall average thickness is estimated to be $\sim 1,373 \pm 6.15$ nm. The fractured cross-sectional image of the a-Si layer shows a smooth and compact morphology, with small columnar grains growing perpendicular to the substrate. The

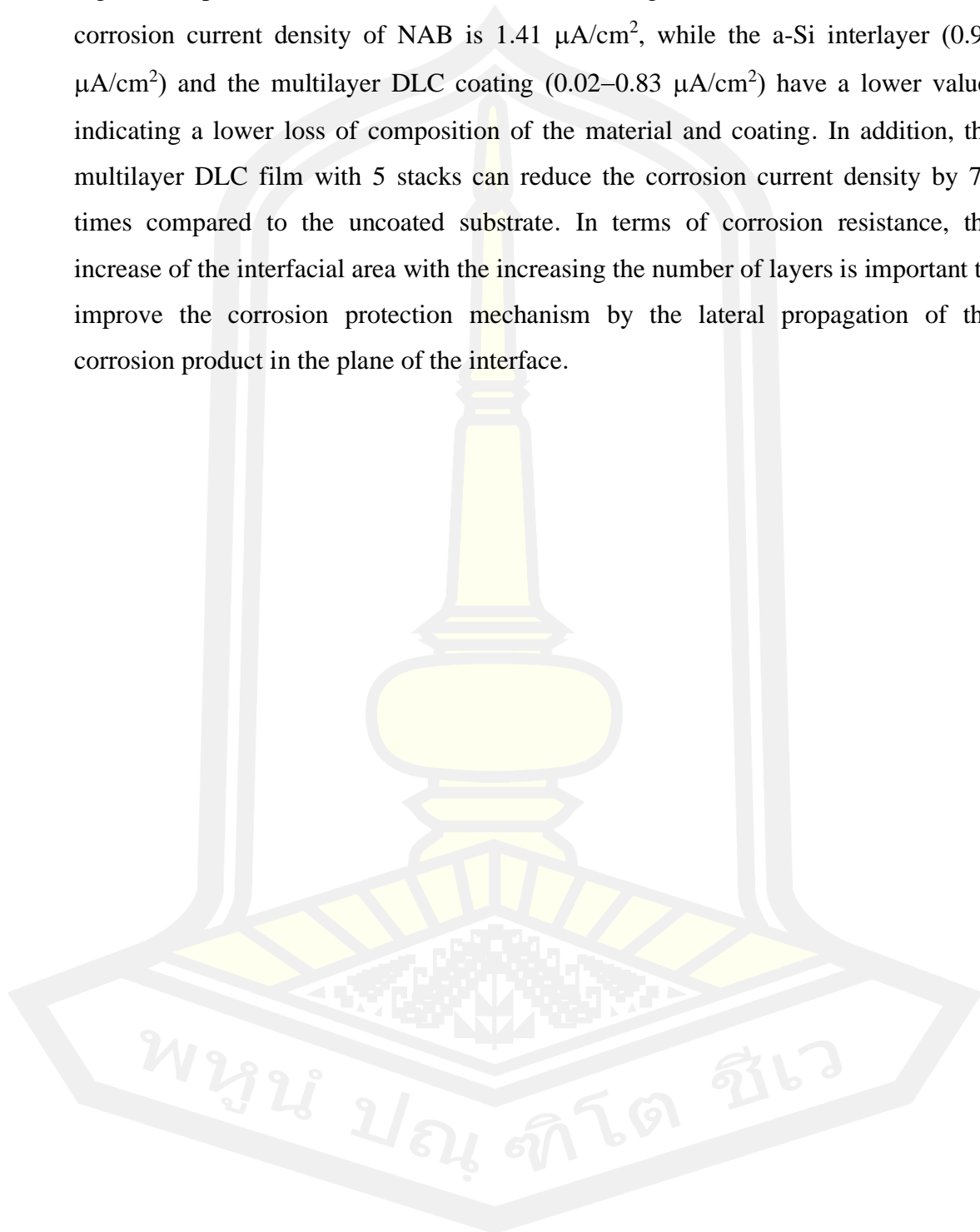
Si-doped DLC and DLC films exhibit the smooth and dense surface microstructures with amorphous structure, whose different contrast indicates the different density of the films. The Raman spectra of the top pure DLC films for the multilayer DLC samples show three peaks of X, D and G with a ratio of I_D/I_G of 1.29, which is consistent with the previous result. The XPS results show that the sp^2 and sp^3 carbons of all samples are 49.44 ± 0.62 and $34.40\pm 1.07\%$, respectively. The concentration of C–O and C=O bonds in the DLC structure is 14.42 ± 0.60 and $1.74\pm 0.15\%$, respectively. It can be concluded that the results of all samples with the same DLC coating conditions are in very good agreement.

The hardness of NAB shows a low value of 3.71 ± 0.34 GPa. While the a-Si interlayer with a hardness of 5.43 ± 0.35 GPa provides good support for the multilayer formation of NAB. The penetration depth of the DLC multilayers increased from 11.70–12.29% of the total thickness when the number of stacks increased from 1 to 5, indicating a decrease in hardness from 17.00 ± 0.88 to 15.57 ± 0.51 GPa. It can be seen that the a-Si interlayer has 3.13 times higher hardness than the uncoated NAB. All the multilayer DLC samples have 4.58 times higher hardness. The change in hardness of the multilayer DLC films can also be explained by the thickness of the top DLC layer. When the deposited multilayer film is more than 1 stack, the thickness of the top DLC layer decreases rapidly, resulting in lower hardness, which is due to the effect of the soft bottom layer.

The micro-scratch test was used to determine the scratch resistance and interfacial adhesion of the film coating. The critical load values for all multilayer DLC films are close to each other, with a high first critical load of ~ 4 N. This means that the multilayer film has a favorable adhesion strength with NAB. For 1 stack of multilayer DLC films, delamination and spalling were observed at the edge of the scratch track, indicating a cohesive failure mode due to the high internal stresses in the thick DLC top layer. It can be concluded that the a-Si adhesive layer and multilayer design have good adhesion strength of the film on NAB at higher film thicknesses above $1\ \mu\text{m}$.

An electrochemical potentiodynamic measurement is used to determine the electrochemical properties of a substrate, a-Si interlayer, and multilayer DLC films in terms of corrosion current density and corrosion potential. A shift of the

potentiodynamic polarization curves of the multilayer coating toward a more positive region compared to the uncoated NAB indicates good corrosion resistance. The corrosion current density of NAB is $1.41 \mu\text{A}/\text{cm}^2$, while the a-Si interlayer ($0.92 \mu\text{A}/\text{cm}^2$) and the multilayer DLC coating ($0.02\text{--}0.83 \mu\text{A}/\text{cm}^2$) have a lower value, indicating a lower loss of composition of the material and coating. In addition, the multilayer DLC film with 5 stacks can reduce the corrosion current density by 70 times compared to the uncoated substrate. In terms of corrosion resistance, the increase of the interfacial area with the increasing the number of layers is important to improve the corrosion protection mechanism by the lateral propagation of the corrosion product in the plane of the interface.



CHAPTER VI

Conclusions and suggestions

6.1 Conclusions

The conclusion was divided into two main parts for chromium-plated and NAB substrates. In the first part, a-Si, a-Si:N, a-Si:H, and a-Si_xC_y:H films were used as interlayers to improve the adhesion on the a-C:H film deposited on the chromium-plated substrate. The deposition rate of all interlayers prepared by the DCMS method has different values depending on the gas source, which were used to estimate the deposition time at the same film thickness. The a-C:H films were deposited using the RF-PECVD method under the same conditions. The average thickness of the a-C:H films and the silicon-based interlayers were controlled as 317±12.99 and 306±14.23 nm, respectively. The surface morphology shows very homogeneous, smooth and dense microstructures without microparticle defects. The cross-sectional morphology between the a-C:H films and the interlayers shows a clear boundary at the interface without delamination and cracking, indicating good adhesive properties. For the a-C:H film deposited on a chromium-plated substrate without an interlayer, delamination from the substrates evident. For the a-Si and a-Si:H interlayers, it can be seen that the interlayers have similar grain sizes and these layers appear to merge with the a-C:H layer at the interface.

The Raman spectra of the a-C:H films clearly show the presence of D and G peaks at 1,413–1,417 cm⁻¹ and 1,562–1,569 cm⁻¹ of Raman shift with a relative intensity I_D/I_G of about 1.26, indicating the typical structure of the amorphous carbon films. These peaks are associated with the vibration of A_{1g} symmetry breathing mode of sp^2 atoms only in the aromatic rings for disorder of graphite (D peak) and with the vibration of E_{2g} stretching mode of sp^2 atoms in both aromatic rings and chains for graphite (G peak). In addition, the X peak was found at about 1,222–1,225 cm⁻¹, which probably originates from the vibrations of a pentagonal atomic ring in the carbon nanostructures. The XPS results show that the bonding of C- sp^2 and C- sp^3 hybridizations with the carbon content of all samples is about 51.26±0.22 and

30.11±2.52%, respectively. Moreover, C–O and C=O bonds derived from residual oxygen and surface oxidation are also found in the a-C:H structure. Therefore, it can be concluded that the a-C:H film prepared in this part with a density of about 2.15 g/cm³ agrees very well under the same deposition conditions.

For all silicon-based interlayers, the XPS results indicate the presence of silicon dioxide and suboxides, mainly due to the adsorption process during the measurement. The low hardness of all the interlayers with density in the range of 1.68–2.05 g/cm³ shows that the a-C:H film is very important for improving the mechanical properties of the chromium-plated substrate. In the a-Si_xC_y:H interlayer, the carbon dopant can be bonded to the silicon atoms and form Si–C, which has a negative effect on the adhesive properties. This behaviour is probably due to the low dangling bond and the high residual stress of the interlayer. The a-C:H/a-Si:H sample exhibited higher L_{c2} and L_{c3} (5.67±0.28 and 15.15±1.16 N) than the other silicon-based interlayers, indicating higher resistance to adhesion failure between the coating and the interlayer, and higher adhesion strength of the interlayer with a substrate, which correlates with the highest hardness of about 20.98±0.63 GPa that is 2.5 times higher than the substrate (8.30±0.48 GPa). In addition, it exhibits the lowest corrosion current density with the lowest porosity, which is about 36 times lower than that of the uncoated chromium-plated substrate. This result indicates that a-Si and a-Si:H are a good supporting interlayer for the formation of a-C:H film. The mixing with hydrogen gas for the a-Si:H interlayer could reduce the residual oxygen, which could reduce the Si–O bonding and improve the adhesion between the interlayer and the a-C:H film. It can be concluded that the protective a-C:H coating with an a-Si:H interlayer has excellent potential to significantly improve the corrosion resistance and hardness properties of the film, which can extend the durability and service life of materials used in abrasive and corrosive environments.

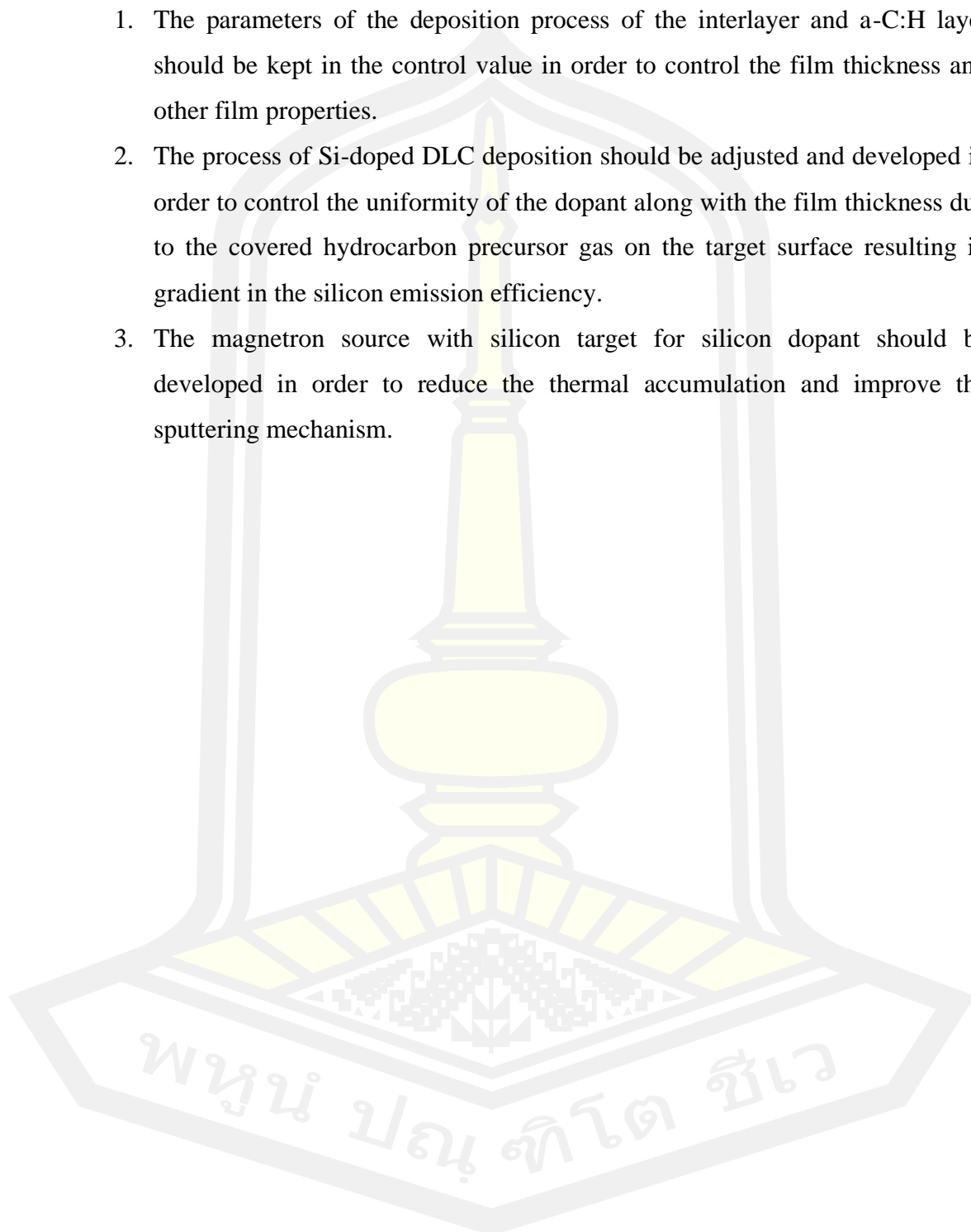
In the second part, the multilayer DLC films were developed and fabricated using the a-Si film as an adhesive layer to improve the mechanical and corrosive resistance of NAB. The a-Si interlayer was prepared using the DCMS method. The DLC film was deposited using the RF-PECVD deposition method. The DCMS and RF-PECVD method were used to deposit the Si-doped DLC film. The a-Si interlayer has a high density of up to 93% of the calculated density, which is a good quality for the

adhesive layer. The DLC and of Si-doped DLC films with densities of 1.98 and 1.86 g/cm³ were used as hard and soft layers, respectively. The multilayer design was investigated in terms of deposition period or stack (1 stack, 3 stacks and 5 stacks) with a controlled film thickness of about 1.3 μm. The XPS results of the a-Si interlayer show the silicon peak (Si2*p* and Si2*s*) and the oxygen-rich peak originated from the silicon precursor during the deposition process and the residual oxygen during the surface exposure to air, respectively. The Raman spectra of DLC and Si-doped DLC films show three peaks of X, D, and G in the range of 1,222 and 1,241 cm⁻¹, 1,417 and 1,422 cm⁻¹ and 1,566 and 1,577 cm⁻¹. The *I*_D/*I*_G ratio of the Si-doped DLC film is higher than that of the DLC film due to the increase in disordered *sp*² clusters caused by the incorporation of silicon atoms into the amorphous carbon structure. From the results of XPS and Raman spectroscopy, it can be concluded that the silicon atoms are not bonded with the carbon atoms to form Si–C bond, which leads to an increase in graphite disorder in a Si-doped DLC structure.

The surface morphology of the multilayer DLC exhibits a dense and smooth surface with an overall average thickness estimated to be ~1,373±6.15 nm. The cross-sectional image of the a-Si layer shows the smooth and compact morphologies with small columnar grains, while the Si-doped DLC and DLC layers show the smooth and dense surface microstructures of the amorphous structure, corresponding to the difference in film density. The a-Si interlayer shows higher hardness than NAB, which is a good support for the multilayer formation of NAB. The hardness of DLC multilayers decreased with increasing stacking from 1 stack to 5 stacks. The change in hardness of DLC multilayers can also be explained by the thickness of the top DLC layer. The a-Si adhesive layer and multilayer design show good adhesion strength of the film on NAB for higher thickness above 1 μm. The shift of the potentiodynamic polarization curves of the multilayer coating toward a more positive region compared to the uncoated NAB indicates the good corrosion resistance. Moreover, using higher number of stacks can significantly reduce the corrosion current density, which can be explained by the lateral propagation of the corrosion product in the plane of the interface.

6.2 Suggestions

1. The parameters of the deposition process of the interlayer and a-C:H layer should be kept in the control value in order to control the film thickness and other film properties.
2. The process of Si-doped DLC deposition should be adjusted and developed in order to control the uniformity of the dopant along with the film thickness due to the covered hydrocarbon precursor gas on the target surface resulting in gradient in the silicon emission efficiency.
3. The magnetron source with silicon target for silicon dopant should be developed in order to reduce the thermal accumulation and improve the sputtering mechanism.



REFERENCES



- [1] H. Frey and H. R. Khan, *Handbook of thin-film technology*, 1st ed. UK, 2003.
- [2] L. B. Freund and S. Suresh, *Thin Film Materials : Stress, Defect and Surface Evolution*, 1st ed. UK, 2003.
- [3] K. S. Sree Harsha, *Principles of Vapor Deposition of Thin Films*, 1st ed. UK: Elsevier, 2006.
- [4] J. Robertson, "Diamond-like amorphous carbon," *Materials Science and Engineering: R: Reports*, vol. 37, no. 4–6. pp. 129–281, 2002, doi: 10.1016/s0927-796x(02)00005-0.
- [5] J. Robertson, "Plasma Deposition of Diamond-Like Carbon," *Jpn. J. Appl. Phys.*, vol. 50, pp. 1–8, 2011.
- [6] H. Moriguchi, H. Ohara, and M. Tsujioka, "History and Applications of diamond-like carbon manufacturing processes," *SEI Technical Review*, no. 82. pp. 52–58, 2016.
- [7] A. Tyagi, R. S. Walia, Q. Murtaza, S. M. Pandey, P. K. Tyagi, and B. Bajaj, "A critical review of diamond like carbon coating for wear resistance applications," *Int. J. Refract. Met. Hard Mater.*, vol. 78, pp. 107–122, 2019, doi: 10.1016/j.ijrmhm.2018.09.006.
- [8] A. H. Lettington, "Applications of diamond-like carbon thin films," *Carbon*, vol. 36, no. 5–6. pp. 555–560, 1998, doi: 10.1016/S0008-6223(98)00062-1.
- [9] H. Ronkainen, "Tribological properties of hydrogenated and hydrogen-free diamond-like carbon coatings," *VTT Publ.*, no. 434, pp. 2–52, 2001.
- [10] B. Schultrich, *Tetraedrally Bonded Amorphous Carbon Films I*, vol. 263, no. PART 1. Germany: Springer-Verlag GmbH Germany, 2018.
- [11] K. Kim, "A study of the frictional characteristics of metal and ceramic counterfaces against electro-deposited coatings for use on automotive seat rails," *Wear*, vol. 320, no. 1, pp. 62–67, 2014, doi: 10.1016/j.wear.2014.08.012.
- [12] C. Wang, B. Li, X. Ling, and J. Zhang, "Superlubricity of hydrogenated carbon films in a nitrogen gas environment: adsorption and electronic interactions at the sliding interface," *RSC Adv.*, vol. 7, no. 5, pp. 3025–3034, 2017, doi: 10.1039/C6RA25505A.

- [13] X. L. Peng and T. W. Clyne, "Residual stress and debonding of DLC films on metallic substrates," *Diam. Relat. Mater.*, vol. 7, no. 7, pp. 944–950, 1998, doi: 10.1016/s0925-9635(97)00331-2.
- [14] C. Wei and J. Y. Yen, "Effect of film thickness and interlayer on the adhesion strength of diamond like carbon films on different substrates," *Diamond and Related Materials*, vol. 16, no. 4-7 SPEC. ISS. pp. 1325–1330, 2007, doi: 10.1016/j.diamond.2007.02.003.
- [15] A. Ramesh and S. N. Melkote, "Modeling of white layer formation under thermally dominant conditions in orthogonal machining of hardened AISI 52100 steel," *Int. J. Mach. Tools Manuf.*, vol. 48, no. 3–4, pp. 402–414, 2008, doi: 10.1016/j.ijmachtools.2007.09.007.
- [16] E. R. Petry *et al.*, "Physicochemical structure of SiC_x:H to improve DLC adhesion on steel," *Surf. Eng.*, vol. 32, no. 10, pp. 779–785, 2016, doi: 10.1080/02670844.2016.1159277.
- [17] C. D. Boeira *et al.*, "A comprehensive study on different silicon-containing interlayers for a-C:H adhesion on ferrous alloys," *Thin Solid Films*, vol. 645, pp. 351–357, 2018, doi: 10.1016/j.tsf.2017.10.043.
- [18] C. D. Boeira, L. M. Leidens, Â. E. Crespi, M. E. H. Maia da Costa, C. A. Figueroa, and A. F. Michels, "Adhesion of hydrogenated amorphous carbon films on ferrous alloy by intermediate nitrogen plasma treatment in silicon-containing interlayers," *Vacuum*, vol. 167, pp. 21–27, 2019, doi: 10.1016/j.vacuum.2019.05.019.
- [19] M. Nöthe, U. Breuer, F. Koch, H. J. Penkalla, W. P. Rehbach, and H. Bolt, "Investigation of the structure and properties of a-C:H coatings with metal and silicon containing interlayers," *Applied Surface Science*, vol. 179, no. 1–4, pp. 122–128, 2001, doi: 10.1016/S0169-4332(01)00274-4.
- [20] Z. H. Xie, R. Singh, A. Bendavid, P. J. Martin, P. R. Munroe, and M. Hoffman, "Contact damage evolution in a diamond-like carbon (DLC) coating on a stainless steel substrate," *Thin Solid Films*, vol. 515, no. 6, pp. 3196–3201, 2007, doi: 10.1016/j.tsf.2006.01.035.

- [21] G. Capote, V. J. Trava-Airoldi, and L. F. Bonetti, "Plasma treatments for metallic surface modification to obtain highly adherent diamond-like carbon coatings," *IEEE Trans. Plasma Sci.*, vol. 42, no. 6, pp. 1742–1746, 2014, doi: 10.1109/TPS.2014.2320854.
- [22] K. A. H. Al Mahmud, M. A. Kalam, H. H. Masjuki, H. M. Mobarak, and N. W. M. Zulkifli, "An updated overview of diamond-like carbon coating in tribology," *Critical Reviews in Solid State and Materials Sciences*, vol. 40, no. 2, pp. 90–118, 2015, doi: 10.1080/10408436.2014.940441.
- [23] A. Li *et al.*, "Investigation of mechanical and tribological properties of super-thick DLC films with different modulation ratios prepared by PECVD," *Mater. Res. Express*, vol. 6, no. 8, 2019, doi: 10.1088/2053-1591/ab1f5d.
- [24] M. Cui, J. Pu, J. Liang, L. Wang, G. Zhang, and Q. Xue, "Corrosion and tribocorrosion performance of multilayer diamond-like carbon film in NaCl solution," *RSC Adv.*, vol. 5, no. 127, pp. 104829–104840, 2015, doi: 10.1039/c5ra21207c.
- [25] F. Cemin, C. D. Boeira, and C. A. Figueroa, "On the understanding of the silicon-containing adhesion interlayer in DLC deposited on steel," *Tribol. Int.*, vol. 94, pp. 464–469, 2016, doi: 10.1016/j.triboint.2015.09.044.
- [26] S. Delfani-Abbariki, A. Abdollah-zadeh, S. M. M. Hadavi, M. Abedi, and S. M. R. Derakhshandeh, "Enhancing the adhesion of diamond-like carbon films to steel substrates using silicon-containing interlayers," *Surf. Coatings Technol.*, vol. 350, pp. 74–83, 2018, doi: 10.1016/j.surfcoat.2018.06.055.
- [27] H. Cao *et al.*, "Microstructure, mechanical and tribological properties of multilayer Ti-DLC thick films on Al alloys by filtered cathodic vacuum arc technology," *Mater. Des.*, vol. 198, 2021, doi: 10.1016/j.matdes.2020.109320.
- [28] Y. Lu, G. Huang, and L. Xi, "Tribological and mechanical properties of the multi-layer DLC film on the soft copper substrate," *Diamond and Related Materials*, vol. 94, pp. 21–27, 2019, doi: 10.1016/j.diamond.2019.02.019.
- [29] S. S. Hadinata, M. T. Lee, S. J. Pan, W. T. Tsai, C. Y. Tai, and C. F. Shih, "Electrochemical performances of diamond-like carbon coatings on carbon steel, stainless steel, and brass," *Thin Solid Films*, 2013, vol. 529, pp. 412–416, doi: 10.1016/j.tsf.2012.05.041.

- [30] S. E. Mousavi, N. Naghshehkesh, M. Amirnejad, H. Shammakhi, and A. Sonboli, "Corrosion performance and tribological behavior of diamond-like carbon based coating applied on Ni–Al–bronze alloy," *Trans. Nonferrous Met. Soc. China (English Ed.)*, vol. 31, no. 2, pp. 499–511, 2021, doi: 10.1016/S1003-6326(21)65512-7.
- [31] O. J. Suarez, J. J. Olaya, M. F. Suarez, and S. E. Rodil, "Corrosion resistance of decorative chromium films obtained from trivalent chromium solutions," *Journal of the Chilean Chemical Society*, vol. 57, no. 1. p. 977, 2012.
- [32] V. S. Protsenko and F. I. Danilov, "Chromium electroplating from trivalent chromium baths as an environmentally friendly alternative to hazardous hexavalent chromium baths: Comparative study on advantages and disadvantages," *Clean Technologies and Environmental Policy*, vol. 16, no. 6. pp. 1201–1206, 2014, doi: 10.1007/s10098-014-0711-1.
- [33] J. Li *et al.*, "The Hardness and Corrosion Properties of Trivalent Chromium Hard Chromium," *Materials Sciences and Applications*, vol. 08, no. 13. pp. 1014–1026, 2017, doi: 10.4236/msa.2017.813074.
- [34] J. K. Dennis and T. E. Such, *Nickel and Chromium Plating*, 3rd ed. 1993.
- [35] I. Plating Resources, "Electroplated metals," 2014.
<http://www.plating.com/electroplatingmetals.htm> (accessed Sep. 15, 2020).
- [36] S. Podgoric, B. J. Jones, R. Bulpett, G. Troisi, and J. Franks, "Diamond-like carbon/epoxy low-friction coatings to replace electroplated chromium," *Wear*, vol. 267, no. 5–8, pp. 996–1001, 2009, doi: 10.1016/j.wear.2009.01.014.
- [37] M. Kaneko, M. Hiratsuka, A. Alanazi, H. Nakamori, K. Namiki, and K. Hirakuri, "Surface reformation of medical devices with DLC coating," *Materials (Basel)*, vol. 14, no. 2, pp. 1–10, 2021, doi: 10.3390/ma14020376.
- [38] I. Richardson, "Guide to Nickel Aluminium Bronze for Engineers," *Copper Development Association*. p. 100, 2016, [Online]. Available:
https://www.nickelinstitute.org/~media/Files/MediaCenter/News/20160205-Guide_to_Nickel_Aluminium_Bronze_for_Engineers.ashx?la=en.

- [39] Q. Luo, Z. Wu, Z. Qin, L. Liu, and W. Hu, "Surface modification of nickel-aluminum bronze alloy with gradient Ni-Cu solid solution coating via thermal diffusion," *Surf. Coatings Technol.*, vol. 309, pp. 106–113, 2017, doi: 10.1016/j.surfcoat.2016.11.013.
- [40] R. J. K. Wood, K. R. Stokes, J. A. Wharton, R. C. Barik, G. Kear, and F. C. Walsh, "The corrosion of nickel-aluminium bronze in seawater," *Corros. Sci.*, vol. 47, no. 12, pp. 3336–3367, 2005.
- [41] Q. Chen *et al.*, "Effect of SiN_x interlayer thickness on adhesion and friction properties of diamond-like carbon films," *Diam. Relat. Mater.*, vol. 94, pp. 186–193, 2019, doi: 10.1016/j.diamond.2019.01.024.
- [42] Â. E. Crespi *et al.*, "Substrate Bias Voltage Tailoring the Interfacial Chemistry of a-SiC_x:H: A Surprising Improvement in Adhesion of a-C:H Thin Films Deposited on Ferrous Alloys Controlled by Oxygen," *ACS Applied Materials and Interfaces*, vol. 11, no. 19, pp. 18024–18033, 2019, doi: 10.1021/acsami.9b03597.
- [43] N. Dwivedi *et al.*, "Probing the role of an atomically thin SiN_x interlayer on the structure of ultrathin carbon films," *Sci. Rep.*, vol. 4, 2014, doi: 10.1038/srep05021.
- [44] W. Yang, D. Xu, Y. Gao, L. Hu, P. Ke, and J. Chen, "Microstructure, adhesion, in vitro corrosion resistance and tribological behavior of (Si:N)-DLC coated pure Ti," *Diam. Relat. Mater.*, vol. 92, pp. 109–116, 2019, doi: 10.1016/j.diamond.2018.12.027.
- [45] M. Azzi, P. Amirault, M. Paquette, J. E. Klemberg-Sapieha, and L. Martinu, "Corrosion performance and mechanical stability of 316L/DLC coating system: Role of interlayers," *Surface and Coatings Technology*, vol. 204, no. 24, pp. 3986–3994, 2010, doi: 10.1016/j.surfcoat.2010.05.004.
- [46] F. Cemin, C. D. Boeira, and C. A. Figueroa, "On the understanding of the silicon-containing adhesion interlayer in DLC deposited on steel," *Tribology International*, vol. 94, pp. 464–469, 2016, doi: 10.1016/j.triboint.2015.09.044.

- [47] L. M. Leidens, Â. E. Crespi, C. D. Boeira, F. G. Echeverrigaray, and C. A. Figueroa, "Hydrogen plasma etching mechanism at the a-C:H/a-SiC_x:H interface: A key factor for a-C:H adhesion," *Applied Surface Science*, vol. 455, pp. 1179–1184, 2018, doi: 10.1016/j.apsusc.2018.05.203.
- [48] Q. Y. Chen, K. M. Shih, Y. H. Shen, Y. Luo, and R. Li, "Effects of SiN_x interlayer on characterisation of amorphous diamond-like carbon films," *Mater. Sci. Technol. (United Kingdom)*, vol. 31, no. 6, pp. 703–708, 2015, doi: 10.1179/1743284714Y.0000000646.
- [49] Y. Yu, S. Shironita, K. Souma, and M. Umeda, "Effect of chromium content on the corrosion resistance of ferritic stainless steels in sulfuric acid solution," *Heliyon*, vol. 4, no. 11, 2018, doi: 10.1016/j.heliyon.2018.e00958.
- [50] E. A. Culpan and A. G. Foley, "The detection of selective phase corrosion in cast nickel aluminium bronze by acoustic emission techniques," *Journal of Materials Science*, vol. 17, no. 4, pp. 953–964, 1982, doi: 10.1007/BF00543513.
- [51] E. S. Skilbred, "Corrosion of Nickel-Aluminium Bronze," 2016.
- [52] J. Wang, J. Pu, G. Zhang, and L. Wang, "Interface architecture for superthick carbon-based films toward low internal stress and ultrahigh load-bearing capacity," *ACS Appl. Mater. Interfaces*, vol. 5, no. 11, pp. 5015–5024, 2013, doi: 10.1021/am400778p.
- [53] "Chrome plating," REX plating, 2000.
- [54] A. Müller, H. Nicolai, and W. Luther, "Survey on technical and economic feasibility of the available alternatives for chromium trioxide on the market in hard/functional and decorative chrome plating," Germany, 2020.
- [55] H. J. Lunk, "Discovery, properties and applications of chromium and its compounds," *ChemTexts*, vol. 1, no. 1, 2015, doi: 10.1007/s40828-015-0007-z.
- [56] E. Svenson, "DuraChrome Hard Chromium Plating," *Plat. Resour.*, no. 321, pp. 1–40, 2006.
- [57] L. M. I. Raj, "Analysis of Hard Chromium Coating Defects and its Prevention Methods," *International Journal of Engineering and Advanced Technology*, vol. 2, no. 5, pp. 427–432, 2013.

- [58] Copper Development Association, "Aluminum bronze alloys — corrosion resistance guide," *Materials & Design*, vol. 4, no. 1. p. 694, 1983, doi: 10.1016/0261-3069(83)90227-3.
- [59] J. A. Wharton, R. C. Barik, G. Kear, R. J. K. Wood, K. R. Stokes, and F. C. Walsh, "The corrosion of nickel-aluminium bronze in seawater," *Corros. Sci.*, vol. 47, no. 12, pp. 3336–3367, 2005, doi: 10.1016/j.corsci.2005.05.053.
- [60] D. K. Kaithari, "Development of Corrosion Resistance Coatings for Sea Water Pipeline," *Int. J. Students' Res. Technol. Manag.*, vol. 4, no. 2, pp. 24–29, 2016, doi: 10.18510/ijstrtm.2016.421.
- [61] L. Boiteau, "Amino Acid N-Carboxy Anhydride," *Encyclopedia of Astrobiology*. p. 136, 2011, doi: DOI 10.1007/978-3-642-11274-4.
- [62] "Carbon Isotopes as a Geochemical Tracer," *Encyclopedia of Astrobiology*. p. 7, 2014, doi: DOI 10.1007/978-3-642-27833-4_228-2.
- [63] J. Reitner and V. Thiel, "Carbon isotopes," in *Encyclopedia of Earth Sciences Series*, 2018, p. 12.
- [64] "Covalent bonding : Orbitals," pp. 540–575.
- [65] "Gina_Peschel-Handout.pdf." 2011, [Online]. Available: http://www.physik.fu-berlin.de/einrichtungen/ag/ag-reich/lehre/Archiv/ss2011/docs/Gina_Peschel-Handout.pdf.
- [66] S. K. Tiwari, V. Kumar, A. Huczko, R. Oraon, A. De Adhikari, and G. C. Nayak, "Magical Allotropes of Carbon: Prospects and Applications," *Critical Reviews in Solid State and Materials Sciences*, vol. 41, no. 4. pp. 257–317, 2016, doi: 10.1080/10408436.2015.1127206.
- [67] P. S. Karthik, A. L. Himaja, and S. P. Singh, "Carbon-allotropes: Synthesis methods, applications and future perspectives," *Carbon Letters*, vol. 15, no. 4. pp. 219–237, 2014, doi: 10.5714/CL.2014.15.4.219.
- [68] L. Liu, F. Lu, J. Tian, S. Xia, and Y. Diao, "Electronic and optical properties of amorphous carbon with different sp^3/sp^2 hybridization ratio," *Applied Physics A: Materials Science and Processing*, vol. 125, no. 5. 2019, doi: 10.1007/s00339-019-2660-3.

- [69] Y. Lin, P. Mallet, and L. Roux, "These Functionalization of two-dimensional nanomaterials based on graphene," Ecole Doctorale de Physique et Sciences de la Matière (ED), 2014.
- [70] A. Sahu, A. Jain, and A. Gulbake, "the Role of Carbon Nanotubes in Nanobiomedicines," *International Journal of Pharmacy and Pharmaceutical Sciences*, vol. 9, no. 6. p. 235, 2017, doi: 10.22159/ijpps.2017v9i6.18522.
- [71] S. Aisenberg and R. Chabot, "Ion-Beam Deposition of Thin Films of Diamond like Carbon," *J. Vac. Sci. Technol.*, vol. 8, no. 1, pp. 112–112, 1971, doi: 10.1116/1.1316258.
- [72] W. Jacob and W. Möller, "On the structure of thin hydrocarbon films," *Appl. Phys. Lett.*, vol. 63, no. 13, pp. 1771–1773, 1993, doi: 10.1063/1.110683.
- [73] D. C. Sutton, G. Limbert, D. Stewart, and R. J. K. Wood, "The friction of diamond-like carbon coatings in a water environment," *Friction*, vol. 1, no. 3. pp. 210–221, 2013, doi: 10.1007/s40544-013-0023-1.
- [74] F. Cemin *et al.*, "The influence of different silicon adhesion interlayers on the tribological behavior of DLC thin films deposited on steel by EC-PECVD," *Surf. Coatings Technol.*, vol. 283, pp. 115–121, 2015, doi: 10.1016/j.surfcoat.2015.10.031.
- [75] L. F. Bonetti, G. Capote, L. V. Santos, E. J. Corat, and V. J. Trava-Airoldi, "Adhesion studies of diamond-like carbon films deposited on Ti6Al4V substrate with a silicon interlayer," *Thin Solid Films*, vol. 515, no. 1. pp. 375–379, 2006, doi: 10.1016/j.tsf.2005.12.154.
- [76] Y. Jeon, Y. S. Park, H. J. Kim, B. Hong, and W. S. Choi, "Tribological properties of ultrathin DLC films with and without metal interlayers," *J. Korean Phys. Soc.*, vol. 51, no. 3, pp. 1124–1128, 2007, doi: 10.3938/jkps.51.1124.
- [77] Y. Ye, S. Jia, D. Zhang, W. Liu, and H. Zhao, "A study for anticorrosion and tribological behaviors of thin/thick diamond-like carbon films in seawater," *Surf. Topogr. Metrol. Prop.*, vol. 6, no. 1, 2018, doi: 10.1088/2051-672X/aaab9a.

- [78] P. L. Sant' Ana *et al.*, "Study of a-C:H thin films deposited by Plasma Immersion Ion Implantation for mechanical and tribological applications," *Nanoscale Reports*, vol. 2, no. 3, pp. 24–32, 2019, doi: 10.26524/nr1933.
- [79] T. Oshiro, F. Begum, M. Yamazato, A. Higa, T. Maehama, and M. Toguchi, "The structures and properties of a-C:H films deposited at a wide range of relative hydrogen gas flow rate by RF sputtering," in *Thin Solid Films*, 2006, vol. 506–507, pp. 92–95, doi: 10.1016/j.tsf.2005.08.096.
- [80] Y. Wang, Y. Ye, H. Li, L. Ji, J. Chen, and H. Zhou, "A magnetron sputtering technique to prepare a-C:H films: Effect of substrate bias," *Applied Surface Science*, vol. 257, no. 6, pp. 1990–1995, 2011, doi: 10.1016/j.apsusc.2010.09.040.
- [81] Y. Xiao, X. Tan, L. Jiang, T. Xiao, P. Xiang, and W. Yan, "The effect of radio frequency power on the structural and optical properties of a-C:H films prepared by PECVD," *J. Mater. Res.*, vol. 32, no. 7, pp. 1231–1238, 2017, doi: 10.1557/jmr.2016.522.
- [82] P. Chabert and N. Braithwaite, *Physics of Radio-Frequency Plasmas*, 1st ed. New York: United Kingdom at the University Press, Cambridge, 2001.
- [83] L. Holland and S. M. Ojha, "Deposition of hard and insulating carbonaceous films on an r.f. target in a butane plasma," *Thin Solid Films*, vol. 38, no. 2, 1976, doi: 10.1016/0040-6090(76)90214-5.
- [84] H. J. Ryu, S. H. Kim, and S. H. Hong, "Effect of deposition pressure on bonding nature in hydrogenated amorphous carbon films processed by electron cyclotron resonance plasma enhanced chemical vapor deposition," *Mater. Sci. Eng. A*, vol. 277, no. 1–2, pp. 57–63, 2000, doi: 10.1016/S0921-5093(99)00566-3.
- [85] J. Camparo and G. Fathi, "Effects of rf power on electron density and temperature, neutral temperature, and Te fluctuations in an inductively coupled plasma," *Journal of Applied Physics*, vol. 105, no. 10, 2009, doi: 10.1063/1.3126488.
- [86] Z. Sun, X. Shi, and E. Liu, "High rate deposition of diamond-like carbon films by magnetically enhanced plasma CVD," *Thin Solid Films*, vol. 355, pp. 146–150, 1999, doi: 10.1016/S0040-6090(99)00484-8.

- [87] S. Mahant, R. Sharma, N. Sharma, S. K. Pradhan, and P. K. Barhai, "Correlation of Mechanical Properties with Surface Morphology of Diamond-Like Carbon Films Deposited By Plasma Enhanced Chemical Vapour Deposition Technique," *Int. J. Innov. Res. Sci. Eng. Technol.*, vol. 3, no. 8, pp. 15510–15517, 2014, doi: 10.15680/ijirset.2014.0308060.
- [88] P. Poolcharuansin, *เอกสารประกอบการสอนรายวิชา ฟิสิกส์พลาสมาเบื้องต้น*, 1st ed. 2014.
- [89] H. T. Kim and S. H. Sohn, "Effects of applied power on hydrogenated amorphous carbon (a-C:H) film deposition by low frequency (60 Hz) plasma-enhanced chemical vapor deposition (PECVD)," *Vacuum*, vol. 86, no. 12, pp. 2148–2151, 2012, doi: 10.1016/j.vacuum.2012.06.007.
- [90] G. Bräuer, "Magnetron Sputtering," in *Comprehensive Materials Processing*, vol. 4, 2014, pp. 57–73.
- [91] S. Swann, "Magnetron sputtering," *Physics in Technology*, vol. 19, no. 2, pp. 67–75, 1988, doi: 10.1088/0305-4624/19/2/304.
- [92] D. Depla, S. Mahieu, and J. E. Greene, "Sputter deposition processes," vol. 281, pp. 1–36.
- [93] VAC AERO International, "An Introduction to Vacuum Pumps," 2016. <https://vacaero.com/information-resources/vacuum-pump-technology-education-and-training/1039-an-introduction-to-vacuum-pumps.html> (accessed Sep. 10, 2020).
- [94] Z. Li, L. Li, Y. Zhao, G. Bu, and P. Shu, "Theoretical and experimental study of dry scroll vacuum pump," *Vacuum*, vol. 84, no. 3, pp. 415–421, 2009, doi: 10.1016/j.vacuum.2009.09.005.
- [95] P. Vacuum, "Working with turbo pumps." 2003, [Online]. Available: [files%5C1915%5CTurbos.pdf](#).
- [96] F. Leiter, "Molecular and turbomolecular pumps," *Handbook of Vacuum Technology*, pp. 419–462, 2016, doi: 10.1002/9783527688265.ch10.
- [97] Pfeiffer vacuum, "Operating instructions; PKR36X/IKR36X," vol., no. pp. 1–60.
- [98] Brooks Instrument, "Installation and operation manual; Heated digital capacitance manometers." pp. 1–64, 2011.

- [99] A. A. Zavarian *et al.*, “Behaviors of capacitive and Pirani vacuum gauges: Case study on time effect,” *Vakuum in Forschung und Praxis*, vol. 30, no. 5, pp. 39–44, 2018, doi: 10.1002/vipr.201800693.
- [100] “NI PXI-2564 16-SPST Topology,” 2022. https://zone.ni.com/reference/en-XX/help/375472H-01/switch/2564_16_spst/ (accessed Apr. 20, 2022).
- [101] N. Lopez-Pinto *et al.*, “Deposition and characterisation of sputtered molybdenum oxide thin films with hydrogen atmosphere,” *Appl. Surf. Sci.*, vol. 563, 2021, doi: 10.1016/j.apsusc.2021.150285.
- [102] H. A. Bland *et al.*, “Superconducting Diamond on Silicon Nitride for Device Applications,” *Sci. Rep.*, vol. 9, no. 1, Dec. 2019, doi: 10.1038/s41598-019-39707-z.
- [103] H. Y. Tai, C. H. Cheng, P. S. Wang, C. I. Wu, and G. R. Lin, “Nearly warm white-light emission of silicon-rich amorphous silicon carbide,” *RSC Adv.*, vol. 5, no. 127, pp. 105239–105247, Dec. 2015, doi: 10.1039/c5ra19775a.
- [104] X. Li, H. Miao, and H. Zhu, “Deposition and characterization of diamond-like carbon films by electron cyclotron resonance microwave plasma enhanced unbalanced magnetron sputtering,” *Chem. Eng. Trans.*, vol. 66, pp. 19–24, 2018, doi: 10.3303/CET1866004.
- [105] Y. M. Bashouti *et al.*, “Hybrid Silicon Nanowires: From Basic Research to Applied Nanotechnology,” in *Nanowires - Recent Advances*, InTech, 2012, pp. 177–210.
- [106] P. S. N. Barimar, C. M. Doyle, B. Naydenov, and J. J. Boland, “Study of the effect of thermal treatment on morphology and chemical composition of silicon-on-insulator,” *J. Vac. Sci. Technol. B, Nanotechnol. Microelectron. Mater. Process. Meas. Phenom.*, vol. 34, no. 4, p. 041806, Jul. 2016, doi: 10.1116/1.4955067.
- [107] M. Gao, H. W. Du, J. Yang, L. Zhao, J. Xu, and Z. Q. Ma, “Variation of passivation behavior induced by sputtered energetic particles and thermal annealing for ITO/SiO_x/Si system,” *Chinese Phys. B*, vol. 26, no. 4, p. 045201, Apr. 2017, doi: 10.1088/1674-1056/26/4/045201.

- [108] M. Y. Bashouti, J. Ristein, H. Haick, and S. Christiansen, "A Non-Oxidative Approach Towards Hybrid Silicon Nanowire- Based Solar Cell Heterojunctions," *Hybrid Mater.*, vol. 1, no. 1, pp. 2–14, Jun. 2013, doi: 10.2478/hyma-2013-0002.
- [109] M. M. Kamble *et al.*, "Hydrogenated Silicon Carbide Thin Films Prepared with High Deposition Rate by Hot Wire Chemical Vapor Deposition Method," *J. Coatings*, pp. 1–11, Feb. 2014, doi: 10.1155/2014/905903.
- [110] Y. Lei, J. Jiang, Y. Wang, T. Bi, and L. Zhang, "Structure evolution and stress transition in diamond-like carbon films by glancing angle deposition," *Appl. Surf. Sci.*, vol. 479, pp. 12–19, 2019, doi: 10.1016/j.apsusc.2019.02.063.
- [111] Q. Tian *et al.*, "Diamond/ β -SiC film as adhesion-enhanced interlayer for top diamond coatings on cemented tungsten carbide substrate," *J. Mater. Sci. Technol.*, vol. 33, no. 10, pp. 1097–1106, 2017, doi: 10.1016/j.jmst.2017.06.005.
- [112] B. Bessaïs, "Ultrathin porous silicon films," in *Handbook of Porous Silicon: 2nd ed.*, vol. 1–2, Springer International Publishing, 2018, pp. 143–151.
- [113] S. Chandran, N. Begam, and J. K. Basu, "Dispersion of polymer grafted nanoparticles in polymer nanocomposite films: Insights from surface X-ray scattering and microscopy," *J. Appl. Phys.*, vol. 116, no. 22, 2014, doi: 10.1063/1.4902964.
- [114] T. C. Huang, R. Gilles, and G. Will, "Thin-film thickness and density determination from X-ray reflectivity data using a conventional power diffractometer," *Thin Solid Films*, vol. 230, no. 2, pp. 99–101, 1993, doi: 10.1016/0040-6090(93)90499-F.
- [115] J. S. Custer *et al.*, "Density of amorphous Si," *Appl. Phys. Lett.*, vol. 64, no. 4, pp. 437–439, 1994, doi: 10.1063/1.111121.
- [116] K. Rakesh Tej Kumar, M. Ramakrishna, and G. Durga Sukumar, "A review on PV cells and nanocomposite-coated PV systems," *International Journal of Energy Research*, vol. 42, no. 7, John Wiley and Sons Ltd, pp. 2305–2319, Jun. 10, 2018, doi: 10.1002/er.4002.

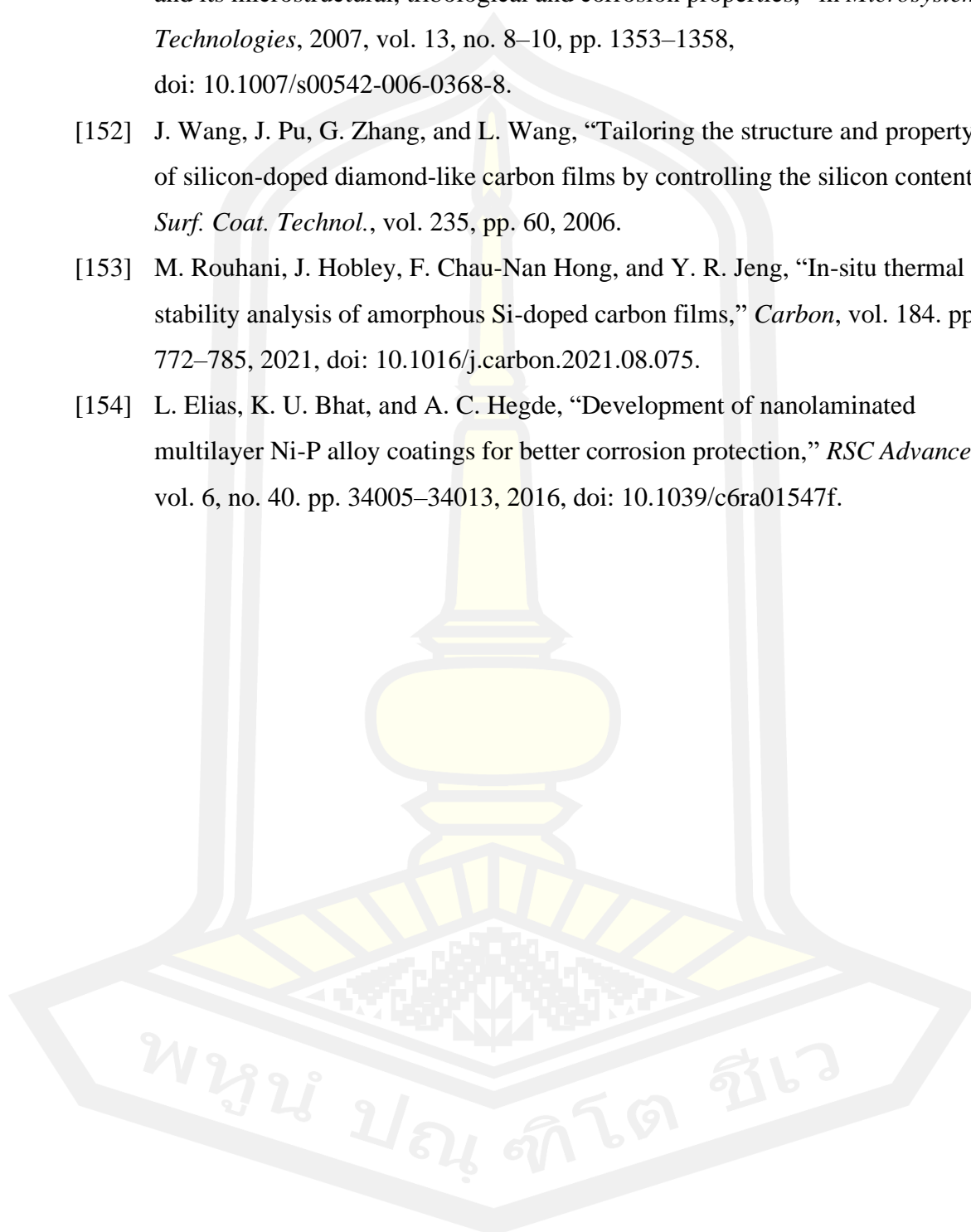
- [117] W. C. Oliver and G. M. Pharr, "An improved technique for determining hardness and elastic modulus using load and displacement sensing indentation experiments," *J. Mater. Res.*, vol. 7, no. 6, pp. 1564–1583, 1992, doi: 10.1557/jmr.1992.1564.
- [118] P. Danesh, B. Pantchev, J. Wiezorek, B. Schmidt, and D. Grambole, "Effect of hydrogen on hardness of amorphous silicon," *Applied Physics A: Materials Science and Processing*, vol. 102, no. 1, pp. 131–135, 2011, doi: 10.1007/s00339-010-6026-0.
- [119] K. P. Henty, "Light Sensing Performance of Amorphous Silicon Thin Film Pin," no. December, 2016.
- [120] S. Peter, K. Graupner, D. Grambole, and F. Richter, "Comparative experimental analysis of the a-C:H deposition processes using CH₄ and C₂H₂ as precursors," *J. Appl. Phys.*, vol. 102, no. 5, 2007, doi: 10.1063/1.2777643.
- [121] C. Lenardi, P. Piseri, V. Briois, C. E. Bottani, A. Li Bassi, and P. Milani, "Near-edge X-ray absorption fine structure and Raman characterization of amorphous and nanostructured carbon films," *J. Appl. Phys.*, vol. 85, no. 10, pp. 7159–7167, May 1999, doi: 10.1063/1.370527.
- [122] R. Hatada, S. Flege, M. N. Ashraf, A. Timmermann, C. Schmid, and W. Ensinger, "The influence of preparation conditions on the structural properties and hardness of diamond-like carbon films, prepared by plasma source ion implantation," *Coatings*, vol. 10, no. 4, Apr. 2020, doi: 10.3390/coatings10040360.
- [123] J. Robertson, "Diamond-like amorphous carbon," *Mater. Sci. Eng. R Reports*, vol. 37, pp. 129–281, 2002.
- [124] K. Niranjana Reddy *et al.*, "Double side coating of DLC on silicon by RF-PECVD for AR application," in *Procedia Engineering*, 2014, vol. 97, pp. 1416–1421, doi: 10.1016/j.proeng.2014.12.423.
- [125] H. Sheng, W. Xiong, S. Zheng, C. Chen, S. He, and Q. Cheng, "Evaluation of the sp^3/sp^2 ratio of DLC films by RF-PECVD and its quantitative relationship with optical band gap," *Carbon Lett.*, vol. 31, no. 5, pp. 929–939, Oct. 2021, doi: 10.1007/s42823-020-00199-x.

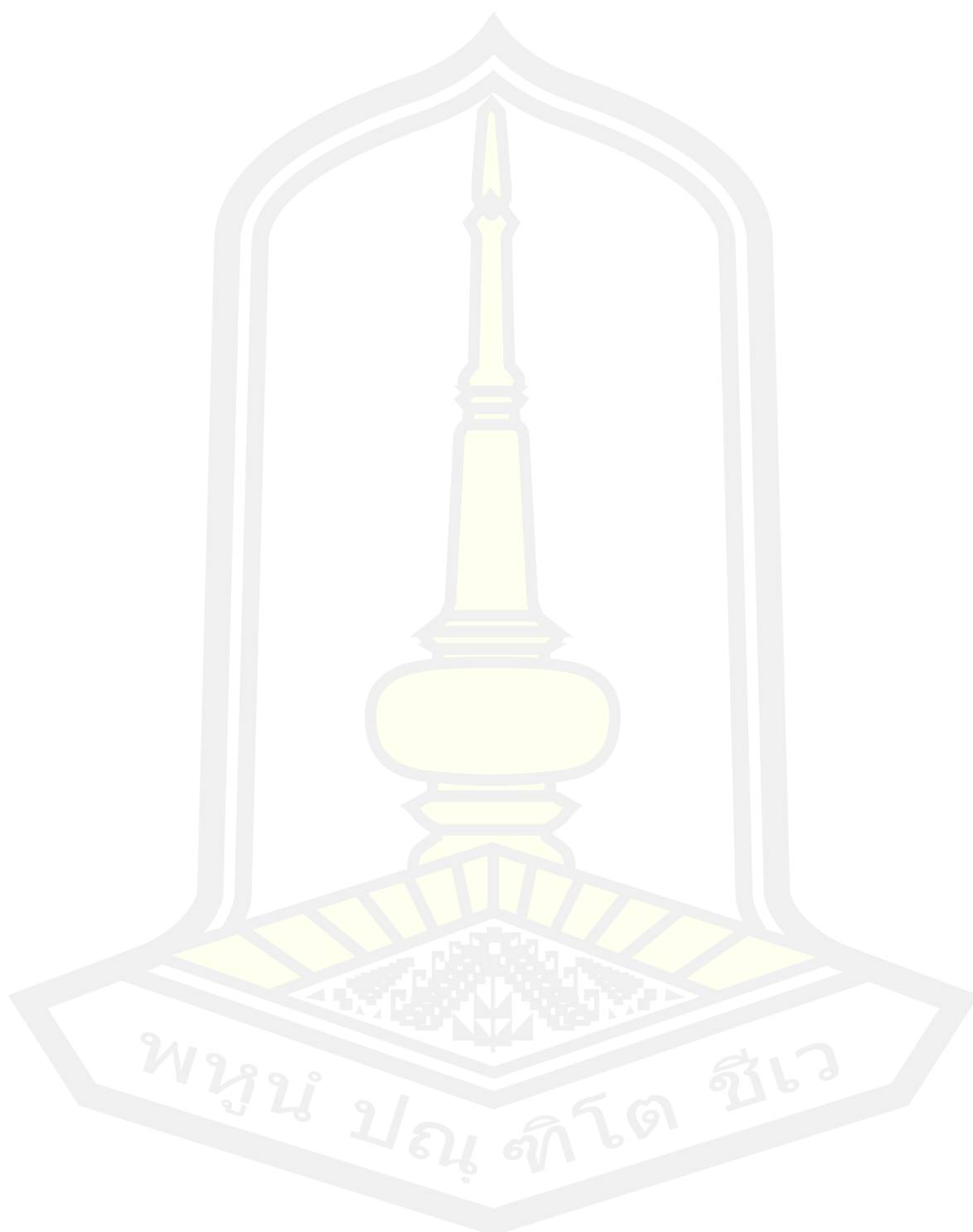
- [126] W. G. Cui, Q. B. Lai, L. Zhang, and F. M. Wang, "Quantitative measurements of sp^3 content in DLC films with Raman spectroscopy," *Surf. Coatings Technol.*, vol. 205, no. 7, pp. 1995–1999, Dec. 2010, doi: 10.1016/j.surfcoat.2010.08.093.
- [127] J. Jiang, J. Hao, P. Wang, and W. Liu, "Superlow friction of titanium/silicon codoped hydrogenated amorphous carbon film in the ambient air," *J. Appl. Phys.*, vol. 108, no. 3, Aug. 2010, doi: 10.1063/1.3462469.
- [128] E. Vaghri, Z. Khalaj, and M. Ghoranneviss, "Preparation and characterization of diamond-like carbon films on various substrates by PECVD system," *Stud. Univ. Babes-Bolyai Chem.*, no. 3, pp. 143–150, 2012, [Online]. Available: <https://www.researchgate.net/publication/239938218>.
- [129] L. Qiang, B. Zhang, K. Gao, Z. Gong, and J. Zhang, "Hydrophobic, mechanical, and tribological properties of fluorine incorporated hydrogenated fullerene-like carbon films," *Friction*, vol. 1, no. 4, pp. 350–358, Dec. 2013, doi: 10.1007/s40544-013-0031-1.
- [130] Y. Wang, K. Gao, and J. Zhang, "Structure, mechanical, and frictional properties of hydrogenated fullerene-like amorphous carbon film prepared by direct current plasma enhanced chemical vapor deposition," *J. Appl. Phys.*, vol. 120, no. 4, Jul. 2016, doi: 10.1063/1.4959216.
- [131] B. Zhang, K. Gao, Y. Yu, and J. Zhang, "Super-Lubricious, Fullerene-like, Hydrogenated Carbon Films," in *Fullerenes and Relative Materials - Properties and Applications*, InTech, 2018.
- [132] J. S. Song, Y. S. Park, and N. H. Kim, "Hydrophobic anti-reflective coating of plasma-enhanced chemical vapor deposited diamond-like carbon thin films with various thicknesses for dye-sensitized solar cells," *Applied Sciences (Switzerland)*, vol. 11, no. 1, pp. 1–9, 2021, doi: 10.3390/app11010358.
- [133] T. Schlebrowski, M. Fritz, L. Beucher, Y. Wang, S. Wehner, and C. B. Fischer, "The Growth Behavior of Amorphous Hydrogenated Carbon a-C:H Layers on Industrial Polycarbonates—A Weak Interlayer and a Distinct Dehydrogenation Zone," *C*, vol. 7, no. 3, p. 59, 2021, doi: 10.3390/c7030059.

- [134] B. Ghosh, F. Guzmán-Olivos, and R. Espinoza-González, “Plasmon-enhanced optical absorption with graded bandgap in diamond-like carbon (DLC) films,” *J. Mater. Sci.*, vol. 52, no. 1, pp. 218–228, 2017, doi: 10.1007/s10853-016-0324-7.
- [135] U. Rittihong *et al.*, “Synchrotron-based spectroscopic analysis of diamond-like carbon films from different source gases,” *Radiat. Phys. Chem.*, vol. 173, 2020, doi: 10.1016/j.radphyschem.2020.108944.
- [136] H. Bückle, “PROGRESS IN MICRO-INDENTATION’ HARDNESS TESTING,” *Metallurgical Reviews*, vol. 4, no. 1. pp. 49–100, 1959, doi: 10.1179/095066059790421746.
- [137] A. Moreno-Barcenas, J. Alvarado Orozco, J. González, G. C. Rodríguez, J. González-Hernández, and A. Garcia, “Diamond-Like Carbon Coatings on Plasma Nitrided M2 Steel: effect of deposition parameters on adhesion properties,” *Resour. Sci.*, vol. 37, no. 1, pp. 355–360, 2018.
- [138] M. A. Hassan, A. R. Bushroa, and R. Mahmoodian, “Identification of critical load for scratch adhesion strength of nitride-based thin films using wavelet analysis and a proposed analytical model,” *Surf. Coatings Technol.*, vol. 277, pp. 216–221, 2015, doi: 10.1016/j.surfcoat.2015.07.061.
- [139] I. Solomon and A. Sarma, “Tribological and corrosion performance of DLC coating on sintered Al alloy,” *Mater. Res. Express*, vol. 6, no. 4, 2019, doi: 10.1088/2053-1591/aafae2.
- [140] P. R. Prabhu, P. Hiremath, D. Prabhu, M. C. Gowrishankar, and B. M. Gurumurthy, “Chemical, electrochemical, thermodynamic and adsorption study of EN8 dual-phase steel with ferrite-martensite structure in 0.5 M H₂SO₄ using pectin as inhibitor,” *Chem. Pap.*, vol. 75, no. 11, pp. 6083–6099, Nov. 2021, doi: 10.1007/s11696-021-01773-x.
- [141] F. Studio Srl, “Polarisation Measurements Used for Corrosion Rates Determination,” *Journal of Sustainable Energy*, vol. 1, no. 1. pp. 2067–5538, 2010, [Online]. Available: <http://www.energy-cie.ro/archives/2010/n1-1-14.pdf>.

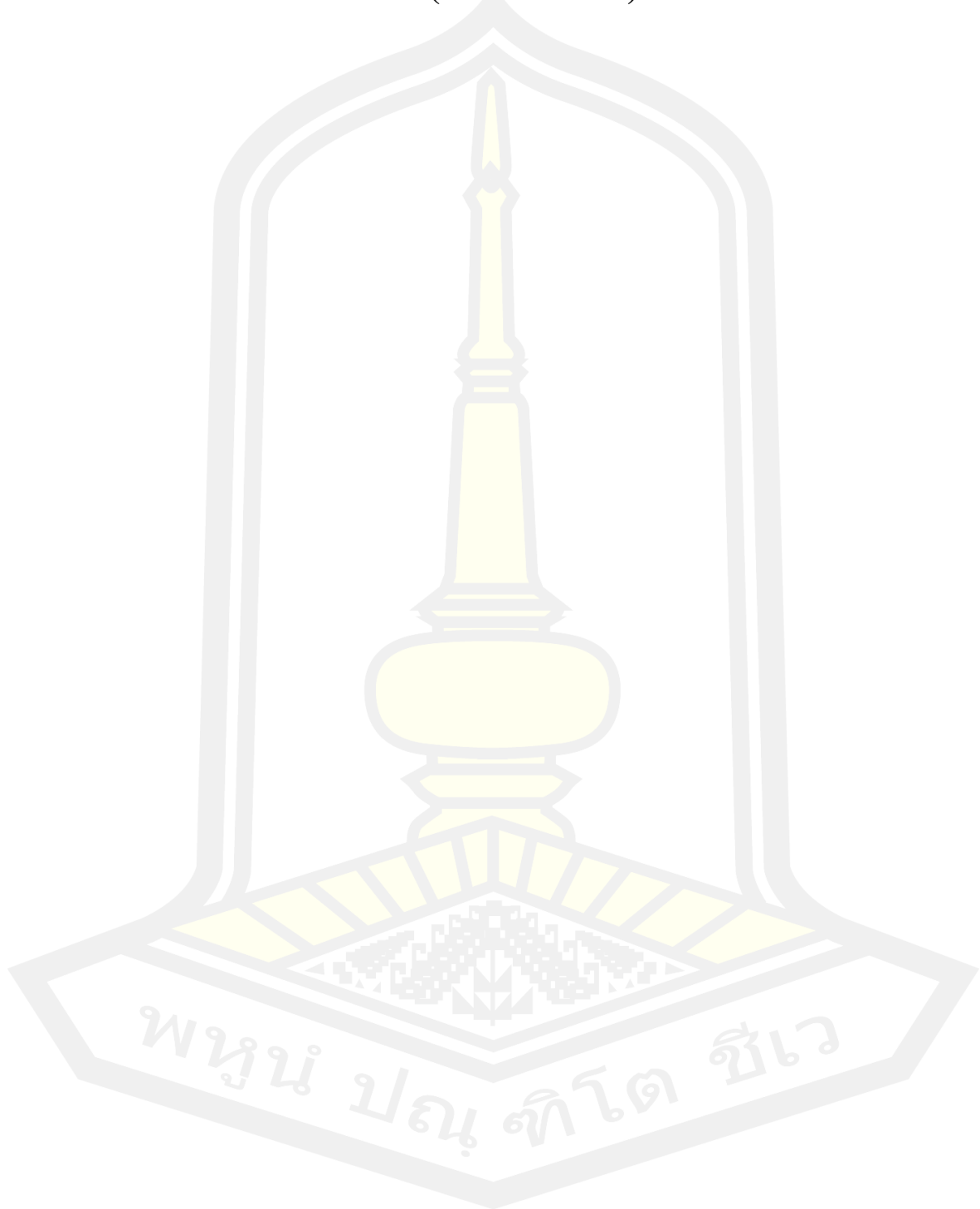
- [142] M. A. Amin, N. El-Bagoury, M. Saracoglu, and M. Ramadan, "Electrochemical and corrosion behavior of cast re-containing inconel 718 alloys in sulphuric acid solutions and the effect of Cl^- ," *Int. J. Electrochem. Sci.*, vol. 9, no. 9, pp. 5352–5374, 2014.
- [143] K. Kakaei, M. D. Esrafil, and A. Ehsani, "Graphene and Anticorrosive Properties," *Interface Science and Technology*, vol. 27, pp. 303–337, 2019, doi: 10.1016/B978-0-12-814523-4.00008-3.
- [144] S. Tunmee *et al.*, "Investigation of pitting corrosion of diamond-like carbon films using synchrotron-based spectromicroscopy," *Journal of Applied Physics*, vol. 120, no. 19, 2016, doi: 10.1063/1.4967799.
- [145] N. W. Khun, E. Liu, G. C. Yang, W. G. Ma, and S. P. Jiang, "Structure and corrosion behavior of platinum/ruthenium/nitrogen doped diamondlike carbon thin films," *J. Appl. Phys.*, vol. 106, no. 1, 2009, doi: 10.1063/1.3154022.
- [146] H. G. Kim, S. H. Ahn, J. G. Kim, S. J. Park, and K. R. Lee, "Electrochemical behavior of diamond-like carbon films for biomedical applications," in *Thin Solid Films*, 2005, vol. 475, no. 1-2 SPEC. ISS., pp. 291–297, doi: 10.1016/j.tsf.2004.07.052.
- [147] I. Bouabibsa, S. Lamri, A. Alhussein, T. Minea, and F. Sanchette, "Plasma investigations and deposition of Me-DLC (Me = Al, Ti or Nb) obtained by a magnetron sputtering-RFPECVD hybrid process," *Surf. Coatings Technol.*, vol. 354, pp. 351–359, 2018, doi: 10.1016/j.surfcoat.2018.09.033.
- [148] M. Yasaka, "X-ray thin-film measurement techniques V. X-ray reflectivity measurement." pp. 1–9, 2016, [Online]. Available: papers3://publication/uuid/C23082F2-548F-4832-A28F-0B0F3D3A080C.
- [149] Y. M. Shulga, N. Y. Shulga, and Y. N. Parkhomenko, "Carbon Nanostructures Reduced From Graphite Oxide as Electrode Materials for Supercapacitors," *Izv. Vyss. Uchebnykh Zaved. Mater. Elektron. Tekhniki = Mater. Electron. Eng.*, no. 3, p. 157, 2015, doi: 10.17073/1609-3577-2014-3-157-167.
- [150] B. Abdallah, M. Kakhia, and S. A. Shaker, "Study of crystallographic, optical and sensing properties of Na_2WO_4 films deposited by thermal evaporation with several thickness," *Mater. Sci. Pol.*, 2019, doi: 10.2478/msp-2019-0080.

- [151] J. Choi, M. Kawaguchi, T. Kato, and M. Ikeyama, "Deposition of Si-DLC film and its microstructural, tribological and corrosion properties," in *Microsystem Technologies*, 2007, vol. 13, no. 8–10, pp. 1353–1358, doi: 10.1007/s00542-006-0368-8.
- [152] J. Wang, J. Pu, G. Zhang, and L. Wang, "Tailoring the structure and property of silicon-doped diamond-like carbon films by controlling the silicon content," *Surf. Coat. Technol.*, vol. 235, pp. 60, 2006.
- [153] M. Rouhani, J. Hopley, F. Chau-Nan Hong, and Y. R. Jeng, "In-situ thermal stability analysis of amorphous Si-doped carbon films," *Carbon*, vol. 184, pp. 772–785, 2021, doi: 10.1016/j.carbon.2021.08.075.
- [154] L. Elias, K. U. Bhat, and A. C. Hegde, "Development of nanolaminated multilayer Ni-P alloy coatings for better corrosion protection," *RSC Advances*, vol. 6, no. 40, pp. 34005–34013, 2016, doi: 10.1039/c6ra01547f.





APPENDIX
(Publications)



Publication in Materials Research Express (2022) : First authorMaterials Research Express

PAPER • OPEN ACCESS**Improvement of corrosion resistance and mechanical properties of chrome plating by diamond-like carbon coating with different silicon-based interlayers**To cite this article: Anthika Lakhonchai *et al* 2022 *Mater. Res. Express* **9** 055604View the [article online](#) for updates and enhancements.**You may also like**

[Effects of Ammonia/Methane Mixtures on Characteristics of Plasma Enhanced Chemical Vapor Deposition n-Type Carbon Films](#)
Hsiang-Chun Hsueh, Huei-Cheng Li, Donyau Chiang *et al.*

[Effect of nitrogen in the properties of diamond-like carbon \(DLC\) coating on Ti-Al-V substrate](#)
L. S Almeida, A R M Souza, L H Costa *et al.*

[Effect of atomic hydrogen exposure on hydrogenated amorphous carbon thin films](#)
Yuichi Haruyama, Daiki Morimoto, Akira Heya *et al.*

**IOP ebooks™**

Bringing together innovative digital publishing with leading authors from the global scientific community.

Start exploring the collection—download the first chapter of every title for free.

Materials Research Express



PAPER

OPEN ACCESS

RECEIVED
16 February 2022REVISED
21 April 2022ACCEPTED FOR PUBLICATION
22 April 2022PUBLISHED
6 May 2022

Original content from this work may be used under the terms of the Creative Commons Attribution 4.0 licence.

Any further distribution of this work must maintain attribution to the author(s) and the title of the work, journal citation and DOI.



Improvement of corrosion resistance and mechanical properties of chrome plating by diamond-like carbon coating with different silicon-based interlayers

Anthika Lakhonchai^{1,*}, Artit Chingsungnoen^{1,*}, Phitsanu Poolcharuansin¹, Narong Chanlek², Sarayut Tunmee³ and Ukit Rittihong³¹ Technological Plasma Research Unit, Department of Physics, Faculty of Science, Maharakham University, Maha Sarakham 44150, Thailand² Synchrotron Light Research Institute (Public Organization), Nakhon Ratchasima 30000, Thailand

* Authors to whom any correspondence should be addressed.

E-mail: L.anthika26@gmail.com and artit.c@msu.ac.th**Keywords:** silicon-based interlayers, radio frequency-plasma chemical vapor deposition, adhesive properties, mechanical properties, corrosive properties, chrome plating

Abstract

In this study, the silicon-based interlayers for hydrogenated amorphous carbon (a-C:H) coating on a chromium-plated substrate are presented. The a-Si, a-Si:N, a-Si:H and a-Si_xC_yH interlayers with a thickness of about 306 nm were deposited by direct current magnetron sputtering technique. The a-C:H films with a thickness of about 317 nm was prepared as a top layer by radio frequency-plasma chemical vapor deposition. The a-C:H films with silicon-based interlayers were characterized by x-ray photoelectron spectroscopy, Raman spectroscopy, field emission-secondary electron microscopy, nanoindentation, micro-scratching, and electrochemical corrosion measurements in terms of their structure, morphology, mechanical and adhesive properties, and corrosion resistance. The a-C:H films with an a-Si:H interlayer exhibit the lowest corrosion current density, which is about 36 times lower than that of the uncoated chromium-plated substrate. In addition, the hardness increases from 8.48 GPa for the uncoated substrate to 20.98 GPa for the a-C:H/a-Si:H sample. The mixing with hydrogen gas could reduce the residual oxygen during the deposition process, which could reduce the Si-O bonding and improve the adhesion strength between the a-C:H film and the a-Si:H interlayer and the a-Si:H interlayer and the substrate. Therefore, it can be concluded that the protective a-C:H coating with an a-Si:H interlayer has excellent potential to significantly improve the durability and extend the service life of materials used in abrasive and corrosive environments.

1. Introduction

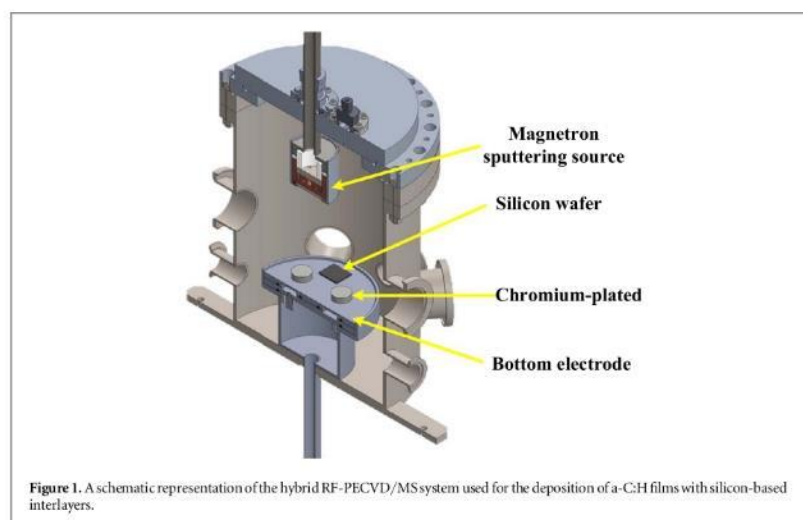
Thin film coating technology is used in various industrial applications to improve material properties due to its excellent characteristics. Several researchers have attempted to investigate the improvement of protective surface engineering by thin film coating for mechanical, tribological and corrosion protection applications [1, 2]. One interesting coating used for these purposes is diamond-like carbon (DLC) coating [3]. DLC coatings are widely used in applications where low friction, high wear resistance and low corrosion rate are of utmost importance due to the combined properties of diamond and graphite [3]. The outstanding and diverse properties of DLC films include mechanical properties, which can increase hardness, and tribological properties, which can reduce the coefficient of friction of the material surface, resulting in low wear rate and improved performance [4]. In addition, DLC films also provide excellent chemical inertness, resulting in high corrosion resistance [5]. DLC films can be used in the magnetic data storage industry for the protective coating of magnetic storage disks and their read/write heads [6]. In the automotive industry, DLC films are applied to the piston ring and cylinder block to reduce the wear rate with constant abrasion and extend the service life [7]. Due to the high

atomic density of DLC films, they are used in the food packaging industry as a coating on PET bottles, fresh and dry food packaging to act as a gas diffusion barrier and extend the shelf life of food [8]. These properties are mainly determined by the sp^2 and sp^3 carbon hybridization and hydrogen content of the DLC film structure [9]. Hydrogenated amorphous carbon (a-C:H) is a type of DLC film with sp^3 carbon content of 5%–50%, hydrogen content of 5%–60%, density of 1.0–2.5 g cm⁻³, hardness of 10–30 GPa, and low friction coefficient of 0.1 [10]. In addition, the properties of the a-C:H film can be tuned by the deposition method and process parameters. However, the major drawback of DLC application is the poor adhesion to the substrate for metallic substrates due to the high internal compressive stress in the film, the inconsistency of chemical bonding, and the incompatibility of thermal expansion coefficients between the film and the substrate, which leads to the delamination of the film and failure [11, 12]. Therefore, the deposition of DLC directly on the substrate limits the thickness of the film and industrial applications.

Several previous researches have studied and solved this problem; they have been grouped into four main methods. The first method is metal doping into the DLC network structure (metal-doped DLC); this method can directly reduce the internal stresses and improve the adhesion and structural properties of the film [13]. The second method is growing the interlayer on the substrate before DLC deposition; the atom of the interlayer can create a strong chemical bond at the interface between the substrate and the DLC film [14]. The third method is plasma surface treatment of the substrate and interlayer to increase the surface energy [15]. The last method, fabrication of a multilayer structure, e.g., a soft layer and a hard layer, is a viable approach to reduce internal stresses and improve adhesion and film thickness [16]. In previous studies, Nöthe *et al* [17] and Xie *et al* [18] have shown that the interlayer coating can generate more robust and more chemical bonds at the interface than metal-doped DLC. Cemin *et al* [19] showed that the coating detaches from the steel substrate after the deposition process even though the substrate was bombarded with argon plasma. Multilayer deposition is a suitable method for the deposition of DLC with good adhesion when a thickness of more than 1 μm is required. Cui *et al* [20] reported that the DLC single layer with silicon transition layer limits the thickness to a range between 1 and 3 μm , while the multilayer DLC coatings can increase the thickness to about 8.0 μm . Therefore, it can be concluded that the interlayers are necessary for DLC coatings on any substrates.

In recent decades, DLC coatings have been successfully used in research and development for coating on various types of metal substrates. Cemin *et al* [21] and Delfani-Abbariki *et al* [22] reported the improvement of adhesion properties of DLC films deposited on a steel substrate using a silicon-based interlayer. Cao *et al* [23] deposited multilayer thick (~10 μm) Ti doped DLC films on an aluminum alloy substrate and reported that the mechanical and tribological properties of the film depend on the microstructure. Mousavi *et al* [24] fabricated DLC films with chromium carbide interlayers to improve the mechanical properties, tribological behavior, and corrosion performance of nickel-aluminum-bronze alloys. Lu *et al* [25] investigated the multilayer DLC coating on a soft copper substrate to improve the tribological and mechanical properties. Hadinata *et al* [26] investigated and compared the electrochemical behavior of DLC films deposited on stainless steel, carbon steel and brass substrates in NaCl solution. All the above literature reviews show that DLC films are being investigated as protective coatings on various substrates, especially metallic substrates, to improve mechanical, tribological and corrosion protection applications. However, according to our literature review, there are no studies on DLC protective coatings on chromium-plated substrates. A chrome plating is a chromium layer that is electroplated onto a metal. Usually, there are two requirements for the chromium-plated layer: decorativeness and hardness. Decorative chrome plating with a thin layer of chromium (~1 μm thick) is used to improve luster or mirror-like shine, improve esthetics, and serve as an easy-to-clean protective layer, making it desirable for various consumer products. Chrome plating is mainly used for bathtub faucets, showers and bathroom fixtures. Although the decorative chromium-plated layer is corrosion resistant in most environments, it tends to form microscopic cracks at the grain boundary during or after chromium plating due to the stresses become greater than the strength of the coating [27]. These cracks form a pattern that intertwines with and sometimes extends to the base metal. A corrosive liquid or gas can penetrate the base metal. Some studies have shown that the use of DLC coatings instead of chromium plating could improve the mechanical, tribological and corrosive properties of the material [28, 29]. However, in addition to this substitution, another possibility is to use the DLC coating directly on a chromium layer, maintaining the esthetics and bright properties of the chromium layer. In addition, DLC coating can solve the corrosion problem of chromium layer and also improve the mechanical and tribological properties of base metals. Therefore, their service life will be prolonged even if they are used near the coast. Although the color of chrome plating changes from blond to shiny black after coating, they can be used for decorative applications to enhance the product value.

Therefore, the present work aims to improve the corrosion resistance and mechanical properties of chromium-plated films by coating the a-C:H film with silicon-based interlayers to improve adhesion strength. The influence of four different types of interlayers prepared by magnetron sputtering technique (MS), including amorphous silicon (a-Si), amorphous silicon nitride (a-Si:N), hydrogenated amorphous silicon (a-Si:H), and hydrogenated amorphous silicon carbide (a-Si_xC_y:H), was investigated. The a-C:H film was prepared using the



radio frequency-plasma enhanced chemical vapor deposition technique (RF-PECVD). The influence of the silicon-based interlayers on the morphology, structural, corrosive, mechanical, and adhesive properties of a-C:H was systematically investigated.

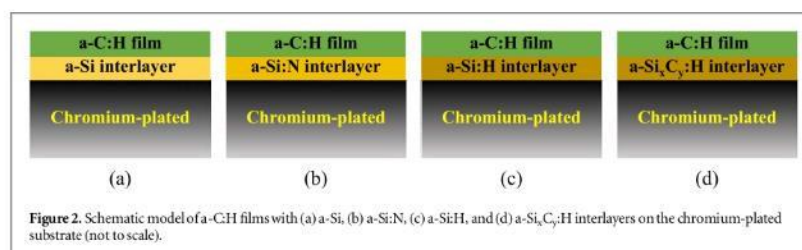
2. Experimental details

In this section, the preparation of the chromium-plated substrate and the cleaning process are presented in detail. The coating process, including the coating system, is described. In addition, you will find information on the characterization of the coating.

2.1. Substrate preparation and coating procedure

In this experiment, the chromium-plated substrate and silicon wafer were used as substrates for a-C:H coating with different silicon-based interlayers. The electroplating process was performed on a brass sample with a diameter of 20 mm and a height of 4 mm. A thick nickel layer was electroplated for corrosion resistance, followed by a thin chromium layer for decorative purposes. The nickel-plated brass was prepared from a solution bath of nickel chloride, nickel sulphate, and boric acid with a DC voltage of -5 V and an immersion time of 8 min. The coating thickness of the nickel was adjusted to about 5 μm . Then, the chromium coating was prepared from a chromate solution (chromium sulphate) with a DC voltage of -7 V and an immersion time of 2.5 min. The coating thickness of the chromium was set to about 0.5 μm . It is used to increase the reflectivity of the nickel coating on a substrate. Therefore, in this work, chromium-plated substrate means nickel-chromium plating, in which nickel and chromium were electrodeposited to form a double-layer surface on a substrate. The mirror-polished silicon wafers (125 mm diameter and 525 ± 15 μm thick) with n-type asinine-doped (100) orientation and resistivity of 0.001 – 0.004 $\Omega\cdot\text{cm}$ were cut into 1×1 cm^2 pieces using a diamond-headed ball tip. Before coating, these substrates were chemically cleaned in an ultrasonic bath with acetone ($\times 1$), methanol ($\times 2$), and deionized water ($\times 3$) sequentially for 10 min each, and then dried with filtered warm air.

A hybrid deposition system combining the techniques of RF-PECVD and MS (called hybrid RF-PECVD/MS system) was used to deposit a-C:H film with different silicon-based interlayers. As shown in figure 1, the magnetron sputtering source was located at the top of the vacuum chamber, while the RF power was installed in the bottom electrode. The chromium-plated substrates and silicon wafers were mounted on the bottom electrode. The p-type silicon with copper backing plate (2 inches diameter and 0.125 inch thick, 99.999% purity), was used as the sputtering target. Argon was used as the sputtering gas, while nitrogen, hydrogen, and acetylene were used as reactive gases that could be doped into the silicon-based interlayer structure during deposition. The flow rates of these gases were controlled with mass flow controllers. RF power supply with a frequency of 13.56 MHz was connected to the matching box and the automatic matching network controller to

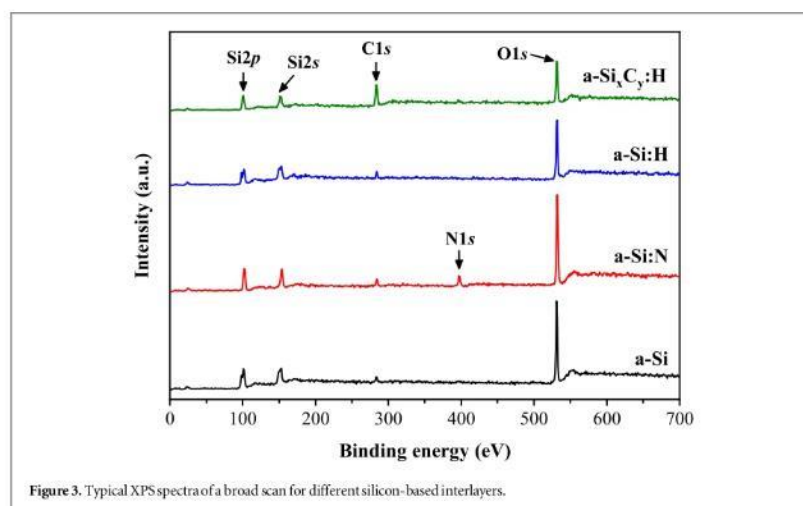


achieve maximum power dissipation. Acetylene mixed with argon and hydrogen was used as a precursor for a-C:H coating. A base pressure of about 1.33×10^{-3} Pa can be achieved with a turbomolecular pump supported by a scroll pump. The pump speed was adjusted by the pendulum valve to maintain the working pressure. The coating processes, including plasma cleaning of the substrate, interlayer coating, and a-C:H coating, which were performed sequentially using the hybrid RF-PECVD/MS system, are described in detail below. Before coating, the substrates were physically and chemically cleaned by bombarding them with a mixture of argon and hydrogen plasma to remove the surface contamination and oxide layer on the top substrate surface. The RF power of 300 W was used to generate the Ar-H₂ plasma, and the processing time was 10 min. Then, the silicon-based interlayer was deposited under the same working pressure of about 6.67 Pa, and the thickness was adjusted to about 300 nm according to the deposition rate. During the deposition of the interlayer, the bottom electrode was connected to the ground. Then, the a-C:H layers were deposited continuously with a power of RF of 300 W and a controlled thickness of about 300 nm. The working pressure for the a-C:H coating was kept at 0.93 Pa, and the flow rate of acetylene, argon and hydrogen remained the same at 10 sccm. The influence of four types of interlayers (a-Si, a-Si:N, a-Si:H, and a-Si_xC_y:H) was investigated. The schematic model of the a-C:H films with different silicon-based interlayers is shown in figure 2.

2.2. Thin-film characterizations

The chemical structure of four types of silicon-based interlayers with a controlled thickness of about 50 nm, including a-Si, a-Si:N, a-Si:H, and a-Si_xC_y:H, was analyzed by x-ray photoelectron spectroscopy (XPS). XPS measurements were performed using a PHI5000 Versa Probe II, ULVAC-PHI, Japan, at the joint research facility SUT-NANOTEC-SLRI, Synchrotron Light Research Institute (SLRI), Thailand. Monochromatic Al-K_α x-ray (1,486.6 eV) was used as the excitation source. The Si2p fine scan was performed with a binding energy range of about 95–108 eV and a step size of 0.05 eV.

The a-C:H films deposited on four silicon-based interlayers with a total thickness of about 600 nm were characterized by different techniques. Morphology, structure, hardness, adhesion, and corrosion resistance were investigated using field emission secondary electron microscopy (FESEM), Raman spectroscopy, nanoindentation, micro-scratching, and electrochemical corrosion measurements. The surface and cross-sectional morphology of the thin films on the silicon wafer was observed by FESEM (HITACHI, model SU8030) at magnification of 50 and 100 kx in secondary electron mode. The structure formation of the thin films on the chromium-plated substrate was analyzed by Raman spectroscopy (Bruker, model Senterra). The surface of the a-C:H films was excited using an Ar laser with a wavelength of 532 nm and a power of 12.5 mW. The scan range was between 50–4,450 cm⁻¹ (3–5 cm⁻¹ resolution) with an aperture size of 50 μm slit. Each spectrum was a co-addition of 30 scans with an integration time of 2 s. The Raman spectra of the samples were deconvoluted with Gaussian peaks using Origin software (version 2018) to determine the intensity ratio of D and G peaks (I_D/I_G) or the I_D/I_G ratio, peak positions, and full width at half maximum (FWHM). The hardness of the coatings and substrate was measured by nanoindentation (Fischer Scope, model HM2000). The Berkovich pyramidal indenter was used with a maximum load of 3 mN for the dynamic mode with 3 times repeatable and a load range of 2–60 mN for the enhanced stiffness procedure (ESP) mode. The adhesive property of a-C:H's with different silicon-based interlayers for chromium-plated substrates was evaluated using the micro-scratching with the critical load values. A progressive load of 0.5–50 N with a scratching speed of 2 mm min⁻¹ and a loading rate of 10 N min⁻¹ was used to achieve the scratching behavior. The corrosion behavior of the thin films deposited on the chromium-plated substrate was measured electrochemically. The samples were exposed to a 3.5 wt% NaCl solution for 30 min. Polarization curves were obtained with an applied potential of -1,000 to 1,000 mV and a sampling rate of 1 mV s⁻¹.



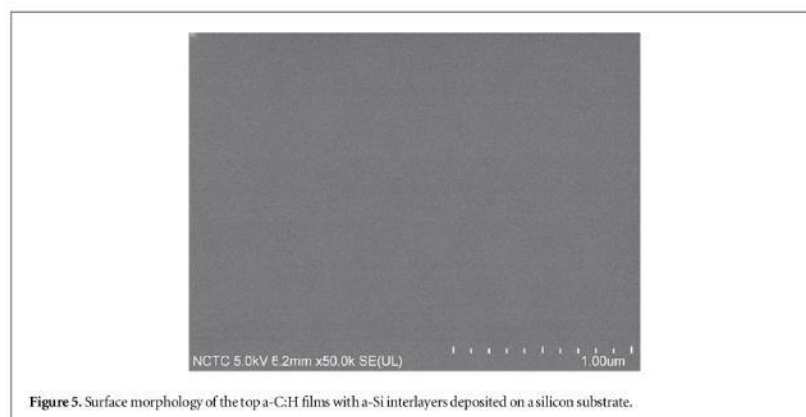
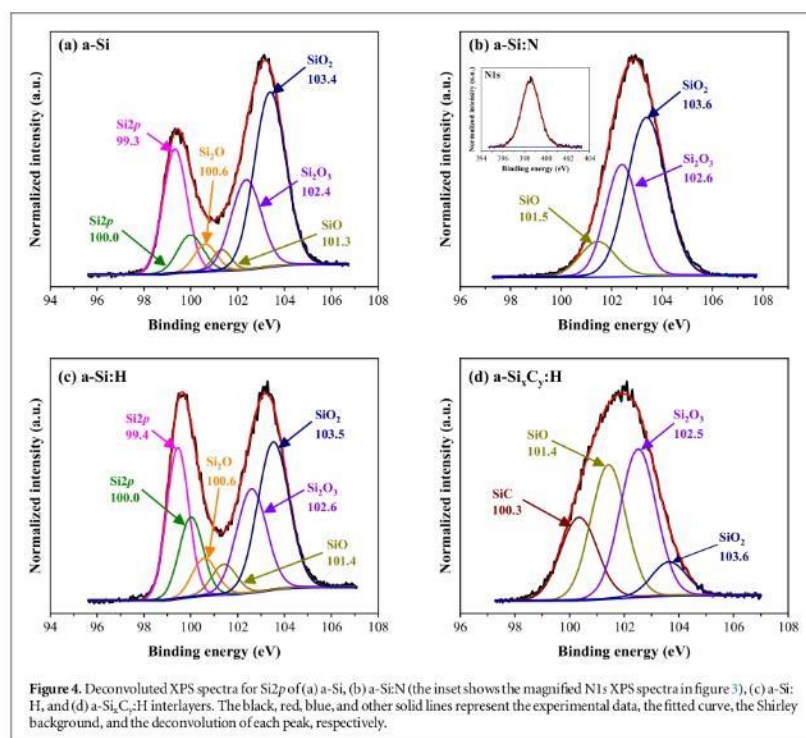
3. Results and discussion

3.1. Structural analysis of the silicon-based interlayer

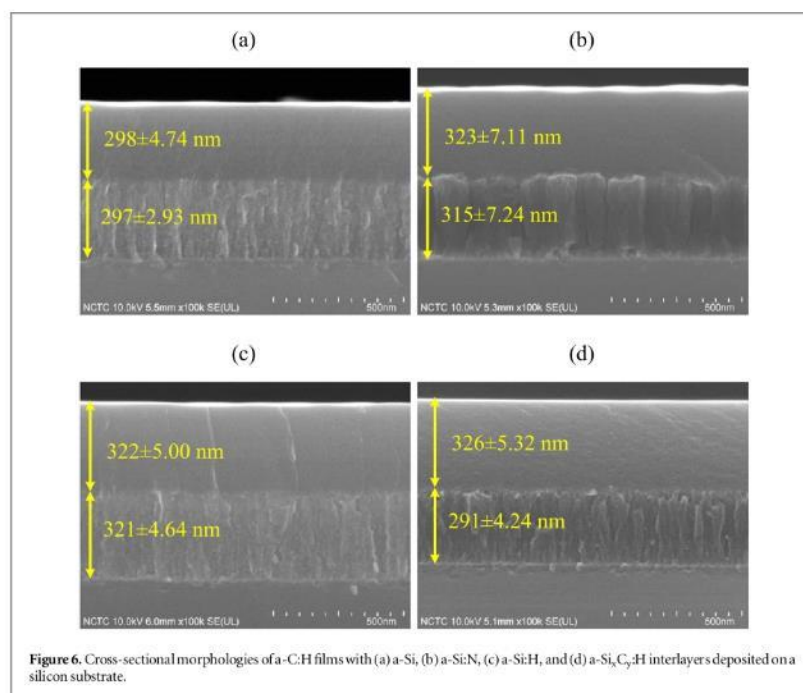
The chemical state of the different interlayers, including a-Si, a-Si:N, a-Si:H, and a-Si_xC_y:H, deposited on the silicon substrate was investigated by XPS measurements. The results of the broad scan XPS spectra for the different silicon-based interlayers, shown in figure 3, mainly contain three peaks at ~102, ~153, and ~532 eV, corresponding to the silicon (Si2p and Si2s) and oxygen (O1s) peaks, respectively [30]. In addition, the peak at ~397 eV of the a-Si:N sample corresponds to nitrogen (N1s) and the peak at ~285 eV of the a-Si_xC_y:H sample corresponds to carbon (C1s), which are dominant compared to the other samples and are associated with the doping gases. The silicon peaks originate from the silicon target, which serves as the main precursor material for silicon-based interlayer deposition. The oxygen-rich peaks are likely to originate mainly from the adsorption process during the measurement and some residual gases in the vacuum chamber during the deposition process [31]. The deconvoluted XPS spectra for Si2p of all interlayers are shown in figure 4. It can be seen that the Si2p spectrum was decomposed into six peaks located at binding energies of about ~99.3, ~100.0, ~100.6, ~101.4 ± 0.08, ~102.5 ± 0.10, and ~103.5 ± 0.10 eV. These peaks were observed from the functional group of Si2p, Si₂O, SiO, Si₂O₃, and SiO₂ and are in agreement with those in other works [32, 33]. It was found that the Si2p spectrum contains two spin splitting peaks, which may be overlapping spin-orbit components resulting in an asymmetric peak shape. The silicon dioxide and suboxides, including Si₂O, SiO, Si₂O₃ and SiO₂, correspond to +1, +2, +3, and +4 oxidation states, respectively. In addition, the a-Si_xC_y:H interlayer also exhibits the Si-C peak with a binding energy of ~100.3 eV, as shown in figure 4(d), which means that the carbon dopant can be bound to the silicon core atoms [34]. In the a-Si:N interlayer, the nitrogen dopant atoms are not bonded to the silicon atoms but are located between the silicon structures, which is consistent with the XPS spectra of the N1s peak, as shown in the inset of figure 4(b).

3.2. Morphology of a-C:H with different silicon-based interlayers

The surface and cross-sectional FESEM images of the a-C:H films with different silicon interlayers were performed to observe their morphological properties. Figure 5 shows the representative surface topography of the a-C:H films with a-Si interlayer as they were deposited. The surface morphology of a sample was detected on the top surface of the a-C:H films. It can be seen that the surface morphology is very homogeneous, smooth and dense with no microparticle defects as also reported by Song *et al* [35] and Schlebrowski [36]. The cross-sectional images of the as-deposited a-C:H films with (a) a-Si, (b) a-Si:N, (c) a-Si:H, and (d) a-Si_xC_y:H interlayers with an average thickness of each layer are shown in figure 6. On the cross-sectional images, the a-C:H layer and the interlayers in all samples can be seen with an average thickness of 317 ± 12.99 and 306 ± 14.23 nm, respectively. The total average thickness of the four samples was 623 ± 13.61 nm. The cross-sectional morphology between the a-C:H layer and the interlayer shows a clear boundary at the interface without



delamination and cracking. This result implies that the a-C:H layers exhibit good adhesion to the silicon-based interlayers. This can be explained by the diffusion of the C and H atoms into the silicon interlayer component during the a-C:H growth. The cross-sectional morphology of the a-C:H films shows a smooth and dense like surface morphology, while the silicon-based interlayers exhibit a predominantly columnar structure of silicon with different grain sizes.

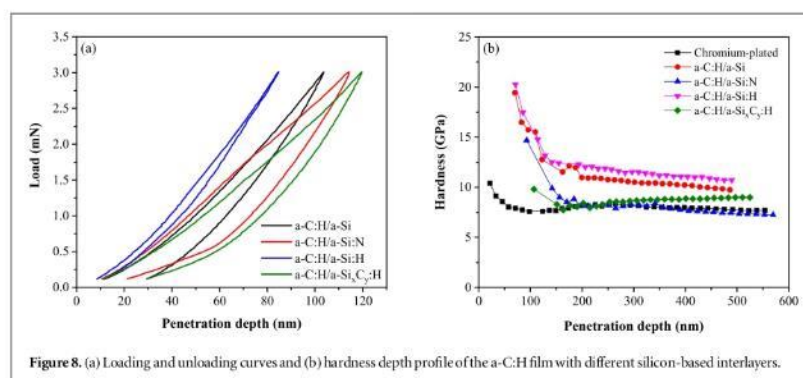
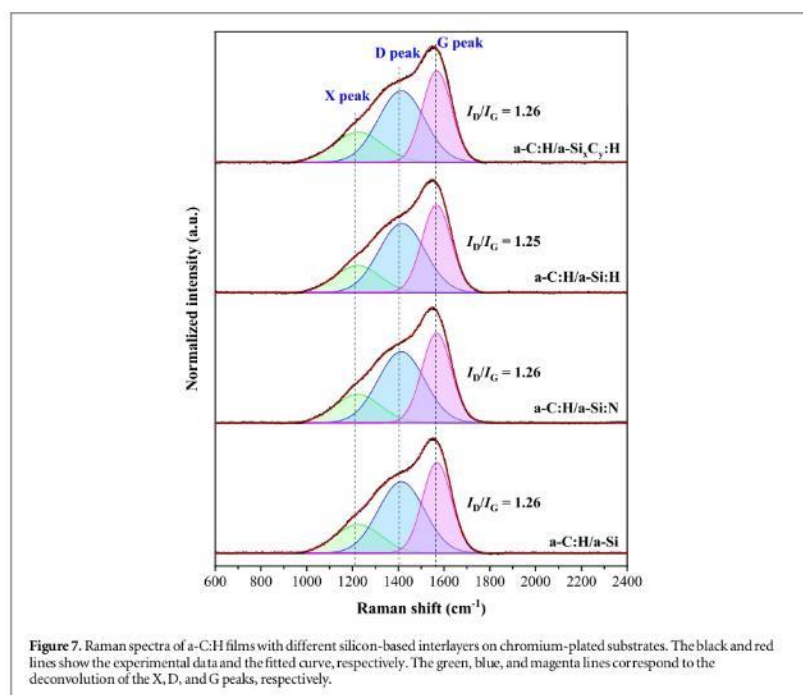


3.3. Structural analysis of a-C:H films with silicon-based interlayers

Raman spectroscopy is widely used to determine the structural and complementary information of DLC films because it detects the chemical bonds in carbon-based materials with a non-destructive method. In general, the Raman spectra of undoped amorphous carbon films with and without hydrogenation show two peaks, the D peak and the G peak. These peaks were usually excited by the oscillation of sp^2 hybridization [9]. In the present study, chrome plating was used as the substrate. To avoid the effect of laser annealing, which could lead to a graphitized diamond-like sample, a short exposure time of (2 s) with a number of 30 scans was used. The Raman spectra of a-C:H films with different silicon-based interlayers are shown in figure 7. The position of the D and G peaks of conventional a-C:H films prepared by the RF-PECVD technique are in the range of 1,334–1,370 cm^{-1} and 1,545–1,599 cm^{-1} [37, 38]. In this work, the D and G peaks were found centered in all samples in the range of 1,413–1,416 cm^{-1} and 1,567–1,569 cm^{-1} , respectively. However, the shift of the D peak depends on the impurities in the films and the occurrence of the X peak. The parameters such as I_D/I_G ratios, peak position and FWHM of the G peak were found to have similar values since the same coating conditions were used. These parameters can be related to the structure, density and location of the sp^2 cluster. In other works, it was reported that the D peak (denoted by D for disorder of graphite) is associated with the vibration of A_{1g} symmetry breathing mode of sp^2 atoms only in aromatic rings, while the G peak (denoted by G for graphite) is associated with the vibration of E_{2g} stretching mode of sp^2 atoms both in aromatic rings and chains [39]. The X peak was found at 1,222–1,225 cm^{-1} and was also observed by Qiang *et al* [40], Wang *et al* [41] and Zhang *et al* [42]. It probably originates from the vibrations of a pentagonal atomic ring in the carbon nanostructures.

3.4. Mechanical properties of a-C:H films with different silicon-based interlayers

For the protective layer on the chromium-plated substrate, the hardness of the a-C:H films is one of the most important factors for tribological application. The nanoindentation test is commonly used to evaluate the hardness of nanoscale materials and was determined by the method of Oliver and Pharr [43]. Figure 8(a) compares the loading and unloading curves of the a-C:H film with different silicon-based interlayers in dynamic mode. The results show that the a-C:H/a-Si and a-C:H/a-Si:H samples have low indentation depth, corresponding to high hardness of about 10.92 ± 0.42 and 20.98 ± 0.63 GPa, respectively. This result indicates



that a-Si and a-Si:H are good supporting interlayer for the formation of the a-C:H film. The a-C:H/a-Si:N and a-C:H/a-Si_xC_y:H show higher penetration depth with lower hardness of about 9.39 ± 0.09 and 8.55 ± 0.14 GPa, respectively. The random network of a-Si, a-Si:H and a-SiC in a-Si_xC_y:H and the nitrogen interstitial in the a-Si:N interlayers could deteriorate the bonding between C and Si and affect the structural and mechanical properties. Figure 8(b) shows the hardness depth profile in the ESP mode of the a-C:H film with different silicon-based interlayers compared to an uncoated chromium-plated substrate. In this ESP mode, the penetration depth was increased to 600 nm (~total film thickness), corresponding to an increase in load from 2 to 60 mN. It was found that the hardness decreases with increasing penetration depth and is close to the hardness value of the chromium-plated substrate. This behavior is consistent with the Bückle's rule, which recommends

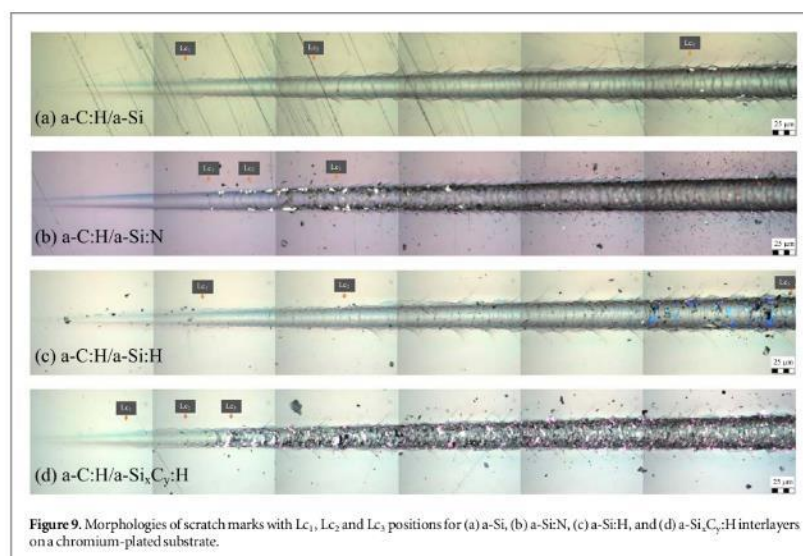


Figure 9. Morphologies of scratch marks with L_{c1} , L_{c2} and L_{c3} positions for (a) a-Si, (b) a-Si:N, (c) a-Si:H, and (d) a-Si₃C₂:H interlayers on a chromium-plated substrate.

that the penetration depth should not exceed 10% of the coating thickness to reduce the influence of the substrate [44]. It can be seen that when the penetration depth is less than 60 nm (10% of the total film thickness), the hardness depth profile is close to the dynamic mode. Therefore, it can be concluded that the a-C:H coating with the a-Si and a-Si:H interlayers can improve the hardness of the chromium-plated substrate (8.48 ± 1.41 GPa), resulting in a longer application lifetime.

3.5. Adhesive properties

Adhesive strength is a very important parameter for a-C:H films to show their properties. The micro-scratch measurements can directly reveal the adhesive behavior in terms of the value of the critical load (L_c). According to the vertical load, the scratch test was performed in a progressive mode, increasing continuously from 0.5 to 50 N. After the scratch test, the scratch behavior was observed with the optical microscope to identify three types of critical loads: The first critical load (L_{c1}) corresponds to the first signal of cohesive failure in the form of spalling and cracking in the scratch track. The second critical load (L_{c2}) corresponds to the beginning of the adhesive failure of the delamination of the film. Finally, the third critical load (L_{c3}) corresponds to the complete delamination of the coating from the scratch track and the complete removal of the interlayer from the substrate. The deposited a-C:H film (~300 nm thick) on a chromium-plated substrate without an interlayer detaches from the substrate after deposition, indicating very poor adhesion. This behavior can be explained by the high residual stress of the films and the incompatibility at the interfacial adhesion between film and substrate [45]. The values of L_{c1} , L_{c2} and L_{c3} of a-C:H films with four different interlayers were determined from the scratch marks as shown in figure 9 and the comparative values are shown in figure 10. In general, the scratching behavior includes three stages: the first stage is microcracking and partial ring cracking, the second stage is full ring cracking, delamination, and chipping and the last stage is substrate exposure [46]. Figures 9(b) and (d) show that the a-C:H films with a-Si:N and a-Si₃C₂:H interlayers delaminate and spall from the substrate and that the films are obviously fractured at the edge of the scratch track after the scratch test, indicating a poor cohesive failure mode. Figures 9(a) and (c) show higher critical load of a-C:H films with a-Si and a-Si:H interlayers, indicating good cohesion of the films and high adhesion strength between the films and the interlayer, and between the interlayer and the substrate. The a-C:H films with a-Si₃C₂:H interlayer exhibit lower L_{c1} , L_{c2} and L_{c3} than the other samples, as shown in figure 10. This behavior could be due to the strong bonding of Si-C, which can reduce the dangling bond at the interface, while the C1s peak in the XPS results indicates excessive carbon doping in the silicon network, leading to high internal stresses in the interlayer. The lowest value for the adhesion of the a-Si₃C₂:H interlayer coincides with the lowest hardness of the a-C:H/a-Si₃C₂:H sample. The adhesion strength of a-C:H films with a-Si:H interlayer show the highest L_{c1} , L_{c2} and L_{c3} values of about 2.47, 5.67, 15.15 N, respectively, indicating the plastic deformation in the conformal cracking phase and the adhesion strength

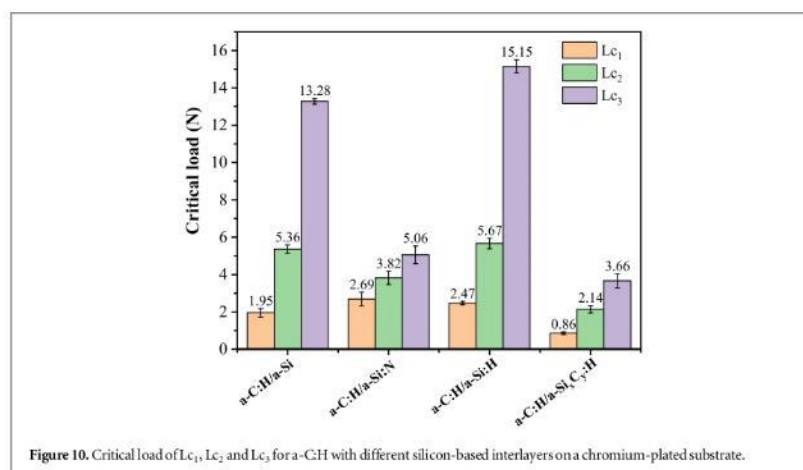


Figure 10. Critical load of Lc₁, Lc₂ and Lc₃ for a-C:H with different silicon-based interlayers on a chromium-plated substrate.

between the a-C:H film and the interlayer and a-Si:H interlayer and substrate. In the a-Si:H interlayer, the interaction between hydrogen and oxygen atoms can reduce the residual oxygen in the silicon networks (reducing the Si-O bonds). In addition, during the deposition process, the hydrogen can remove the oxide layer from the surface of the chromium plating (reducing the Cr-O bonds), which could promote the bonding of Si-C and Cr-Si between the two interfaces, resulting in the highest Lc₃ value. This behaviour could increase the resistance to adhesive failure (higher Lc₂ value) between the a-C:H layer and the a-Si:H interlayer with strong bonding at the interface with respect to the a-Si interlayer. As for the Lc₁ value, the good adhesive strength (Lc₂) of the a-C:H/a-Si:H sample should support the growth of the a-C:H layer, which has a higher Lc₁ value than the a-C:H/a-Si sample, indicating the plastic deformation in the conformal cracking phase.

3.6. Electrochemical corrosion analysis

To confirm the corrosion resistance of the a-C:H coating on the chromium-plated substrate, the electrochemical corrosion measurement was carried out for investigation with the 3.5 wt% NaCl solution at room temperature. The electrochemical corrosion measurement is an efficient method with simple procedures and high sensitivity, which reflects the lifetime and corrosion behavior of bulk materials and thin films. The corrosion behavior of the a-C:H films with different silicon-based interlayers compared to the bare chromium-plated substrate is shown in figure 11 (a). The x-axis and y-axis interceptions between the anodic and cathodic branches of the polarization curves were considered as the corrosion current density (i_{corr}) and corrosion potential (E_{corr}) [47]. Lower corrosion current density and higher corrosion potential indicate lower corrosion rate and better corrosive properties [47, 48]. From figure 11 (a), it can be seen that all a-C:H films with different silicon-based interlayers show a shift in corrosion potential to a more positive value compared to the uncoated substrate, indicating better corrosion resistance of the a-C:H film. The coating layers require a higher applied potential for dissolution or corrosion than the substrate. The corrosion current density is $0.71 \mu\text{A cm}^{-2}$ for an uncoated substrate, which is higher than the coated samples. The a-C:H/a-Si:H sample has the lowest corrosion current density ($0.02 \mu\text{A cm}^{-2}$), indicating the lowest metal loss from the material and coating. Therefore, the lowest corrosion current density means the best corrosion resistance. This result could be correlated with the hardness and adhesion strength of the a-C:H/a-Si:H coatings. Moreover, porous defects or pinholes in the films are one of the most important factors that can be associated with the corrosion behavior. Porosity (P) was determined based on polarization resistance (R_p) using equation (1) [49],

$$P = \frac{R_{pm(\text{substrate})}}{R_{p(\text{coating-substrate})}} \times 10^{-|\Delta E_{corr}/\beta_a|} \quad (1)$$

The anodic (β_a) and cathodic (β_c) Tafel slopes and the corrosion current (i_{corr}) values can be used to calculate the polarization resistance as follows [50],

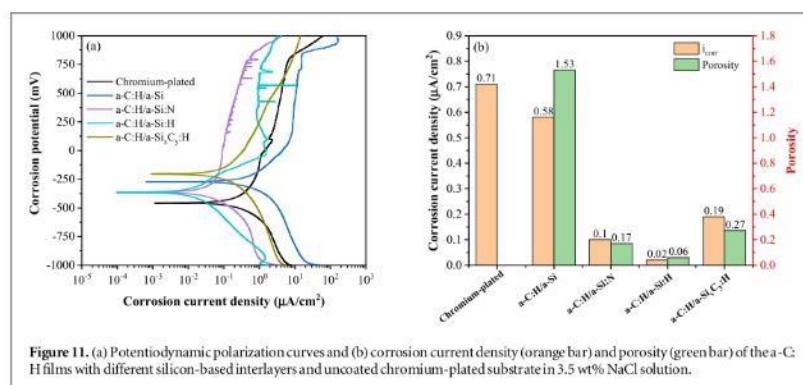


Figure 11. (a) Potentiodynamic polarization curves and (b) corrosion current density (orange bar) and porosity (green bar) of the a-C:H films with different silicon-based interlayers and uncoated chromium-plated substrate in 3.5 wt% NaCl solution.

Table 1. Electrochemical results from polarization curves for uncoated and coated substrates.

Samples	Corrosion current density ($\mu\text{A cm}^{-2}$)	β_a (V/decade)	β_c (V/decade)	Porosity
Chromium-plated	0.71	1.74	0.39	—
a-C:H/a-Si	0.58	0.30	0.24	1.53
a-C:H/a-Si:N	0.10	1.09	0.32	0.17
a-C:H/a-Si:H	0.02	0.30	0.31	0.06
a-C:H/a-Si _x C _y :H	0.19	0.65	0.35	0.27

$$R_p = \frac{\beta_a \times \beta_c}{2.3I_{corr}(\beta_a \times \beta_c)} \quad (2)$$

where $R_{pm(substrate)}$ is the polarization resistance of the substrate, $R_{p(coating-substrate)}$ is the polarization resistance of the coated film and ΔE_{corr} is the difference of the corrosion potential between the film coated and the substrate.

The calculated porosity, as shown in table 1, is consistent with the corrosion current density values. A lower porosity means a lower corrosion current density. In the case of the a-C:H/a-Si:H sample, porosity has the lowest values, corresponding to the lowest corrosion current density (best corrosion resistance) as shown in figure 11 (b). Other factors such as good adhesion also correlate with corrosion behaviour. For the a-C:H/a-Si:H sample, the porosity is lower than for the a-C:H/a-Si and a-C:H/a-Si_xC_y:H samples, resulting in better corrosion resistance. Although the a-C:H/a-Si_xC_y:H sample has the lowest adhesion properties, its corrosion resistance is better than that of the a-C:H/a-Si sample. This behaviour could be explained by the fact that the carbon and hydrogen atoms in the acetylene gas used as the dopant induce the formation of a C-sp³ matrix in the a-Si_xC_y:H interlayer, thus improving the corrosion resistance. In the case of the a-C:H/a-Si sample, the sample shows good adhesive properties but is very porous, resulting in the lowest corrosion resistance.

4. Conclusion

In this study, a-C:H films were prepared with a-Si, a-Si:N, a-Si:H, and a-Si_xC_y:H interlayers on a chromium-plated substrate. The thickness of the a-C:H films and silicon-based interlayers was controlled as 317 ± 12.99 and 306 ± 14.23 nm, respectively. The morphology between the a-C:H films and the interlayers shows a clear boundary at the interface without delamination and cracking. The Raman spectra of the a-C:H films clearly show the presence of D and G peaks with a relative intensity I_D/I_G of about 1.26, indicating the structure of the amorphous carbon films. For the silicon-based interlayers, the XPS results indicate the presence of silicon dioxide and suboxides, which is mainly due to the adsorption process during the measurement. For the a-Si_xC_y:H interlayer, the carbon dopant can be bonded to the silicon atoms to form Si-C, which has a negative effect on the adhesive properties. This behavior is probably due to the low dangling bond and high residual stress of the interlayer. The a-Si:H interlayers exhibited higher L_{C1} , L_{C2} and L_{C3} than the other silicon-based interlayers, indicating higher resistance to cohesive and adhesive failure, which should promote the corrosion resistance and hardness of the film. Therefore, based on the adhesion, hardness, and corrosive properties, the a-C:H film with

the a-Si:H interlayer can be very useful to meet the multifunctional applications of the chromium-plated products.

Acknowledgments


This research and innovation activity was funded by the National Research Council of Thailand (NRCT). The authors thank the Synchrotron Light Research Institute (Public Organization) for providing facilities and support.


Data availability statement

All data that support the findings of this study are included within the article (and any supplementary files).

ORCID iDs

Anthika Lakhonchai  <https://orcid.org/0000-0003-3416-3134>

Artit Chingsungnoen  <https://orcid.org/0000-0003-3194-9254>

Phitsanu Poolcharuansin  <https://orcid.org/0000-0001-9650-9888>

References

- [1] Freund L B and Suresh S 2003 *Thin Film Materials: Stress, Defect and Surface Evolution* 1st ed. (UK: Cambridge University Press)
- [2] Sree Harsha K S 2006 *Principles of Vapor Deposition of Thin Films* 1st ed. (UK: Elsevier Science)
- [3] Rajak D K, Kumar A, Behera A and Menezes P L 2021 Diamond-like carbon (DLC) coatings: classification, properties, and applications *Appl. Sci.* **11** 4445
- [4] Folea M, Roman A and Lupulescu N B 2010 An overview of DLC coatings on cutting tools performance *Acad. J. Manuf. Eng.* **8** 30–6
- [5] Tyagi A, Walia R S, Murtaza Q, Pandey S M, Tyagi P K and Bajaj B 2019 A critical review of diamond like carbon coating for wear resistance applications *Int. J. Refract. Met. Hard Mater.* **78** 107–22
- [6] Dwivedi N, Rismani-Yazdi E, Yeo R J, Goohpattader P S, Satyanarayana N, Srinivasan N, Druz B, Tripathy S and Bhatia C S 2014 Probing the role of an atomically thin SiN_x interlayer on the structure of ultrathin carbon films *Sci Rep.* **4** 1–10
- [7] Vahidi A, Fonseca D, Oliveira J, Cavaleiro A, Ramalho A and Ferreira F 2021 Advanced tribological characterization of DLC coatings produced by Ne-HiPIMS for the application on the piston rings of internal combustion engines *Appl. Sci.* **11** 1–11
- [8] Nakaya M, Uedono A and Hotta A 2015 Recent progress in gas barrier thin film coatings on PET bottles in food and beverage applications *Coatings.* **5** 987–1001
- [9] Robertson J 2002 Diamond-like amorphous carbon *Mater. Sci. Eng. R Reports.* **37** 129–281
- [10] Schultrich B 2018 *Tetraedrally Bonded Amorphous Carbon Films I* (Germany: Springer-Verlag GmbH Germany)
- [11] Wei C and Yen J Y 2007 Effect of film thickness and interlayer on the adhesion strength of diamond like carbon films on different substrates *Diam. Relat. Mater.* **16** 1325–30
- [12] Petry E R, Boeira C D, Cemin F, Leidens L M, Bim L T, Larrude D G, Maia da Costa M E H and Figueroa C A 2016 Physicochemical structure of SiC_xH to improve DLC adhesion on steel *Surf. Eng.* **32** 779–85
- [13] Konkunhot N, Photongkam P and Wongpanya P 2019 Improvement of thermal stability, adhesion strength and corrosion performance of diamond-like carbon films with titanium doping *Appl. Surf. Sci.* **469** 471–86
- [14] Wang K, Zhou H, Zhang K, Liu X, Feng X, Zhang Y, Chen G and Zheng Y 2021 Effects of Ti interlayer on adhesion property of DLC films: a first principle study *Diam. Relat. Mater.* **111** 108188
- [15] Wasy A, Balakrishnan G, Lee S H, Kim J K, Kim D G, Kim T G and Song J I 2014 Argon plasma treatment on metal substrates and effects on diamond-like carbon (DLC) coating properties *Cryst. Res. Technol.* **49** 55–62
- [16] Li A, Li X, Wang Y, Lu Z, Wang Y, Zhang G and Wu Z 2019 Investigation of mechanical and tribological properties of super-thick DLC films with different modulation ratios prepared by PECVD *Mater. Res. Express* **6** 086433
- [17] Nothe M, Breuer U, Koch F, Penkalla H J, Rehbach W P and Bolt H 2001 Investigation of the structure and properties of a-C:H coatings with metal and silicon containing interlayers *Appl. Surf. Sci.* **179** 122–8
- [18] Xie Z H, Singh R, Bendavid A, Martin P J, Munroe P R and Hoffman M 2007 Contact damage evolution in a diamond-like carbon (DLC) coating on a stainless steel substrate *Thin Solid Films* **515** 3196–201
- [19] Cemin F, Bim L T, Menezes C M, Maia da Costa M E H, Baumvol J J R, Alvarez F and Figueroa C A 2015 The influence of different silicon adhesion interlayers on the tribological behavior of DLC thin films deposited on steel by EC-PECVD *Surf. Coatings Technol.* **283** 115–21
- [20] Cui M, Pu J, Liang J, Wang L, Zhang G and Xue Q 2015 Corrosion and tribocorrosion performance of multilayer diamond-like carbon film in NaCl solution *RSC Adv.* **5** 104829–40
- [21] Cemin F, Boeira C D and Figueroa C A 2016 On the understanding of the silicon-containing adhesion interlayer in DLC deposited on steel *Tribol. Int.* **94** 464–9
- [22] Delfani-Abbariki S, Abdollah-Zadeh A, Hadavi S M M, Abedi M and Derakhshandeh S M R 2018 Enhancing the adhesion of diamond-like carbon films to steel substrates using silicon-containing interlayers *Surf. Coatings Technol.* **350** 74–83
- [23] Cao H, Ye X, Li H, Qi F, Wang Q, Ouyang X, Zhao N and Liao B 2021 Microstructure, mechanical and tribological properties of multilayer Ti-DLC thick films on Al alloys by filtered cathodic vacuum arc technology *Mater. Des.* **198** 109320
- [24] Mousavi S E, Naghshehkhesh N, Amirnejad M, Shammakhi H and Sonboli A 2021 Corrosion performance and tribological behavior of diamond-like carbon based coating applied on Ni–Al–bronze alloy *Trans. Nonferrous Met. Soc. China (English)* **31** 499–511

- [25] Lu Y, Huang G and Xi L 2019 Tribological and mechanical properties of the multi-layer DLC film on the soft copper substrate *Diam. Relat. Mater.* **94** 21–7
- [26] Hadinata S S, Lee M T, Pan S J, Tsai W T, Tai C Y and Shih C F 2013 Electrochemical performances of diamond-like carbon coatings on carbon steel, stainless steel, and brass *Thin Solid Films* **529** 412–6
- [27] Nguyen V P, Dang T N and Le C C 2019 Effect of residual stress and microcracks in chrome plating layer to fatigue strength of axle-shaped machine parts *Appl. Mech. Mater.* **889** 10–6
- [28] Podgoric S, Jones B J, Bulpitt R, Troisi G and Franks J 2009 Diamond-like carbon/epoxy low-friction coatings to replace electroplated chromium *Wear* **267** 996–1001
- [29] Kaneko M, Hiratsuka M, Alanazi A, Nakamori H, Namiki K and Hirakuri K 2021 Surface reformation of medical devices with DLC coating *Materials (Basel)* **14**, 1–10
- [30] Bland H A, Thomas E L H, Klemencic G M, Mandal S, Morgan D J, Papageorgiou A, Jones T G and Williams O A 2019 Superconducting diamond on silicon nitride for device applications *Sci. Rep.* **9** 1–9
- [31] Li X, Miao H and Zhu H 2018 Deposition and characterization of diamond-like carbon films by electron cyclotron resonance microwave plasma enhanced unbalanced magnetron sputtering *Chem. Eng. Trans.* **66** 19–24
- [32] Barimar P S N, Doyle C M, Naydenov B and Boland J J 2016 Study of the effect of thermal treatment on morphology and chemical composition of silicon-on-insulator *J. Vac. Sci. Technol. B, Nanotechnol. Microelectron. Mater. Process. Meas. Phenom.* **34** 041806
- [33] Gao M, Du H W, Yang J, Zhao L, Xu J and Ma Z Q 2017 Variation of passivation behavior induced by sputtered energetic particles and thermal annealing for ITO/SiO₂/Si system *Chinese Phys. B* **26** 045201
- [34] Kamble M M et al 2014 Hydrogenated silicon carbide thin films prepared with high deposition rate by hot wire chemical vapor deposition method *J. Coatings* **2014** 1–11
- [35] Song J S, Park Y S and Kim N H 2021 Hydrophobic anti-reflective coating of plasma-enhanced chemical vapor deposited diamond-like carbon thin films with various thicknesses for dye-sensitized solar cells *Appl. Sci.* **11** 1–9
- [36] Schlebrowski T, Fritz M, Beucher L, Wang Y, Wehner S and Fischer C B 2021 The growth behavior of amorphous hydrogenated carbon a-C:H Layers on Industrial Polycarbonates-A Weak Interlayer and a Distinct Dehydrogenation Zone *C. 759*
- [37] Niranjana Reddy K, Varade A, Krishna A, Joshua J, Saseen D, Chellamalai M and Shashi Kumar P V 2014 Double side coating of DLC on silicon by RF-PECVD for AR application *Procedia Eng.* **97** 1416–21
- [38] Sheng H, Xiong W, Zheng S, Chen C, He S and Cheng Q 2021 Evaluation of the sp^3/sp^2 ratio of DLC films by RF-PECVD and its quantitative relationship with optical band gap *Carbon Lett.* **31** 929–39
- [39] Cui W G, Lai Q B, Zhang L and Wang F M 2010 Quantitative measurements of sp^3 content in DLC films with Raman spectroscopy *Surf. Coatings Technol.* **205** 1995–9
- [40] Qiang L, Zhang B, Gao K, Gong Z and Zhang J 2013 Hydrophobic, mechanical, and tribological properties of fluorine incorporated hydrogenated fullerene-like carbon films *Friction* **1** 350–8
- [41] Wang Y, Gao K and Zhang J 2016 Structure, mechanical, and frictional properties of hydrogenated fullerene-like amorphous carbon film prepared by direct current plasma enhanced chemical vapor deposition *J. Appl. Phys.* **120** 1–7
- [42] Zhang B, Gao K, Yu Y and Zhang J 2018 Super-Lubricious, Fullerene-like, Hydrogenated Carbon Films *Fullerenes and Relative Materials - Properties and Applications* (UK: Headquarters IntechOpen Limited) (<https://doi.org/10.5772/intechopen.70412>)
- [43] Oliver W C and Pharr G M 1992 An improved technique for determining hardness and elastic modulus using load and displacement sensing indentation experiments *J. Mater. Res.* **7** 1564–83
- [44] Bückle H 1959 Progress in micro-indentation' hardness *Metal. Rev.* **4** 49–100
- [45] Moreno-Barcenas A, Alvarado Orozco J, González J, Rodríguez G C, González-Hernández J and García A 2018 Diamond-like carbon coatings on plasma nitrided M2 steel: effect of deposition parameters on adhesion properties *Resour. Sci.* **37** 355–60
- [46] Hassan M A, Bushroa A R and Mahmoodian R 2015 Identification of critical load for scratch adhesion strength of nitride-based thin films using wavelet analysis and a proposed analytical model *Surf. Coatings Technol.* **277** 216–21
- [47] Amin M A, El-Bagoury N, Saracoglu M and Ramadan M 2014 Electrochemical and corrosion behavior of cast re-containing inconel 718 alloys in sulphuric acid solutions and the effect of Cl⁻ *Int. J. Electrochem. Sci.* **9** 5352–74
- [48] Kakaei K, Esrafilidi M D and Ehsani A 2019 Graphene and anticorrosive properties, interface *Sci. Technol.* **27** 303–37
- [49] Khun N W, Liu E, Yang G C, Ma W G and Jiang S P 2009 Structure and corrosion behavior of platinum/ruthenium/nitrogen doped diamond like carbon thin films *J. Appl. Phys.* **106** 1–9
- [50] Kim H G, Ahn S H, Kim J G, Park S J and Lee K R 2005 Electrochemical behavior of diamond-like carbon films for biomedical applications *Thin Solid Films* **475** 291–7

Publication in Thin Solid Films (2022) : First author

Thin Solid Films 747 (2022) 139140



Contents lists available at ScienceDirect

Thin Solid Films

journal homepage: www.elsevier.com/locate/tsf

Comparison of the structural and optical properties of amorphous silicon thin films prepared by direct current, bipolar pulse, and high-power impulse magnetron sputtering methods

Anthika Lakhonchai, Artit Chingsungnoen^{*}, Phitsanu Poolcharuansin, Nitisak Pasaja, Phuwanai Bunnak, Mongkhon Suwanno

Technological Plasma Research Unit, Department of Physics, Faculty of Science, Mahasarakham University, Khanriang Sub-District, Kantarawichai District, Mahasarakham 44150, Thailand

ARTICLE INFO

Keywords:

Amorphous silicon
Thin film
Direct current magnetron sputtering
Bipolar pulse magnetron sputtering
High-power impulse magnetron sputtering
Structural properties
Optical properties

ABSTRACT

This paper presents a comparative study of amorphous silicon (a-Si) thin films deposited by three different techniques: direct current magnetron sputtering (DCMS), bipolar pulse magnetron sputtering (bipolar pulse MS) and high-power impulse magnetron sputtering (HIPIMS). The structural properties of the a-Si films with a thickness of ~112 nm were characterized by X-ray reflectivity and Raman spectroscopy. The surface morphology, optical and mechanical properties of a-Si films with a thickness of ~400 nm were investigated using a field emission secondary electron microscope, an atomic force microscope, spectroscopic ellipsometry and nanoindentation. It was found that for the same time-averaged discharge power, the deposition rate of the HIPIMS method was lower compared to DCMS and bipolar pulse MS. The a-Si film prepared by HIPIMS method had the lowest root mean square roughness of 0.65 nm and the highest density of 2.21 g/cm³. These results are consistent with the highest refractive index (400–700 nm) of 3.66 and a hardness of 9.09±0.19 GPa in the film, indicating that the HIPIMS method produces denser films than the DCMS and bipolar pulse MS methods. The amorphous silicon thin films fabricated by HIPIMS have the potential to improve the structural and mechanical properties for high performance thin film semiconductor applications.

1. Introduction

Amorphous silicon (a-Si) based thin films deposited by magnetron sputtering methods have been applied extensively for flexible photovoltaic cells, thin-film transistors in liquid crystal displays, etc [1,2]. For tribological applications, diamond-like carbon (DLC) coating on a metallic surface requires an interlayer to promote adhesion between the substrate and the coating. In most cases, amorphous silicon has been used as an interlayer because it can form strong carbide bonds with the overcoat and react with the metallic surface to form a silicide. The formation of these chemical bonds plays a crucial role in improving adhesion [3]. The a-Si and the a-Si:H (hydrogenated versions) were deposited by both physical and chemical vapor deposition. Usually, they are grown by plasma-enhanced chemical vapor deposition using a silane base as a precursor in a radio frequency (RF) plasma that requires toxic process gasses. In addition, this technique makes it very difficult to control the energy of the radicals at low substrate temperature. These

neutral radicals are easily incorporated into the growing surface and strongly affect the microstructure of the films [4].

Alternative methods for fabricating a-Si-based thin films include magnetron sputtering techniques, which offer many advantages, including low cost, low-temperature deposition, high-quality films, and a friendly operating environment. Direct current magnetron sputtering (DCMS) is used to achieve a high sputtering rate of the target material in the simplest case [5]. In combination with a reactive gas, a composite film can be grown. Another possibility is bipolar pulse magnetron sputtering (bipolar pulse MS), where the voltage is reversed for a short time to attract some of the electrons from the plasma and neutralize the charge accumulated on surface of the target. This technique can be used to deposit amorphous silicon following an annealing to induce crystallization [6]. In RF magnetron sputtering, the deposition rate is usually very low, and the electron flux on the substrate can cause significant heating [7]. Moreover, the major cost of this technique is the RF power supplies, which limit its use in industrial production. On the other hand,

^{*} Corresponding author.

E-mail address: artit.c@msu.ac.th (A. Chingsungnoen).

<https://doi.org/10.1016/j.tsf.2022.139140>

Received 31 May 2021; Received in revised form 12 January 2022; Accepted 24 January 2022

Available online 18 February 2022

0040-6090/© 2022 Elsevier B.V. All rights reserved.

high-power impulse magnetron sputtering (HiPIMS) tends to have high ionization fractions, which can improve the film structure over conventional sputtering techniques [8–10].

As mentioned above, different types of power supplies can be used in magnetron sputtering, and different sputtering methods can directly affect film properties. Although many studies have fabricated and characterized a-Si thin films, few have compared both the structural and optical properties of films prepared using different sputtering methods. Therefore, this work aims to investigate the structural, optical, and mechanical properties of amorphous silicon thin films deposited by DCMS, bipolar pulse MS and HiPIMS methods. The researchers believe that the results of this study could help to develop high performance thin film semiconductors that can be deposited on large and low cost substrates.

2. Materials and methods

2.1. Thin-film preparation

The system setup used to prepare the amorphous silicon thin films is shown schematically in Fig. 1. This system consists of the main vacuum chamber (29.5 cm in diameter and 36.2 cm in height), which was connected to the turbomolecular pump backed with a scroll pump. A pendulum valve was used to adjust the operating pressure during the cleaning and deposition processes. Substrates were placed on the bottom electrode and cleaned with argon plasma before coating. A silicon (Si) target (99.999% purity, 4.25 inches in diameter, and 0.25 inches in thickness) with a copper backing plate was used as the sputtering target. Magnetron sputtering sources with DC, bipolar pulse, and high-power impulse power supplies were assigned to the top electrode. Both electrodes were cooled with cold water to prevent the temperature from rising during the coating process. A mass flow controller (Brooks-GF040, 0–92 sccm) was used to control the argon flow rate.

Single-sided polished mirrors of p-type boron-doped (100) Si wafers ($10 \times 10 \text{ mm}^2$ in size) and pure (100) Ge wafers (25.4 mm in diameter) were used as substrates. These substrates were conventionally organically cleaned in an ultrasonic bath with acetone (x1), methanol (x2), and

then deionized water (x3) for 10 min and then dried with filtered warm air before being loaded into the vacuum chamber. Prior to deposition, the chamber was evacuated for ~60 min to achieve a base pressure of approximately $1.33 \times 10^{-3} \text{ Pa}$. This process reduced residual gases that may have affected the quality of the films. Argon plasma was then generated at an argon flow rate of 10 sccm and an operating pressure of 13.33 Pa at a power of RF of 200 W. The processing time for cleaning was 10 min to remove the surface contamination and native oxide from the substrates. After that, the substrates were covered with the shutter. Then, a silicon target was pre-sputtered for 5 min at a power of 400 W at DC to remove surface contamination. In the next step, the shutter was opened and the bottom electrode was connected to ground. For the deposition process of a-Si thin films, the argon flow rate and operating pressure were set to 10 sccm and 0.64 Pa, respectively. The influence of different types of plasma discharges, namely DCMS, bipolar pulse MS, and HiPIMS, was investigated. The discharge power of these methods was controlled around 200 W, which corresponded to the power density applied to the 4.25-inch Si sputtering target of 2.19 W/cm^2 . A commercial power supply (Advanced Energy; Pinnacle Plus+) was used for the DC and bipolar pulse magnetron sputtering, while the HiPIMS power supply was developed in-house. The duty cycle was calculated from the ratio of the negative pulse width in one period and expressed as a percentage. The negative pulse width of the bipolar pulse was $17 \mu\text{s}$ with a frequency of 50 kHz (period of $20 \mu\text{s}$), which corresponds to a duty cycle of 85%. For HiPIMS, a duty cycle of 1% was used, corresponding to a negative pulse width of $100 \mu\text{s}$ and a frequency of 100 Hz (period of $10,000 \mu\text{s}$). Based on the X-ray reflectivity (XRR) curve fitting and deposition time control, the thickness and deposition rate of the a-Si films prepared by each method were evaluated. Therefore, different deposition times were manipulated to achieve a film thickness of ~112 and ~400 nm. The conditions used for substrate cleaning, target cleaning and deposition are summarized in Table 1.

2.2. Characterization

Amorphous silicon thin films with thickness of ~112 and ~400 nm were prepared by DCMS, bipolar pulse MS, and HiPIMS methods. The a-

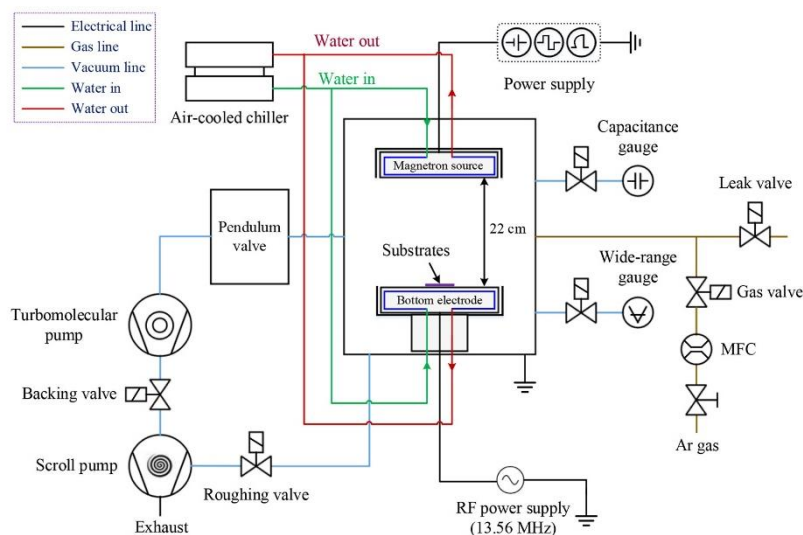


Fig. 1. A schematic diagram and configuration of magnetron sputtering system.

Table 1
The parameters used for deposition of a-Si thin films.

Parameters and process	Substrate cleaning		Target cleaning			Deposition		
	RF-plasma	DCMS	DCMS	Bipolar pulse MS	HiPIMS	DCMS	Bipolar pulse MS	HiPIMS
Method	RF-plasma	DCMS	DCMS	Bipolar pulse MS	HiPIMS			
Discharge power (W)	300	400	200	200	200			
Pulse frequency (kHz)	–	–	–	50	0.1			
Pulse width (μ s)	–	–	–	17	100			
Duty cycle (%)	–	–	100	85	1			
Ar flow rate (sccm)	10	10	10	10	10			
Operating pressure (Pa)	0.64	0.64	0.64	0.64	0.64			
Processing time (second)	600	300	762	772	910			
~112 nm	600	300	2721	2760	3252			
~400 nm								

Si films with a thickness of ~ 112 nm were characterized by XRR (Bruker: D8 Advance Diffractometer) and Raman spectroscopy (Bruker: SENTERRA), while the film with a thickness of ~ 400 nm were investigated by a field emission secondary electron microscope (FESEM) (HITACHI: SU8230), atomic force microscope (AFM) (Bruker: Dimension Icon), spectroscopic ellipsometry (J. A. Woollam: M2000), and nanoindentation (Hysitron: TI Premier). The surface morphology of the samples was observed using FESEM with an accelerating voltage of 3 kV and magnifications up to 100,000X. The surface roughness, expressed as root mean square roughness (R_q) was estimated using AFM. The structural properties were measured by Raman spectroscopy using a 532 nm and 12.5 mW Ar laser. The aperture size of 50 μ m slit and two exposures with an integration time of 20 s were used for a final spectrum. XRR with $\text{Cu-K}\alpha$ radiation ($\lambda = 0.154$ nm) was used to evaluate the density and thickness of the films. Kiessig fringes, due to interference between X-rays partially reflected from air-film and film-substrate interfaces, were interpreted using Leptos 7 software. The refractive index (n) and extinction coefficient (k) as a function of wavelength were evaluated by spectroscopic ellipsometry. To determine the optical constants, a B-spline model representing the thin film structure was created using CompleteEASE software (version 4.98) from J. A. Woollam Co., Inc. The optical model was designed as Si (substrate)/ SiO_2 (native oxide)/a-Si (B-spline layer)/ SiO_2 (surface oxidation). The node resolution of 0.1 eV (1.242–5.043 eV) was defined to fit the wavelength range extension with a mean squared error below 1.3. Nanoindentation tests were performed using a pyramidal Berkovich indenter on a-Si films (~ 400 nm) coated on Ge with a maximum load of 600 μ N. Each sample was indented five times in five different positions with an indenter loaded and unloaded at a rate of 120 μ N/s, holding the maximum load for 2 s.

3. Results and discussion

3.1. Deposition rate

There are different types of power supplies that can be used in magnetron sputtering such as DC, bipolar pulse, HiPIMS and RF. The different power supplies affect the rates of sputtering and densifying of the growing films. Therefore, to study the effect of sputtering voltage on static deposition rate as shown in Fig. 2, the same average power and deposition time must be used. The static deposition rate is defined by the growth of film thickness per unit time [10]. As can be seen in Fig. 3, the HiPIMS method has the lowest deposition rate (7.38 nm/min). For the HiPIMS method, the most common explanation for the lowest deposition rate is the self-sputtering effect. This phenomenon could be due to the fact that the ionized sputtered material near the target surface is attracted back to the target surface, which leads to a decrease in the

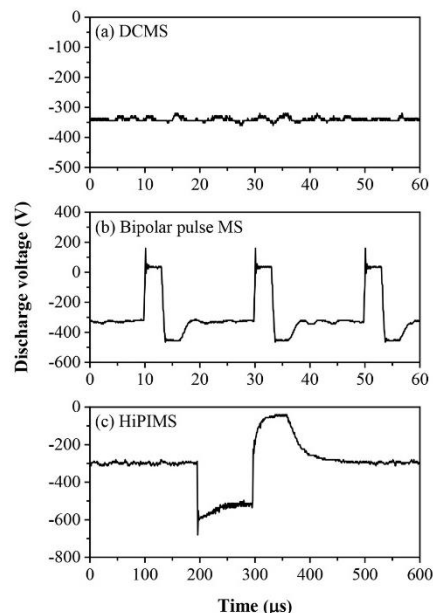


Fig. 2. Time-dependent target voltages during the (a) DCMS, (b) Bipolar pulse MS, and (c) HiPIMS discharges.

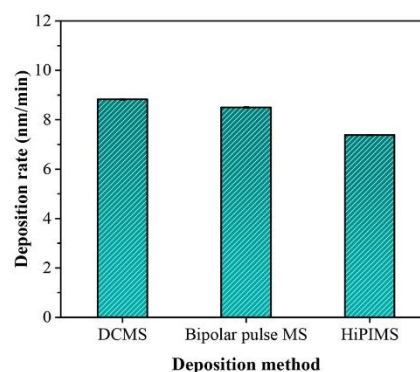


Fig. 3. Deposition rate of a-Si thin films prepared by DCMS, Bipolar pulse MS, and HiPIMS methods.

deposition rate [11,12]. In a report by Samuelsson et al [13], it was found that the deposition rates of HiPIMS are normally in the range of 30–85% compared to DCMS, depending on the target material. However, in this work, the deposition rate of the Si target was found to be about 84% of the DCMS rate. The deposition rate of the bipolar pulse MS is slightly lower than the DCMS rate because the sputtering process occurs only during an applied negative bias. A positive reverse bias affects the removal of charges accumulated on the surface of the target. In order to control the thickness of the a-Si layers (~ 112 and ~ 400 nm),

the different deposition times for the for DCMS, bipolar pulse MS and the HiPIMS methods were adjusted.

3.2. Surface characterization

The FESEM micrographs (Fig. 4a) and AFM images (Fig. 4b) show the surface microstructure of the a-Si samples prepared by DCMS, bipolar pulse MS and HiPIMS methods. It can be seen that all films have very low surface roughness, which hardly produces any contrast in FESEM. The root mean square roughness was estimated from $10 \times 10 \mu\text{m}^2$ of AFM scan area. The R_q surface roughnesses of the a-Si films deposited by DCMS, bipolar pulse MS, and HiPIMS methods were 0.90, 0.77, and 0.65 nm, respectively, indicating a smooth surface with R_q below 1 nm. The HiPIMS method resulted in a considerable surface roughness, which was lower than the other techniques. This result could be due to the more effective bombardment of the film with sputtered ions during the growth process. Therefore, while the positive pulse (15% reversed duty cycle) during the bipolar pulse MS process can push the argon ions from the plasma into the film, the surface roughness obtained with the bipolar pulse MS was lower than DCMS.

3.3. Structural properties

In this work, Raman spectroscopy was used to study the structural properties of the amorphous silicon films, and the Raman spectra could be correlated to essential deposition conditions [14] Fig. 5. shows the Raman spectra of a-Si thin films (~112 nm) prepared by the three different sputtering methods. Each spectrum can be separated into three regions. A dominant peak at $\sim 300 \text{ cm}^{-1}$ corresponds to the Ge substrate [15,16]. The thin a-Si films exhibit two broad peaks at 131 ± 3 and $473 \pm 3 \text{ cm}^{-1}$ associated with transverse acoustic (TA) and transverse optic

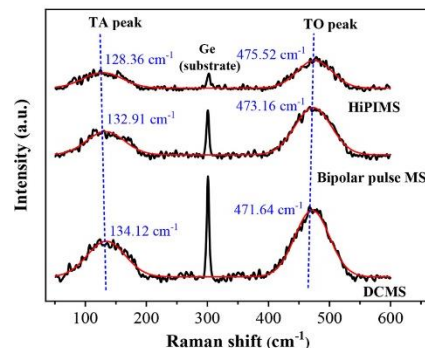


Fig. 5. Raman spectra of a-Si thin films (~112 nm) on Ge substrate with difference deposition methods.

(TO) vibrational modes, respectively [17]. It was found that the location of the TA peak shifted to lower frequencies and the TO peak shifted to higher frequencies when the method changed from DCMS to bipolar pulse MS and HiPIMS. These shifts could be related to the development of structural ordering in the amorphous silicon matrix in the films [14]. In the HiPIMS method, high power impulses with a low duty cycle caused the atoms and ions that collided with the substrate to have a higher energy distribution than in DCMS and bipolar pulse MS. Therefore, the nucleation and microstructure can be affected, and crystalline phases can be formed [18]. Moreover, it can be seen that the a-Si film prepared by HiPIMS method has lower peak intensity of Ge substrate than the bipolar pulse MS and DCMS. This behavior could be due to the density of the a-Si film. Higher density corresponds to lower penetration and signal received from the Ge substrate. However, the measurement of the actual density of the films will be mentioned in the next section.

XRR is a non-destructive, powerful and popular scattering technique that can determine the thickness, density, and roughness of thin film coatings [19]. In this work, the a-Si thin films were deposited on both Si and Ge substrates. For a Si substrate with a density of 2.33 g/cm^3 , the critical angle of the amorphous silicon film may merge with the substrate, and the density may have an error due to the close density effect between the film and the substrate [20]. Therefore, the Ge substrate with a higher density of 5.32 g/cm^3 was used for the XRR characterization. The XRR Kiessig fringes of all samples were measured and generated, as shown by the experimental data (black curves) and the corresponding simulation data (red curves) in Fig. 6(a). It can be seen that the apparent double critical angle of the XRR curves is due to the different density range [21] between the Ge substrate and the a-Si layer. These experimental data were fitted using Leptos 7 software with a layered structure model consisting of the outermost SiO_2 layer (native oxide), the a-Si layer and the innermost GeO layer (native oxide); see inset in Fig. 6(a) Fig. 6.(b) shows the thickness and density of the prepared a-Si thin films. It can be seen that the controlled thickness of all samples was about 112 nm. In this work, it was found that the density of the a-Si films deposited by HiPIMS (2.21 g/cm^3) was about 5–7% higher compared to the DCMS and bipolar pulse MS methods. It is known that HiPIMS produces a high degree of ionization, high plasma density and high ion flux towards the substrate, which in turn enables the deposition of higher quality thin films compared to DCMS and bipolar pulse MS [12, 22,23]. However, the density of the a-Si films prepared using HiPIMS was found to be about 97% of the calculated density (2.285 g/cm^3) [24]. Slightly lower density of the prepared a-Si films could be due to the contribution of vacancy volume in the atoms, which form a continuous random network during the film growth [25].

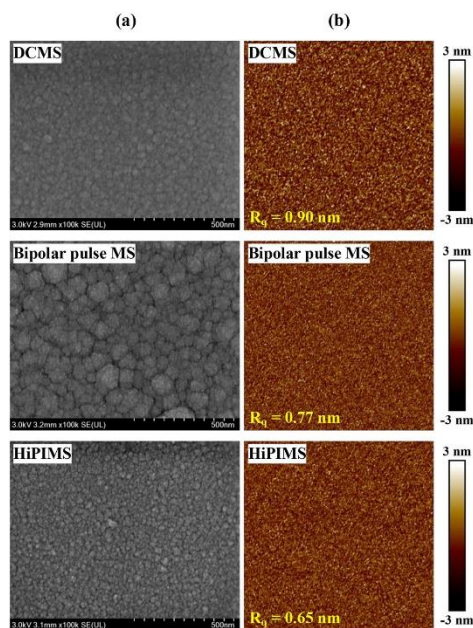


Fig. 4. (a) FESEM images and (b) 2D AFM topography of the surface of a-Si thin films prepared using DCMS, Bipolar pulse MS, and HiPIMS methods.

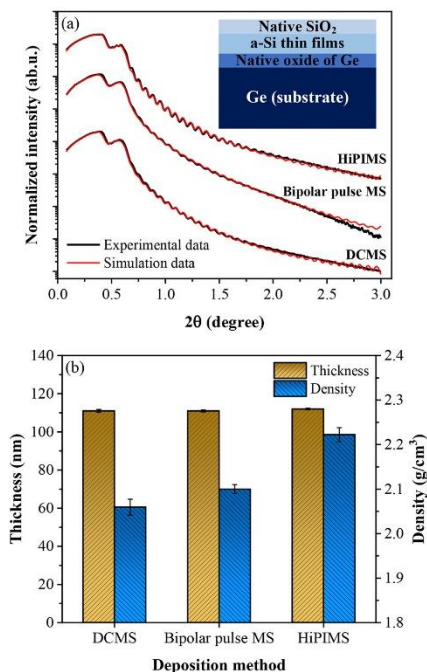


Fig. 6. (a) XRR curves (the inset shows the film structure model), and (b) fitted results of thickness and density of a-Si thin films on Ge substrate with different deposition methods.

3.4. Optical properties

Spectroscopic ellipsometry measurements on semi-absorbing films are more complicated to study than on transparent films because the refractive index and extinction coefficient are not always known before the measurement. In addition, the optical properties of amorphous silicon are sensitive to the preparation conditions. In this work, the CompleteEASE program with a coupled B-spline layer was used to solve these problems. The B-spline layer, which allows arbitrary flexibility of n and k with respect to wavelength, is suitable for partially transparent and partially absorbing materials such as a-Si, a-Ge, TiO₂, and DLC films [26,27]. The optical properties of the a-Si films (~400 nm) on Si substrate prepared by magnetron sputtering method are shown in Fig. 7. The typical ellipsometric angles Psi (Ψ) and Delta (Δ) were measured over the wavelength range 250–1000 nm. The highest amplitude of the interference oscillations for the HiPIMS mode indicates the lowest UV and IR absorptions Fig. 8. shows the refractive index and extinction coefficient of a-Si thin films on Si substrate extracted from the optimized fit through the B-spline layer. The refractive index shows a broad peak expected for amorphous materials [28]. The a-Si thin film from HiPIMS gave an average refractive index of 3.66 (400–700 nm), which is higher than the bipolar pulse MS (3.05) and DCMS (2.94). The refractive index for amorphous silicon is related to the mass density of the fabricated film [29]. Therefore, the higher value of refractive index can be used to support the higher film density obtained with HiPIMS mode. This result is consistent with the XRR and deposition rate measurements, which show a denser film with a lower growth rate using the HiPIMS method. The extinction coefficient is directly correlated with the absorption

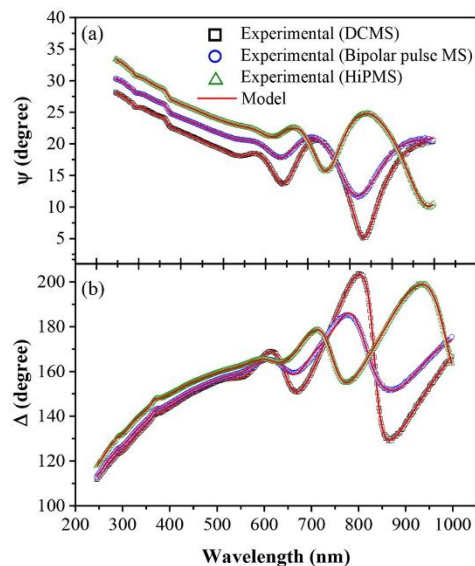


Fig. 7. Experimental and modeled values of (a) Psi and (b) Delta as a function of wavelength for a-Si thin films on a Si substrate.

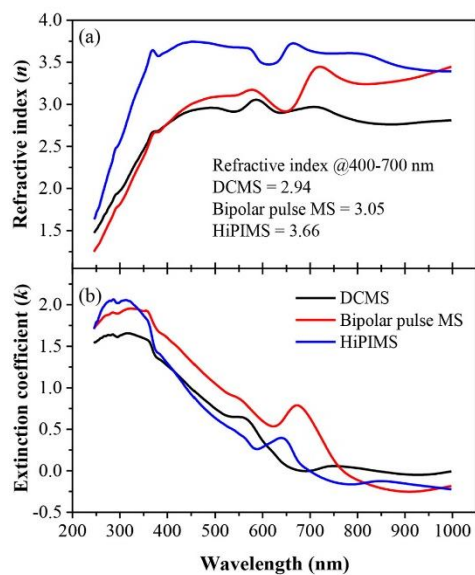


Fig. 8. (a) Refractive index (n) and (b) Extinction coefficient (k) of all samples as a function of the wavelength.

coefficient [30,31].

3.5. Mechanical properties

Hardness is one of the most important factors determining the mechanical properties of films, and it is also closely related to the density of the films. In this test, the thickness of the a-Si film on the Ge substrate was set to about 400 nm. The typical load/unload curves are shown in Fig. 9(a). The maximum penetration depths were about 97, 95, and 67 nm for DCMS, bipolar pulse MS, and HiPIMS, respectively. Thus, in this case, the penetration depths were in the range of 16–24% of the film thickness. We know that Bückle rule recommends not to indent more than 10% of the film thickness to avoid the influence of the substrate [32]. However, we cannot indent with the lowest load while keeping the indentation depth below 10%. In some cases of a low-density thin film on a high-density substrate, the relative penetration depth was found to be greater than 0.1 because of the confinement of the plastically deformed volume by lateral spreading within the softer thin film [33]. The hardness of the a-Si samples can be determined by the Pharr-Oliver method [34], as shown in Fig. 9(b). The Ge substrate had a hardness of 10.02 ± 0.27 GPa. The hardness of the a-Si films deposited by DCMS, bipolar pulse MS, and HiPIMS methods were 5.62 ± 0.70 , 5.72 ± 0.60 , and 9.09 ± 0.19 GPa, respectively. These hardness values are within the range reported (10.15 ± 0.26 GPa for a-Si films [35], 9.6 ± 0.3 GPa for

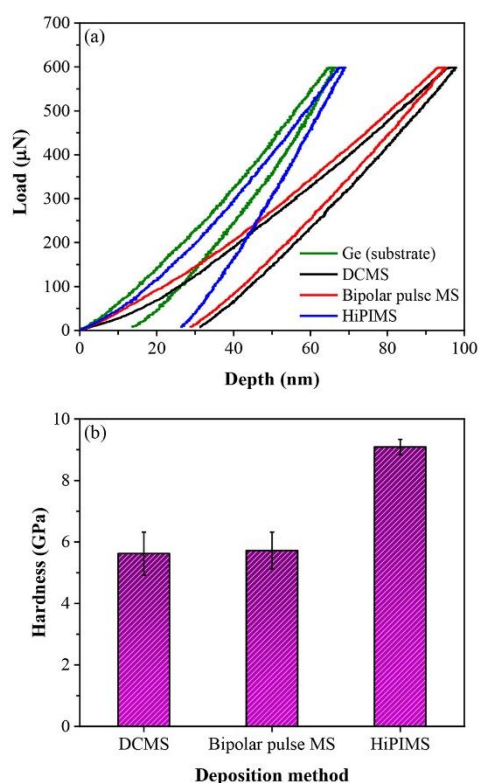


Fig. 9. (a) Typical loading-unloading curves and (b) average hardness of a-Si films on Ge substrate with different deposition methods.

hydrogen-free a-Si films [36], and 10 ± 1 GPa for germanium substrate [37]). It can be considered that the HiPIMS method gives the highest hardness value. This agrees with the density of the film determined by the XRR technique, confirming a close correlation between the hardness and density of thin films.

4. Conclusion

In this work, the a-Si thin films were deposited by DCMS, bipolar pulse MS and HiPIMS methods. High-power impulse magnetron sputtering gave the lowest deposition rate with the same time-averaged discharge powers. The different sputtering methods resulted in different film properties, with the density of the film being the most important factor affecting the other properties. To compare the structural, optical and mechanical properties, the thickness of the a-Si films on the silicon and germanium substrates was set to 112 and 400 nm. All films showed very low surface roughness, and the HiPIMS method resulted in considerable surface smoothness, which was higher than the other techniques. The Raman spectra of the prepared films showed a broad peak associated with the typical amorphous structure of silicon. The XRR results showed that the film density was 2.05, 2.10, and 2.21 g/cm³, corresponding to DCMS, bipolar pulse MS and HiPIMS, respectively. Spectroscopic ellipsometry confirmed that the a-Si film obtained with HiPIMS had an average refractive index higher than that of the bipolar pulse MS and DCMS. This optical parameter is directly correlated with the mass density of the prepared film. They are in agreement with the XRR and deposition rate measurements, which showed a denser film with the lower growth rate of the HiPIMS method. It is evident that the a-Si films prepared by HiPIMS were harder than the films prepared by the other techniques, which could be related to the density of the films. These results suggest that the HiPIMS method achieves better film properties due to the highly ionized plasma and energetic ion bombardment. It can improve the film density along with the lower surface roughness compared to the conventional magnetron sputtering method.

Credit author statement

All persons who meet authorship criteria are listed as authors, and all authors certify that they have participated sufficiently in the work to take public responsibility for the content, including participation in the concept, design, analysis, writing, or revision of the manuscript. Furthermore, each author certifies that this material or similar material has not been and will not be submitted to or published in any other publication.

Authorship contributions

Category 1. Conception and design of study: Anthika Lakhonchai, Artit Chingsungnoen, Phitsanu Poolcharuansin; acquisition of data: Anthika Lakhonchai, Artit Chingsungnoen, Phitsanu Poolcharuansin; analysis and/or interpretation of data: Anthika Lakhonchai, Artit Chingsungnoen, Phitsanu Poolcharuansin, Nitisak Pasaja, Phuwanai Bunnak, Mongkhon Suwanno.

Category 2. Drafting the manuscript: Anthika Lakhonchai, Artit Chingsungnoen, Phitsanu Poolcharuansin; revising the manuscript critically for important intellectual content: Anthika Lakhonchai, Artit Chingsungnoen, Phitsanu Poolcharuansin, Phuwanai Bunnak.

Category 3. Approval of the version of the manuscript to be published: Anthika Lakhonchai, Artit Chingsungnoen, Phitsanu Poolcharuansin; analysis and/or interpretation of data: Anthika Lakhonchai, Artit Chingsungnoen, Phitsanu Poolcharuansin, Nitisak Pasaja, Phuwanai Bunnak, Mongkhon Suwanno.

Declaration of Competing Interest

The authors declare that they have no known competing financial interests or personal relationships that could have appeared to influence the work reported in this paper.

Acknowledgments

This research was financially supported by the Faculty of Science, Maharakham University (Grant Year 2021). The authors thank Adrian Plant for valuable suggestions and editorial comments on this manuscript.

References

- C. Nocito, V. Koncar, Flexible photovoltaic cells embedded into textile structures, *Smart Text. Their Appl.* (2016) 401–422, <https://doi.org/10.1016/B978-0-08-100574-3.00018-7>.
- Y. Alajlani, A. Alaswad, F. Placido, D. Gibson, A. Diyaf, Inorganic thin film materials for solar cell applications, *Ref. Modul. Mater. Sci. Mater. Eng.* (2018) 1–15, <https://doi.org/10.1016/B978-0-12-803581-8.10355-8>.
- K.A.H. Al Mahmud, M.A. Kalam, H.H. Masjuki, H.M. Mobarak, N.W.M. Zulkifli, An updated overview of diamond-like carbon coating in tribology, *Crit. Rev. Solid State Mater. Sci.* 40 (2015) 90–118, <https://doi.org/10.1080/10408436.2014.940441>.
- M.S. Feng, C.W. Liang, D. Tseng, Effects of plasma enhanced chemical vapor deposition substrate heating on the electrical properties of α -Si:H thin film transistors, *J. Electrochem. Soc.* 141 (1994) 1040–1045, <https://doi.org/10.1149/1.2054838>.
- D.M. Mitin, V.A. Aleksandrov, A.A. Skaptsov, S.B. Venig, A.A. Serdobintsev, Features of the growth of amorphous silicon thin films synthesized by magnetron sputtering, *J. Surf. Investig. X-Ray, Synchrotron Neutron Tech.* 9 (2015) 555–557, <https://doi.org/10.1134/S1027451015030313>.
- L.R. Bailey, G. Proudfoot, B. Mackenzie, N. Andersen, A. Karlsson, A. Ulyashin, High rate amorphous and crystalline silicon formation by pulsed DC magnetron sputtering deposition for photovoltaics, *Phys. Status Solidi Appl. Mater. Sci.* 212 (2015) 42–46, <https://doi.org/10.1002/pssa.201431768>.
- D. Dergez, M. Schneider, A. Bittner, N. Pawlak, U. Schmidt, Mechanical and electrical properties of RF magnetron sputter deposited amorphous silicon-rich silicon nitride thin films, *Thin Solid Films* 606 (2016) 7–12, <https://doi.org/10.1016/j.tsf.2016.03.029>.
- G. West, P. Kelly, P. Barker, A. Mishra, J. Bradley, Measurements of deposition rate and substrate heating in a HiPIMS discharge, *Plasma Process. Polym.* 6 (2009) S543–S547, <https://doi.org/10.1002/ppap.200931202>.
- J. Sharp, I.C. Müller, P. Mandal, A. Abbas, M. Nord, A. Doye, A. Ehasarian, P. Hovsepian, I. MacLaren, W.M. Rainforth, Characterisation of a high-power impulse magnetron sputtered C/Mo/W wear resistant coating by transmission electron microscopy, *Surf. Coatings Technol.* 377 (2019), 124853, <https://doi.org/10.1016/j.surfcoat.2019.08.007>.
- A. Anders, Deposition rates of high power impulse magnetron sputtering: physics and economics, *J. Vac. Sci. Technol. A Vacuum, Surfaces, Film* 28 (2010) 783–790, <https://doi.org/10.1116/1.3299267>.
- J.T. Gudmundsson, N. Brenning, D. Lundin, U. Helmersson, High power impulse magnetron sputtering discharge, *J. Vac. Sci. Technol. A* 30 (2012), 030801, <https://doi.org/10.1116/1.3691832>.
- D. Lundin, K. Sarakinos, An introduction to thin film processing using high-power impulse magnetron sputtering, *J. Mater. Res.* 27 (2012) 780–792, <https://doi.org/10.1557/jmr.2012.8>.
- M. Samuelsson, D. Lundin, J. Jensen, M.A. Raadu, J.T. Gudmundsson, U. Helmersson, On the film density using high power impulse magnetron sputtering, *Surf. Coatings Technol.* 205 (2010) 591–596, <https://doi.org/10.1016/j.surfcoat.2010.07.041>.
- A.T. Voutsas, M.K. Hatalis, J. Boyce, A. Chiang, Raman spectroscopy of amorphous and microcrystalline silicon films deposited by low-pressure chemical vapor deposition, *J. Appl. Phys.* 78 (1995) 6999–7006, <https://doi.org/10.1063/1.360468>.
- J.H. Parker, D.W. Feldman, M. Ashkin, Raman scattering by silicon and germanium, *Phys. Rev.* 155 (1967) 712–714, <https://doi.org/10.1103/PhysRev.155.712>.
- M. Wakaki, M. Iwase, Y. Show, K. Koyama, S. Sato, S. Nozaki, H. Morisaki, Raman spectroscopy of germanium films deposited with cluster-beam technique, *Phys. B Condens. Matter.* 219–220 (1996) 535–537, [https://doi.org/10.1016/0921-4526\(95\)00803-9](https://doi.org/10.1016/0921-4526(95)00803-9).
- R.L.C. Vink, G.T. Barkema, W.F. van Der Weg, Raman spectra and structure of amorphous Si, *Phys. Rev. B - Condens. Matter Mater. Phys.* 63 (2001), 115210, <https://doi.org/10.1103/PhysRevB.63.115210>.
- J. Alami, P. Eklund, J.M. Andersson, M. Lattemann, E. Wallin, J. Bohlmark, P. Persson, U. Helmersson, Phase tailoring of Ta thin films by highly ionized pulsed magnetron sputtering, *Thin Solid Films* 515 (2007) 3434–3438, <https://doi.org/10.1016/j.tsf.2006.10.013>.
- M. Yasaka, X-ray thin-film measurement techniques V. X-ray reflectivity measurement, *Rigaku J* 26 (2010) 1–9.
- P. Kumar, M. Gupta, U.P. Deshpande, D.M. Phase, V. Ganesan, J. Stahn, Density and microstructure of a-C thin films, *Diam. Relat. Mater.* 84 (2018) 71–76, <https://doi.org/10.1016/j.diamond.2018.03.008>.
- A.C. Ferrari, A. Libassi, B.K. Tanner, V. Stolojan, J. Yuan, J. Yuan, L.M. Brown, S. E. Rodil, B. Kleinsorge, J. Robertson, Density, sp^3 fraction, and cross-sectional structure of amorphous carbon films determined by x-ray reflectivity and electron energy-loss spectroscopy, *Phys. Rev. B - Condens. Matter Mater. Phys.* 62 (2000) 11089–11103, <https://doi.org/10.1103/PhysRevB.62.11089>.
- M. Samuelsson, *Fundamental Aspects of HiPIMS Under Industrial Conditions*, Linköping University, 2012. Ph.D. Thesis.
- K. Ait Aissa, A. Achour, J. Camus, L. Le Brizoul, P.Y. Jouan, M.A. Djouadi, Comparison of the structural properties and residual stress of AlN films deposited by dc magnetron sputtering and high power impulse magnetron sputtering at different working pressures, *Thin Solid Films* 550 (2014) 264–267, <https://doi.org/10.1016/j.tsf.2013.11.075>.
- J.S. Custer, M.O. Thompson, D.C. Jacobson, J.M. Poate, S. Roorda, W.C. Sinke, F. Spaepen, Density of amorphous Si, *Appl. Phys. Lett.* 64 (1994) 437–439, <https://doi.org/10.1063/1.111121>.
- D. Gračin, K. Juraic, I. Bogdanovic-Radovic, Estimation of amorphous silicon thin film density by optical methods, *Vacuum* 80 (2005) 146–150, <https://doi.org/10.1016/j.vacuum.2005.08.016>.
- J.W. Weber, T.A.R. Hansen, M.C.M. Van De Sanden, R. Engeln, B-spline parametrization of the dielectric function applied to spectroscopic ellipsometry on amorphous carbon, *J. Appl. Phys.* 106 (2009), 123503, <https://doi.org/10.1063/1.3257237>.
- J. Mohrmann, T.E. Tiwald, J.S. Hale, J.N. Hilfiker, A.C. Martin, Application of a B-spline model dielectric function to infrared spectroscopic ellipsometry data analysis, *J. Vac. Sci. Technol. B* 38 (2020), 014001, <https://doi.org/10.1116/1.5126110>.
- M. Serenyi, T. Lohner, P. Petrik, C. Frigeri, Comparative analysis of amorphous silicon and silicon nitride multilayer by spectroscopic ellipsometry and transmission electron microscopy, *Thin Solid Films* 515 (2007) 3559–3562, <https://doi.org/10.1016/j.tsf.2006.10.137>.
- S. Kumar Selvaraja, M. Schaeckers, W. Bogaerts, D. Van Thourhout, Deposited amorphous silicon-on-insulator technology for nano-photonics integrated circuits, *Opt. Commun.* 313 (2014) 210–216, <https://doi.org/10.1016/j.optcom.2013.10.033>.
- D. Gonçalves, E.A. Irene, Fundamentals and applications of spectroscopic ellipsometry, *Quim. Nova* 25 (2002), <https://doi.org/10.1590/s0100-40422002000600025>, 1050–1050.
- J. Sánchez-González, A. Díaz-Parralejo, A.L. Ortiz, F. Guiberteau, Determination of optical properties in nanostructured thin films using the Swanepoel method, *Appl. Surf. Sci.* 252 (2006) 6013–6017, <https://doi.org/10.1016/j.apsusc.2005.11.009>.
- H. Bäckle, Progress in micro-indentation hardness testing, *Metall. Rev.* 4 (1959) 49–100, <https://doi.org/10.1179/095066659790421746>.
- W. Zhang, J. Li, Y. Xing, X. Nie, F. Lang, S. Yang, X. Hou, C. Zhao, Experimental study on the thickness-dependent hardness of SiO₂ thin films using nanoindentation, *Coatings* 11 (2021) 1–12, <https://doi.org/10.3390/coatings11010023>.
- W.C. Oliver, G.M. Pharr, An improved technique for determining hardness and elastic modulus using load and displacement sensing indentation experiments, *J. Mater. Res.* 7 (1992) 1564–1583, <https://doi.org/10.1557/jmr.1992.1564>.
- P. Danesh, B. Pantchev, J. Wiezorek, B. Schmidt, D. Grambole, Effect of hydrogen on hardness of amorphous silicon, *Appl. Phys. A Mater. Sci. Process.* 102 (2011) 131–135, <https://doi.org/10.1007/s00339-010-6026-0>.
- B. Pantchev, P. Danesh, J. Wiezorek, Nanoindentation of hydrogenated amorphous silicon, *Philos. Mag.* 90 (2010) 4027–4039, <https://doi.org/10.1080/14786435.2010.502151>.
- L.J. Vandeperre, F. Giuliani, S.J. Lloyd, W.J. Clegg, The hardness of silicon and germanium, *Acta Mater* 55 (2007) 6307–6315, <https://doi.org/10.1016/j.actamat.2007.07.036>.

Publication in Materials Research Express (2019) : First author

Materials Research Express

PAPER

Comparing the performance of transparent, conductive ZnO/Ag/ZnO thin films that have an interlayer coating formed by either DC magnetron sputtering or HiPIMS

To cite this article: Anthika Lakhonchai *et al* 2019 *Mater. Res. Express* **6** 126410

View the [article online](#) for updates and enhancements.



IOP | ebooks™

Bringing you innovative digital publishing with leading voices to create your essential collection of books in STEM research.

Start exploring the collection - download the first chapter of every title for free.

Materials Research Express



PAPER

RECEIVED
19 September 2019REVISED
1 November 2019ACCEPTED FOR PUBLICATION
13 November 2019PUBLISHED
27 November 2019

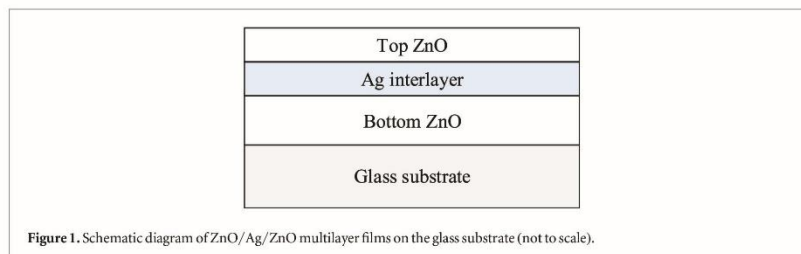
Comparing the performance of transparent, conductive ZnO/Ag/ZnO thin films that have an interlayer coating formed by either DC magnetron sputtering or HiPIMS

Anthika Lakhonchai¹, Artit Chingsungnoen^{1,2} , Phitsanu Poolcharuansin^{1,2} , Nitisak Pasaja^{1,2}, Mati Horprathum³, Ukit Rittihong⁴, Chanan Euaraksakul⁴, Sarayut Tunmee⁴, Narong Chanlek⁴ and Hiroki Akasaka⁵¹ Technological Plasma Research Unit, Department of Physics, Faculty of Science, Maharakham University, Maha Sarakham 44150, Thailand² Thailand Center of Excellence in Physics, Commission on Higher Education, 328 Si Ayutthaya Road, Bangkok 10400, Thailand³ Opto-Electrochemical Sensing Research Team, Spectroscopic and Sensing Devices Research Unit, National Electronics and Computer Technology Center, Pathumthani 12120, Thailand⁴ Synchrotron Light Research Institute (Public Organization), Nakhon Ratchasima 30000, Thailand⁵ Department of Mechanical Engineering, Tokyo Institute of Technology 152-8552, JapanE-mail: artit.c@msu.ac.th**Keywords:** transparent electrodes, ZnO/Ag/ZnO multilayer films, DC magnetron sputtering, high power impulse magnetron sputtering**Abstract**

Transparent electrodes (TEs) are essential components in many optoelectronic devices. Although indium tin oxide (ITO) has an excellent trade-off between optical transparency and electrical sheet resistance, it still suffers from several drawbacks, including the increasing cost of indium and poor long-term flexibility due to work hardening. This work presents the development of a new class of TEs based on ultrathin ZnO/Ag/ZnO samples in which Ag films with different film thickness are used as the metallic interlayer. XRD, XPS depth profiling, UV-vis-NIR spectrophotometer, Hall effect measurement, and a four-point probe system were used to characterize the properties of the fabricated films. Optimum thicknesses of Ag and ZnO top layer films were determined as those having high optical transmittance and good electrical conductivity. The main objective of this work has been to investigate how the density of the Ag interlayer in ZnO/Ag/ZnO film samples affects their optical and electrical properties. Silver layers prepared using DC magnetron sputtering (DCMS) have different densities to those prepared using high power impulse magnetron sputtering (HiPIMS). The optimum figure of merit at $3.53 \times 10^{-3} \Omega^{-1}$ was achieved for ZnO (0.6 nm)/Ag (9 nm)/ZnO (20 nm) multilayer films in which the Ag interlayer was fabricated using the HiPIMS method.

1. Introduction

Transparent electrodes are emerging as one of the most promising technologies for electronic products in which low resistance electrical contacts that do not block light are required, e.g., in flat-screen displays, organic LEDs, touch panels, and energy-saving windows [1–4]. Moreover, the market for transparent displays is predicted to be worth \$87.2 billion by the year 2025 [5]. Transparent conductive oxide (TCO) films that combine good electrical conductivity with good transparency of visible light are key components in these optoelectronic devices. The most important commercial material used to make TCO films is indium tin oxide (ITO) because of its unique characteristics: high visible transmittance and low resistivity. However, if the increase in usage of ITO films in flat panel displays and solar cells continues at its current pace, not only will the price of ITO continue to rise, but indium will soon start to become scarce [6]. The development of alternative TCO materials is necessary to resolve this serious problem [7, 8]. Although several indium-free films such as SnO₂/Ag/SnO₂ (SAS) [9], TiO₂/Ag/TiO₂ (TAT) [10] and FTO/Ag/FTO (FAF) [11] multilayer films have been suggested as transparent electrodes. They were also prepared by conventional DC or RF sputtering process and cheaper than ITO.



Recently, zinc oxide (ZnO)-based thin films for use in optoelectronic devices have attracted interest because they have high stability in hydrogen plasma; have low growth temperature; are non-toxic; and the constituent materials of the films are cheap and abundant [12–15]. Zinc oxide thin films have been prepared using thermal evaporation [16], chemical vapor deposition (CVD) [17], metal-organic chemical vapor deposition (MOCVD) [18], plasma-enhanced chemical vapor deposition (PECVD) [19, 20], Sol-gel [21], pulsed laser deposition (PLD) [22], and magnetron sputtering methods. Among these techniques, DCMS and HiPIMS are the effective techniques for producing stable, and large-size thin films [23, 24].

Much research is currently being conducted into improving conductivity and transparency by doping ZnO with Al, Ga, B, or F [25, 26]. However, the achievable electrical properties of the films grown by industrially applicable processes such as DCMS are still inferior to that of ITO. Aluminum-doped zinc oxide (ZnO:Al or Al_2O_3 -ZnO (AZO)) with thicknesses in the range of several hundred nanometers have to be applied to reach a sufficiently low sheet resistance of only a few Ω/sq , which is what is required for flat panel displays. However, conventional single-layer TCO electrodes are of limited use in high-performance flexible devices due to the films having high sheet resistance and poor mechanical properties because of their relatively large thicknesses [27, 28]. In order to reduce the TCO layer thickness while maintaining the low sheet resistance and high transparency, multilayer transparent electrodes TCO/metal/TCO, in which a thin metal layer is sandwiched between two TCO layers, can be used. In this configuration, the electrical conductivity is primarily controlled by the metal interlayer while the top TCO layer produces an antireflection effect and also acts as a protective layer. The TCO layer on the bottom side can decrease surface roughness and provides good electrical contact [11].

In this work, an ultrathin ZnO/Ag/ZnO sample was prepared using the magnetron sputtering method. Silver thin film was selected as the interlayer because it combines high bulk conductivity with good optical behavior, i.e., low-loss and color-neutral transparency. Zinc oxide is also known to be an excellent seed layer for the growth of Ag [29, 30], and it has a high refractive index leading to an improved anti-reflection effect. Because the preparation method of the Ag interlayer, i.e., whether it is DCMS or HiPIMS, can directly affect the performance of transparent electrodes, this study is mainly focused on comparing the optical and electrical properties of two types of ZnO/Ag/ZnO samples: samples in which the Ag interlayers were prepared using DCMS and samples in which the Ag interlayers were prepared using HiPIMS. In addition, the effect of the thickness of the top ZnO layer on the sheet resistance was also investigated.

2. Experimental details

The ZnO/Ag/ZnO multilayer films as shown in figure 1 were consecutively deposited onto glass substrates at room temperature using a dual magnetron sputtering system with pure Zn (99.99% purity) and Ag (99.99% purity) targets. The glass substrates were ultrasonically cleaned once in acetone, twice in methanol, and three times in deionized water with 10 min on each occasion. They were then blown dry with filtered dry air before being loaded into the deposition chamber through a load lock chamber. Figure 2 shows a schematic diagram of the magnetron sputtering system, which consists of a vacuum chamber (volume of 6.5 liters, diameter of 211 mm, and a height of 186 mm) and a pumping section consists of a diffusion pump backed with a rotary pump to produce the base pressure of 1.33×10^{-4} Pa. The substrate-to-target distance was kept constant at 80 mm. The Zn target was sputtered in a reactive mode using a bipolar pulse power supply, and the Ag target was sputtered in a metal mode using both DC and HiPIMS power supplies. The flows of high purity argon (99.999%) and oxygen (99.999%) for film deposition were independently controlled by two mass flow controllers. Before deposition, the targets were pre-sputtered for 3 min to remove any contamination. The sputtering conditions used for the deposition are summarized in table 1. A quartz crystal microbalance, in this case, an INFICON STM-2XM, was used within the vacuum chamber to measure film thicknesses on the substrates in real time.

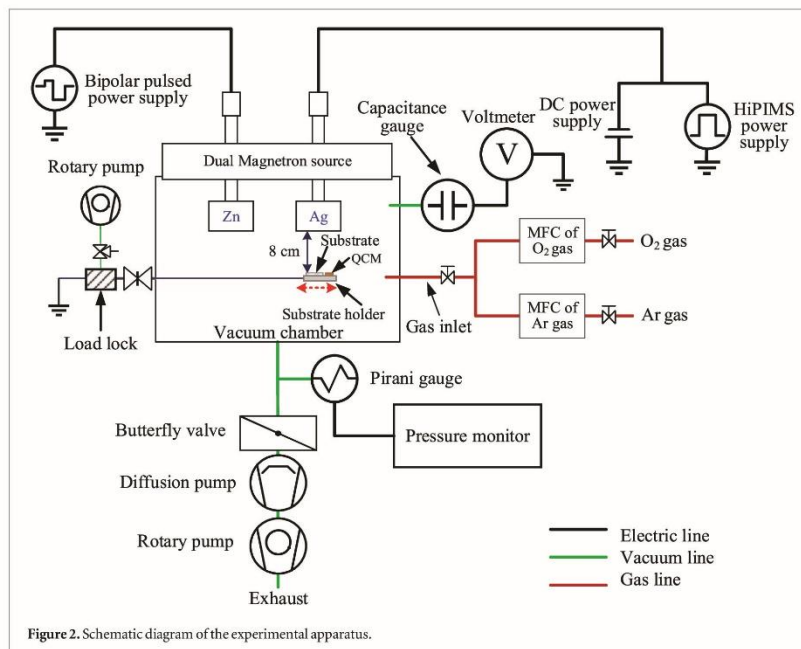


Table 1. Sputtering conditions of ZnO/Ag/ZnO multilayer films.

Deposition parameters	Conditions		
	Bottom and top ZnO layer	DCMS	Ag interlayer
Techniques	Reactive pulsed DC magnetron sputtering (50 kHz, duty cycle 15%)	DCMS	HiPIMS (100 Hz, duty cycle 1%)
Target	Zn (99.99%)		Ag (99.99%)
Target diameter/thickness (inch)	2/0.250		
Sputtering power (W)	50		33
Gas flow rate (sccm)	Ar = 10, O ₂ = 10		Ar = 20
Initial pressure (Pa)	$\approx 1.33 \times 10^{-4}$		
Working pressure (Pa)	≈ 0.64		≈ 0.70
Substrate temperature (°C)	Room temperature (≈ 22)		
Substrate-to-target distance (mm)	80		

After deposition, the crystallinity and crystal orientation of the ZnO/Ag/ZnO multilayer films were investigated using an x-ray diffractometer (XRD Bruker D8 Advance) with Cu-K α radiation ($\lambda = 0.154$ nm). The chemical composition and depth profiling were characterized using x-ray photoelectron spectroscopy (XPS, PHI5000 VersaProbeII, ULVAC-PHI) with a monochromatic Al-K α x-ray source (1486.6 eV). The optical transmittance was measured using a UV-vis-NIR spectrophotometer (CARY 7000) in the wavelength range of 200–2000 nm. The sheet resistance of the samples was evaluated using a linear four-point probe (JANDEL

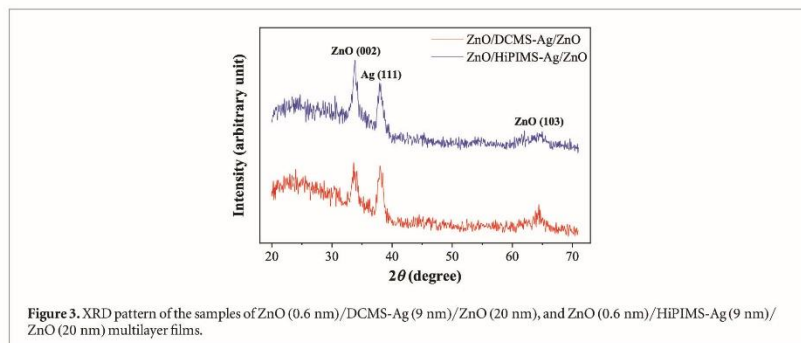


Figure 3. XRD pattern of the samples of ZnO (0.6 nm)/DCMS-Ag (9 nm)/ZnO (20 nm), and ZnO (0.6 nm)/HiPIMS-Ag (9 nm)/ZnO (20 nm) multilayer films.

Table 2. X-ray diffraction data summary of (111) plane of Ag interlayer films prepared using different methods.

Sample	2θ (°)	FWHM (°)	D (nm)
ZnO (0.6 nm)/DCMS-Ag (9 nm)/ZnO (20 nm)	38.04441	1.36393	6.44
ZnO (0.6 nm)/HiPIMS-Ag (9 nm)/ZnO (20 nm)	38.02774	0.99829	8.80

RM3). Resistivity, carrier concentration, and Hall mobility were measured using the Hall effect measurement device (ECOPIA-HMS-3000) taken in a magnetic field of 0.55 T.

3. Results and discussion

3.1. Crystal structure analysis

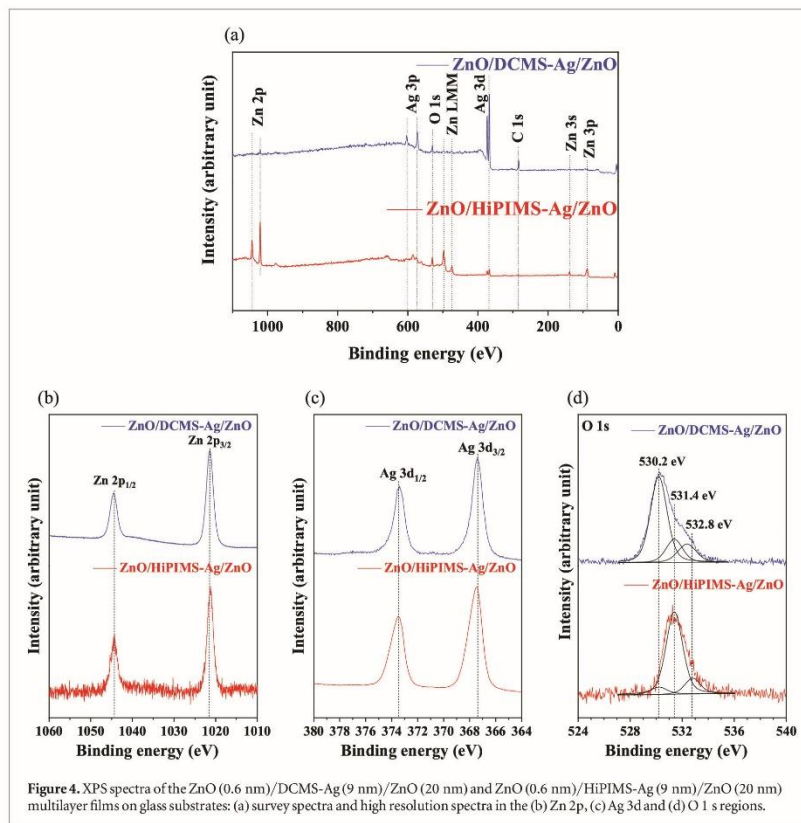
Figure 3 shows XRD patterns of the ZnO (0.6 nm)/DCMS-Ag (9 nm)/ZnO (20 nm) and ZnO (0.6 nm)/HiPIMS-Ag (9 nm)/ZnO (20 nm) multilayer films deposited on glass substrates. The diffraction peaks detected at $2\theta = 33.746^\circ$ (DCMS-Ag) and 33.805° (HiPIMS-Ag) correspond to the (002) planes of ZnO (JCPDS No. 65-3411). These two peaks were indexed to the hexagonal wurtzite crystal structure of the ZnO. Because the top ZnO (0.6 nm) is extremely thin, the appearance of weak diffraction peaks suggests there was insufficient time for the formation of the initially preferred film orientation. The (002) peak position observed in this study was slightly lower than 34.467° for bulk ZnO (COD 10 11 258) [31], and this was attributed to some residual stress in the film, likely originating from a mismatch in the thermal expansion coefficients of ZnO and the Ag interlayer. The full width at half maximum (FWHM) of the diffraction peak can be used to estimate the average crystallite size (D) in the grown films using Scherrer's formula [31, 32]:

$$D = \frac{0.94\lambda}{FWHM \cos \theta} \quad (1)$$

Table 2 shows the peak position, full width at half maximum (FWHM), and the average crystallite size that corresponds to the (111) plane of Ag (JCPDS No. 87-0720). The average crystallite size of HiPIMS-Ag is larger than that prepared by DCMS due to a high degree of ionization, high plasma density, and high ion flux towards the substrate, which in turn allows higher quality thin films to be deposited in comparison with DCMS [33, 34].

3.2. XPS depth profile

Figure 4(a) shows the XPS spectra of the ZnO/Ag/ZnO sample with ZnO (0.6 nm)/DCMS-Ag (9 nm)/ZnO (20 nm) and ZnO (0.6 nm)/HiPIMS-Ag (9 nm)/ZnO (20 nm) multilayer films in the range of 0–1100 eV. The spectra reveal the presences of Zn, O, Ag, and C on the surfaces of both multilayer films. The observation of the Ag layer in the XPS spectra suggests the top ZnO layers have an ultra-thin thickness. Typically, the analysis depth for XPS is less than 5 nm. The presence of carbon is attributed to surface contamination during the sample preparation and handling. The high-resolution XPS spectra in the Zn 2p, Ag 3d and O 1s are shown in figures 4(b)–(d), respectively. The Zn 2p_{3/2} and Zn 2p_{1/2} peaks of both multilayer films were observed at binding

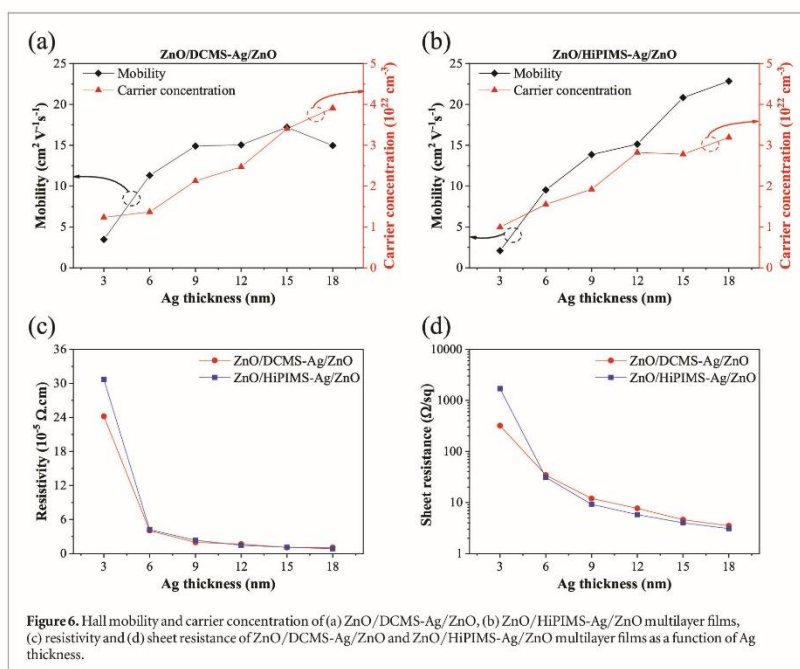
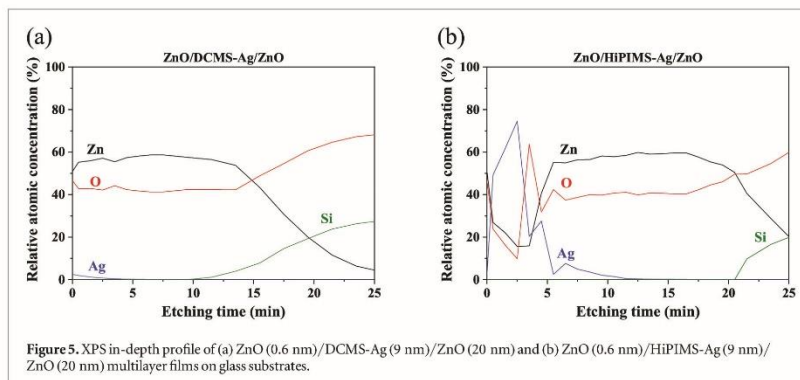


energies of 1021.4 and 1044.5 eV, respectively, confirming the formation of ZnO on the surfaces. The Ag 3d_{3/2} and Ag 3d_{1/2} peaks were found at the binding energies of 367.4–367.6 and 373.4–373.6 eV, respectively, which is a characteristic of metallic silver. The O 1s peaks of both multilayer films were deconvoluted into three peaks at the binding energies of 530.2, 531.4 and 532.8 eV which are associated with ZnO, dissociated oxygen or OH species on the surface and C-O/C = O, respectively.

The depth profile of chemical composition was carried out using Ar ion etching with a beam energy of 4 keV and a beam size of $2 \times 2 \text{ mm}^2$. The result is shown in figure 5. The depth profiles of both multilayer films exhibit three asymmetric regions corresponding to ZnO/Ag/ZnO samples with different sputtering times for the bottom and top ZnO layers. The etching time for the Ag interlayer prepared using HiPIMS is longer than that prepared using DCMS, suggesting that the HiPIMS-Ag interlayer has a higher density than the DCMS-Ag interlayer. This result could be attributed to the increased metal ion bombardment commonly seen in HiPIMS discharges due to the momentum transfer between the growing film, and the incoming metal ions being very efficient because the film and bombarding species are of equal mass, which in turn leads to a less porous microstructure.

3.3. Performance of transparent electrodes

Figures 6(a)–(d) show the carrier concentration, Hall mobility, resistivity, and sheet resistance as a function of the thickness of the Ag interlayer for the ZnO/DCMS-Ag/ZnO and ZnO/HiPIMS-Ag/ZnO multilayer films. As shown in figures 6(a) and (b), the increase in the carrier concentration and Hall mobility could be explained by increasing nuclei growth and formation of isolated islands. These increases were affected by the transformation from an island-like distribution to a continuous thin film as the Ag interlayer thickness increased [35, 36]. Generally, the electrical conductivity of metallic films can be divided into three zones. As initially isolated



metallic nanoparticles form a fractal structure during the deposition process, the interconnection leads to nanoclusters with more irregular shapes and broader size distributions. At extremely thin films (dielectric zone), the isolated nature of discontinuous particles, show very low mobility and conductivity. The electron transport in the dielectric zone is governed by an activated tunnelling process. As the film thickness increases, the electrical conductivity and mobility rapidly increase as isolated particles start to coalesce (percolation zone). At film thicknesses close to the electron mean free path, the film exhibits near metallic conductivity (metallic zone) in which the higher e-e scattering rate can suppress to the mobility [37, 38].

Figures 6(c)–(d) shows that the resistivity and sheet resistance of the films decreased rapidly with increasing film thickness from 3 to 6 nm and only slightly decreased with a further increase in the film thickness up to 18 nm. The decrease in resistivity is mainly due to the increases in both carrier concentration and Hall mobility

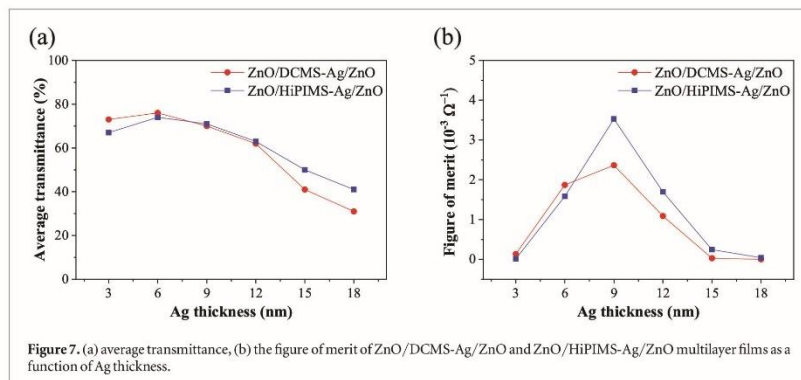


Figure 7. (a) average transmittance, (b) the figure of merit of ZnO/DCMS-Ag/ZnO and ZnO/HiPIMS-Ag/ZnO multilayer films as a function of Ag thickness.

due to the Ag layer thickness increasing. At an Ag thickness below 6 nm, the formation of isolated islands increases the resistivity due to the decrease in grain size or other discontinuities of the film, resulting in an increase in carrier scattering [39]. When the thickness of the Ag is greater than 6 nm, the sheet resistance of the ZnO/HiPIMS-Ag/ZnO samples is slightly lower than that of the ZnO/DCMS-Ag/ZnO samples. In general, an increase in film density of 5%–15% can be seen when HiPIMS is used [40] because this method creates films with denser microstructure due to the higher ionized metal flux fraction as well as the higher incident ion energy, which in turn contribute to greater energy transfer to the growing films in comparison with DCMS.

Figure 7(a) shows the average transmittance from 380 to 780 nm of the ZnO/DCMS-Ag/ZnO and ZnO/HiPIMS-Ag/ZnO samples as a function of Ag thickness. It was found that in both cases the average transmittances increased with increasing Ag thickness from 3 to 6 nm. However, the average transmittance gradually decreased as the Ag thickness is further increased above 6 nm. At the smaller thicknesses (less than 3 nm), the growth of the ultrathin Ag interlayer has an island structure (Volmer–Weber growth) with random distribution, which results in the Ag particles scattering and reflecting incident light [41–44]. These phenomena can generate plasmon resonance absorption that contributes to the lower light transmittance. When the Ag layer is 6 nm thick, the islands start to coalesce into a continuous film. Therefore, the scattering and reflecting were reduced as the gap between Ag particles decreased [41]. When the thickness of the Ag is less than 6 nm, most of the islands coalesce, resulting in the average transmittance decreasing because the light reflection increases. When the Ag thickness is increased from 12 to 18 nm, the average transmittance value of ZnO/HiPIMS-Ag/ZnO samples exhibits a higher transmittance due to the higher densification of the Ag film creating a more homogeneous surface on the Ag interlayer.

Although the electrical properties of the ZnO/Ag/ZnO samples can be improved by increasing the Ag thickness, the optical transmittance is reduced when the film thickness is increased. Therefore, to determine the optimal thickness of an Ag interlayer and to quantitatively estimate the performance of TEs, the figure of merit (FOM, Φ), as defined by Haacke [45], was used to describe the relationship between the electrical and optical properties, can be written as

$$\Phi = \frac{T^{10}}{R_{sh}}, \quad (2)$$

where T is the average transmittance in the visible range and R_{sh} is the sheet resistance. The FOM as a function of Ag thickness of ZnO/DCMS-Ag/ZnO and ZnO/HiPIMS-Ag/ZnO multilayer films is shown in figure 7(b). This result shows that the optimized Ag interlayer thickness is 9 nm in both the ZnO/DCMS-Ag/ZnO and ZnO/HiPIMS-Ag/ZnO samples, with high FOM values of 2.36×10^{-3} and $3.53 \times 10^{-3} \Omega^{-1}$, respectively. Although both DCMS-Ag and HiPIMS-Ag exhibit similar transmittance, the higher FOM for the ZnO/HiPIMS-Ag/ZnO sample is mainly attributed to the lower sheet resistance. However, these figure of merit can be improved using the post-deposition annealing for increasing of the conductivity of the ZnO layer [46] or using the nitrogen doping to decrease sheet resistance due to nitrogen incorporation caused shallow neutral acceptor states in ZnO [47].

Figure 8 shows the sheet resistance, average transmittance, and the FOM of ZnO/HiPIMS-Ag (9 nm)/ZnO (20 nm) samples as a function of the top ZnO layer thickness. The sheet resistance significantly increases from 10 to 2100 Ω/sq , and the average transmittance slightly increases from 68 to 75% when the thickness of the top ZnO layer increases from 0.6 to 3.0 nm. These results show that another important factor affects the electrical

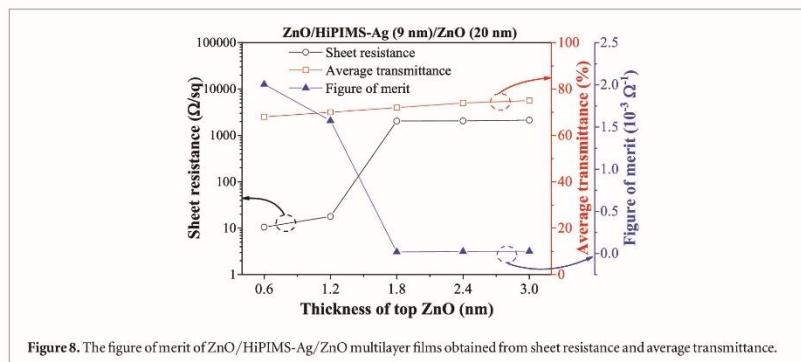


Figure 8. The figure of merit of ZnO/HiPIMS-Ag/ZnO multilayer films obtained from sheet resistance and average transmittance.

and optical properties of ZnO/Ag/ZnO samples is the thickness of the top ZnO layer. The thickness of the top ZnO layer directly affects the sheet resistance due to its limiting charge transport from the top ZnO layer through the Ag interlayer. In contrast, the thicker top ZnO layer reduces the surface plasmon resonant absorption and enhances the antireflection, thus increasing the transmittance. It was observed that the FOM decreases with increasing thickness of the top ZnO layer, the decrease in FOM being due to the rapid increase in sheet resistance associated with the increase in thickness of top ZnO layer. The ZnO/HiPIMS-Ag/ZnO samples with a 0.6 nm-thick top ZnO layer give the highest FOM of $2.0 \times 10^{-3} \Omega^{-1}$ because they have the lowest sheet resistance. Although the ZnO/Ag/ZnO multilayer system reported by Mohamed [47] showed the top ZnO layer with the thickness around 40 nm gives the highest value in the figure of merit, the ZnO here is doped with nitrogen to decrease the sheet resistance. Therefore, he can use thicker of top ZnO layer than this work. However, in this work, only the mixture of 10 sccm oxygen, and 10 sccm argon was used to prepare top ZnO layer. Because the effect of N_2 doped ZnO films can induce small transparency for visible light due to nitrogen incorporation caused shallow neutral acceptor states in ZnO [48].

4. Conclusion

In this research, ultrathin ZnO/Ag/ZnO multilayer films were fabricated on a glass substrate. The ZnO thin films were prepared using a reactive magnetron sputtering, while the Ag interlayer was prepared using the DCMS and HiPIMS methods. The performance of transparent electrodes as a function of the thickness of Ag interlayer was investigated. The result from XRD of the ZnO/Ag/ZnO samples shows a sharp (002) peak for the ZnO with a hexagonal wurtzite structure and (111) peak for the Ag with the face-centered cubic structure. The XPS in-depth profiles show that the ZnO/Ag/ZnO multilayer films have an asymmetric structure due to the different thicknesses of the bottom and top ZnO layers. The sputtering time for the Ag interlayer prepared using HiPIMS is longer than that prepared using DCMS. Therefore, Ag film deposited using HiPIMS should be denser than that deposited using DCMS. Hall effect measurement, UV-vis-NIR spectroscopy, and a four-point probe were used to characterize the properties of the fabricated films as a function of thicknesses of the Ag and top ZnO layer. It was found that a 9 nm-thick Ag interlayer gives the highest Haacke's FOM. The values being 3.53×10^{-3} and $2.36 \times 10^{-3} \Omega^{-1}$ for layers prepared by HiPIMS and DCMS, respectively, suggesting that HiPIMS is the better method for preparation of the metallic Ag interlayer. The thickness of the top ZnO layer of 0.6 nm exhibits the lowest sheet resistance and gives the best FOM, while the higher thickness of top ZnO will limit charge transport from the top ZnO layer through the Ag interlayer and thus reduce the FOM. Due to the high-density microstructure of the Ag interlayer prepared by HiPIMS, the ZnO/Ag/ZnO multilayer films with an ultra-thin film of top ZnO are attractive candidates to be used as TEs. Such TEs will have superior performance compared to those with an Ag interlayer prepared using DCMS.

Acknowledgments

This research was partially funded by the Thailand Center of Excellence in Physics (ThEP) and Faculty of Science, Mahasarakham University, grant number ThEP-61-EQP-MSU2. The author acknowledges all facilities and support from the National Electronics and Computer Technology Center, the Synchrotron Light Research Institute (Public Organization), and the Tokyo Institute of Technology.

ORCID iDs

Artit Chingsungnoen  <https://orcid.org/0000-0003-3194-9254>Phitsanu Poolcharuansin  <https://orcid.org/0000-0001-9650-9888>

References

- [1] Zadsar M, Fallah H R, Mahmoodzadeh M H and Tabatabaei S V 2012 The effect of Ag layer thickness on the properties of WO₃/Ag/MoO₃ multilayer films as anode in organic light emitting diodes *J. Lumin.* 132 992–7
- [2] Khan F, Baek S H and Kim J H 2014 Influence of Ag doping on structural, optical, and photoluminescence properties of nanostructured AZO films by sol-gel technique *J. Alloys Comp.* 584 190–4
- [3] Zhou H P, Xu S, Zhao Z and Xiang Y 2014 Inductively coupled hydrogen plasma processing of AZO thin films for heterojunction solar cell applications *J. Alloys Comp.* 610 107–12
- [4] Betz U, Kharrazi O M, Marthy J, Escola M F and Atamny F 2006 Thin films engineering of indium tin oxide: large area flat panel displays application *Surf. Coat. Technol.* 200 5751–9
- [5] DisplayBank Special Report 2012 Transparent Display Technology and Market Forecast (<https://technology.ihc.com/api/binary/408837attachment=true>)
- [6] Afre R A, Sharma N, Sharon M and Sharon M 2018 Transparent conducting oxide films for various applications: a review *Rev. Adv. Mater. Sci.* 53 78–89
- [7] Liu Y, Li Y and Zeng H 2013 ZnO-based transparent conductive thin films: doping, performance, and processing *J. Nanomater.* 196521 1–9
- [8] Minami T 2005 Transparent conducting oxide semiconductors for transparent electrodes *Semicond. Sci. Technol.* 20 S35
- [9] Yoon S M and Jang G E 2016 Growth and characteristics of SnO₂/Ag/SnO₂ multi layer film with thickness variation of SnO₂ layer *Mater. Sci. Forum* 864 169–74
- [10] Loka C, Moon S W, Choi Y and Lee K-S 2018 High transparent and conductive TiO₂/Ag/TiO₂ multilayer electrode films deposited on sapphire substrate *Adv. Mater. Lett.* 14 125–32
- [11] Yu S, Li L, Lyu X and Zhang W 2016 Preparation and investigation of nano-thick FTO/Ag/FTO multilayer transparent electrodes with high figure of merit *Sci. Rep.* 6 20399
- [12] Miao D, Jiang S, Zhao H, Shang S and Chen Z 2014 Characterization of AZO and Ag based films prepared by RF magnetron sputtering *J. Alloys Comp.* 616 26–31
- [13] Yong-Hui Z, Zeng-Xia M, Hui-Li L and Xiao-Long D 2017 Review of flexible and transparent thin-film transistors based on zinc oxide and related materials *Chin. Phys. B* 26 047307
- [14] Muslih E Y and Kim K H 2017 Preparation of zinc oxide (ZnO) thin film as transparent conductive oxide (TCO) from zinc complex compound on thin film solar cells: a study of O₂ effect on annealing process *IOP Conf. Ser.: Mater. Sci. Eng.* 214 012001
- [15] Nunes P, Fortunato E, Tonello P, Fernandes F B, Vilarinho P and Martins R 2002 Effect of different dopant elements on the properties of ZnO thin films *Vacuum* 64 281–5
- [16] Palimar S, Bangera K V and Shivakumar G K 2013 Study of the doping of thermally evaporated zinc oxide thin films with indium and indium oxide *Appl. Nanosci.* 3 549
- [17] Fay S and Shah A 2008 *Transparent Conductive Zinc Oxide: Basics and Applications in Thin Film Solar Cells* (Berlin: Springer) pp 235–302
- [18] Ni J et al 2005 MOCVD-derived highly transparent, conductive zinc- and tin-doped indium oxide thin films: precursor synthesis, metastable phase film growth and characterization, and application as anodes in polymer light-emitting diodes *J. Am. Chem. Soc.* 127 5613–24
- [19] Barankin M D, Gonzalez E II, Ladwig A M and Hicks R F 2007 Plasma-enhanced chemical vapor deposition of zinc oxide at atmospheric pressure and low temperature *Sol. Energy Mater. Sol. Cells* 91 924–30
- [20] Chao C H and Wei D H 2015 Synthesis and characterization of high c-axis ZnO thin film by plasma enhanced chemical vapor deposition system and its UV photodetector application *J. Vis. Exp.* 104 e53097
- [21] Chen W J, Liu W L, Hsieh S H and Hsu Y G 2012 Synthesis of ZnO:Al transparent conductive thin films using sol-gel method *Procedia Eng.* 36 54–61
- [22] Franklin J B, Zou B, Petrov P, McComb D W, Ryan M P and McLachlan M A 2011 Optimized pulsed laser deposition of ZnO thin films on transparent conducting substrates *J. Mater. Chem.* 21 8178
- [23] Ellmer K 2000 Magnetron sputtering of transparent conductive zinc oxide: relation between the sputtering parameters and the electronic properties *J. Phys. D: Appl. Phys.* 33 R17
- [24] Lin W 2008 Properties of doped ZnO transparent conductive thin films deposited by RF magnetron sputtering using a series of high quality ceramic targets *Rare Met.* 27 32–5
- [25] Minami T, Sato H, Nanto H and Takata S 1985 Group III impurity doped zinc oxide thin films prepared by RF magnetron sputtering *Jpn. J. Appl. Phys.* 24 L781
- [26] Dixon S C, Scanlon D O, Carmalt C J and Parkin I P 2016 N-Type doped transparent conducting binary oxides: an overview *J. Mater. Chem. C* 4 6946–61
- [27] Guillén C and Herrero J 2011 TCO/metal/TCO structures for energy and flexible electronics *Thin Solid Films* 520 1–17
- [28] Boscarino S, Crupi I, Mirabella S, Simone F and Terrasi A 2014 TCO/Ag/TCO transparent electrodes for solar cells application *Appl. Phys. A* 116 1287–91
- [29] Sahu D R and Huang J L 2006 High quality transparent conductive ZnO/Ag/ZnO multilayer films deposited at room temperature *Thin Solid Films* 515 876–9
- [30] Crupi I, Boscarino S, Strano V, Mirabella S, Simone F and Terrasi A 2012 Optimization of ZnO:Al/Ag/ZnO:Al structures for ultra-thin high-performance transparent conductive electrodes *Thin Solid Films* 520 4432–5
- [31] Warren B E 1990 *X-ray diffraction* (New-York: Dover) pp 253
- [32] Aslan M H, Oral A Y, Mensur E, Gül A and Başaran E 2004 Preparation of c-axis oriented zinc oxide thin films and the study of their microstructure and optical properties *Sol. Energy Mater. Sol. Cells* 82 543–52
- [33] Zhang H, Cherg J-H and Chen Q 2019 Recent progress on high power impulse magnetron sputtering (HiPIMS): the challenges and applications in fabricating VO₂ thin film *AIP Adv.* 9 035242

- [34] Wu B, Haehnlein I, Shchelkanov I, McLain J, Patel D, Uhlig J, Jurczyk B, Leng Y and Ruzic D-N 2018 Cu films prepared by bipolar pulsed high power impulse magnetron sputtering *Vacuum* 150 216–21
- [35] Das S, Choi H W and Alford T L 2014 Effect of Ag layer thickness on the electrical transport and optical properties of ZnO/Ag/MoOx transparent composite electrodes and their use in P₃HT:PC₆₁BM-based organic solar cells *Mater. Lett.* 133 183–5
- [36] Oh D, No Y S, Kim S Y, Cho W J, Kwack K D and Kim T W 2011 Effect of Ag film thickness on the optical and the electrical properties in CuAlO₂/Ag/CuAlO₂ multilayer films grown on glass substrates *J. Alloys Comp.* 509 2176–9
- [37] Lugovskoy A V and Bray I 2001 Electron-electron scattering rate in thin metal films *Phys. Rev. B* 65 045405
- [38] Wei H and Eilers H 2009 From silver nanoparticles to thin films: evolution of microstructure and electrical conduction on glass substrates *J. Phys. Chem. Solids* 70 459–65
- [39] Kim H, Horwitz J S, Kushto G, Piqué A, Kafafi Z H, Gilmore C M and Chrisey D B 2000 Effect of film thickness on the properties of indium tin oxide thin films *J. Appl. Phys.* 88 6021
- [40] Samuelsson M, Lundin D, Jensen J, Raadu M A, Gudmundsson J T and Helmersson U 2010 On the film density using high power impulse magnetron sputtering *Surf. Coat. Technol.* 205 591–6
- [41] Miao D, Jiang S, Shang S and Chen Z 2014 Highly transparent and infrared reflective AZO/Ag/AZO multilayer film prepared on PET substrate by RF magnetron sputtering *Vacuum* 106 1–4
- [42] Sabin K P, Srinivas G, Shashikala H D, Dey A, Sridhara N, Sharma A K and Barshili H C 2017 Highly transparent and conducting ITO/Ag/ITO multilayer thin films on FEP substrates for flexible electronics applications *Sol. Energy Mater. Sol. Cells* 172 277–84
- [43] Sharma V, Kumar P, Kumar A, Surbhi, Asokan K and Sachdev K 2017 High-performance radiation stable ZnO/Ag/ZnO multilayer transparent conductive electrode *Sol. Energy Mater. Sol. Cells* 169 122–31
- [44] Charles A B *Vacuum Deposition onto Webs, Films and Foils* (United States of America: Elsevier) pp 241–50
- [45] Haacke G 1976 New figure of merit for transparent conductors *J. Appl. Phys.* 47 4086
- [46] Chen P S, Peng C-H, Chang Y-W, Lin T W and Lee S W 2016 Improved indium-free transparent ZnO/Metal/ZnO electrode through a statistical experimental design method *Adv. Mater. Sci. Eng.* 7258687 1–12
- [47] Mohamed S H 2008 Effects of Ag layer and ZnO top layer thicknesses on the physical properties of ZnO/Ag/ZnO multilayer system *J. Phys. Chem. Solids* 69 2378–84
- [48] Burinskas S, Dudonis J, Milcius D, Karaliunas M and Kuokštis E 2010 Synthesis of ZnO:N thin films by reactive DC magnetron sputtering *Lith. J. Phys.* 50 325–33

Enhancement of output power density in a modified polytetrafluoroethylene surface using a sequential O₂/Ar plasma etching for triboelectric nanogenerator applications

Teerayut Prada¹, Viyada Harnchana^{1,2} (✉), Anthika Lakhonchai³, Artit Chingsungnoen³ (✉), Phitsanu Poolcharuansin³, Narong Chanlek⁴, Annop Klamchuen⁵, Prasit Thongbai^{1,2}, and Vittaya Amornkitbamrung^{1,2}

¹ Department of Physics, Khon Kaen University, Khon Kaen 40002, Thailand

² Institute of Nanomaterials Research and Innovation for Energy (IN-RIE), NANOTEC-KKU RNN on Nanomaterials Research and Innovation for Energy, Khon Kaen University, Khon Kaen 40002, Thailand

³ Technological Plasma Research Unit, Department of Physics, Faculty of Science, Mahasarakham University, Maha Sarakham 44150, Thailand

⁴ Synchrotron Light Research Institute (Public Organization), Nakhon Ratchasima 30000, Thailand

⁵ National Nanotechnology Center (NANOTEC), NSTDA, Pathum Thani 12120, Thailand

© Tsinghua University Press and Springer-Verlag GmbH Germany, part of Springer Nature 2021

Received: 19 December 2020 / Revised: 24 March 2021 / Accepted: 25 March 2021

ABSTRACT

In this work, the surface modification using a two-steps plasma etching has been developed for enhancing energy conversion performance in polytetrafluoroethylene (PTFE) triboelectric nanogenerator (TENG). Enhancing surface area by a powerful O₂ and Ar bipolar pulse plasma etching without the use of CF₄ gas has been demonstrated for the first time. TENG with modified surface PTFE using a sequential two-step O₂/Ar plasma has a superior power density of 9.9 W·m⁻², which is almost thirty times higher than that of a pristine PTFE TENG. The synergistic combination of high surface area and charge trapping sites due to chemical bond defects achieved from the use of a sequential O₂/Ar plasma gives rise to the intensified triboelectric charge density and the enhancement of power output of PTFE-based TENG. The effects of plasma species and plasma etching sequence on surface morphologies and surface chemical species were investigated by a field emission scanning electron microscopy (FESEM), atomic force microscopy (AFM), and X-ray photoelectron spectroscopy (XPS). The correlation of surface morphology, chemical structure, and TENG performance was elucidated. In addition, the applications of mechanical energy harvesting for lighting, charging capacitors, keyboard sensing and operating a portable calculator were demonstrated.

KEYWORDS

two-step plasma etching, O₂ and Ar plasma, CF₄ free, triboelectric nanogenerator, power output enhancement

1 Introduction

Triboelectric nanogenerators (TENGs) have recently received extensive attention as a new technology of energy harvesting to serve the increasing demand of energy in the internet of things (IoT) era. TENG has now become one of the most efficient approaches to harvest mechanical energy at low frequencies that offers numerous promising advantages including high electrical power density, facile fabrication, and the ability to harvest a wide range of mechanical energy forms. The operation of TENG is based upon a combination of contact electrification and electrostatic induction [1–3]. Energy conversion efficiency is established to be a function of triboelectric charge density upon contact electrification effect, which depends on a pair of materials that should have a large difference in their electro-negativities [4, 5]. Apart from material selection, contact area is regarded as a crucial factor that influences TENG performance by increasing surface charge density upon electrification event. Many approaches have therefore been proposed for modifying surface morphologies of polymeric materials, such as lithography

process [6–10], plasma etching [11–31], block copolymer method [32, 33], microneedle-structured method [34, 35], and chemical treatment [36–38].

Polytetrafluoroethylene (PTFE), or Teflon, is a commonly used material because of F atom makes it the most attractive to electrons. In addition, properties of PTFE, which are chemical resistance, thermal resistance, low coefficient of friction or good lubricity, and biocompatibility also provide a variety of applications in TENG device [11, 25, 27]. Electrification effect in PTFE is generally enhanced by surface modification which can essentially improve the electrical output of the PTFE-based TENGs [39–43]. The majority of reported PTFE-based TENGs employed inductively coupled plasma (ICP) etching [11–31], while other technique, such as sanding with sandpaper, was also demonstrated [42, 44]. ICP is known as one of the most effective routes to create nanostructures on polymeric material surfaces by using tetrafluoromethane (CF₄), oxygen (O₂), and argon (Ar) gases [28–30, 45]. Since CF₄ is toxic to humans and environment, avoiding the use of CF₄ gas would be beneficial for the fabrication of high-performance PTFE-based TENG.

Address correspondence to Viyada Harnchana, viyada@kku.ac.th; Artit Chingsungnoen, artit.c@msu.ac.th

Article

Development of a Multihole Atmospheric Plasma Jet for Growth Rate Enhancement of Broccoli Seeds

Khattiya Srakaew ¹, Artit Chingsungnoen ^{1,*}, Waraporn Sutthisa ², Anthika Lakhonchai ¹, Phitsanu Poolcharuansin ¹, Poramate Chunpeng ¹, Catleya Rojviriyaya ³, Kanjana Thumanu ³ and Sarayut Tunmee ³

¹ Technological Plasma Research Unit, Department of Physics, Faculty of Science, Maharakham University, Maha Sarakham 44150, Thailand; khattiya.ball@gmail.com (K.S.); Lanthika26@gmail.com (A.L.); phitsanu.p@msu.ac.th (P.P.); poramat.c@msu.ac.th (P.C.)

² Department of Biology, Faculty of Science, Maharakham University, Maha Sarakham 44150, Thailand; waraporn.s@msu.ac.th

³ Synchrotron Light Research Institute (Public Organization), Nakhon Ratchasima 30000, Thailand; catleya@slri.or.th (C.R.); kanjanat@slri.or.th (K.T.); sarayut@slri.or.th (S.T.)

* Correspondence: artit.c@msu.ac.th; Tel.: +66-8971-10157

Abstract: This work aims to develop a multihole atmospheric pressure plasma jet (APPJ) device to increase the plasma area and apply it to a continuous seed treatment system. Broccoli seed was used to study the effects of an atmospheric pressure plasma jet on seed germination and growth rate. An argon flow rate of 4.2 lpm, a plasma power of 412 W, and discharge frequency of 76 kHz were used for seed treatment. The contact angle decreased strongly with the increase in treatment time from 20 s to 80 s. The broccoli seed's outer surface morphology seemed to have been slightly modified to a smoother surface by the plasma treatment during the treatment time of 80 s. However, the cross-sectional images resulted from Synchrotron radiation X-ray tomographic microscopy (SRXTM) confirmed no significant difference between seeds untreated and treated by plasma for 80 s. This result indicates that plasma does not affect the bulk characteristics of the seed but does provide delicate changes to the top thin layer on the seed surface. After seven days of cultivation, the seed treated by plasma for 30 s achieved the highest germination and yield.

Keywords: atmospheric pressure plasma jet; surface treatment; growth rate enhancement



Citation: Srakaew, K.; Chingsungnoen, A.; Sutthisa, W.; Lakhonchai, A.; Poolcharuansin, P.; Chunpeng, P.; Rojviriyaya, C.; Thumanu, K.; Tunmee, S. Development of a Multihole Atmospheric Plasma Jet for Growth Rate Enhancement of Broccoli Seeds. *Processes* **2021**, *9*, 1134. <https://doi.org/10.3390/pr9071134>

Academic Editor: Dariusz Dziki

Received: 13 June 2021

Accepted: 28 June 2021

Published: 29 June 2021

Publisher's Note: MDPI stays neutral with regard to jurisdictional claims in published maps and institutional affiliations.



Copyright: © 2021 by the authors. Licensee MDPI, Basel, Switzerland. This article is an open access article distributed under the terms and conditions of the Creative Commons Attribution (CC BY) license (<https://creativecommons.org/licenses/by/4.0/>).

1. Introduction

Under laboratory conditions, plasmas are generated by applying a voltage between two electrodes. At sufficiently high power, the ionized gases consist of equal concentrations of positive and negative charges and many neutral species. In general, plasmas can be classified according to temperature into thermal and nonthermal plasmas, which are also termed cold plasmas [1]. Because it can operate at low temperatures, surface treatment with cold plasma has been used in numerous industries worldwide, such as semiconductor technology, medicine and cosmetics, packaging technology, textiles, and agriculture [2–4]. In atmospheric pressure cold plasma, ion temperature is close to room temperature. In contrast, the electron temperatures can easily be of the order of several eV (1 eV \cong 11,600 K). This electron temperature range (<10 eV) is responsible for rotational and vibrational excitations of molecules [5]. However, the small fraction of tail electrons in the electron energy distribution function (EEDF) with energies of the order 10 eV or even higher can generate many different chemical processes [6]. For example, the steady-state density of radicals in a nitrogen plasma jet (the mole fraction of water molecules in nitrogen gas is 0.01) with an electron temperature of 1 eV have been calculated by Uhm [7]. The results show that most reactive nitrogen species have a density of around 10^{14} – 10^{16} molecules/cm³ [7]. Argon plasma is frequently used for physical process treatment due to an effective energy transfer to the solid surface. The argon ions bombarding the surface can dislodge contamination

BIOGRAPHY

NAME	MissAnthika Lakhonchai
DATE OF BIRTH	26 October 1994
PLACE OF BIRTH	Udon Thani
ADDRESS	61/11 Nong Phai Sub-district, Mueang Udon Thani District, Udon Thani 41330
EDUCATION	2007 Elementary School, Municipal 7 Rotfai Songkhro School, Mak Khaeng Sub-district, Mueang Udon Thani District, Udon Thani 41000 2013 High School, Non Sung Pittayakhan School, Non Sung, Mueang Udon Thani District, Udon Thani, 41330 2017 Bachelor of Science (Physics), Department of Physics, Faculty of Science, Maharakham University, Khamriang Sub-district, Kantarawichai District, Maha Sarakham 44150 2019 Master of Science (Physics), Department of Physics, Faculty of Science, Maharakham University, Khamriang Sub-district, Kantarawichai District, Maha Sarakham 44150 2022 Doctor of Philosophy (Physics), Department of Physics, Faculty of Science, Maharakham University, Khamriang Sub-district, Kantarawichai District, Maha Sarakham 44150
Research grants & awards	Science Achievement Scholarship of Thailand, SAST
Research output	A. Chingsungnoen, T. Dasri, P. Poolcharuansin, A. Lakhonchai, N. Tidngim, P. Eiamchai, N. Nuntawong, and V. Amornkitbamrung, "Effect of Acetylene Concentration on Structural Properties of Hydrogenated Amorphous Carbon Films Prepared using Showerhead Plasma Chemical Vapor Deposition," Chiang Mai J. Sci., vol. 45, no. 6, pp. 2471–2480, 2018. A. Lakhonchai, A. Chingsungnoen, and P. Poolcharuansin, "Aluminum-doped zinc oxide thin films prepared by reactive dc magnetron sputtering with metal, transition, and oxide modes," KKU Sci., vol. 47, no. 2, pp. 327–338, 2019.

A. Lakhonchai, A. Chingsungnoen, P. Poolcharuansin, N. Pasaja, M. Horprathum, U. Rittihong, C. Euaraksakul, S. Tunmee, N. Chanlek, and H. Akasaka, "Comparing the performance of transparent, conductive ZnO/Ag/ZnO thin films that have an interlayer coating formed by either DC magnetron sputtering or HiPIMS," *Mater. Res. Express*, vol. 6, no. 12, pp.1–10 (126410), 2019.

T. Prada, V. Harnchana, A. Lakhonchai, A. Chingsungnoen, P. Poolcharuansin, N. Chanlek, and V. Amornkitbamrung, "Enhancement of output power density in a modified polytetrafluoroethylene surface using a sequential O₂/Ar plasma etching for triboelectric nanogenerator applications," *Nano Res.*, 2021.

K. Srakaew, A. Chingsungnoen, W. Sutthisa, A. Lakhonchai, P. Poolcharuansin, P. Chunpeng, C. Rojviriyaya, K. Thumanu, and S. Tunmee, "Development of a Multihole Atmospheric Plasma Jet for Growth Rate Enhancement of Broccoli Seeds," *Process.*, vol. 9, no. 7, 1134. 2021.

A. Lakhonchai, A. Chingsungnoen, P. Poolcharuansin, N. Pasaja, P. Bunnak, and M. Suwanno, "Comparison of the structural and optical properties of amorphous silicon thin films prepared by direct current, bipolar pulse, and high-power impulse magnetron sputtering methods," *Thin Solid Films*, vol. 747, 2022.

A. Lakhonchai, A. Chingsungnoen, P. Poolcharuansin, N. Chanlek, S. Tunmee, and U. Rittihong, "Improvement of corrosion resistance and mechanical properties of chrome plating by diamond-like carbon coating with different silicon-based interlayers," *Mater. Res. Express*, vol. 9, no. 5, pp.1–14 (055604), 2022.